Alfred-Wegener-Institut Helmholtz Zentrum für Polar- und Meeresforschung
Forschungsstelle Potsdam, Sektion Periglazialforschung

Universität Potsdam, Institut für Erd- und Umweltwissenschaften

---

Remote Sensing of Rapid Permafrost Landscape Dynamics

Dissertation
zur Erlangung des akademischen Grades
„doctor rerum naturalium“
(Dr.rer.nat.)
in der Wissenschaftsdisziplin „Fernerkundung“

als publikationsbasierte Arbeit eingereicht an der Mathematisch-Naturwissenschaftlichen Fakultät der Universität Potsdam

von

Ingmar Nitze

Potsdam, November 2017

Table of contents

Abstract

The global climate is warming and the northern high latitudes are affected particularly rapidly. Large areas of this region, or 24% of the northern hemisphere, are influenced by perennially frozen ground or permafrost. As permafrost is predominantly dependent on cold mean annual air temperatures, climate warming threatens the stability of permafrost. Since large amounts of organic carbon are stored within permafrost, its thaw would potentially release large amounts of greenhouse gases, which would further enhance climate warming (permafrost carbon feedback).

Thermokarst and thermo-erosion are an indicator of rapid permafrost thaw, and may also trigger further disturbances in their vicinity. The vast Arctic permafrost regions and the wide distribution of thaw landforms makes the monitoring of thermokarst and thermo-erosion an important task to better understand the response of permafrost to the changing climate. Remote sensing is a key methodology to monitor the land surface from local to global spatial scales and could provide a tool to quantify such changes in permafrost regions. With the opening of satellite archives, advances in computational processing capacities and new data processing technology, it has become possible to handle and analyze rapidly growing amounts of data.

In the scope of the changing climate and its influence of permafrost in conjunction with recent advances in remote sensing this thesis aims to answer the following key research questions:

1. How can the extensive Landsat data archive be used effectively for detecting typical land surface changes processes in permafrost landscapes?

2. What is the spatial distribution of lake dynamics in permafrost and which are the dominant underlying influencing factors?

3. How are key disturbances in permafrost landscapes (lake changes, thaw slumps and fire) spatially distributed and what are their primary influence factors?

To answer these questions, I developed a scalable methodology to detect and analyze permafrost landscape changes in the ~29,000 km^2 Lena Delta in North-East Siberia. I used all available peak summer data from the Landsat archive from 1999 through 2014 and applied a

highly automated robust trend-analysis based on multi-spectral indices using the Theil-Sen algorithm. With the trends of surface properties, such as albedo, vegetation status or wetness, I was able identify local scale processes, such as thermokarst lake expansion and drainage, river bank erosion, and coastal inundation, as well as regional surface changes, such as wetting and greening at 30m spatial resolution. This method proved to be robust in indicating typical landscape change processes within an Arctic coastal lowland environment dominated by permafrost, which has been challenging for the application of optical remote sensing data. The scalability of the highly automated processing allows for further upscaling and advanced automated landscape process analysis.

For a targeted analysis of well-known disturbances affecting permafrost (thermokarst lakes, retrogressive thaw slumps and wildfires), I used advanced remote sensing and image processing techniques in conjunction with the processed trend data. Here I combined the trend analysis with machine-learning classification and object based image analysis to detect lakes and to quantify their dynamics over a period from 1999 through 2014 within four different Arctic and Subarctic regions in Alaska and Siberia totaling 200,000 km². I found very strong precipitation driven lake expansion (+48.48 %) in the central Yakutian study area, while the study areas along the Arctic coast showed a slight loss of lake area (Alaska North Slope: -0.69%; Kolyma Lowland: -0.51%) or a moderate lake loss (Alaska Kobuk-Selawik Lowlands: -2.82%) due to widespread lake drainage. The lake change dynamics were characterized by a large variety of local dynamics, which are dependent on several factors, such as ground-ice conditions, surface geology, or climatic conditions.

In an even broader analysis across four extensive north-south transects covering more than 2.3 million km², I focused on the spatial distribution and key factors of permafrost region disturbances. I found clear spatial patterns for the abundance of lakes (predominantly in ice-rich lowland areas), retrogressive thaw slumps (predominantly in ice-rich, sloped terrain, former glacial margin), and wildfires (boreal forest). Interestingly, apart from frequent drainage at the continuous-discontinuous permafrost interface, lake change dynamics showed spatial patterns of expansion and reduction that could not be directly related to specific variables, such as climate or permafrost conditions over large continental-scale transects. However, specific variables could get related to specific lake dynamics in within locally defined regions.

Trend datasets of vegetation status (NDVI) were combined with high-resolution detailed geomorphological land-cover classification information and climate data to map tundra productivity in a heterogeneous landscape in northern Alaska. After decades of increasing productivity (greening), recently tundra vegetation showed a reverse trend of decreased productivity, which is predicted to continue with increasing temperatures and precipitation.

In this thesis project I developed methods to analyze rapid landscape change processes of various scales in northern high latitudes with unprecedented detail by relying on spatially and temporally high resolution Landsat image time series analysis across very large regions. The findings allow a unique and unprecedented insight into the landscape dynamics of permafrost over large regions, even detecting rapid permafrost thaw processes, which have a small spatial footprint and thus are difficult to detect. The multi-scaled approach can help to support local-scale field campaigns to precisely prepare study site selection for expeditions, but also pan-arctic to global-scale models to improve predictions of permafrost thaw feedbacks and soil carbon emissions in a warming climate.

Zusammenfassung

Das globale Klima erwärmt sich und die hohen nördlichen Breiten sind besonders stark davon betroffen. Ein großer Teil dieser Region, ca. 24% der Nordhalbkugel, sind von saisonal oder dauerhaft gefrorenen Böden, dem Permafrost beeinflusst. Aufgrund der starken Abhängigkeit von kalten Temperaturen ist Permafrost besonders anfällig gegenüber der Klimaerwärmung. Große Mengen organischen Kohlenstoffs sind bisher im Permafrost gebunden, ein Auftauen könnte die Emission großer Mengen von Treibhausgasen in die Atmosphäre bewirken, was eine noch stärkere Erwärmung zur Folge hätte (Permafrost Kohlenstoff Kreislauf).

Thermokarst und Thermoerosion sind Indikatoren für schnelles Permafrosttauen, was wiederum weitere Erosion und Störungen der näheren Umgebung auslösen kann. Die weitläufige arktische Permafrostregion mit seiner weiten Verbreitung von Auftaulandformen macht die Beobachtung von Thermokarst und Thermoerosion eine wichtige Aufgabe um die Auswirkungen der Klimaerwärmung auf den Permafrost zu verstehen. Fernerkundung ist eine Schlüsselmethode um die Landoberfläche im lokalen bis globalen Maßstab zu beobachten und Veränderungen in der Permafrostregion zu quantifizieren. Mit der Öffnung und freien Verfügbarkeit von Satellitenarchiven, dem technischen Fortschritt der Informatik und neuen Prozessierungstechniken ist es möglich geworden riesige Datenmengen aus exponentiell wachsenden Datenarchiven zu prozessieren.

In Anbetracht des fortschreitenden Klimawandels und dessen Einfluss auf den Permafrost in Kombination mit dem technologischen Fortschritt in der Fernerkundung und Informatik zielt diese Dissertation auf die Beantwortung folgender wissenschaftlicher Fragestellungen:

1. Wie kann das frei verfügbare Landsatarchiv effektiv genutzt werden um Veränderungen der Landoberfläche großräumig in Permafrostregionen zu detektieren?

2. Wie ist die räumliche Verteilung von Seeveränderungsdynamiken in Permafrostregionen und was sind deren Haupteinflussfaktoren?

3. Wie sind die wichtigsten Störungen in Permafrostlandschaften (Seeveränderungen, rückschreitende Erosionsformen und Feuer) raumlich verteilt und was sind deren Haupteinflussfaktoren?

Um diese wissenschaftlichen Fragen zu beantworten, habe ich eine skalierbare Methode entwickelt um Landschaftsveränderungen im Permafrost im ca. 29.000 km² großen Lena Delta in Nordost-Sibirien zu detektieren und zu analysieren. Hierbei wurden alle Hochsommeraufnahmen des Landsatarchives von 1999 bis 2014 verwendet und eine hochautomatisierte, robuste Trendanalyse auf multi-spektralen Indizes mit Hilfe des Theil-Sen Algorithmus durchgeführt. Mit der Information über zeitliche Trends der Beschaffenheit der Landoberfläche, wie z.B. Albedo, Vegetation oder Feuchtigkeit, konnten sowohl lokale Veränderungen, wie z.B. die Expansion oder Drainage von Thermokarstseen, Ufererosion oder Überflutung küstennaher Gebiete, als auch regionale Dynamiken wie Vegetations- oder Feuchtigkeitsveränderungen mit einer räumlichen Auflösung von 30m gemessen werden. Dieses Vorgehen erwies sich als robuste Methode um typische Landschaftsveränderungen in von Permafrost dominierten arktischen Tiefländern, welche sich bisher als äußerst schwierig für optische Fernerkundung erwiesen. Die Skalierbarkeit der hochautomatisierten Prozesskette erlaubt die Ausweitung auf eine großflächige, automatische Landschaftsprozessanalyse.

Für die zielgerichtetete Analyse von bekannten Permafrost beeinflussenden Störungen (Thermokarstseen, rückschreitende Erosion, and Feuer) wurden fortgeschrittene Fernerkundungs- und Bildprozessierungsmethoden in Verbindung mit den prozessierten Trenddaten angewandt. Hierbei kombinierte ich die Trendanalyse mit Machine-Learning Klassifikationsverfahren und objektbasierter Bildanalyse um Seen und deren Dynamiken im Zeitraum von 1999 bis 2014 in vier verschiedenen arktischen und subarktischen Studiengebieten in Alaska und Sibirien mit einer Gesamtfläche von 200.000 km². Das zentraljakutische Studiengebiet wies eine starke niederschlagsbedingte Seeausdehnung auf (+48,48%), während die küstennahen Regionen einen leichten (Alaska North Slope: -0,69%; Kolyma Lowland: -0.51%) oder moderaten Rückgang (Alaska Kobuk-Selawik Lowlands: -2.82%) der Wasserfläche durch teils weitverbreitete Seedrainage verzeichneten. Die Seeveränderungen waren durch starke räumliche Unterschiede gekennzeichnet, welche von unterschiedliche Faktoren wie Bodeneisgehalt, Oberflächengeologie oder klimatischen Bedingungen beeinflusst wurden.

In einer noch großflächigeren Analyse von über 2,3 Mio. km² Fläche fokussierte ich mich auf die räumliche Verteilung der Hauptfaktoren von Störungen im Permafrost. Dabei kamen

deutliche Muster der Seeverteilung (hauptsächlich in bodeneisreichen Tiefländern), von rückschreitenden Erosionsformen (vorwiegend in eisreichem und hügeligen Terrain entlang ehemaliger Eisrandlagen) und Feuer (borealer Wald) zu Tage. In großräumigem Maßstab konnten Seeveränderungen, abgesehen von weitverbreiteter Seedränage an der Grenze zwischen kontinuierlichem und diskontinuierlichem Permafrost, hingegen keine eindeutigen Einflussfaktoren wie Klima, Permafrostbedingungen oder Geomorphologie zugeordnet werden. Lediglich in vereinzelten räumlich begrenzten Gebieten bestimmten einzelne spezifische Einflussfaktoren die Seeveränderung.

In dieser dissertation entwickelte Vegetationstrenddaten wurden zusammen mit einer detaillierten geomorphologischen Landbedeckungsklassifizierung sowie mit Klimadaten kombiniert um die Produktivität der Tundravegetation in Nordalaska im Zusammenhang mit dem sich wandelnden Klima zu kartieren und vorherzusagen. Nach Jahrzehnten verstärkter Vegetationsentwicklung, ist seit kurzem ein umgekehrter Trend mit verringerter Produktivität zu beobachten, welcher sich mit weiter steigenden Temperaturen und erhöhtem Niederschlage fortsetzen wird.

In diesem Projekt entwickelte ich Methoden zur multi-skaligen Analyse unterschiedlicher schneller Landoberflächenänderungen in hohen nördlichen Breiten in bisher seltener Detailgenauigkeit basierend auf zeitlich hochaufgelösten Landsat Satellitenzeitseriendaten über große räumliche Ausdehnung. Die Ergebnisse erlauben einen einzigartigen und bisher nicht dagewesenen großflächigen Einblick in Permafrostlandschaftsdynamiken, sogar von kleinflächigen und daher schwierig zu detektierenden Veränderungsprozessen. Der multi-skalige Prozessierungsansatz kam einerseits zur Unterstützung und Planung von Feldkampagnen und zur Detektion und Auswahl von relevanten Studiengebieten zum Einsatz, und kann auch für die Parametrisierung und Validierung von pan-arktischen und globalen Modellen zur Vorhersage von Rückkopplungseffekten im Permafrost und Kohlenstoffemissionen in einem sich erwärmenden Klima verwendet werden.

Abbreviations and Nomenclature

Notation	Full Name / Description
%	Percent
<	Smaller than
>	Greater than
±	Plus-minus
°C	Temperature in degrees Celsius (centigrade)
AbT	Abalakhskaya Terrace
ACIA	Arctic climate impact assessment
ACP	Arctic Coastal Plain
AF	Arctic Foothills
AK	Alaska
AKS	Alaska Kobuk-Selawik Lowlands
AVHRR	Advanced Very High Resolution Radiometer
AWI	Alfred Wegener Institute for Polar- and Marine Research
BeT	Bestyakhskaya Terrace
BFAST	Breaks For Additive Season and Trend Algorithm
BRT	Boosted Regression Tree
C	Continuous Permafrost
CAVM	Circum-Arctic Vegetation Map
CH4	Methane
CI	Confidence Interval
CLC	Coalescent low-center polygons
C-LW	Change land to water
CO2	Carbon Dioxide
C-PF	Continuous Permafrost
CS	coastal saline water
C-WL	Change water to land
CYA	Central Yakutia
D	Discontinuous Permafrost
DBEST	Detecting Breakpoints and Estimating Segments in Trend Algorithm
DEM	Digital Elevation Model
D-PF	Discontinuous Permafrost
DS	Drained slopes
DUE	Data User Element
e.g.	exempli gratia (for example)
ECMWF	European Centre for Medium-Range Forecast
ECV	Essential Climate Variable
EmT	Emilskaya Terrace
EROS	Earth Resources Observation and Science Center
ESA	European Space Agency
ESPA	EROS Science Processing Architecture
ETM+	Enhanced Thematic Mapper

FC	Flat-center polygons
FMask	Landsat Masking Algorithm
GCOS	Global Climate Observing System
GFC	Global Forest Change
GHG	Greenhouse Gas
GINA	Geographic Information Network of Alaska
GLOVIS	USGS Global Visualization Viewer
GPS	Global Positioning System
ha	Hectare
HC	High-center polygons
I	Isolated (permafrost)
Ice	Ice/snow
ICP	Inner Coastal Plain
IPA	International Permafrost Association
IPCC	Intergovernmental Panel on Climate Change
K	Temperature in Kelvin
km²	Square Kilometer
KOL	Kolyma Lowland
L1T	Level-1 Terrain Corrected
LaSRC	Surface Reflectance Code
LC	Low-center polygons
LGM	Last Glacial Maximum
LO	Lake object
LULC	Land Use Land Cover
MAAT	Mean Annual Air Temperature
MAP	Mean Annual Precipitation
MaT	Maganskaya Terrace
MERIS	MEdium Resolution Imaging Spectrometer
MLC	Machine-learning Classification
MODIS	Moderate Resolution Imaging Spectrometer
MSI	Multi-spectral Index
NDMI	Normalized Difference Moisture Index
nDTLB	Nonpatterned drained thaw lake basins
NDVI	Normalized Difference Vegetation Index
NDWI	Normalized Difference Water Index
NIR	Near Infrared
NOAA	National Oceanic and Atmospheric Administration
NSL	North Slope
NW	Northwest
OBIA	Object-based image analysis
OCP	Outer Coastal Plain
OLI	Operational Land Imager
OOB	Out-of-bag accuracy
p	Probability
PANGAEA	Data Publisher for Earth & Environmental Science

Pg	Petagram
PRD	Permafrost Region Disturbance
px	Pixel
RC	Riparian corridors
RCP	Representative Concentration Pathways
RF	Random Forest
RTS	Retrogressive thaw slump
S	Sporadic (permafrost)
SB	Sandy barrens
SD	Sand dunes
S-L	Stable land
SMR	Soil moisture regime
SNAP	Scenarios Network of Alaska and Arctic Planning
SPOT	Satellite pour l'Observation de la Terre
S-W	Stable water
SWIR1	Shortwave Infrared 1
SWIR2	Shortwave Infrared 2
T1	Transect 1
T2	Transect 2
T3	Transect 3
T4	Transect 4
TBFM	Trend Based Fire Mask
TCB	Tasseled Cap Brightness
TCG	Tasseled Cap Greenness
TCW	Tasseled Cap Wetness
TK	Thermokarst
TL	Teshekpuk Lake
TM	Thematic Mapper
TOA	Top-of-Atmosphere
TyT	Tyungyulyuyskaja Terrace
USGS	United States Geological Survey
UTM	Universal Transverse Mercator
VHR	Very high resolution
WMO	World Meteorological Organization
WRS-2	World Reference System-2
YAC	Yedoma-Alas Complex
YK	Yukon-Kuskokwim
YOCP	Younger Outer Coastal Plain
z.B.	zum Beispiel (german: for example)

1. Introduction

1.1 Scientific Background

1.1.1 Climate and Permafrost

The Earth's climate has been changing over the last decades and is projected to be affected by further increasing temperatures (IPCC, 2013). In the northern high latitudes, the climate is warming about twice as strong as the entire northern Hemisphere, an effect which is termed Arctic amplification (Serreze & Barry, 2011). Temperatures are projected to increase on average by 5°C to more than 10°C until the end of the century (IPCC, 2013) (Scenario RCP 8.5) over large parts of the northern high latitudes (see Figure 1.1).

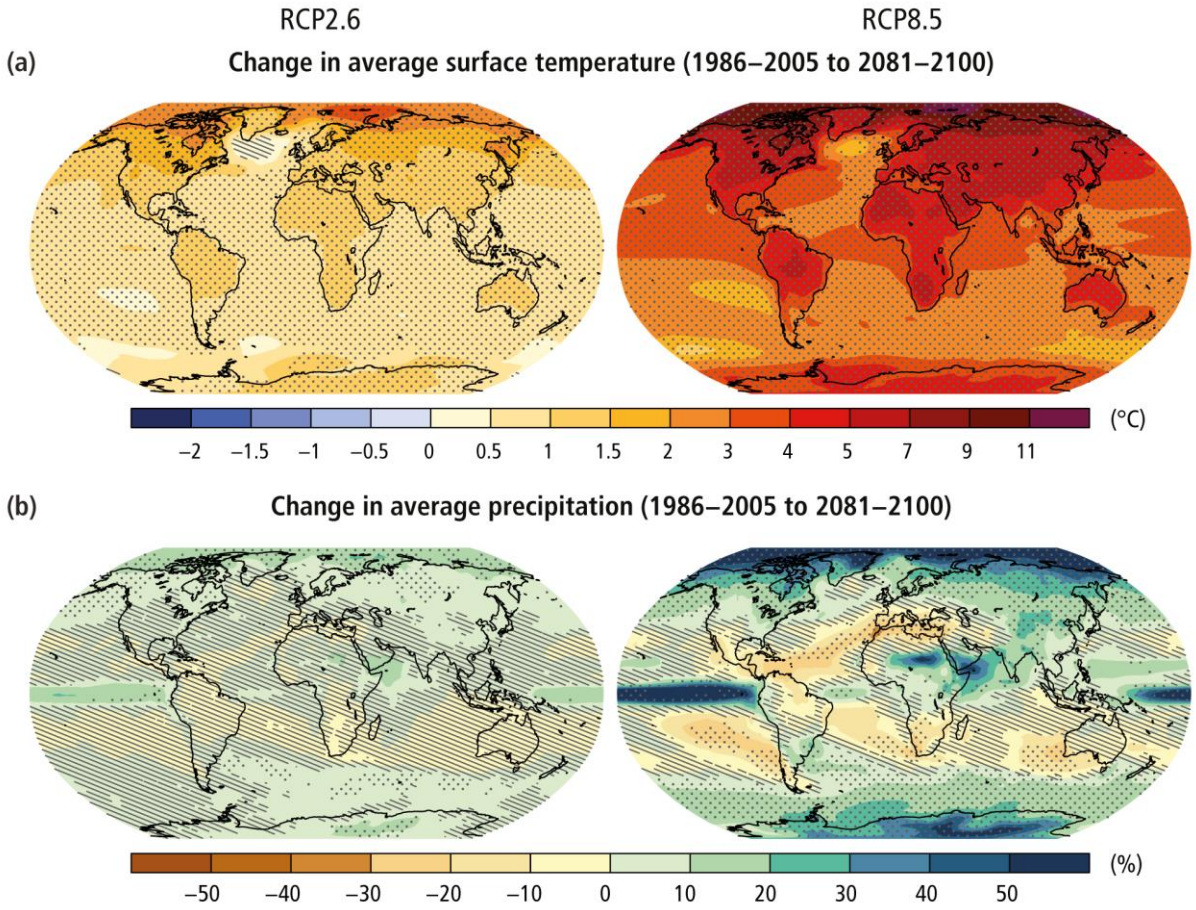

Figure 1.1: Global climate change model results for temperature (a) and precipitation (b) anomalies based on low (left) (RCP 2.6) and high (right) (RCP8.5) emission scenarios for the end of the 21st century compared to the recent climate (1986-2005) (from IPCC, 2013).

Arctic warming particularly affects the cryosphere, including ice sheets, glaciers, sea ice, freshwater ice, snow cover, and permafrost. As the cryosphere is largely dependent on cold temperatures, it is highly vulnerable against further increasing temperatures.

The permafrost region is located where some of the strongest climate changes are projected and covers about 23 million km² or 24% of the land mass of the northern hemisphere (Zhang, Barry, Knowles, Heginbottom, & Brown, 2008). Permafrost occurs mainly across the large, unglaciated regions of Siberia and North America (see Figure 1.2), as well as high mountain regions such as the Tibetan Plateau. Permafrost is defined as any ground material, which has a temperature of 0°C or less for at least two consecutive years (Van Everdingen, 2005). It is primarily dependent on a negative thermal energy balance, resulting from low mean annual air temperatures as the primary large scale forcing as well as more local or regional influences on the ground-thermal regime, such as land cover, snow depth, surface hydrology, and geology (Shur & Jorgenson, 2007). Changes of these primary drivers may exceed thresholds where permafrost becomes subject to degradation (Jorgenson, Racine, Walters, & Osterkamp, 2001) and eventually irreversible thaw (Schaefer, Lantuit, Romanovsky, Schuur, & Witt, 2014)This potentially leads to the thaw of permafrost organic matter, microbial decomposition, and the release of carbon to the atmosphere as carbon dioxide or methane (Walter Anthony, Anthony, Grosse, & Chanton, 2012). The release of these potent greenhouse gases could trigger further warming and therefore intensify permafrost thaw, also known as the permafrost carbon feedback (Schuur, et al., 2015). Since permafrost is a significant reservoir of soil organic matter, currently storing about 1035±150 Pg SOC in the upper 3 m of soils (Schuur, et al., 2015), widespread permafrost thaw has a strong potential to impact the global carbon budget. The permafrost carbon feedback, not yet considered in IPCC global climate models (Lawrence, Slater, & Swenson, 2012) and thus climate projections, may represent an additional challenge to reach political climate targets such as the Paris Agreement goal to limit climate warming to 1.5°C above pre-industrial values.

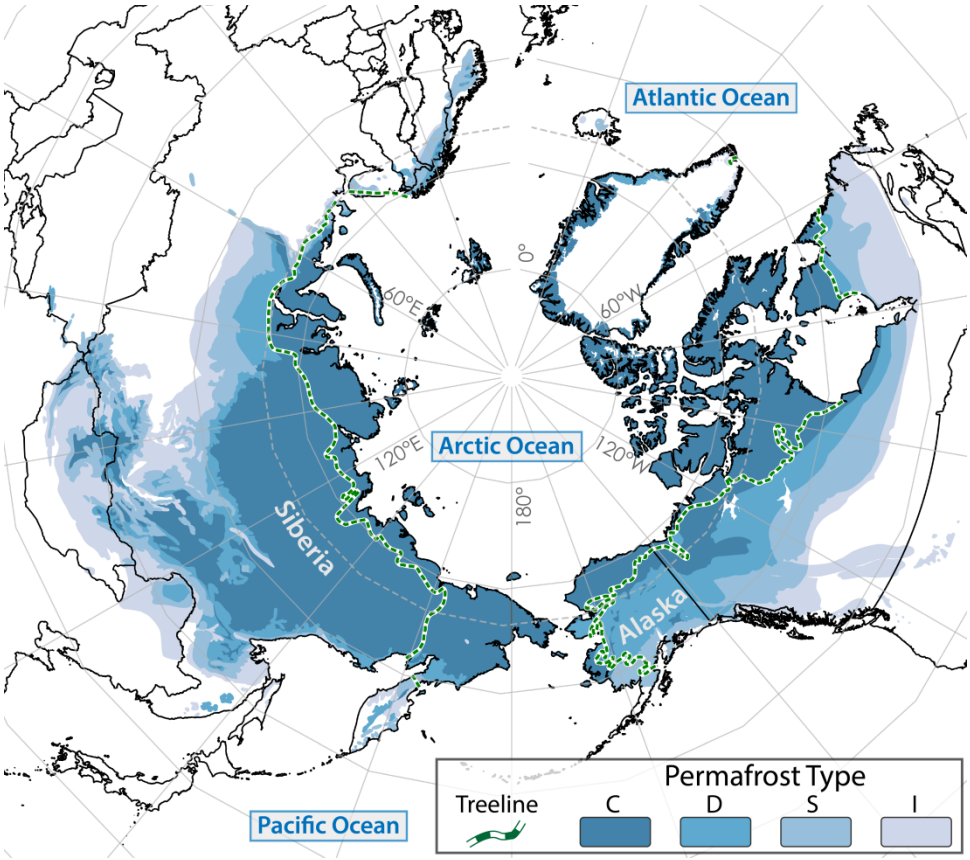

Figure 1.2: Distribution of Permafrost on the northern Hemisphere (Brown, Ferrians Jr, Heginbottom, & Melnikov, 1997) and the modern treeline (Walker, et al., 2005)

In addition to the projected large scale climatic changes, permafrost is also affected by local dynamics, which have the potential to quickly alter the local thermal state of permafrost and lead to degradation and thaw. One such process is thermokarst, where permafrost degrades quickly after initial thaw of excess ground ice (Grosse, Jones, & Arp, 2013; Jorgenson & Shur, 2007). Typically, after initial thaw of ground ice and subsidence ponds are developing. Consequentially, ponds expand into the surrounding permafrost and thaw the permafrost around and below. Once the water body becomes deep enough to not completely refreeze each winter, it decouples the ground from the cold winter air temperatures and forms a talik (unfrozen sediments within permafrost) below the lake bottom. The unfrozen taliks are an important zone for microbial decomposition of former permafrost organic matter (Schuur, et al., 2008). This decomposition triggers the release of carbon, largely in the form of methane, into the atmosphere. Larger water bodies retain summer heat energy and further enhance active and now year-round thaw of the underlying permafrost even during winter. Finally, laterally growing lakes or ponds may drain after reaching a drainage gradient due to incision or bank overflow as well as talik penetration and ground-water connection in thin

discontinuous permafrost, leaving parts of the former lake basin exposed to cold mean annual air temperatures again. Permafrost thus can build up again in high northern latitudes. In some lowland regions, this process of lake formation, growth, and drainage may undergo several generations and cycles (see Figure 1.3) (Jorgenson & Shur, 2007; Grosse, Jones, & Arp, 2013). The occurrence of thermokarst lakes even under very cold climatic conditions suggests that this disturbance is not purely climate-driven and makes thermokarst lake dynamics a widespread and highly important landscape shaping process within permafrost regions

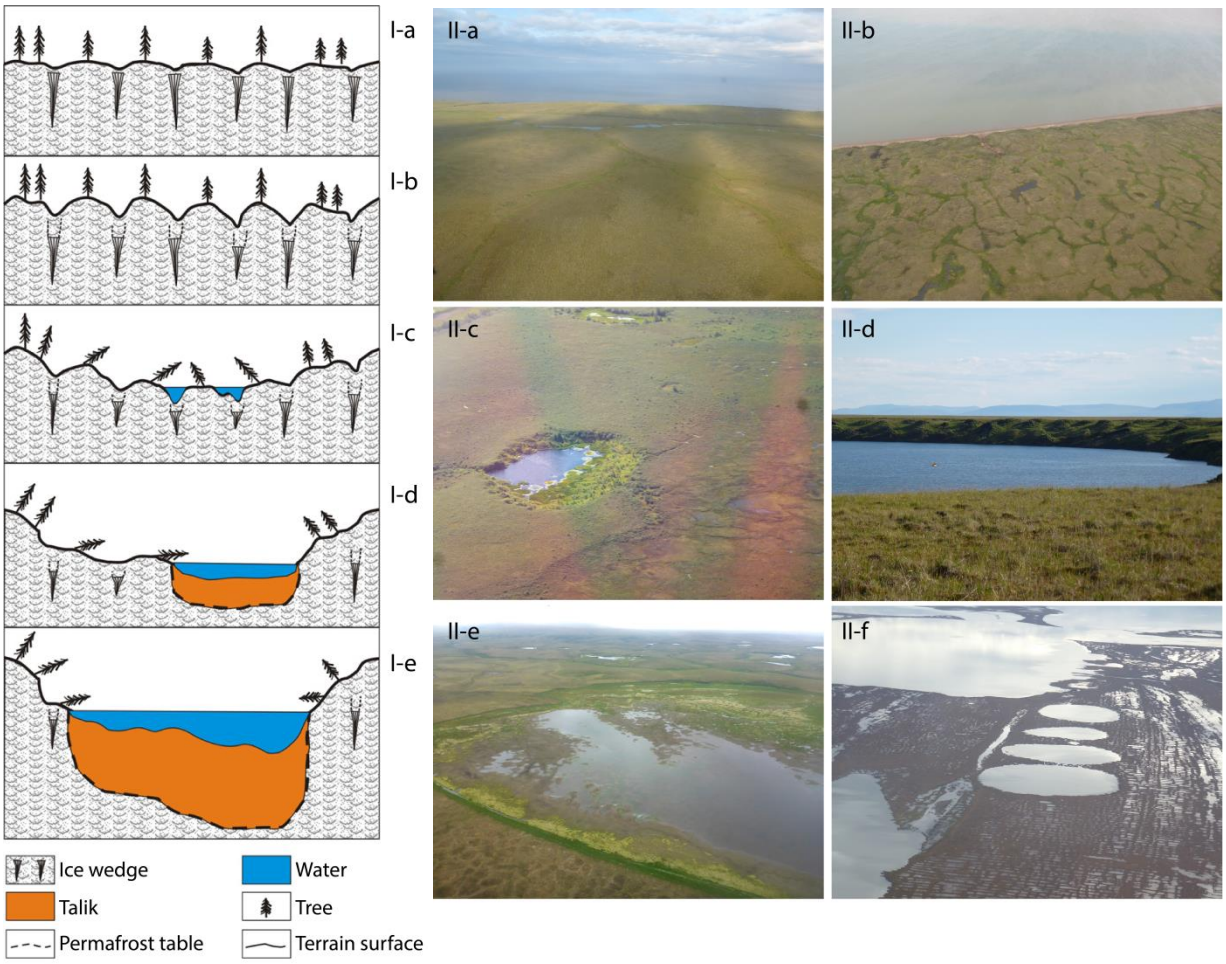

Figure 1.3: Schematic drawing of thermokarst evolution (from Grosse, Jones, & Arp, 2013) and corresponding examples from tundra regions in Alaska and northern Siberia. I-a: Nearly undisturbed permafrost; I-b: Initial thermokarst with surface deformation due to ice-wedge degradation; I-c: Development of thermokarst ponds; I-d: Small thermokarst lake with shallow developing talik; I-e: Large thermokarst lake with deep talik. II-a: Nearly undisturbed permafrost in NE-Siberia; II-b: Ice-wedge degradation in N-Alaska; II-c: Small thermokarst lake/pond in W-Alaska (photo: J.Strauss); II-d: Large deep thermokarst lake in NE-Siberia; II-e: Recently drained thermokarst lake with bare lake-sediments, initial vegetation and lake remnants in W-Alaska; II-f: Complex thermokarst landscape with several generations of thermokarst lakes and basins.

(Olefeldt, et al., 2016).

Land surface changes in permafrost regions can be an indicator of permafrost degradation due to disturbances such as thermokarst or thermo-erosion. In turn, these permafrost region disturbances (PRD) can have a direct influence on the surrounding ground stability. Therefore, they can cause further degradation and trigger new PRD beyond their original extent. The most influential PRD include thermokarst lake development, retrogressive thaw slumps, or fire, but also anthropogenic influences, such as agriculture, road construction or mining of mineral resources. Their irregular abundance and often rapid development, from days to several years, makes it difficult to track and monitor these disturbances across large regions.

Although sparsely populated, changes in permafrost may also influence the livelihood of communities in the permafrost region (Crate, et al., 2017; Marino, 2012). The stability of infrastructure (Nelson, Anisimov, & Shiklomanov, 2001), availability of natural resources, such as drinking water (Chambers, et al., 2007; White, Gerlach, Loring, Tidwell, & Chambers, 2007), traditional subsistence lifestyle (White, Gerlach, Loring, Tidwell, & Chambers, 2007), but also the existence of entire northern communities (Marino, 2012) might be highly endangered as a consequence of the rapidly warming climate and degrading permafrost in the Arctic.

Due to these many factors, permafrost is a key component of northern environments that requires monitoring in order to understand the local to global consequences of climate change in the Arctic. Local-scale changes from permafrost thaw, due to their widespread abundance and rapid development, may potentially have global-scale implications. The importance of permafrost on the climate system has been recognized by the scientific community and political stakeholders and was therefore identified as an Essential Climate Variable (ECV) by the World Meteorological Organization (WMO) (GCOS, 2010). Although permafrost is defined as an ECV, to date it is not sufficiently implemented in global-scale climate models (Schaefer, Lantuit, Romanovsky, Schuur, & Witt, 2014). Recently, first approaches have been undertaken to model the influence of permafrost carbon feedbacks on the global climate (Koven, et al., 2011; Schneider von Deimling, et al., 2015). However, many variables are still missing or are insufficiently implemented to fully understand the influence of climate change on permafrost and vice versa and current models have a wide range of uncertainties (Lawrence, Slater, & Swenson, 2012). The knowledge gap concerning the abundance,

distribution, and rates of rapid landscape dynamics within the permafrost region and the gap between spatial scales of field investigations to climate model grids continue to be one of the main obstacles for estimating the impact of permafrost thaw on global climate in this century. To overcome this knowledge gap, this project aimed at observing and quantifying the processes that are related to permafrost changes over large regions.

1.1.2 Remote Sensing

Permafrost regions are characterized by harsh environmental conditions, remoteness and an expansive spatial extent, which makes detailed field-based observations and monitoring only feasible on local spatial scales in limited accessible sites. For the detection and monitoring of regional or larger scale landscape processes, remote sensing has been proven to be an excellent methodology (Westermann, Duguay, Grosse, & Kääb, 2015). Remote sensing helps to analyze changing landscape information over large regions, in different spectral wavelengths, and with several acquisitions over longer periods.

Airborne earth observation data are available since the mid-20th century for many Arctic regions, but accessibility and especially observation frequency of the data is usually very limited for these sources. With the launch of the Landsat mission in the 1970's, with its several generations of satellites, a new age of global-scale space-borne earth observation was launched. In addition to the 30m multi-spectral Landsat data, many other optical imaging sensors and platforms (e.g. SPOT, MODIS, Sentinel 1-3, Worldview) were launched over the last 20 years, adding a wide variety of potential earth-observation data, from single snapshot very-high-resolution (VHR) acquisitions, to high frequency observations, but only low spatial resolution.

With the opening of the Landsat archive for free data usage in 2008 (Woodcock, et al., 2008) and the latest open-data strategy of many space agencies, the amount of freely available remote sensing data has been growing quickly. This plethora of image data stimulated completely new data-centric applications, which focus on change analyses using multi-temporal acquisitions, a practice, which would have been cost-prohibitive without freely available data (Wulder, Masek, Cohen, Loveland, & Woodcock, 2012) (Zhu Z. , 2017). Until recently, remote sensing based time-series analysis was largely carried out with low resolution data, such as MODIS, MERIS or AVHRR. With these data, spatially extensive processes, such as vegetation changes, or large-scale land-cover patterns can be monitored (Hansen, DeFries,

Townshend, & Sohlberg, 2000; Friedl, et al., 2002). Local-scale changes, which are typical for landscape dynamics in permafrost regions, e.g. thermokarst lake expansion or retrogressive thaw slump growth, are usually too small to be detected with spatial resolutions of 250 m or coarser. Therefore, data in finer resolution are necessary to detect the major indicators of permafrost landscape dynamics and to quantify these on decadal time scales.

With the growth of data archives, processing and storage capabilities fortunately have grown as well to allow efficient storage and processing of large amounts of image data. These different factors promoted the application of time-series analysis with finer resolution data (Hansen, et al., 2013; Pekel, Cottam, Gorelick, & Belward, 2016). The analysis of permafrost features and dynamics in the high latitudes may also benefit from these developments, since observable features often are small in extent and characterized by rapid changes but also spread out over large regions.

Due to frequent cloud cover, low sun angles and a very short summer season, optical remote sensing in the high latitudes is a highly challenging task (Stow, et al., 2004). However, at the same time the polar proximity provides a strong overlap of satellite overpasses, improving the satellite revisit times two- to five-fold, compared to tropical regions. Such high imaging frequency partially offsets the challenging conditions. Other sensor systems, e.g. radar can be a suitable alternative or addition to optical sensors, because they are independent of favorable weather conditions or illumination. However, their automated operational application for land monitoring over longer time-series is rather limited, due to the lack of a consistent data stream in the past caused by the strong variety and limited availability of sensors, inconsistent acquisition patterns and costly data access. With the launch of radar missions that provide data for free (e.g. Sentinel-1), operational applications started to include these potentially valuable data sources.

With new technical approaches to analyze the continuously growing stream and archives of earth observation data, it is now possible to analyze temporal trends and patterns. In conjunction with a sufficiently high spatial resolution, new pathways emerge for the remote sensing-based analysis of changes in permafrost landscapes.

1.1.3 Research Questions

Due to the latest technological advances and arising questions of permafrost science we aim to answer the following research questions.

1. How can the extensive Landsat data archive be used effectively for detecting typical land surface changes processes in permafrost landscapes?

2. What is the spatial distribution of lake dynamics in permafrost and which are the dominant underlying influencing factors?

3. How are key disturbances in permafrost landscapes (lake changes, thaw slumps and fire) spatially distributed and what are their primary influence factors?

1.2 General Approach

Within this project I used optical remote sensing data, machine-learning and advanced image processing techniques to answer the key research questions. The remote sensing processing included the development of highly automated processing chains for the creation of datasets, which then were used for the detection of spatio-temporal changes in permafrost landscapes. A highly automated processing chain allows for the fast processing of large amounts of data with minimal user intervention in order upscale processing and analysis to large regions. The processing chain developed here was built in the programming language *python* and wraps all individual processing steps together from image acquisition (data ordering, download, file operations) to image pre-processing (image stacking, masking, sub-setting) to radiometric data operations (calculation of multi-spectral indices), to multi-temporal image analysis. The same principle of automation was applied to the processing of higher-level information, where I used state-of-the-art machine-learning classification and object based image-analysis for the detection and characterization of lake changes, retrogressive thaw slumps, and wildfire burn scars.

For the support and validation of the remote sensing based methods, I gathered different local scale data during several field expeditions to the Lena Delta region in north-eastern Siberia (2014), northern Alaska (2015, 2016), and western Alaska (2016), as well as synthesized such data from collaborators. During field campaigns I acquired ground based information, such as

GPS data, lake bathymetry profiles, and airborne information from aerial survey flights. More detailed information on specific methodologies is given in Chapters 2 to 5.

1.3 Thesis Structure

The introductory chapter provides background information, state-of-the-art and key objectives for this study. The main part is structured into four chapters where each chapter consists of one original research article, which are published, in revision (minor) or in preparation for submission to international peer-reviewed journals. The details of the publications are listed in 1.4. The study in chapter 2 “Detection of landscape dynamics in the Arctic Lena Delta with temporally dense Landsat time-series stacks” describes a methodology to derive typical change processes in the north-east Siberian Lena Delta, which is based on automated image processing and robust trend analysis of data from the Landsat archive. The study in chapter 3 “Landsat-Based Trend Analysis of Lake Dynamics across Northern Permafrost Regions” uses the developed trend analysis as well as machine learning and advanced image processing techniques to find lake dynamics in four Arctic and Subarctic regions in Alaska and Siberia. The study in chapter 4 “Remotely sensing recent permafrost region disturbances across Arctic to Subarctic transects” analyzes the extent, distribution and key influencing factors of permafrost related disturbances (lakes, retrogressive thaw slumps and wildfire) based on the developed methodologies in chapters 2 and 3, as well as additional publicly available data sources. This study covers over 2.3 million km² over four large north-south transects in North America and Siberia, which envelop a wide range of permafrost types, geological and ecological conditions. The study in chapter 5 “Tundra landform and vegetation productivity trend maps for the Arctic Coastal Plain of northern Alaska” presents the methodology and technical aspects of the analysis of the response of tundra vegetation productivity on recent and predicted future climate change in northern Alaska using remote sensing data, GIS analysis and modelling approaches. The accompanying paper in the appendix of this thesis, “Reduced arctic tundra productivity linked with landform and climate change interactions”, focusses on the results and implications of tundra productivity changes.

Chapter 6 synthesizes and discusses the results of the presented studies and puts them into the broader scientific context. The final chapter provides an outlook of yet untapped fields, which should be addressed in future research.

1.4 Author's contributions

1.4.1 Chapter 2

Nitze, I., & Grosse, G. (2016). Detection of landscape dynamics in the Arctic Lena Delta with temporally dense Landsat time-series stacks. *Remote Sensing of Environment*, *181*, 27-41.

Ingmar Nitze designed the study, carried out the programming, data processing and analysis, and wrote the manuscript. Guido Grosse provided guidance for the study design and reviewed, edited, and revised the manuscript. Ingmar Nitze and Guido Grosse conducted field work in the Lena Delta for ground truthing activities.

1.4.2 Chapter 3

Nitze, I., Grosse, G., Jones, B.M., Arp, C.D., Ulrich, M., Fedorov, A., & Veremeeva, A. (2017). Landsat-Based Trend Analysis of Lake Dynamics across Northern Permafrost Regions. *Remote Sensing*, *9*(7), 640.

Ingmar Nitze designed the framework of this study, developed the data processing and analysis pipeline, conducted the analysis, and wrote the manuscript with input of the co-authors. Guido Grosse provided guidance for the framework of this study and revised and commented the manuscript. Ingmar Nitze and Guido Grosse conducted ground truthing activities in the Lena Delta, on the Alaska North Slope, and in Northwestern Alaska. All other authors conducted field work in one of the study regions and provided local lake specific data, field knowledge specific to each study site, and revised and commented the manuscript.

1.4.3 Chapter 4

Nitze, I., Grosse, G., Jones, B.M., Boike, J. & Romanovsky V. (*in prep*). Remotely sensing recent permafrost region disturbances across Arctic to Subarctic transects. *Nature Communations*

Ingmar Nitze designed the study, developed the data processing and analysis pipeline, conducted the analysis, and wrote the manuscript. Guido Grosse provided guidance for the framework of this study and revised and commented the manuscript. Ingmar Nitze and Guido Grosse conducted ground truthing activities in the Lena Delta, on the Alaska North Slope, and in Northwestern Alaska. Benjamin Jones provided oblique aerial imagery for specific sites.

All other authors conducted field work in one of the study regions and provided local specific data, valuable field knowledge specific to each study site, and revised and commented the manuscript.

1.4.4 Chapter 5

Lara M.J., Nitze, I. Grosse, G. & McGuire, A.D. (*in revision*). Tundra landform and vegetation productivity trend maps for the Arctic Coastal Plain of northern Alaska. *Nature Scientific Data.*

Mark J. Lara designed the study, developed the analysis, including remote sensing processing, GIS Analysis and modelling, and wrote the manuscript. Ingmar Nitze and Guido Grosse developed and processed NDVI trend data and edited, commented and revised the manuscript. Guido Grosse and A. David McGuire edited, commented and revised the manuscript and provided site specific and permafrost related knowledge.

1.4.5 Appendix Paper 1

Lara M.J., Nitze, I. Grosse, G. Martin, P., and McGuire, A.D. (*in revision*). Reduced arctic tundra productivity linked with landform and climate change interactions. *Nature Scientific Reports.*

Mark J. Lara designed the study, analyzed the data, developed the polygonal tundra map, and wrote the manuscript. Ingmar Nitze and Guido Grosse developed and processed NDVI trend data and edited, commented and revised the manuscript. Philip Martin was pivotal in the conceptualization of the polygonal tundra map. A. David McGuire assisted in model forecasting. All authors reviewed the manuscript and made significant contributions to the writing.

2. Detection of landscape dynamics in the Arctic Lena Delta with temporally dense Landsat time-series stacks

Nitze, I.[1,2] & Grosse, G.[1,2]

[1] AlfredWegener Institute Helmholtz Centre for Polar and Marine Research, Periglacial Research Unit, Potsdam, Germany

[2] Institute of Earth and Environmental Science, University of Potsdam, Potsdam, Germany

Published in: Remote Sensing of Environment, Vol.181, 2016

Citation: Nitze, I., & Grosse, G. (2016). Detection of landscape dynamics in the Arctic Lena Delta with temporally dense Landsat time-series stacks. *Remote Sensing of Environment*, *181*, 27-41. DOI: 10.1016/j.rse.2016.03.038

2.1 Abstract

Arctic permafrost landscapes are among the most vulnerable and dynamic landscapes globally, but due to their extent and remoteness most of the landscape changes remain unnoticed. In order to detect disturbances in these areas we developed an automated processing chain for the calculation and analysis of robust trends of key land surface indicators based on the full record of available Landsat TM, ETM+, and OLI data. The methodology was applied to the ~29,000 km^2 Lena Delta in Northeast Siberia, where robust trend parameters (slope, confidence intervals of the slope, and intercept) were calculated for Tasseled Cap Greenness, Wetness and Brightness, NDVI, and NDWI, and NDMI based on 204 Landsat scenes for the observation period between 1999 and 2014. The resulting datasets revealed regional greening trends within the Lena Delta with several localized hot-spots of change, particularly in the vicinity of the main river channels. With a 30-m spatial resolution various permafrost-thaw related processes and disturbances, such as thermokarst lake expansion and drainage, fluvial erosion, and coastal changes were detected within the Lena Delta region, many of which have not been noticed or described before. Such hotspots of permafrost change exhibit significantly different trend parameters compared to non-disturbed areas. The processed dataset, which is made freely available through the data archive PANGAEA, will be a useful resource for further process specific analysis by researchers and

land managers. With the high level of automation and the use of the freely available Landsat archive data, the workflow is scalable and transferrable to other regions, which should enable the comparison of land surface changes in different permafrost affected regions and help to understand and quantify permafrost landscape dynamics.

2.2 Introduction

The Arctic has been subject to a significant increase in air temperatures during the last decades, which are projected to further rise about 6 °C in terrestrial and around 10 °C in marine areas by the end of the 21st century (IPCC, 2013 — RCP 6.0). Such significant and, on geological time scales, sudden changes of climatic conditions have a potentially massive impact on thaw-vulnerable permafrost landscapes, which cover about 24 % of the northern hemisphere's land mass (Zhang, Barry, Knowles, Heginbottom, & Brown, 2008). Increasing air and ground temperatures can lead to widespread thaw of permafrost soils and frozen deeper deposits, which are estimated to account for a carbon stock of more than 1.5 times that of the atmosphere (Hugelius, et al., 2014; Strauss, et al., 2013). Thaw and further warming of portions of this soil carbon pool would initiate and accelerate the decomposition of the largely inactive frozen soil carbon to carbon dioxide and methane, which in turn will contribute to further warming. The result is a positive feedback cycle with potentially global implications for climate and society (Grosse, et al., 2011; Schuur, et al., 2015). In particular, low-lying permafrost-dominated Arctic river deltas, located at the interface of terrestrial and marine realms, are highly vulnerable to landscape-scale changes driven by global warming. Important factors for these regions are permafrost thaw and terrain subsidence as well as changes in runoff patterns and sediment transport, seasonality and ice regimes, and relative sea level and coastline position (Burn & Kokelj, 2009; Ericson, Vörösmarty, Dingman, Ward, & Meybeck, 2006; Solomon, 2005; Walker H. J., 1998; Terenzi, Jorgenson, Ely, & Giguère, 2014).

Therefore, it is necessary to closely monitor the dynamics of Arctic river deltas to better estimate landscape scale climate change impacts and to quantify carbon fluxes. Due to the large size and remoteness of Arctic regions, many local and medium scale geomorphological, ecological, and hydrological processes remain unnoticed because field studies can only focus on limited and logistically accessible sites. Data on landscape-scale changes is sparse and heterogeneously distributed among few field study sites (e.g., Samoylov field station in the

southern Lena Delta, Siberia) or natural resource exploration sites (e.g. Prudhoe Bay, Alaska). Various remote sensing data and techniques can provide excellent tools for detecting, monitoring, and scaling rapid disturbances as well as gradual changes in permafrost landscapes and overcome knowledge gaps. Field and high resolution remote sensing studies that have focused on local spatial extents include observations of permafrost thaw dynamics (Raynolds, et al., 2014), surface hydrology (Karlsson, Lyon, & Destouni, 2014; Muster, Langer, Heim, Westermann, & Boike, 2012; Plug, Walls, & Scott, 2008) or coastal erosion (Günther, Overduin, Sandakov, Grosse, & Grigoriev, 2013; Lantuit, et al., 2011).

Broad-scale processes in the Arctic or even globally, such as hydrological, vegetation or climate dynamics, are generally monitored with remote sensing data at a high temporal-, but a limited spatial resolution of 250m or coarser (Stow, et al., 2004; Beck & Goetz, 2011; Fensholt & Proud, 2012; Goetz, et al., 2011; Urban, et al., 2014). While these approaches capture hemispheric-scale patterns, a large proportion of relevant landscape changes occurs at rather small spatial scales with high temporal dynamics, such as thermokarst lake changes or thaw slump development and escapes observations. The magnitude and abundance of these processes thus remains unnoticed in most places.

With increasing computation capacities and novel processing techniques in conjunction with the free availability of the entire Landsat archive, it becomes viable to exploit this valuable and consistent data source to assess multi-scaled land surface dynamics in the high latitude permafrost regions. Recently, the focus of monitoring high resolution land cover changes or disturbances shifted from the analysis of single, widely spaced observations towards a high-frequency multi-temporal analysis using the entire Landsat archive, with over 40 years of continuous acquisitions. Examples include mostly forestry applications, for example disturbance and recovery monitoring (Fraser R. , Olthof, Carrière, Deschamps, & Pouliot, 2012; Hansen, et al., 2013; Kennedy, Cohen, & Schroeder, 2007; Olthof & Fraser, 2014; Pflugmacher, Cohen, & Kennedy, 2012), monitoring of glacial flow velocities (Rosenau, Scheinert, & Dietrich, 2015), or observations of snow cover persistence in Alaska (Macander, Swingley, Joly, & Raynolds, 2015). These studies are predominantly based on the analysis of temporal trajectories of multi-spectral indices (MSI) or the original spectral bands. In terrestrial permafrost areas, robust linear trend analysis of Landsat Tasseled Cap (TC) index time-series has been proposed (Fraser R. , Olthof, Carrière, Deschamps, & Pouliot, 2012) and

applied in different studies of land changes in Northwestern Canada, such as post-fire forest recovery (Fraser R. H., et al., 2014), the evolution of thaw slumps (Brooker, Fraser, Olthof, Kokelj, & Lacelle, 2014) and land cover change classification (Olthof & Fraser, 2014). Other studies on disturbances and changes in permafrost regions, based on multi-temporal Landsat data are available, such as thermokarst lake evolution or permafrost degradation (Beck, Ludwig, Bernier, Lévesque, & Boike, 2015; Karlsson, Lyon, & Destouni, 2014; Plug, Walls, & Scott, 2008). However, these studies do not fully exploit the temporal capabilities of the full Landsat archive.

In this study we present the multi-temporal analysis of Landsat-based land surface properties for the entire Lena river delta, an approximately 29,000 km2 large permafrost-dominated region in Northern Siberia, for the 1999 to 2014 period. We provide robust calculations of linear trends of different well-established MSI (Landsat Tasseled Cap, NDVI [Vegetation], NDWI [Water], NDMI [Moisture]) and use these to assess the recent dynamics in this deltaic lowland landscape. We further identify and highlight diverse permafrost related processes and disturbances associated with the calculated spectral trends on different temporal and spatial scales.

2.3 Study Area and Data

2.3.1 Study Area

The Lena Delta is located in northeastern Siberia's continuous permafrost zone between 72° and 74°N and 123° to 130°E (Figure 2.1). With an approximate size of 29,000 km² it is the largest Arctic river delta and one of the largest deltas globally (Walker H. J., 1998; Schneider, Grosse, & Wagner, 2009). It is surrounded by the Laptev Sea with the adjacent New Siberian Islands to the north and the Chekanovsky and Kharaulakh mountain ranges to the south.

The delta is characterized by numerous river channels and more than 1500 islands of various sizes (Are & Reimnitz, 2000; Grigoryev, 1993). Morphologically, the delta can be divided into three distinct terraces (Grigoryev, 1993; Schwamborn, Rachold, & Grigoriev, 2002). The first terrace, further divided into the recent and the Holocene floodplains, is the youngest and currently active part of the delta and covers most of the east-northeastern areas as well as the

southern and southwestern-most parts. Its surface predominantly consists of wetlands with ice wedge-polygonal tundra and thermokarst lakes (Morgenstern, Grosse, & Schirrmeister, 2008). The second terrace, also referred to as the Arga Complex, is located in the northwestern part and contains mostly sandy, comparably dry soils with low ground-ice content. Large, mostly oriented lakes and depressions are abundant in this area (Morgenstern, Grosse, & Schirrmeister, 2008). The third and oldest terrace appears in isolated patches in the southern delta region, and consists of remnants of a Late Pleistocene accumulation plain (Schirrmeister, et al., 2003). It is characterized by very ice-rich, organic-rich, fine grained sediments (Yedoma), which form a polygonal tundra landscape with deep thermokarst lakes and basins as well as thermoerosional gullies (Morgenstern A. , Grosse, Günther, Fedorova, & Schirrmeister, 2011).

The geological and hydrological surface conditions are well reflected in the vegetation types. Within the 1st and the 3rd terraces, wet or moist Tundra is the dominating land-cover. However, drier tundra conditions are not uncommon. On the 2nd terrace and particularly in the northwestern delta region, seasonally drier conditions prevail with dry tundra being the most typical land-cover interspersed with wet or moist tundra, (see Figure 2.2) (Schneider, Grosse, & Wagner, 2009).

Near-surface permafrost soils of the Lena Delta contain a large organic carbon pool that is potentially vulnerable to mobilization upon thaw (Zubrzycki, Kutzbach, Grosse, Desyatkin, & Pfeiffer, 2013). Deeper sediments, in particular in the 3rd terrace, also contain a large organic carbon pool and may be thaw vulnerable due to their high ground ice content (Schirrmeister, et al., 2011).

The study area's climate is typical for the High Arctic with a mean annual temperature of -12.5 °C, measured at Samoylov station in the southern Lena Delta (Boike, et al., 2013) (observation period: 1998- 2011). The seasonal temperature differences are pronounced with mean temperatures of 10.1 °C in July and−33.1 °C in February. Precipitation amounts are low with an average of about 200 mm, predominantly falling as rain during the short summer period. In the study area, the permafrost is continuous with depths of around 500-600m, though there is potential for permafrost-penetrating taliks underneath the major delta channels. The active layer depths range from 30 to 90 cm (Boike, et al., 2013; Grigoryev,

1993). Vegetation cover in the Lena Delta is dominated by sedge, grass, moss and dwarf shrub wetlands (Schneider, Grosse, & Wagner, 2009).

The Lena Delta is affected by pronounced seasonal runoff dynamics partially driven by a very large watershed integrating contributions from several climate zones. A significant spring flood during snowmelt and ice breakup results in water levels increased by several meters and temporary flooding of low-lying areas, followed by a strong drop of water levels in channels and a gradual decline of discharge through the summer season (Fedorova, et al., 2015; Yang, et al., 2002).

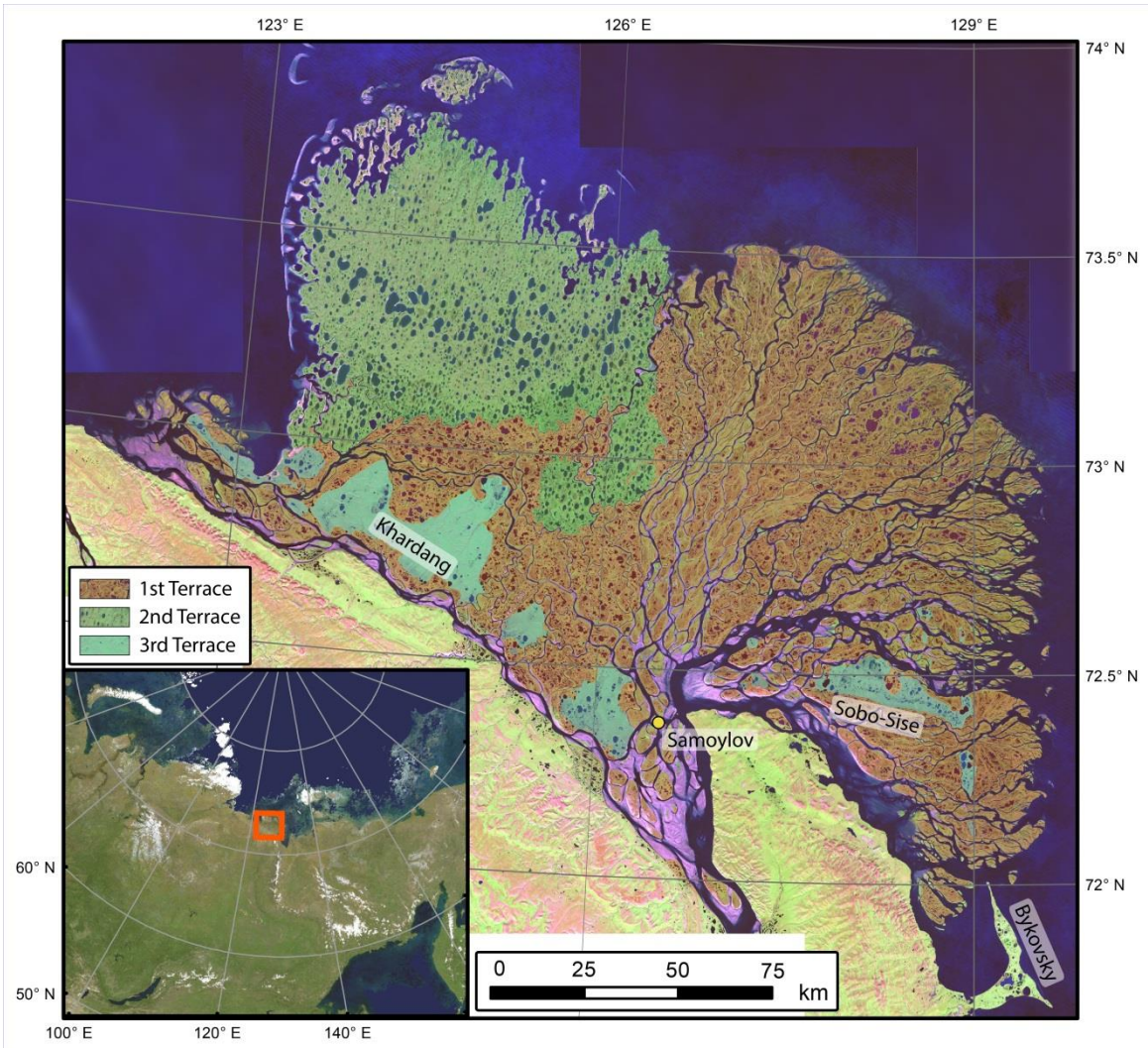

Figure 2.1: Synthetic Landsat mosaic of Lena Delta indicated with main geomorphological terraces. Mosaic based on modeled reflectance values of multi-temporal trend-analysis. RGB bands (SWIR-1, NIR, Red). Terrace extent (terraces 2 and 3) from Morgenstern, Röhr, Grosse and Grigoriev (2011).

2.3.2 Data

The entire Landsat (LS) image archive of Thematic Mapper (TM), Enhanced Thematic Mapper+ (ETM+) and Observing Land Imager (OLI) sensors was searched and filtered over all Worldwide-Reference System-2 (WRS-2) tiles intersecting the Lena Delta. In total 14 WRS-2 tiles were selected for this study (Table 2.1). The data were acquired in radiometrically and geometrically terrain-corrected state (processing level L1T) from the United States Geological Service (USGS) via the GLOVIS and Earth Explorer platforms. The imagery has a spatial resolution of 30m and largely similar spectral characteristics. All common spectral bands (blue, green, red, near-infrared / NIR, short-wave-infrared-1 and -2 / SWIR1 and SWIR2) were used for analysis while the remaining bands were excluded from further processing. Images from the first Landsat sensor generation (Multispectral Scanner / MSS) were not taken into consideration at this point, because of their coarser spatial resolution and lower spectral fidelity.

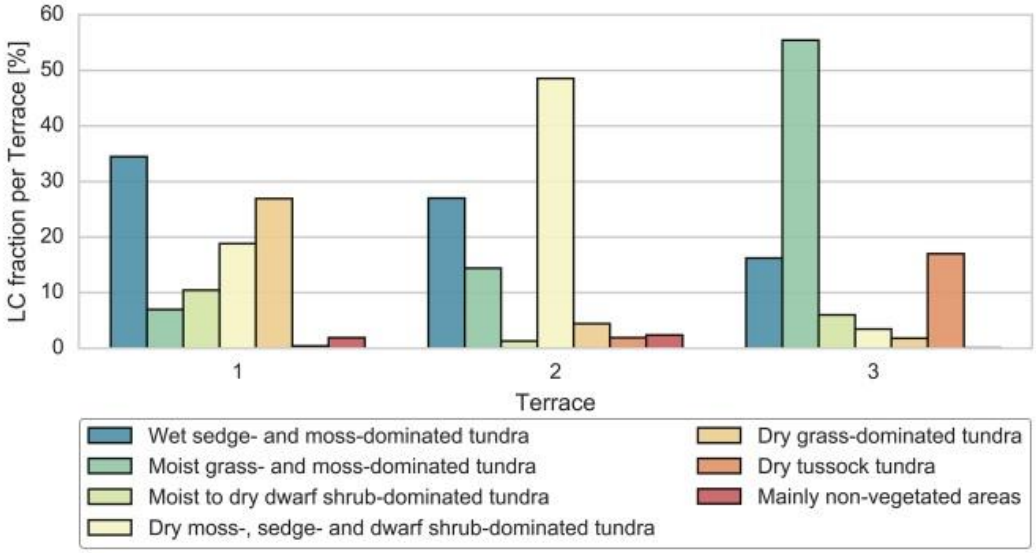

Figure 2.2: Land cover fraction per terrace on land areas. Land cover types from Schneider et al. (2009). Water classes are excluded.

The image selection was filtered to acquisition dates between July 1st and August 30th to represent the peak growing season, chosen to match the acquisition period of other Landsat based trend analysis studies in high latitudes for better comparability (Fraser R. H., et al., 2014; Ju & Masek, 2016). Maximum cloud coverage was set to 80 % in order to minimize the

influence of confounding factors such as clouds and shadows. The availability of Landsat images in the study area started for the majority of locations in 2000. In some locations, the archive reaches back until year 1999. Therefore, the full time-series spans 14 to 15 years. In total 204 images fulfilled the selected criteria regarding date of acquisition and cloud cover. The spatial distribution of data availability exhibits an inhomogeneous pattern with a gradient from the eastern and northeastern coastal regions of the Lena Delta, where only few scenes are available, towards the southern parts, which exhibit a better coverage (cf. Figure 2.5). Owing to the high latitude the image acquisition paths have large overlapping areas, thus leading to an increased theoretical acquisition frequency compared to lower latitudes. The majority of the study area is captured by 4 to 5 overlapping image paths, resulting in a repetition cycle of 3 to 5 days in a single satellite setup and even higher frequency with more than one satellite available. However, this advantage of strong overlap and potential high acquisition frequency is dampened by the strong cloudiness, short snow free season, and the lack of on-board data archiving on Landsat-5 while at the same time this region is very remote from receiving stations (Goward, et al., 2006).

The data availability over time has been rather inconsistent. The number of available image tiles over the entire study areas fluctuated between a minimum of 2 in years 1999 and 30 per year in 2013. Since 2007 the data availability has been rather favorable and improved further with the launch of Landsat-8 in 2013 (Figure 2.3). If shoulder seasons in June and September were included in the processing and analysis, the number of images would be 346, an increase of about 70 %.

Table 2.1: All WRS-2 tiles over the Lena Delta with number of available images within selected criteria

WRS-2 Path	WRS-2 Row	# images	WRS-2 Path	WRS-2 Row	# images
127	10	1	131	9	25
128	9	1	132	8	21
128	10	15	132	9	24
129	9	15	133	8	22
130	8	2	133	9	19
130	9	11	134	8	13
131	8	17	135	8	18

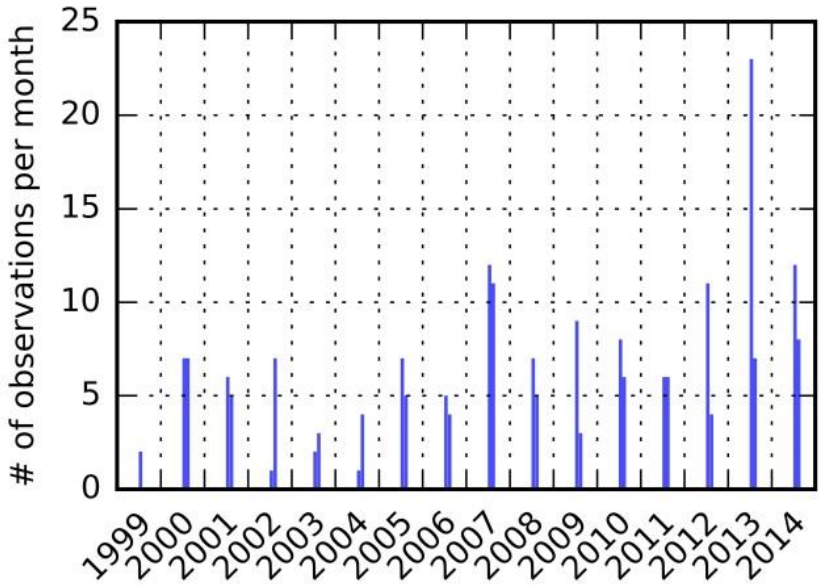

Figure 2.3: Number of Landsat scenes within selection criteria per month of the entire study area during the observation period.

2.3.3 Methods/processing

Our processing chain from the downloaded raw images to the final product consists of many different steps, which can be grouped into pre-processing, and analysis/trend calculation (Figure 2.4). The preprocessing included radiometric corrections, spatial corrections and reprojection as well as data subsetting. The final time-series processing includes multi-spectral index calculation and trend analysis. The time-series processing predominantly follows the robust linear trend analysis of Landsat Tasseled Cap Indices proposed by Fraser et al. (2012).

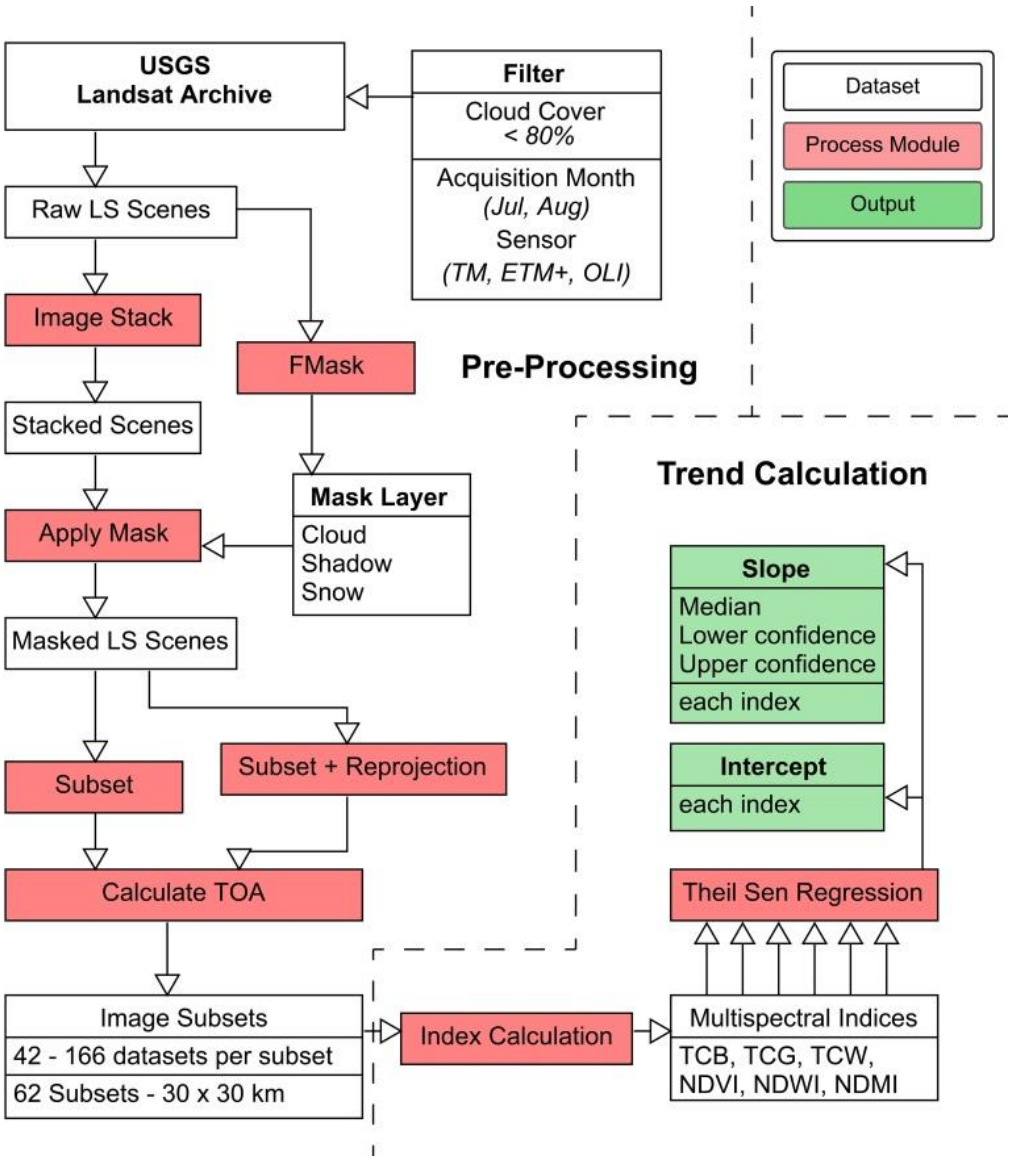

Figure 2.4: Flowchart of image processing chain.

Preprocessing

First, all archived Landsat data files were extracted and sorted by their spatial location (WRS-2 path/row). The FMask algorithm in Version 3.2.1 beta (Zhu & Woodcock, 2012) was applied to each image with its standard settings. This algorithm detects clouds, shadows and snow/ice in Landsat images of all generations. The FMask layer was then used to mask out all non-valid data: Clouds, Shadows, Snow/Ice and NoData. Owing to the large amount of data, the study site was subdivided into 62 subsets of 30 × 30 km large tiles, which equals 1000 × 1000 pixels per image tile. As the Lena Delta has a large spatial extent spanning three UTM

zones (51 to 53), several reprocessing steps were necessary to achieve a common spatial reference in conjunction with an exact spatial alignment of each pixel. UTM Zone 52N in WGS 84 was chosen as the master projection, as it is centrally located in the study area and warrants the least distortion over the entire dataset. The masked image tiles with the master projection were clipped to the particular subset/tile boundaries, where applicable. Those with a different native projection were reprojected with a cubic convolution kernel and aligned to the common pixel footprint during the subsetting process using *gdalwarp* of the *gdal utilities* functions. Finally all subsets were radiometrically calibrated to top-of-atmosphere (TOA) reflectances in order to create seasonally normalized and comparable data among sensors.

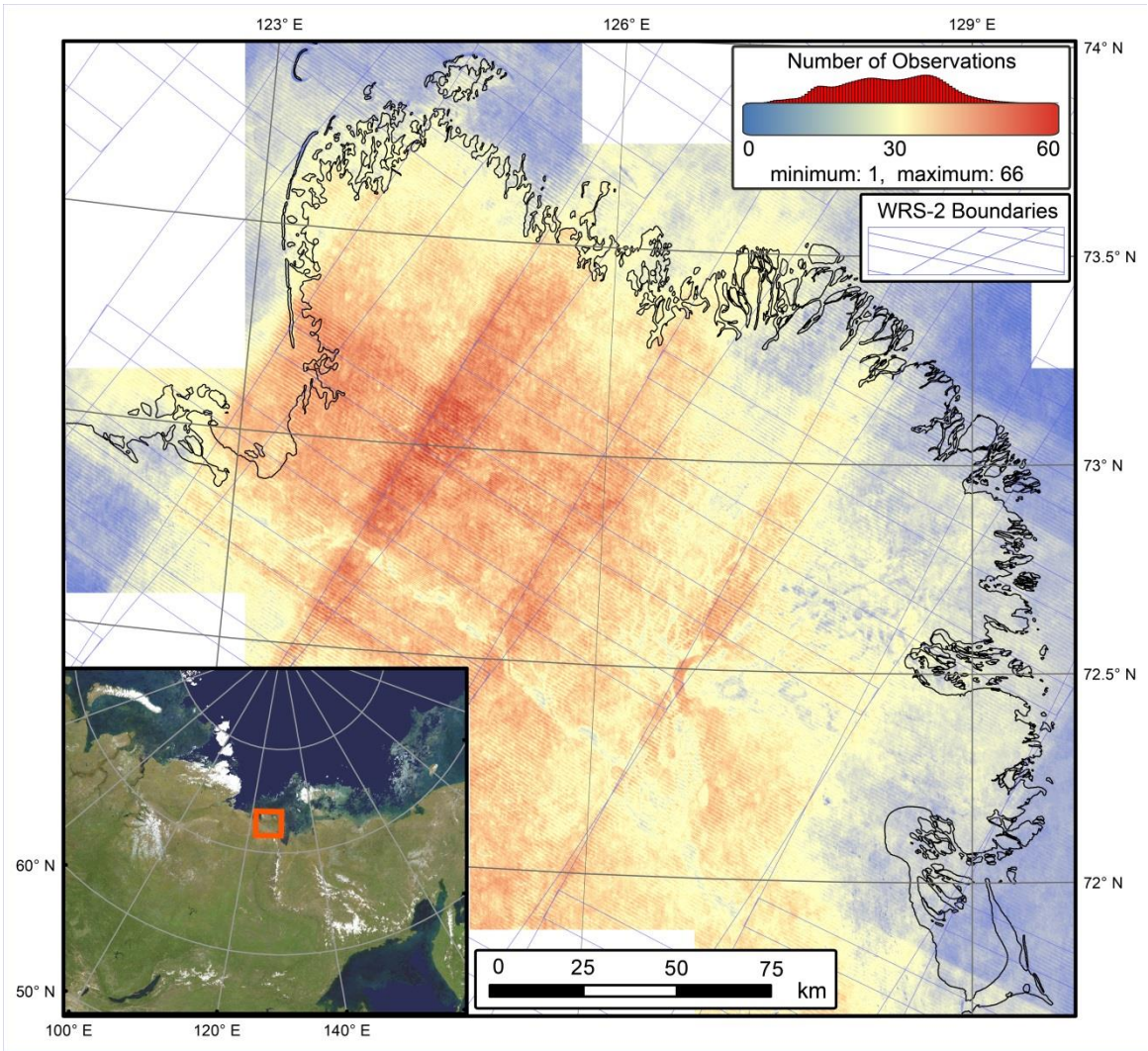

Figure 2.5: Number of unobstructed observations after pre-processing over the study period between 1999 and 2014 super-imposed with WRS-2 boundaries.

Trend Calculation

For the final processing, all available datasets were stacked to four-dimensional data-cubes with one temporal, one spectral and two spatial dimensions. The spectral domain consists of the six common optical Landsat bands (Blue, Green, Red, NIR, SWIR-1, SWIR-2). Several multispectral indices, serving as proxies for different land-surface properties, were calculated over each image of the data stack. For this analysis we included the Landsat specific Tasseled Cap indices Brightness (TCB), Greenness (TCG), and Wetness (TCW) (Baig, Zhang, Shuai, & Tong, 2014; Crist, 1985; Huang, Wylie, Yang, Homer, & Zylstra, 2002) as well as other not sensor-specific indices, such as the Normalized Difference Vegetation Index (NDVI) (Rouse Jr, Haas, Schell, & Deering, 1974), the Normalized Difference Water Index (NDWI) (Gao, 1996) and the Normalized Difference Moisture Index (NDMI) (Wilson & Sader, 2002). They were chosen to reflect a variety of surface characteristics like vegetation status, surface moisture or open water. The TC indices were calculated with the sensor-specific formulas for TOA reflectance data (Table 2.2).

$$TCx = \rho_B * F_B + \rho_G * F_G + \rho_R * F_R + \rho_{NIR} * F_{NIR} + \rho_{SWIR1} * F_{SWIR1} + \rho_{SWIR2} * F_{SWIR2} \quad (2.1)$$

$$NDVI = \frac{\rho_{NIR} - \rho_R}{\rho_{NIR} + \rho_R} \quad (2.2)$$

$$NDWI = \frac{\rho_G - \rho_{NIR}}{\rho_G + \rho_{NIR}} \quad (2.3)$$

$$NDMI = \frac{\rho_{NIR} - \rho_{SWIR1}}{\rho_{NIR} + \rho_{SWIR1}} \quad (2.4)$$

Table 2.2: Landsat Tasseled Cap Factors for Landsat TM, ETM and OLI top-of-atmosphere reflectance values.

	Band Factors						
Sensor - Index	F_B	F_G	F_R	F_{NIR}	F_{SWIR1}	F_{SWIR2}	Reference
L5 - TCB	0.2043	0.4158	0.5524	0.5741	0.3124	0.2303	Crist (1985)
L5 – TCG	-0.1603	-0.2819	-0.4934	0.7940	-0.0002	-0.1446	
L5 – TCW	0.0315	0.2021	0.3102	0.1594	-0.6806	-0.6109	
L7 - TCB	0.3561	0.3972	0.3902	0.6966	0.2286	0.1596	Huang et al. (2002)
L7 – TCG	-0.3344	-0.3544	-0.4556	0.6966	-0.0242	-0.2630	
L7 – TCW	0.2626	0.2141	0.0926	0.0656	-0.7629	-0.5388	
L8 – TCB	0.3029	0.2786	0.4733	0.5599	0.5080	0.1872	Baig et al. (2014)
L8 – TCG	-0.2941	-0.243	-0.5424	0.7276	-0.0713	-0.1608	
L8 – TCW	0.1511	0.1973	0.3283	0.3407	-0.7117	-0.4559	

With the final step, the linear trends for each index were calculated in the temporal domain, using the robust Theil-Sen (T-S) regression method (Sen, 1968; Theil, 1992), which is insensitive to around 30 % outliers and has been found to outperform standard least-squares regression on remote sensing data (Fernandes & Leblanc, 2005). Furthermore, this technique has been successfully applied to the trend detection of Landsat TC time-series in the Canadian North-West for temporal analysis of forested areas and thaw slump activity (Fraser R. H., et al., 2014; Olthof & Fraser, 2014; Brooker, Fraser, Olthof, Kokelj, & Lacelle, 2014). The T-S regression method is based on the calculation of paired slopes, thus, the calculation of slopes from every point in time to each other. The median of these calculated slopes is taken as the master slope over the entire time-series.

$$\text{ts\_slope} = median\left(\sum_{\substack{j=1\\i=1}}^{n} \frac{(y_i - y_j)}{(t_i - t_j)}\right) \quad (2.5)$$

The intercept is defined as:

$$\text{intercept} = \text{median}(y) - \text{ts\_slope} * \text{median}(t) \quad (2.6)$$

The final output was written into geospatial raster files with the same spatial resolution and footprint of the input Landsat data with four bands each. Every output file contains information on slope, intercept scaled to year 2014, and the upper and lower confidence

intervals of the slope (α = 0.05). T-S calculations were carried out with the *scipy.stats* package in the *python* programming language. Output products were calculated for each MSI.

2.4 Results

The calculated trends of the Tasseled Cap- and normalized multispectral indices (MSI) exhibit time-series trajectories on multiple scales ranging from local disturbances to regional processes. In the following subsections, different changes observed on multiple spatial scales will be presented and analyzed.

2.4.1 Regional Scale changes

Regional-scale trends in vegetation and moisture patterns become clearly apparent in the resulting datasets. The different MSI trend directions and magnitudes indicate the type and magnitude of changes within the study area (Figure 2.6).

Table 2.3: Statistics of trend slopes (mean and standard deviations) and trend intercept (mean, baseline July 1 2014), over the entire study area and divided by terrace.

	Lena Delta			1st terrace			2nd terrace			3rd terrace		
	Slope		Intercept	Slope		Intercept	Slope		Intercept	Slope		Intercept
Index	mean	std	mean	mean	std	mean	mean	std	mean	mean	std	mean
TCB	0.0168	0.0139	0.2910	0.0158	0.0149	0.2622	0.0179	0.0128	0.3092	0.0197	0.0118	0.3374
TCG	0.0194	0.0139	0.0122	0.0208	0.0145	0.0178	0.0126	0.0075	-0.0114	0.0364	0.0105	0.0464
TCW	0.0271	0.0149	-0.0805	0.0257	0.0158	-0.0596	0.0260	0.0123	-0.1121	0.0389	0.0131	-0.1011
NDVI	0.0359	0.0323	0.4605	0.0375	0.0381	0.4519	0.0261	0.0202	0.3504	0.0501	0.0191	0.4968
NDMI	0.0271	0.0413	0.0993	0.0192	0.0475	0.1453	0.0394	0.0248	-0.0049	0.0417	0.0290	0.1064
NDWI	-0.0364	0.0302	-0.4102	-0.0390	0.0348	-0.3764	-0.0249	0.0199	-0.3215	-0.0487	0.0174	-0.4524

Vegetation/greening

The terrestrial domain of the Lena Delta exhibits a gradual moderate greening trend, which is evident in both vegetation indices TCG and NDVI (Figures 2.5-2.6). For TCG, a mean decadal increase of 0.0194 ± 0.0139 (1 standard deviation) (Table 2.3) is calculated, whereas NDVI has a mean decadal increase of 0.0359 ± 0.0323 in terrestrial areas over the entire delta.

An in-depth analysis reveals regional differences between the delta terraces, but also further localized variation of the greening trends.

The second terrace shows the smallest increase among all subregions with only a weak positive trend of TCG and NDVI (Table 2.3). In contrast, the first and third terraces exhibit a stronger than average greening trend, with the third terrace showing a more pronounced greening apparent in both TCG and NDVI. The small STD of the TCG and NDVI trends within the third terrace indicate a more homogeneous greening within this sub-region.

Apart from the differentiation between the terraces, the strongest greening trends predominantly occur in the southern and eastern delta regions around the main river channels and the adjacent mainland areas to the south. A similar, but more isolated, greening hot-spot can be observed in the active northern central delta region. All of the detected hot-spots are located along the widest river channels, which presumably are the most active parts of the Lena Delta and under a stronger influence of the comparably warm waters of the Lena river.

The Intercept values, which are the predicted TCG and NDVI values for 2014, follow a strong regionalization based on the delta terraces (Figures 2.7-2.8). Both vegetation indices exhibit the highest values on the third terrace and the active floodplain. On the Holocene floodplain of the first terrace and the second terrace with mostly dry and sandy substrate, both indices are generally lower.

Wetness/moisture

The calculated slopes of TCW and NDMI exhibit a general wetting trend over the majority of the study area with some spatial variation. The strongest increase in wetness can be found in the eastern coastal regions, the northern active delta region, Khardang Island, and Bykovsky Peninsula. The wetness trend in these regions correlates well with the observed increase in Greenness. However, at the same time the second terrace is also subject to a wetting trend without the simultaneous greening. The trends of both indices correlate generally well, but disagree to some extent. Such differences can be observed on the western Bykovsky Peninsula or the east-northeastern delta region.

As already observed with the vegetation indices, both moisture sensitive MSI exhibit strong regional patterns varying by terrace unit, where the first terrace has the highest TCW intercept values. These are likely caused by the influence of the Lena river with its annual flood during its ice break-up in late spring. Within this particular sub-region the eastern and northern coastal areas show the highest wetness values. The second and third terraces in contrast exhibit lower absolute intercept values in the TCW and NDMI, indicating generally drier surfaces.

Brightness/albedo

TCB exhibits a weak positive trend over the majority of the study area. Spatial differences can be observed, however as opposed to the other indices, there are no distinct patterns between the different terraces for the slope component of the trend analysis. In contrast, the intercept exhibits increasing values from the first-, to the second-, to the third terrace.

NDWI

NDWI has a strong inverse correlation with NDVI and predominantly represents the temporal behavior of the greenness instead of water or wetness. The regional scale information is redundant to greenness and therefore omitted from further regional scale analysis. However, NDWI is kept for the analysis of local scale changes, due to its ability to discriminate between water and non-water information.

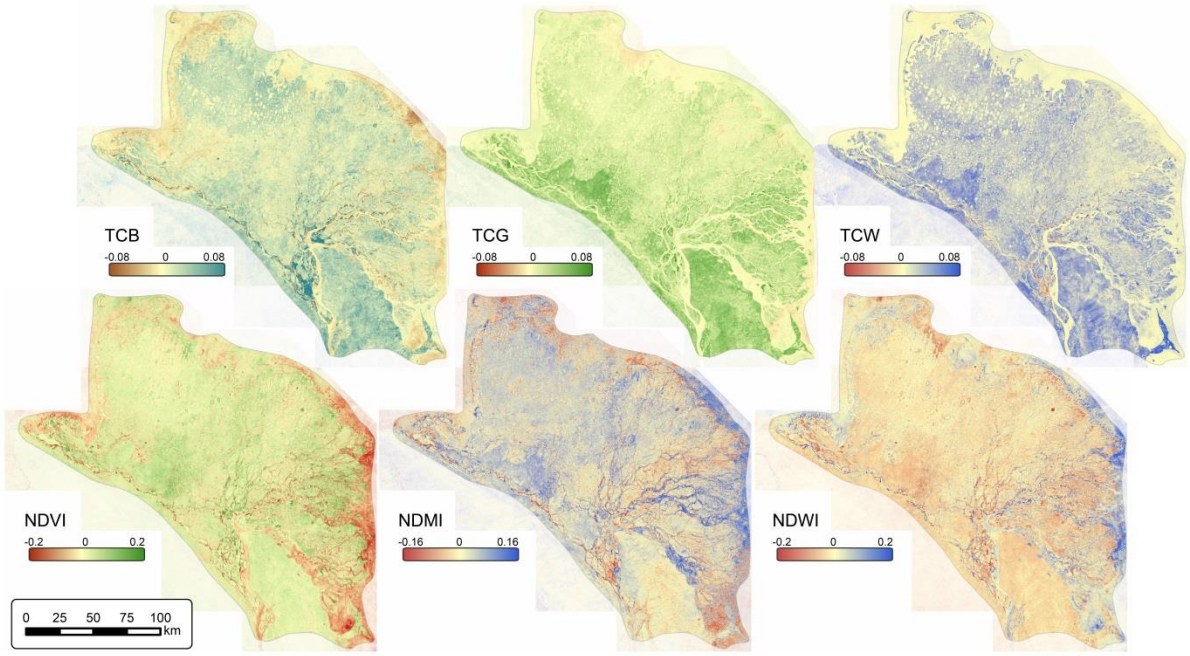

Figure 2.6: Regional overview of decadal trend slope of multi-spectral indices (TCB, TCG, TCW, NDVI, NDMI, NDWI).

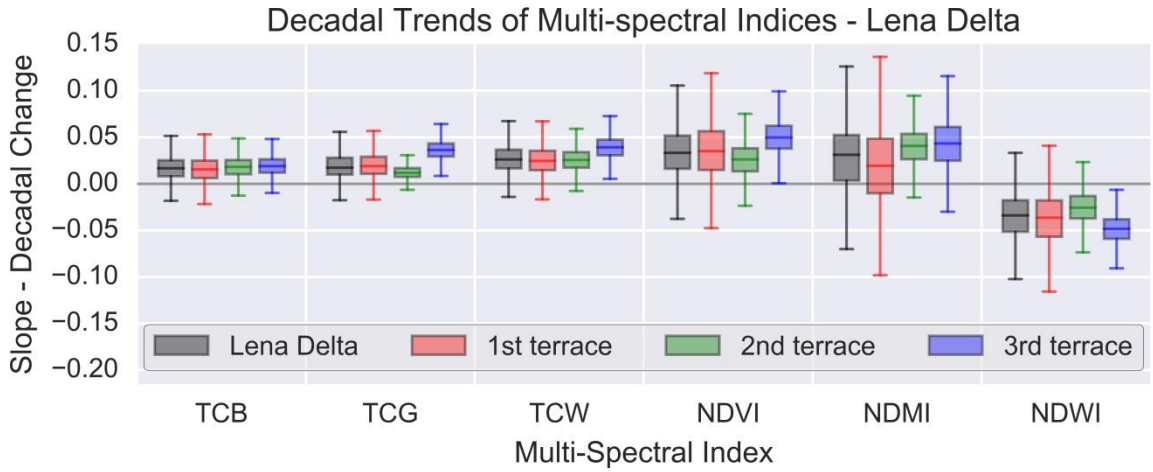

Figure 2.7: Boxplots of trend slopes of each index over the entire Lena delta, and subdivided by geomorphological terrace.

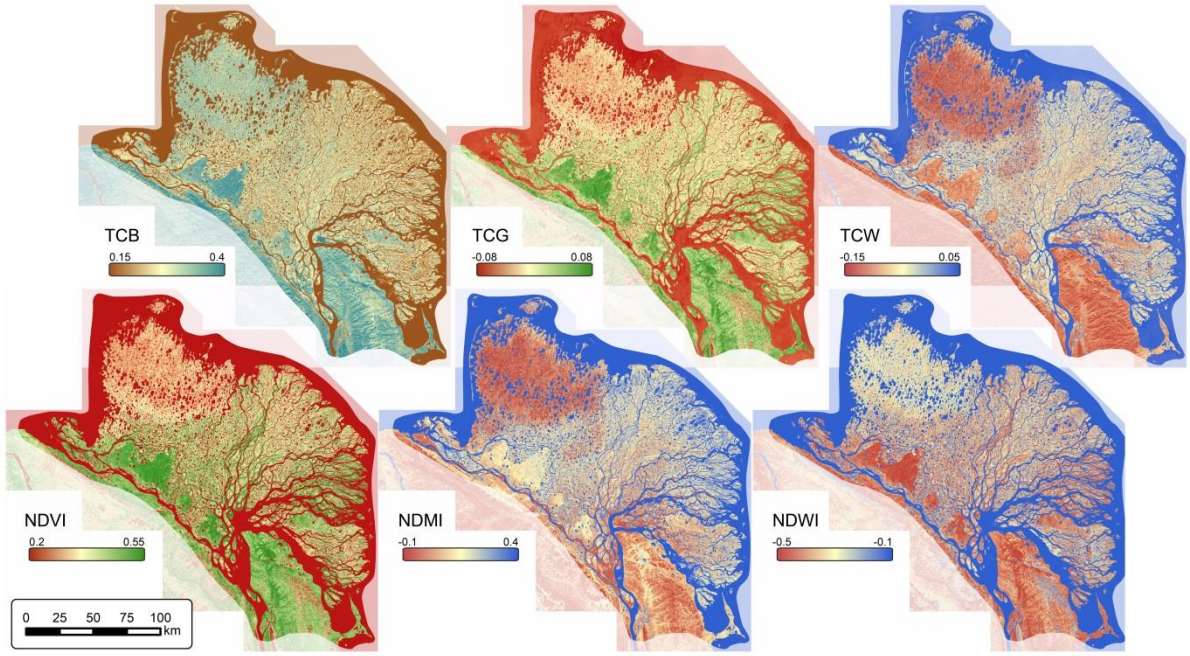

Figure 2.8: Regional overview of trend intercept of multi-spectral indices scaled to year 2014 (TCB, TCG, TCW, NDVI, NDMI, NDWI).

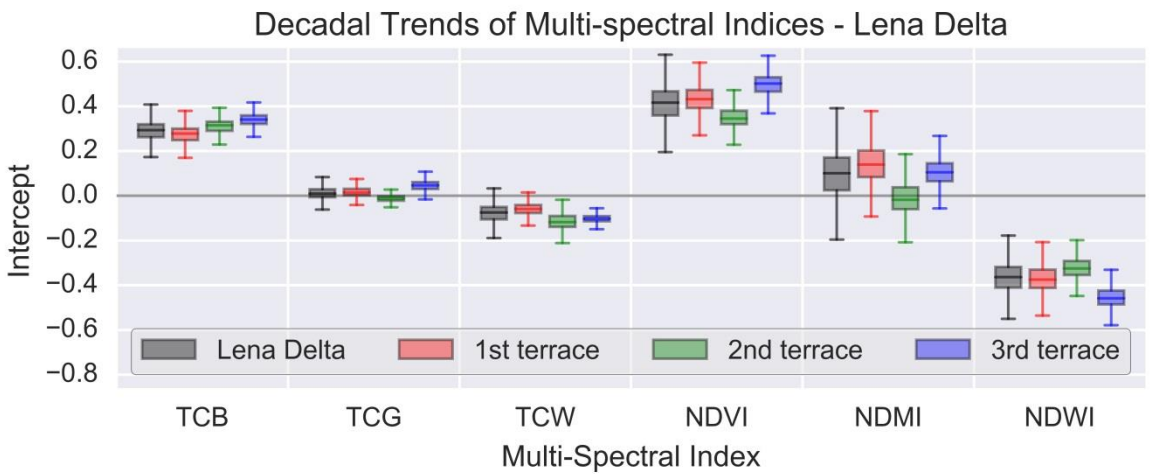

Figure 2.9: Boxplots of trend intercept of each index over the entire Lena delta, and subdivided by geomorphological terrace.

2.4.2 Local scale changes

With a spatial resolution of 30 m, the trend analysis of Landsat time-series excels in the detection of local scale features and trends of land surface properties associated with changes in such features compared to other high-temporal, but coarse-resolution data such as from

MODIS. In the following section, we highlight examples of different typical changes for specific sites on or around the island of Sobo-Sise in the southeastern Lena Delta, where we conducted permafrost field studies in summer 2014 (Figure 2.10). The detected changes include thermokarst processes, such as lake expansion and drainage and fluvial processes, such as erosion and deposition. Examples of coastal dynamics are presented from the northwestern delta region (Figure 2.10).

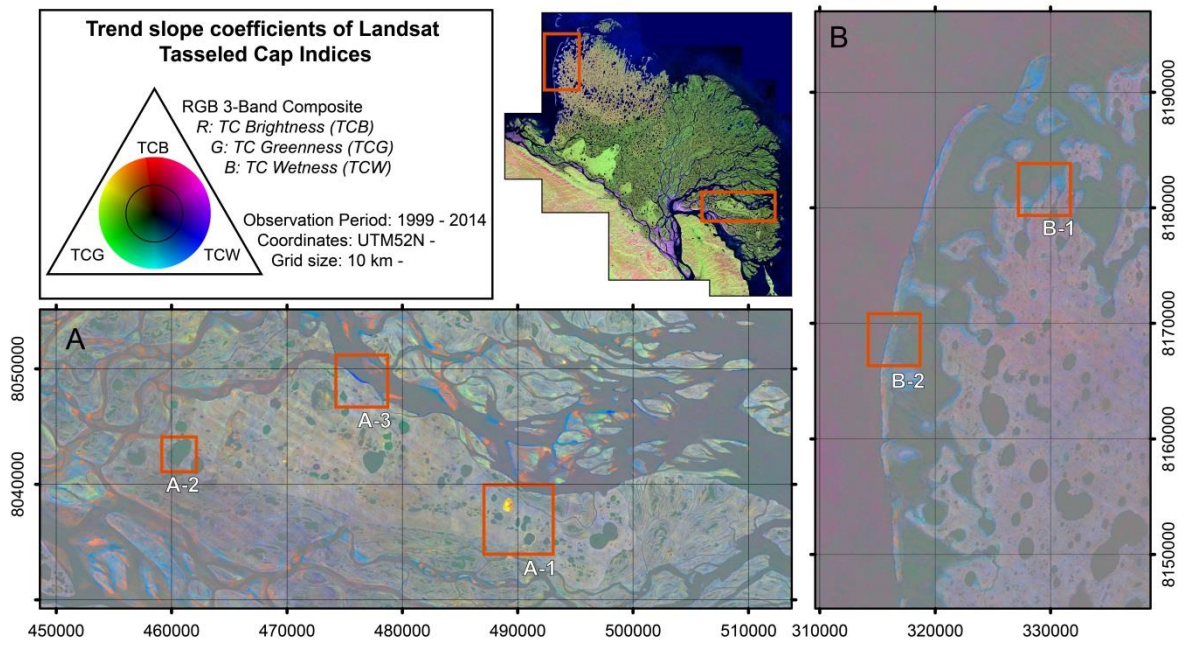

Figure 2.10: RGB composite maps of Tasseled Cap Index trend slopes of Sobo-Sise Island (A) and the northwestern coastal region (B). Subset locations marked with red boxes. A-1: Thermokarst lake drainage; A-2: Thermokarst lake expansion; A-3: Fluvial erosion and sandbank migration; B-1: Coastal inundation; B-2: Barrier island migration. Band combination - Red: TC Brightness, Green: TC Greenness, Blue: TC Wetness.

Thermokarst lake changes

Lake drainage

Several examples of rapidly changing thermokarst lakes were found in the study area, predominantly on the third terrace or the active parts of the Lena Delta. In many cases, partial or complete drainage was noticed during the observation period. A prime example of this disturbance type is located on the island of Sobo-Sise in the eastern Lena Delta, where a mid-

sized thermokarst lake (ca. 1 km²) completely drained during the observation period (Site A-1, Figures. 2.9-2.10). Due to the drainage, the surface at this site was subject to a transition from water to bare exposed lake sediment to partial vegetation cover over time (Figure 2.11), which is very well documented in the trajectories of the different MSI-trends (Figure 2.12). The TCB index exhibits a strong positive trend, driven by the change from a dark water surface to a brighter soil and later vegetation surface. Both vegetation indices strongly increase after the drainage event due to the growth of initial vegetation, most likely tall sedges rapidly growing and thriving on nutrient-rich lake sediments. Additionally, all water or moisture sensitive indices (TCW, NDMI, NDWI) trace the transition from water to a terrestrial surface with a strong negative trend. The drainage event occurred between 2003 and 2005 (Figure 2.12), a more precise period cannot be determined from this dataset due to a lack of observations during this period. Spatially, intra-basin differences can be detected that are caused by local variation in vegetation emergence patterns or wetness conditions within the drained lake basin as shown in the cross-section of index slopes (Figure 2.12). Outside the basin, all slopes exhibit a spatially consistent pattern with values close to zero.

In the entire Lena Delta region, more than 40 full or partial lake drainage events were observed, causing highly significant trends (T-S confidence intervals, α=0.05) with the same trend directions and similar magnitudes that are clearly distinguishable from stable land forms or regional-scale changes (see Section 2.3.1). Most lake drainage events occurred in the active parts of the Lena Delta, predominantly in the vicinity of river channels, which tap and drain lakes by lateral erosion.

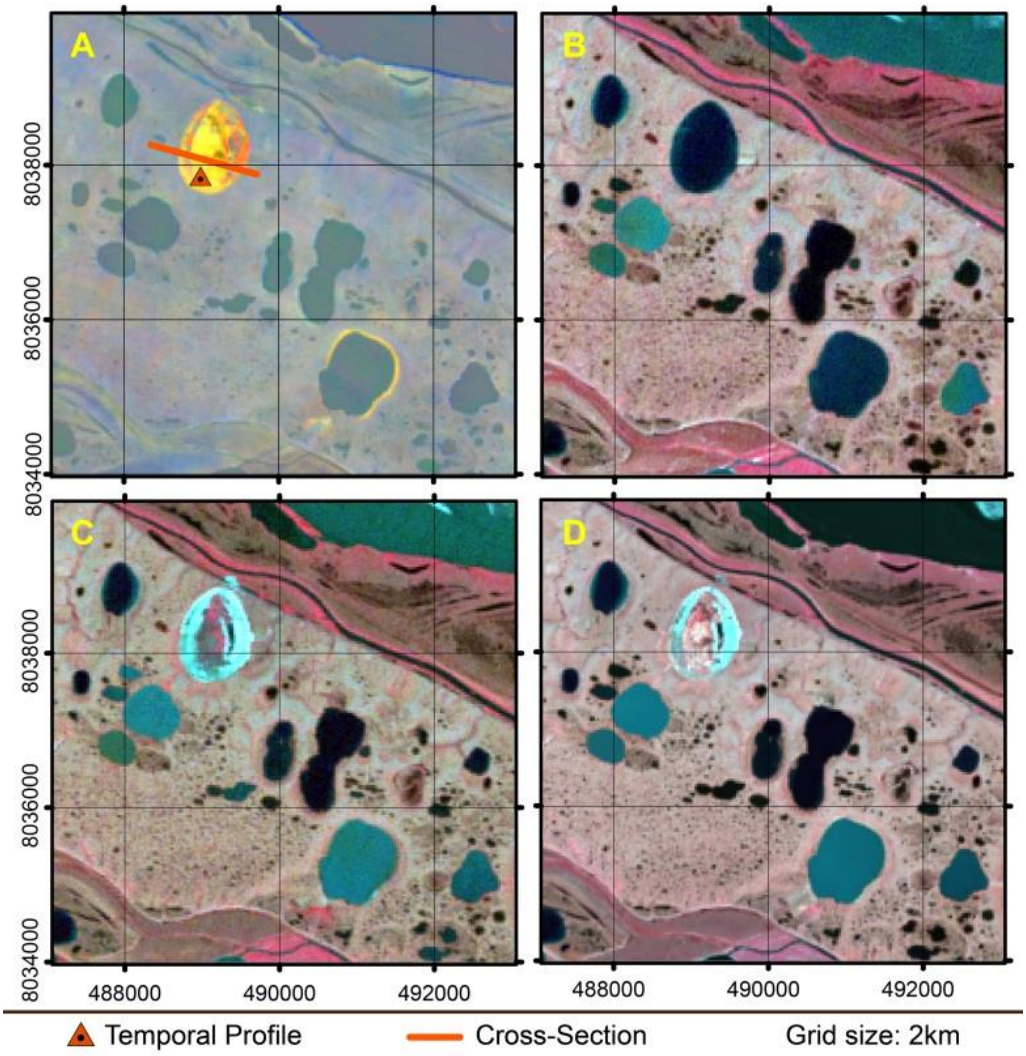

Figure 2.11: RGB composite maps of Tasseled Cap Index trend slopes (TCB–TCG–TCW) and Landsat color-infrared images (NIR-R-G) of thermokarst lake drainage (A-1). A: Trend slopes of drained thermokarst lake with temporal profile location and cross-section. B: Landsat-7 acquired on July 28th 2000. C: Landsat-5 acquired on July 25th 2007. D: Landsat-8 acquired on July 16th 2013. Map coordinates: UTM52N.

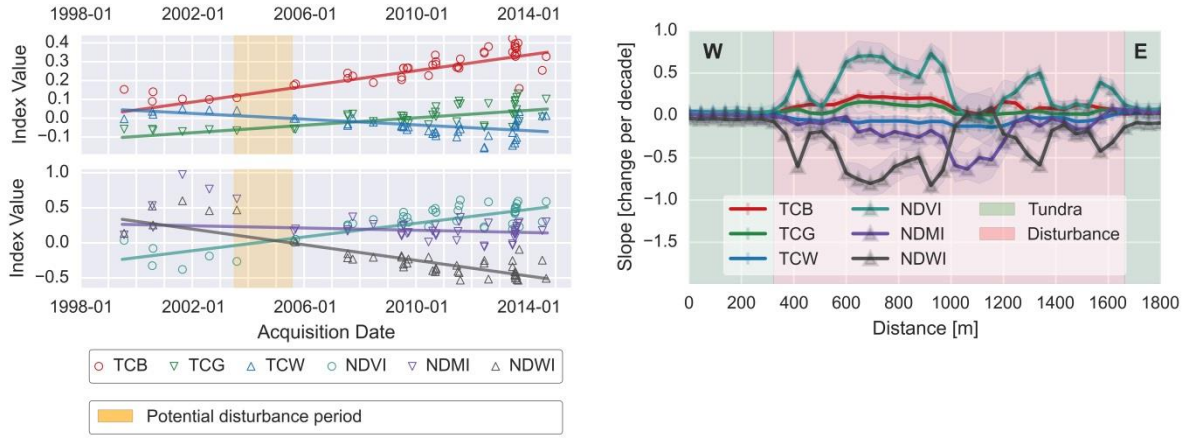

Figure 2.12: Temporal profile of and cross-section through drained thermokarst lake (A-1). Left: Temporal profile of Tasseled Cap (top) and normalized (bottom) multi-spectral indices from 1999 to 2014 with Theil-Sen trend lines. Potential timing of disturbance indicated in the background. Right: Cross section of trend slopes of all multi-spectral indices through drained thermokarst lake basin super-imposed by land cover and disturbance locations.

Lake expansion

Thermokarst lake expansion, a typical process in permafrost landscapes involving thermal and mechanical erosion of shore bluffs containing ice-rich permafrost, was observed for most of the lakes in the study area. In contrast to the sudden drainage, this process is characterized by a gradual erosion of lake shores, usually with average rates of tens of cm to few meters per year for typical thermokarst lakes (Jones B. M., et al., 2011).

For this process, the transition from vegetated tundra surface to water exhibits trends in the opposite direction of a lake drainage site (Figures 2.13-2.14). The water sensitive indices TCW and NDWI exhibit a strong positive trend in a pure change pixel (0.03, 0.253), whereas NDVI and TCB react with a negative trend of -0.245 and -0.047, respectively. TCG and NDMI however, do not seem to be sensitive to this kind of change, as indicated by values close to zero. Due to the slow expansion in conjunction with the pixel size of 30 meters, this type of change is subject to a large number of mixed pixels. Depending on the rate of the lake expansion and the point in time where the respective pixel or parts thereof became subject to change the trend slopes may lie in between the pure end-members of water and tundra. Additional factors such as suspended sediment loads also influence the trend slopes.

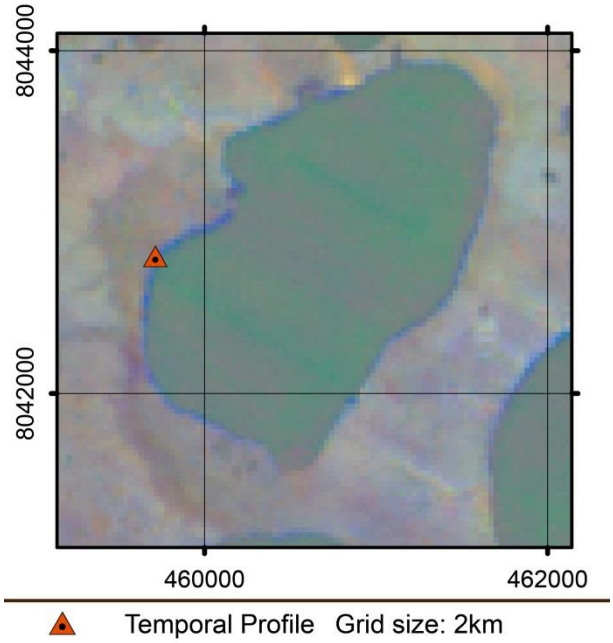

Figure 2.13: RGB composite map of Tasseled Cap Index trend slopes (TCB−TCG−TCW) of thermokarst lake expansion on Sobo-Sise Island (A-2). Map coordinates: UTM52N.

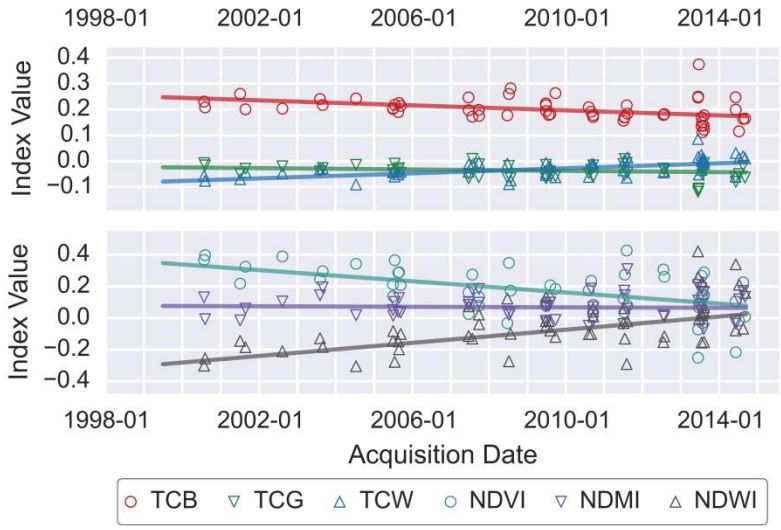

Figure 2.14: Temporal profile of Tasseled Cap (top) and normalized (bottom) multi-spectral indices from 1999 to 2014 with Theil-Sen trend lines of eroding lake shore (A-2).

Fluvial dynamics

The Lena Delta is a highly active hydrological system with different fluvial processes, including the erosion of terrestrial areas, the accumulation and movement of sandbanks (cf. Figures 2.10, 2.16), and other morphological changes such as shifting river channels. Examples of rapid fluvial erosion can be found in the southern portion of the delta where the main channels of the river cut into the elevated surface of the third delta terrace consisting of ice-rich Yedoma permafrost deposits. This erosion causes the formation of steep cliffs of up to 25 meters in height. A prime example is located on the northern shore of Sobo-Sise island, where erosion rates of up to 20 m per year are detected and a vertical bluff has formed (Figure 2.15). This rapid cliff retreat creates pronounced trend slopes with a strong increase in the water sensitive indices and a decrease in both vegetation indices as well as TCB (Figures 2.16-2.17). All change magnitudes within the transition zone are significant and deviate strongly from the surrounding tundra and water surfaces (Figure 2.17).

The spatially most extensive changes take place in the main channels of the Lena Delta. Downstream migration of sandbanks in shallow waters is a typical process in the active parts of the delta. These changing areas are characterized by strong slopes in the calculated trends, representing the transition from water to sand or vice versa. The trend directions of these processes are similar to the above presented changes. They show a stronger magnitude in TCB trends, but weaker trends in both VIs since these islands consist of bright sandy surfaces and have only sparse or no vegetation. The slope magnitude is lower than transitions from a permanently vegetated surface to water with an increased sensitivity of NDMI. Opposite trends are observed in areas of emerging sandbanks due to sediment accumulation. In contrast to the other indices, TCG appears to be rather insensitive to changes in riverbed morphology, due to little involvement of vegetation.

Figure 2.15: Cliff face of rapidly eroding ice-rich permafrost deposits (A-3) on Sobo-Sise Island, eastern Lena Delta. Photo: G.Grosse

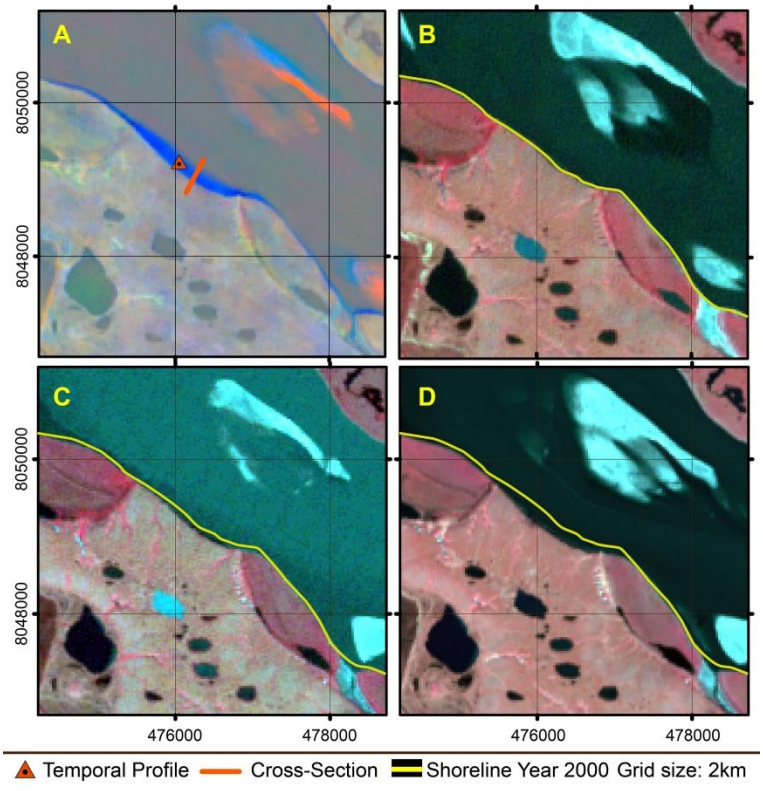

Figure 2.16: RGB composite maps of Tasseled Cap Index trend slopes (TCB–TCG–TCW) and Landsat color-infrared images (NIR-R-G) of rapidly eroding cliff (A-3). A: Trend slopes of rapidly eroding cliff on Sobo-Sise island and migrating sandbanks within the Lena river. B: Landsat-7 acquired on July 28th 2000. C: Landsat-5 acquired on July 25th 2007. D: Landsat-8 acquired on July 16th 2013. Images superimposed with shoreline of year 2000. Map coordinates: UTM52N.

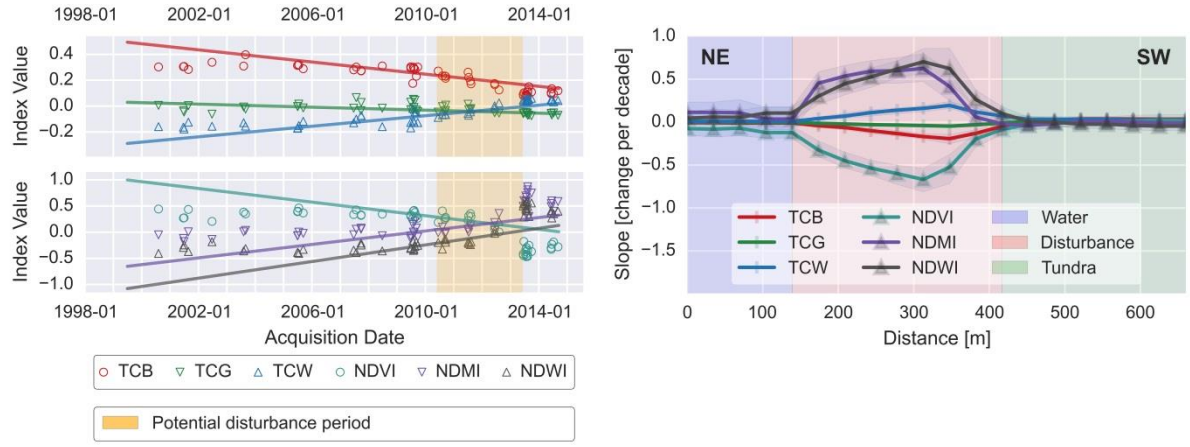

Figure 2.17: Temporal profile of and cross-section through rapidly eroding cliff (A-3). Left: Temporal profile of Tasseled Cap (top) and normalized (bottom) multi-spectral indices from 1999 to 2014 with Theil-Sen trend lines. Potential timing of disturbance indicated in the background. Right: Cross section of trend slopes of all multi-spectral indices through cliff super-imposed by land cover and disturbance locations.

Coastal Processes

The Lena Delta has an extensive and morphologically diverse coastline. Coastal erosion and marine flooding can be detected along some parts of the coastline of the study area. Positive trend slopes of the moisture sensitive indices are a dominant feature of the flat northwestern coastal zone, hence indicating a transition to water. Due to the mostly very flat and sometimes slightly undulating terrain the spatial extent of submerged areas varies strongly (Figure 2.18).

The long stretch of barrier islands on the western delta shore is characterized by a slow eastward migration towards the coast with yearly rates of around 3-8 m. However, along the observed stretch of around 60 km these rates are highly variable locally. On their seaward side all index trends indicate the transition from land to water. On the leeward side the signal is mixed, where some places exhibit a drying trend with an accumulation of sandy substrate, but others being subject to flooding (Figure 2.18).

The remaining, active parts of the Lena Delta generally exhibit a more stable pattern. However, various other types of coastal dynamics can be observed, such as sediment deposition and erosion around major outlets, the transformation of near-shore lakes to lagoons or thermal erosion on coasts of the Bykovsky Peninsula, and warrant a detailed analysis in the future.

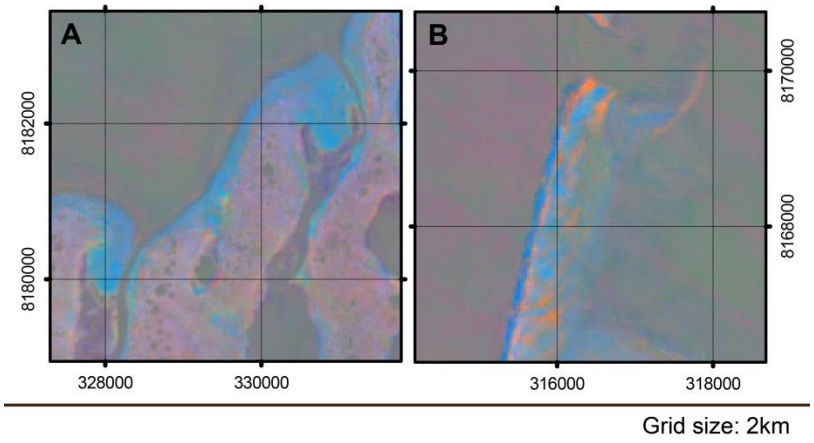

Figure 2.18: RGB composite map of Tasseled Cap Index trend slopes (TCB−TCG−TCW) of coastal dynamics. A: Marine inundation along northwestern shore (B-1). B: Barrier island migration along northwestern shore (B-2). Map coordinates: UTM52N.

2.5 Discussion

2.5.1 Regional scale changes

The trend analysis of dense Landsat time-series has the potential to reveal gradual as well as sudden landscape changes in the permafrost dominated Arctic Lena Delta on multiple temporal- and spatial scales. General regional trends for the Lena Delta, such as a near ubiquitous increase in both vegetation indices (NDVI, and TCG), indicate large scale greening, which is in agreement with previous observations of an overall Arctic greening trend in most tundra landscapes, based on coarse resolution satellite data (Beck & Goetz, 2011; Epstein, et al., 2012; Raynolds, Comiso, Walker, & Verbyla, 2008; Verbyla, 2008) Landsat data (Raynolds, Walker, Verbyla, & Munger, 2013), or field studies (Myers-Smith, et al., 2011). The specifically strong increase in both Vegetation Indices in the eastern near-coastal delta regions, as well as in the active floodplains of the delta, can likely be attributed to the influence of diminishing sea ice cover in the recent decades. Ice-free periods for the Laptev Sea increased by around 10 days per decade (Markus, Stroeve, & Miller, 2009), which likely promoted increasing air temperatures and vegetation changes in the Lena Delta similar to other Arctic coastal regions (Post, et al., 2013). An increase in NDVI of tundra environments has been linked to the increase in biomass and productivity, e.g. through shrub encroachment, caused by rising summer temperatures (Bhatt, et al., 2010; Forbes, Fauria, &

Zetterberg, 2010; Raynolds, Comiso, Walker, & Verbyla, 2008). Sea-ice loss driven land temperature changes may also lead to increased permafrost degradation in coastal regions, including the Lena Delta (Lawrence, Slater, Tomas, Holland, & Deser, 2008).

However, increasing air temperature alone does not explain the spatial pattern of greening, as the coastal areas of the second terrace do not exhibit such a strong magnitude. According to the Landsat- and field data-based land cover classification of Schneider et al. (2009) the areas most affected by greening are covered by "Moist to dry dwarf shrub-dominated tundra", while the land cover in the less affected northwestern regions is dominated by "Dry moss-, sedge- and dwarf shrub-dominated tundra". The differences in land cover and probably also vegetation trends in both regions seem to be partially tied to subsurface substrate conditions and terrace morphology (Ulrich, Grosse, Chabrillat, & Schirrmeister, 2009). While the first terrace is dominated by ice-rich sandy and silty sediments with overall flat and therefore regularly flooded terrain, the second terrace is dominated by ice-poor fluvial sands and a more undulating terrain that is usually not flooded anymore. Therefore, local environmental conditions need to be considered in order to explain the cause of tundra greening trends. In the Lena Delta, wet and moist sites such as the active floodplain or some coastal areas seem to be more affected by tundra greening than dry sites. Several factors, such as plant type or local factors like moisture have been found to influence the vegetation response on warming (Elmendorf, et al., 2012), which is in agreement with the patterns of greening we observe.

The detected regional changes in wetness or moisture cannot be directly related to any single process. While summer precipitation is an important driver of the tundra water balance in the Lena Delta (Boike, Wille, & Abnizova, Climatology and summer energy and water balance of polygonal tundra in the Lena River Delta, Siberia, 2008), the observed spatial patterns of soil moisture trends are difficult to explain with precipitation alone that would rather affect the entire region. Increasing soil moisture in very low-lying coastal areas in the eastern delta may already be influenced by rising sea-levels and thus higher susceptibility to flood events, which has been observed in other deltas (Terenzi, Jorgenson, Ely, & Giguère, 2014). Increasing moisture levels of terrestrial sites farther from the coast may be related to changing hydrological runoff conditions or to active layer deepening in conjunction with near-surface ground-ice thaw. Field data on all these factors are sparse in the Lena Delta and a final conclusion cannot be made at this point.

Some locations with very ice-rich sediments, e.g. the Bykovsky Peninsula and the third delta terrace in general, exhibit a strong wetting trend. Local-scale ground ice-thaw (e.g., ice wedge collapse or thaw pond formation) may be a factor of increasing surface moisture, which has been observed in several areas around the Arctic (Liljedahl, et al., 2016). However, the spatial resolution may not be sufficient to safely link the spectral changes to processes on such fine scales and diffuse spatial patterns. Additional studies on a more local scale and better information about widespread ground-ice thaw may help to improve the interpretation of these trends.

Changes in soil moisture in the Lena Delta will have a significant effect on biogeochemical cycling in permafrost-affected soils, where aerobic versus anaerobic conditions in the active layer determine whether organic matter is decomposed into methane or carbon dioxide (Kutzbach, Wagner, & Pfeiffer, 2004; Sachs, Giebels, Boike, & Kutzbach, 2010). Many different factors could influence moisture sensitive MSI, particularly in a regional-scale analysis.

An inter-comparison with field based measurements, high resolution imagery, or specific soil moisture-related analysis could help to validate and better understand these trend findings in the future. Our trend dataset could thus provide valuable information for selection of future field study sites in locations that exhibit interesting trends in land surface properties.

2.5.2 Local scale changes

In contrast to the subtle regional-scale analysis, the spatio-temporal observation of specific local scale landscape disturbances allows for a much more straight-forward analysis. Landscape disturbances produced highly significant trend magnitude deviations from the general regional-scale observations. The trajectories of the trend analysis allow for a direct interpretation of disturbances. The drainage of thermokarst lakes for example is characterized by decreasing values in all moisture/water sensitive indices (TCW, NDMI and NDWI), whereas the brightness and vegetation sensitive indices (TCB, TCG, NDVI) exhibit a strong increase, driven by the changing surface properties. In contrast to regional changes of the land area, NDWI proved to be useful in the local scale detection of water surfaces and thus to detect changes in water body extent.

Each of the presented examples were significant outliers from the non-change regions and have therefore the potential to be used for further process classification and improved quantification of disturbances in permafrost and river delta landscapes.

2.5.3 Data quality

The inclusion of multiple generations of Landsat sensors is suitable for such applications, with minor remaining issues. The high preprocessing level and calculation of sensor-specific TOA-reflectance values results in a major radiometric normalization of imagery. With this level of pre-processing, the sensor signal can be expected to be highly normalized among the different sensors with an uncertainty of less than 5% between TM and ETM+ (Markham & Helder, 2012). Similar studies, which are mostly based on TM and ETM+ data, either did not mention sensor calibration issues (Fraser R. H., et al., 2014) or only minor differences between the sensor signal (Ju & Masek, 2016). Within our analysis, we did not find noticeable differences between the different sensors. Minor radiometric differences may still occur due to slight differences in radiometric bandwidths for the sensors. However, the Tasseled Cap MSI are designed to take these into account, in contrast to the normalized MSI (NDVI, NDMI, NDWI).

The usage of ETM+SLC-OFF data causes some noise to the calculated trend products with slight striping artefacts in cross-direction of the Landsat flight paths. These artefacts are more pronounced with fewer observations, as the relative difference in the number of image acquisitions is stronger between SLC gap and no-gap areas. Within the different trend components the artefacts are more pronounced for slope than intercept and exhibit slightly different magnitudes between the indices.

Multiple MSI were used to represent different surface properties. The vegetation sensitive MSI (NDVI and TCG) generally exhibit a strong correlation, but differ in their sensitivity. The same behavior of the moisture sensitive MSI NDMI and TCW can be explained by the different dynamic ranges, but also their calculation and inclusion of different spectral bands. There is no clear preference of a MSI for either vegetation or moisture and the differences can be seen as complementary information. NDWI, which has been chosen as another water or moisture sensitive index, reacts strongly to vegetation and is therefore only suitable for pure water detection, a useful property for local disturbance detection. TCB, which has been

chosen as a proxy for albedo, exhibits a rather unexpected positive trend over large areas, where TCW also increases over time. An increase in NIR reflectance caused by a simultaneous greening may be a factor, as the NIR band is a major factor in the calculation of TCB. The sensor-specific weighing factors are probably not completely appropriate, so that the TCB trend probably exhibits a slight bias. For local disturbances with strong change magnitudes, there is no measurable influence of this effect. Over presumably invariant water surfaces, the TC based trends have a very stable behavior with a narrow range around zero.

2.5.4 Data usage and outlook

We here provide the first comprehensive high-resolution land cover trend dataset for the entire Lena Delta, where joint Russian-German research focusing on permafrost and ecosystem dynamics around the centrally located field research station Samoylov Island has now taken place for almost 2 decades (Boike, et al., 2013; Hubberten, Wagner, Pfeiffer, Boike, & Gukov, 2006). Therefore, our dataset can be a valuable resource for numerous applications including general Land-Use/Land- Cover (LULC) change classifications, detection and quantification of specific deltaic processes or disturbances, and field work preparation. With improved process knowledge based on this spatial dataset, costly field work and validation campaigns can be much better targeted on specific locations.

With the free and open access to the Landsat archive and a highly automated and generic processing chain, our methodology can be easily transferred to other sites, which allows for a great opportunity to compare different regions regarding their response to disturbances and land cover changes in a rapidly changing Arctic. The strong normalization and generalization, due to the usage of long and dense time-series in conjunction with a robust linear regression method, ensure the robustness and transferability between different localities. However, additional types of information, such as more complex time-series models for an improved seasonality analysis or the detection of time-series breakpoints could be desirable for a more detailed investigation of specific landscape features. Going forward, the model complexity has to be determined by the objective, with a rather generalized simple model for large datasets or more complex and dynamic time-series models for the analysis of vegetation dynamics or breakpoints with sophisticated time-series methods such as BFAST (Verbesselt, Hyndman, Newnham, & Culvenor, 2010) or DBEST (Jamali, Jönsson, Eklundh, Ardö, & Seaquist, 2015). Going beyond the Landsat-data, interesting opportunities are provided by the

successful launch of ESA's Sentinel-2 satellite that collects comparable multispectral data. Sentinel-2 data could be integrated in the processing chain to further increase the observation density and future monitoring capabilities in high latitude permafrost regions.

2.6 Conclusion

The entire Landsat archive was used to calculate robust trends of key surface indicators within the ~29,000 km2 Lena Delta in north-eastern Siberia. A generic and highly automated processing chain was developed to quickly process data for large and remote permafrost areas.

The robust trends of different multi-spectral indices (Landsat Tasseled Cap, NDVI, NDMI, NDWI) revealed several processes in multiple-spatial scales. On a regional basis, noticeable greening trends were detected in the active parts of the Lena Delta. Surface wetness changes were observed in different sub-regions either associated with near-coastal areas, ice-rich permafrost of the third delta terrace, or major delta channels. Typical local disturbances, such as thermokarst lake dynamics, fluvial and coastal processes were identified and analyzed in their temporal development with the presented methodology. With Landsat's spatial resolution of 30 meters, compared to other sensors with short revisit times, even small localized disturbances were detected. Due to the high process automation and standardization, our approach can be easily applied to other study sites, which may help to understand and quantify critical disturbances within remote permafrost landscapes across extensive regions.

2.7 Data Archive

Spatial datasets produced in this study have been archived in the open access PANGAEA repository (http://doi.pangaea.de/10.1594/ PANGAEA.854640). A detailed dataset description is given on the website.

2.8 Acknowledgements

This research was supported by ERC Starting Grant #338335 and the Initiative and Networking Fund of the Helmholtz Association (#ERC- 0013). The authors thank the field team of the Lena Delta 2014 expedition. Furthermore, we would like to thank the anonymous reviewers for their valuable comments, and the developers and contributors of the used software packages.

2.9 Appendix A. Supplementary Data

Supplementary data associated with this article can be found in the online version, at http://dx.doi.org/10.1016/j.rse.2016.03.038. These data include the Google map of the most important areas described in this article.

3. Landsat-Based Trend Analysis of Lake Dynamics across Northern Permafrost Regions

Nitze, I.[1,2]; Grosse, G.[1,2]; Jones, B.M.[3]; Arp, C.D.[4]; Ulrich, M.[5]; Fedorov, A.[6,7] & Veremeeva, A.[8]

[1] Alfred Wegener Institute Helmholtz Centre for Polar and Marine Research, Periglacial Research Unit, Potsdam, Germany

[2] Institute of Earth and Environmental Science, University of Potsdam, Potsdam, Germany

[3] U.S. Geological Survey, Alaska Science Center, Anchorage, AK, USA

[4] Water and Environmental Research Center, University of Alaska Fairbanks, Fairbanks, AK, USA

[5] Institute for Geography, Leipzig University, Leipzig, Germany

[6] Melnikov Permafrost Institute, Yakutsk, Russia

[7] North-Eastern Federal University, Yakutsk, Russia

[8] Institute of Physicochemical and Biological Problems in Soil Science, Russian Academy of Sciences, Pushchino, Russia

Published in: Remote Sensing, Vol. 9.7, 2017

Citation: Nitze, I., Grosse, G., Jones, B. M., Arp, C. D., Ulrich, M., Fedorov, A., & Veremeeva, A. (2017). Landsat-based trend analysis of lake dynamics across northern permafrost regions. Remote Sensing, 9(7), 640. DOI: 10.3390/rs9070640

3.1 Abstract

Lakes are a ubiquitous landscape feature in northern permafrost regions. They have a strong impact on carbon, energy and water fluxes and can be quite responsive to climate change. The monitoring of lake change in northern high latitudes, at a sufficiently accurate spatial and temporal resolution, is crucial for understanding the underlying processes driving lake change. To date, lake change studies in permafrost regions were based on a variety of different sources, image acquisition periods and single snapshots, and localized analysis, which hinders the comparison of different regions. Here, we present a methodology based on machine-learning based classification of robust trends of multi-spectral indices of Landsat data (TM, ETM+, OLI) and object-based lake detection, to analyze and compare the individual, local and regional lake dynamics of four different study sites (Alaska North Slope, Western Alaska, Central Yakutia, Kolyma Lowland) in the northern permafrost zone from

1999 to 2014. Regional patterns of lake area change on the Alaska North Slope (−0.69%), Western Alaska (−2.82%), and Kolyma Lowland (−0.51%) largely include increases due to thermokarst lake expansion, but more dominant lake area losses due to catastrophic lake drainage events. In contrast, Central Yakutia showed a remarkable increase in lake area of 48.48%, likely resulting from warmer and wetter climate conditions over the latter half of the study period. Within all study regions, variability in lake dynamics was associated with differences in permafrost characteristics, landscape position (i.e., upland vs. lowland), and surface geology. With the global availability of Landsat data and a consistent methodology for processing the input data derived from robust trends of multi-spectral indices, we demonstrate a transferability, scalability and consistency of lake change analysis within the northern permafrost region.

3.2 Introduction

More than 25% of the lakes on Earth are located in the northern high latitude region (Lehner & Döll, 2004). The distribution of lakes can primarily be explained by prior glaciation histories, the presence of peatlands, and the presence of ice-rich permafrost (Smith, Sheng, & MacDonald, 2007). Lakes and ponds can occupy more than 20–40% of the landscape in Arctic lowland regions (Grosse, Jones, & Arp, 2013; Muster, et al., 2017). Grosse et al. (2013) estimate that more than half of the lakes found in permafrost regions are likely of thermokarst origin; however, many other lake types in the Arctic are recognized (Jorgenson & Shur, 2007; Jones, et al., 2017). Thus, thermokarst lakes and non-thermokarst lakes are a key component of northern ecosystems and have a strong impact on carbon, energy and water fluxes (Walter Anthony, et al., 2016; Langer, et al., 2016; Olefeldt, et al., 2016; Boike, et al., 2016). Arctic lakes have developed in a highly dynamic environmental setting that is subject to both hydroclimatic and geomorphic changes (Arp, Jones, Schmutz, Urban, & Jorgenson, 2010; Lantz & Turner, 2015). With respect to thermokarst lakes, they may undergo several generations that include phases of formation, growth, drainage, and reformation (Grosse, Jones, & Arp, 2013; Jorgenson, Shur, & Pullman, 2006; Jones B. M., et al., 2011). With a rapidly warming Arctic the direction and magnitude of these dynamics and fluxes may change dramatically due to changes in lake hydrology, lake ice characteristics, and permafrost degradation (Arp, Jones, Urban, & Grosse, 2011; Liljedahl, et al., 2016; Lindgren, Grosse, Romanovsky, & Farquharson, 2016). Therefore, monitoring of lake-rich Arctic regions at high

temporal and spatial resolution as well as across very large regions is crucial for understanding their response to climate change and consequently their feedbacks with various environmental conditions. The dynamics of northern high latitude lakes may also serve as a critical climate change indicator or essential climate variable.

Until recently, global or continental scale water datasets have been too limited in spatial resolution to capture the entire range of lake sizes, such as MODIS-derived products at 250 m resolution (Carroll & Loboda, 2017). Now, global water body change datasets based on Landsat data have been developed (Donchyts, et al., 2016; Pekel, Cottam, Gorelick, & Belward, 2016), but in particular high-latitude regions may not be represented with high accuracies due to snow, ice, persistent cloud cover, sediment suspension or poor data quality. Moreover, these studies mostly focus on overall water body change, not lakes in particular. Due to the sheer number of lakes in the northern high latitude region, ranging in the many millions (Muster, et al., 2017; Paltan, Dash, & Edwards, 2015; Muster, Heim, Abnizova, & Boike, 2013), and the considerable extent of the northern permafrost region (~23 million km^2) (Zhang, Barry, Knowles, Heginbottom, & Brown, 2008), their broad range in size and dynamics makes the monitoring of these locally dominant and important landscape features across the permafrost region a challenging task. Remote sensing, with its capability of establishing calibrated observations over decadal-scale time periods and at sufficiently high spatial resolution (≤30 m), is therefore a key tool to achieve a better insight into permafrost region lake dynamics.

Several local and regional studies focus on the dynamics of selected thermokarst lake regions in the permafrost domain using a variety of spatial and temporal remotely sensed datasets (Lantz & Turner, 2015; Jones B. M., et al., 2011; Karlsson, Lyon, & Destouni, 2014; Smith L. C., Sheng, MacDonald, & Hinzman, 2005; Olthof, Fraser, & Schmitt, 2015; Riordan, Verbyla, & McGuire, 2006; Roach, Griffith, & Verbyla, 2013; Kravtsova & Tarasenko, The Dynamics of thermokarst lakes under climate change since 1950, 2011). The findings from these studies indicate that regional lake dynamic trends often follow a general pattern. Within the continuous permafrost zone, regional lake area trends were found to be mostly positive or neutral, but lake area loss may exceed lake growth in some regions. Eventually, some lakes ultimately drain, predominantly caused by bank overflow or reaching a drainage gradient (Jones B. M., et al., 2011; Jones & Arp, 2015; Hinkel, et al., 2007). These processes of lake growth and drainage are typical for thermokarst lakes (Grosse, Jones, & Arp, 2013; Jorgenson

& Shur, 2007). Some studies find an increase in the number of lakes independent of the regional lake area changes, which may be caused by new thermokarst lake initiation and splitting of larger lakes into multiple remnant lakes (Jones B. M., et al., 2011; Smith L. C., Sheng, MacDonald, & Hinzman, 2005). Lake area increase has been observed over several regions in North America (Arp, Jones, Urban, & Grosse, 2011; Olthof, Fraser, & Schmitt, 2015; Plug, Walls, & Scott, 2008), and Siberia (Smith L. C., Sheng, MacDonald, & Hinzman, 2005; Walter, Zimov, Chanton, Verbyla, & Chapin, 2006; Boike, et al., 2016). In contrast, lake area loss was found in Western Alaska (Jones B. M., et al., 2011) in Northwestern Canada (Lantz & Turner, 2015; Labrecque, Lacelle, Duguay, Lauriol, & Hawkings, 2009), and in the northeastern part of European Russia (Elsakov & Marushchak, 2011), and Siberia (Boike, et al., 2016; Kravtsova & Bystrova, 2009). In the discontinuous permafrost zones (<90% permafrost cover), a decrease of lake area has been observed for most regions (Smith L. C., Sheng, MacDonald, & Hinzman, 2005; Riordan, Verbyla, & McGuire, 2006; Roach, Griffith, & Verbyla, 2013). On a local scale, however, large variation of lake area increase, stability, or decrease may occur. Disappearing or shrinking lakes are often caused by increased evaporation and/or the development of connectivity to groundwater following permafrost thaw (Roach, Griffith, & Verbyla, 2013; Jepsen, Voss, Walvoord, Minsley, & Rover, 2013; Yoshikawa & Hinzman, Shrinking thermokarst ponds and groundwater dynamics in discontinuous permafrost near Council, Alaska, 2003). However, the variation in regional net lake change and related hydrological dynamics across different environmental settings depends on a large number of factors affecting hydrological dynamics such as climate, permafrost, geology, topography, and landscape age.

Most prior remote sensing studies focused on lake area changes have been temporally limited, relying on the comparison of imagery from two to three time slices e.g. (Jones B. M., et al., 2011; Karlsson, Lyon, & Destouni, 2014; Smith L. C., Sheng, MacDonald, & Hinzman, 2005; Boike, et al., 2016). The analyses typically spanned several decades, since the availability of aerial or space-borne imagery at higher temporal frequency in sufficient spatial resolution was not available until recent years. With high spatial resolution images (<5 m) waterbodies can be accurately delineated even to very small sizes (<100 m²) (Andresen & Lougheed, 2015; Sannel & Brown, 2010). However, due to the limited extent and availability of very high resolution imagery, the studies were usually focused on rather small, image-footprint limited regions (Andresen & Lougheed, 2015; Sannel & Brown, 2010; Necsoiu, Dinwiddie, Walter, Larsen, & Stothoff, 2013; Ulrich, et al., 2017). With the focus on single observations so far,

the potentially strong intra-annual variation of water-bodies (Olthof, Fraser, & Schmitt, 2015; Tarasenko, 2013) cannot be sufficiently accounted for. Moreover, the diversity of data sources and acquisition timing results in limited comparability between different studies. In contrast, moderate or low spatial resolution (≥250 m) remote sensing observations offer temporally high resolution, large area monitoring capabilities, with the drawback that the monitoring of a very large portion of small thermokarst lakes remains impossible at these spatial resolutions.

With the increase of computation capacities and free data availability, the extensive Landsat imagery archive has become increasingly popular for environmental monitoring purposes on local to global scales (Pekel, Cottam, Gorelick, & Belward, 2016; Hansen, et al., 2013; Wulder, et al., 2016). This type of data stream at relatively high spatial and temporal resolutions, with an observation period spanning several decades, allows very detailed observations of the often small-scale but widespread land surface dynamics in permafrost landscapes. Trend analyses based on widely used Landsat multi-spectral indices have been applied for land cover change monitoring to various sites in northwestern Canada (Fraser R. H., et al., 2014; Brooker, Fraser, Olthof, Kokelj, & Lacelle, 2014), the Siberian Lena Delta (Nitze & Grosse, 2016) or even continental scales (Ju & Masek, 2016). With the application of spectral unmixing, sub-pixel lake changes were reliably detected and analyzed (Olthof, Fraser, & Schmitt, 2015). The combination of sub-pixel analysis and its temporal and spatial capabilities makes Landsat a potentially valuable data source for the detection of lake dynamics.

Due to the rapid nature of reported lake and landscape changes occurring in the northern high latitudes, we developed a workflow to analyze Landsat-based trend data with machine-learning classification (MLC) and object-based image analysis (OBIA) for the detection and analysis of lake dynamics in two lake-rich regions in Alaska and two lake rich regions in Siberia spanning a total of 200,000 km². The regions cover different permafrost types (continuous and discontinuous) as well as different eco-zones (coastal lowland tundra to boreal forest), allowing us to test the applicability of our approach over large regions and a wide range of environmental conditions within the permafrost region. Our analysis aims at detecting decadal scale changes in the surface water balance while reducing sensitivity to short-term fluctuations. With the global availability of Landsat data and a consistent methodology for processing the input data derived from robust multi-spectral trends, we here

demonstrate a transferable, scalable and consistent lake change analysis within the northern permafrost region.

3.3 Study Sites

We chose four different study sites (Figure 3.1) to test our combined MLC and OBIA approach in regions with different environmental properties, including the permafrost type, lake-abundance, eco-zone, and the availability of auxiliary data for comparison and validation. In addition to the environmental conditions, the extent of the study sites was selected to remain within one UTM Zone.

In Alaska, the central part of the northern Arctic Coastal Plain and Foothills (North Slope, NSL) and the Kobuk-Selawik Lowlands (AKS) region in Western Alaska were selected. In Siberia, we analyzed the Central Yakutian Lena river basin (CYA) as well as the lower Kolyma Lowland region in Northeastern Siberia (KOL). Each region is described in detail below.

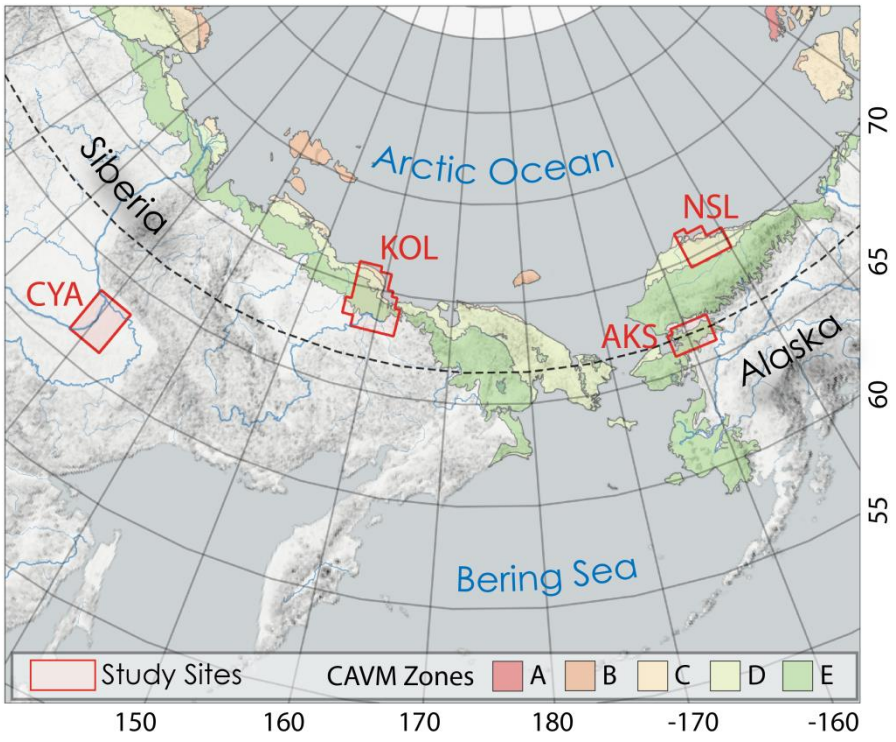

Figure 3.1: Overview Map of eastern Siberia and Alaska with study sites and Circum-Arctic Vegetation Map (CAVM) Zones after (Walker, et al., 2005).

3.3.1 Alaska North Slope (NSL)

The Alaska North Slope (NSL) study site is located along the northern coast of Alaska north of the Brooks Range and completely within the continuous permafrost that reaches depths of 300 to 600 m (Hinkel, et al., 2012; Jorgenson, et al., 2008). For our study, we chose a 31,715 km² study region centered around Teshekpuk Lake. This region is characterized by a very high density of lakes and drained thermokarst lake basins, which cover around 20% and 50 to 65% of the land surface, respectively (Jones & Arp, 2015; Hinkel, et al., 2012). The area has an arctic continental climate with a mean annual air temperature (MAAT) of −11.2 °C and a mean annual precipitation (MAP) of 115 mm at Barrow (NOAA, 2017) (1981–2010).

The study site is separated into several distinct geological zones, Young Outer Coastal Plain (YOCP), Outer Coastal Plain (OCP), Inner Coastal Plains (ICP), and the Arctic Foothills (AF) which are characterized by different thermokarst features (Farquharson, Mann, Grosse, Jones, & Romanovsky, 2016) (Figure 3.2). The YOCP and OCP are directly located closer to the Beaufort Sea and are characterized by flat terrain with mostly fine grained ice-rich marine silt (YOCP) or sand (OCP) and numerous shallow lakes, drained thermokarst lake basins, and other lowland thermokarst features (Jones & Arp, 2015; Arp, Jones, Urban, & Grosse, 2011; Lenz, et al., 2016). The ICP in the southern and central part is characterized by undulating terrain with sandy deposits of marine and eolian origin and with a high density of lakes that have shallow margins and deep centers (Jorgenson & Shur, 2007; Hinkel, et al., 2012; Sellman, Brown, Lewellen, McKim, & Merry, 1975; Jones, et al., 2009). The AF in the southern margin of our study area are characterized by sloped rolling topography, fine-grained, ice-rich yedoma deposits (Kanevskiy, et al., 2013; Schirrmeister, Froese, Tumskoy, Grosse, & Wetterich, 2013) and a low abundance of relatively deep lakes. The land cover generally is dominated by low tundra vegetation of vegetation subzones C, D, and E as well as surface water bodies (Walker, et al., 2005). In particular along the eastern coastline, economic development affects land cover in the form of hydrocarbon exploration and extraction activities such as construction of roads, pipelines, exploration and extraction pads, pump stations, housing, and other facilities (Raynolds, et al., 2014).

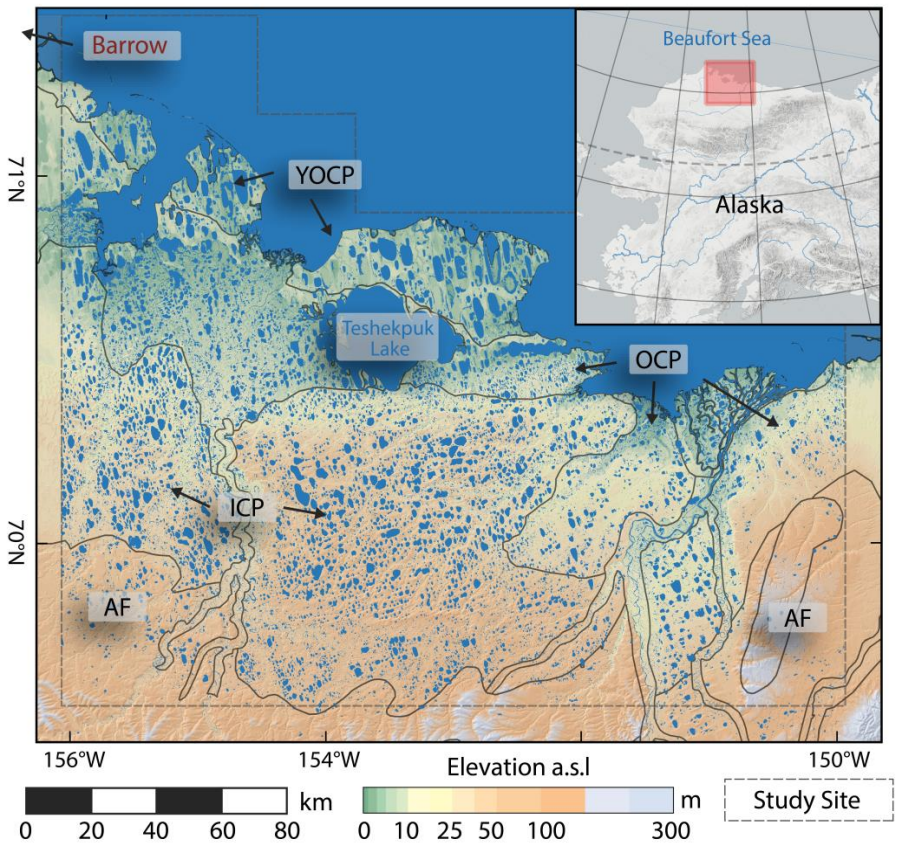

Figure 3.2: Overview Map of Alaska North Slope study site (NSL) with generalized geological subzones. YOCP: Younger Outer Coastal Plain; OCP: Outer Coastal Plain; ICP: Inner Coastal Plain; AF: Arctic Foothills.

3.3.2 Alaska Kobuk-Selawik Lowlands (AKS)

The Alaska Kobuk-Selawik Lowlands (AKS) study site is located in the northwestern coastal region of Alaska bordering the Kotzebue Sound to the west and continuing further east along the Kobuk and Selawik river valleys near the Arctic Circle (Figure 3.3). The study site has a size of 31,135 km². The region is located at the transition between the continuous and discontinuous permafrost zones (Jorgenson, et al., 2008). Based on the climate record of Kotzebue, the region has a subarctic continental climate with a MAAT of −5.1 °C and a MAP of 279 mm (NOAA, 2017) (1981–2010).

The AKS site contains a large variety of landscape types with river valleys and deltas, alluvial plains, coastal lowlands, and gently rolling uplands (Larsen, O'Donnell, Schmidt, Kristenson, & Swanson, 2017). Some regions feature ice-rich permafrost with a high abundance of thermokarst lakes and basins, while other areas are permafrost-free (Cable, Romanovsky, &

Jorgenson, 2016). These lowland features are encompassed by several hill ranges, which are partially located within the study area.

The land cover mostly consists of water bodies. The vegetation in the permafrost transition zone ranges from wetland tundra in the coastal area to the shrub tundra of vegetation subzone E (Walker, et al., 2005) in the river deltas and valleys, to boreal forest in the eastern portion of the study area (Jorgenson, et al., 2009).

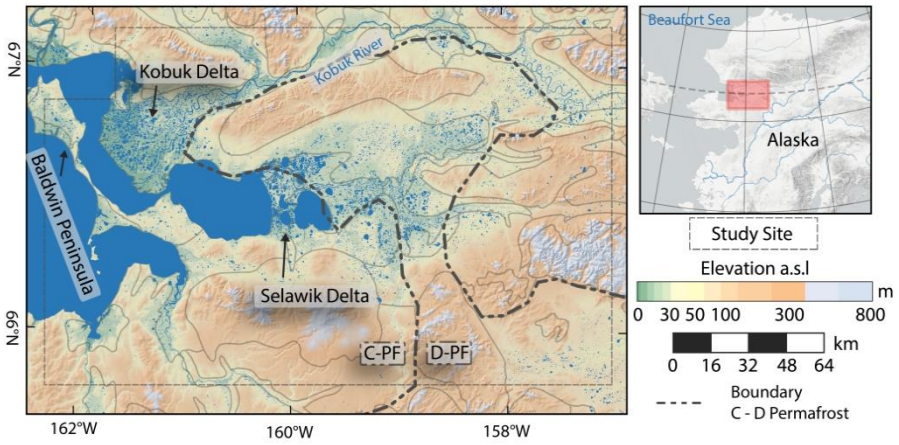

Figure 3.3: Overview Map of Alaska Kobuk-Selawik Lowlands study site (AKS) with generalized geological subzone boundaries. C-PF: Continuous permafrost; D-PF: Discontinuous permafrost. Permafrost zonation after Jorgenson et al. (2008).

3.3.3 Central Yakutia (CYA)

The Central Yakutia (CYA) study site is located in the middle Lena river basin around the city of Yakutsk and encompasses an area of 56,700 km². Central Yakutia belongs to the continuous permafrost zone with permafrost that reaches depths of 450 m (Ivanov, 1984) and is subject to extreme continental climate conditions. Yakutsk has a MAAT of −9.7 °C (1930–2010) with strong seasonal air temperature differences that can exceed 60 K between very warm summers and extremely cold winters (Fedorov, Ivanova, Park, Hiyama, & Iijima, 2014). The MAP is low at 234 mm, but can be subject to strong decadal variation (Ulrich, et al., 2017). Large streams, like the Lena or Aldan rivers, have a strong influence on the landscape by shaping large valleys and alluvial plains, which are seasonally flooded during spring ice-break-up (Yang, et al., 2002).

Permafrost in this study area is dominated by ice-rich silty yedoma ice-complex deposits, which are almost completely thawed below thermokarst basins (termed “alas” in this region)

and ice-poor sandy floodplains (Soloviev, 1959). Within the study site, several distinct terraces with predominantly very ice-rich deposits can be differentiated (Ulrich, et al., 2017; Nitze & Grosse, 2016) (Figure 3.4). On these terraces there are abundant thermokarst lakes and alas basins. Over recent decades, there has been an increase in the development of thermokarst lakes (Ulrich, et al., 2017; Fedorov, Ivanova, Park, Hiyama, & Iijima, 2014).

Boreal forest with larch, pine, and birch is the dominant land cover within this study site, while grasslands are ubiquitous within alas basins. The region is affected by frequent wildfires during the warm summer months (Boike, et al., 2016; Hansen, et al., 2013). Compared to the other study sites, this region is considerably influenced by land use activities in the form of agriculture, forestry, and infrastructure development for several centuries and in particular over recent decades (Crate, et al., 2017).

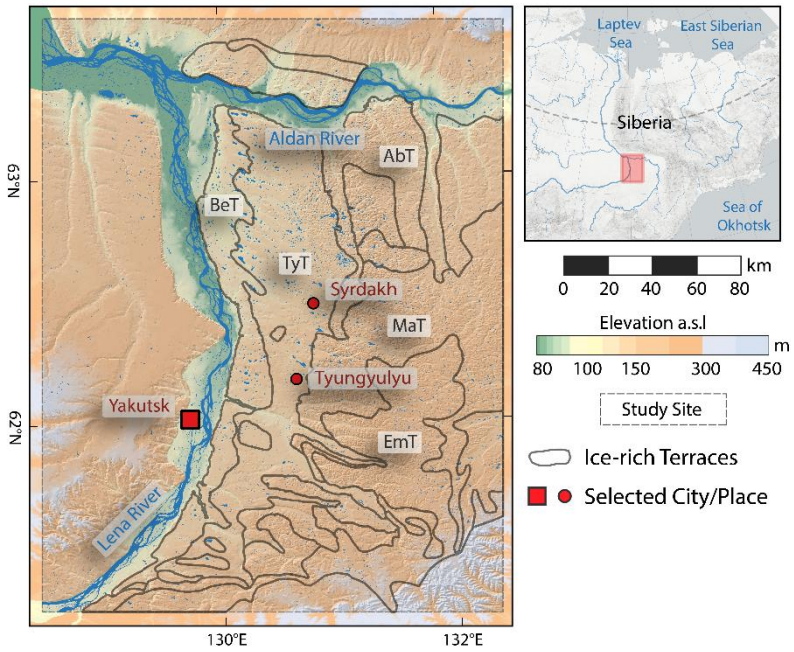

Figure 3.4: Overview Map of Central Yakutia study site (CYA) with generalized geological subzones on the eastern banks of the Lena river after Soloviev (1959). BeT: Bestyakhskaya Terrace; TyT: Tyungyulyuyskaja Terrace; AbT: Abalakhskaya Terrace; MaT: Maganskaya Terrace; EmT: Emilskaya Terrace.

3.3.4 Kolyma Lowland (KOL)

The Kolyma Lowland study site (KOL) west and northwest of the Kolyma river mouth is completely located within the continuous permafrost zone of northeastern Siberia with depths of 300 to 500 m (Kaplina, 1981; Ershov, 1989), and encompasses an area of 73,339 km². The

region has a polar tundra climate with a MAAT of −9.2 °C and MAP of 237 mm at Cherskiy (2009 to 2014).

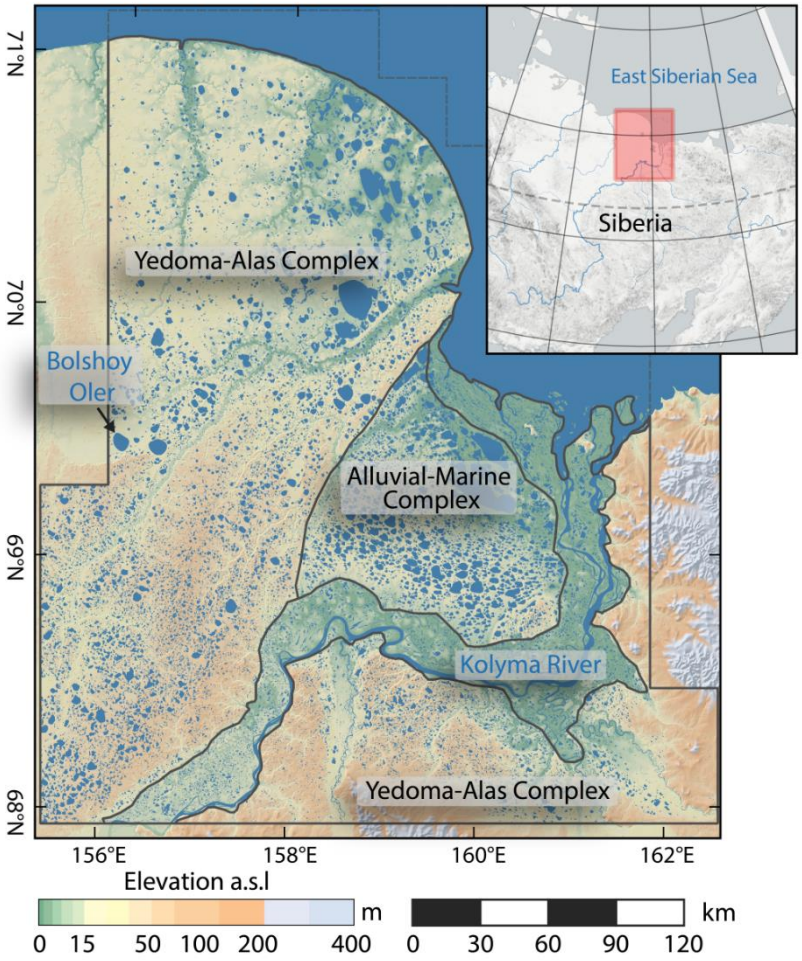

Figure 3.5: Overview Map of Kolyma Lowland site (AKS) with generalized geological subzones after Shmelev et al. (2017).

The region is mostly flat terrain and consists of different geological regions (Shmelev, et al., 2017) (Figure 3.5). The western and southern part is dominated by fine-grained and ice-rich late Pleistocene yedoma deposits interspersed with thermokarst basins and river valleys and an abundance of thermokarst lakes and basins (Yedoma-Alas Complex) (Veremeeva & Glushkova, 2016). Within this zone, the low lying northern coastal regions are dominated by thermokarst basins, which cover 80–100% of the area, whereas the southern part, north and south of the Kolyma river, has a higher abundance of ice-rich yedoma deposits, covering about 30–50% of the area (Veremeeva & Glushkova, 2016).

West of the Kolyma river mouth, the Alluvial-Marine Complex, composed of sandy deposits (Spector, 1980), forms the landscape and exhibits a high abundance of large oriented lakes. Along its course the Kolyma river forms a wide floodplain and a delta on its outflow into the East Siberian Sea. On its eastern margin, the study site is bordered by hill ranges of up to 700 m. The land cover is dominated by tundra lowlands of vegetation subzones C, D, and E (Walker, et al., 2005). The southeastern part of the study site, around the town of Cherskiy, is situated in the northern taiga zone.

3.4 Data and Methods

3.4.1 Data and Trend Analysis

In this study, we used the entire archive of Landsat data available for our four study regions between 1999 and 2014 filtered to the peak summer months July and August, and a cloud cover of less than 70%. We used only Landsat data from TM, ETM+ and OLI sensors, which have a common spatial resolution (30 m) and (six) overlapping spectral bands: Blue, Green, Red, Near-Infrared (NIR), Shortwave Infrared 1 (SWIR1), and Shortwave Infrared 2 (SWIR2). In order to keep data commonality for all sites, we decided not to include and analyze imagery before 1999. Large parts of Northeastern Siberia and Northwestern Alaska are affected by a very sparse acquisition frequency before 1999.

Data were acquired from United States Geological Survey (USGS) via the EROS Science Processing Architecture (ESPA) ordering system. All scenes were ordered as surface reflectance data and provided with the pre-processed FMask layer (Zhu, Wang, & Woodcock, 2015), which includes pixel quality flag information on cloud, snow, and shadow presence for each scene. The preprocessed scenes were downloaded and processed using an automated processing pipeline consisting of several steps: file extraction; masking of snow/ice, clouds, and shadows; re-projection (where necessary) and sub-setting. The data were structured into subsets of 30 × 30 km and projected into each site's primary UTM zone.

After data-preprocessing, robust linear trends based on the Theil-Sen regression algorithm (Fraser R. H., et al., 2014; Olthof & Fraser, 2014; Sen, 1968; Theil, 1992) were calculated for each pixel and six different multi-spectral indices (MSI): Tasseled Cap Brightness (TCB), Tasseled Cap Greenness (TCG), Tasseled Cap Wetness (TCW), Normalized Difference

Vegetation Index (NDVI), Normalized Different Water Index (NDWI), and Normalized Different Moisture Index (NDMI). These indices are well established for Landsat and have been widely used in land cover remote sensing applications (Fraser R. H., et al., 2014; Brooker, Fraser, Olthof, Kokelj, & Lacelle, 2014; Ju & Masek, 2016; Rover, Ji, Wylie, & Tieszen, 2012; Raynolds & Walker, 2016; Kennedy, Yang, & Cohen, 2010). The trend calculation output consists of four trend parameters: slope, intercept, lower confidence interval, and upper confidence interval. Therefore each pixel carries 24 different types of information, i.e., four parameters for each of the six MSI. More detailed information on the processing chain is available in Nitze and Grosse (2016).

Since lakes and their areal changes are the main scope of this study, we chose a combined approach of machine-learning classification (MLC) of the pre-calculated spatio-temporal trend information in conjunction with object based image analysis (OBIA).

3.4.2 Pixel-Based Machine-Learning Classification

We first applied a supervised MLC approach which translates the spectral-temporal signal into semantic information and separates the trend information into four target classes. These include two static classes, stable water *(S-W)* and stable land *(S-L)*, as well as two dynamic classes, water to land *(C-WL)* and land to water *(C-LW)* (cf. Table 3.1). For the classification process we used a Random Forest (RF) (Breiman, 2001) MLC algorithm. This non-parametric method has been established as one of the most accurate and widely used algorithms (Nitze, Barrett, & Cawkwell, 2015; Barrett, Nitze, Green, & Cawkwell, 2014; Belgiu & Dragut, 2016) for remote sensing and other classification applications because of its robustness, independence of statistical data distributions, and capabilities to work with a wide array of input data types.

Table 3.1: Classification scheme with class name, class ID, number of training samples and examples of observed land cover or changes.

Class Name	Class ID	Number of Training Samples	Examples of Observed Land Cover or Changes
Stable water	S-W	148	Lakes, sea water, river
Stable land	S-L	270	Tundra, forest, bare ground
Change water to land	C-WL	193	Lake drainage (water to bare ground, water to vegetation), river channel migration
Change land to water	C-LW	84	Thermokarst lake expansion, riverbank erosion, coastal erosion

Training Sampling

We selected 568 training samples within and in close proximity to our study sites with respect to a variety of surface conditions, such as permafrost type, geological properties, vegetation types, water color and target classes. The extensive choice of ground truth locations, beyond the footprint of our study sites, allows us to account for a wider range of landscape surface conditions.

The ground truth selection process is based on a hybrid of random sampling and stratified manual sampling. As the change regions (classes *C-WL* and *C-LW*) cover only a small fraction of the study areas, we manually selected and over-sampled the training data for these classes. A purely random or gridded approach would have led to very small sample sizes of the change classes and was therefore not applicable. As stable land can have a variety of different surface conditions, we increased its sample size to attribute for this variety. The same reasoning was applied for the choice of training areas for lake drainage, which has a wide range of potential spectral and temporal signatures depending on the speed of drainage and post-drainage re-vegetation. In contrast, changes from land to water have a narrower range of appearances and therefore needed a smaller size of training samples. The calculated Landsat trend data as well as high-resolution images and local knowledge of in situ conditions were used for determining suitable locations of the manually selected and determined ground truth locations.

Classification Method Details

Slope, intercept as well as the lower and upper confidence intervals (CI) for each of the six MSI were used as input features for the pixel-based classification process. In addition, the difference between upper and lower CI (confidence interval range) was calculated. Therefore, 30 input variables were used in the MLC (Table 3.2).

The RF classification model was trained using the 568 training samples (see Table 3.1) with 200 decision trees. This number of trees has been found to be sufficient for most classification purposes (Nitze, Schulthess, & Asche, 2012). Two different methods were used for quality assessment of the classification. First, the RF-specific internal quality parameter out-of-bag accuracy (OOB) (Breiman, 2001) was used, which provides the classification accuracy through bootstrapped sampling. Second, a 5-fold cross-validation was carried out, based on a

stratified randomized sampling of the ground truth data and the overall accuracy and Cohen's kappa were used as a metrics of the classification quality.

Table 3.2: Used input features for the MLC classification process. Each trend metric (n = 5) was calculated for each Multi-spectral index (n = 6) leading to 30 features.

Multi-Spectral Index	Trend Metric
TC Brightness	Slope
TC Greenness	Intercept
TC Wetness	Lower CI
NDVI	Upper CI
NDWI	CI Range
NDMI	

The classification output contains a hard classification output with the four pre-defined classes (Table 3.1). Furthermore, a confidence layer for each class was calculated, which contains the classification probability of each single class in a range from 0 to 1.

The classification with four defined classes (cf. Table 3.1, *S-W*, *S-L*, *C-LW*, and *C-WL*) yielded a perfect separation on the ground truth data of the defined classes. With both evaluation methods, the RF-internal OOB as well as the and the 5-fold cross-validation, all accuracy measures (OOB, overall accuracy, Cohen's kappa) achieved 100%. This shows a very high separability of pure pixels or endmembers of the four defined classes.

3.4.3 Object-Based Image Analysis

Lake Object Creation

Based on the hard classification results, lake objects (LO) were defined (Figure 3.6). Connected pixels of water and both change classes were aggregated into objects, where only 4-point-connected pixels, with neighborhood along pixel edges, were defined as a single LO. Each LO represents either a lake with adjacent change regions, e.g., an expanding or partially draining lake; a lake without any change; or an area which underwent full transition such as a completely drained or newly formed lake.

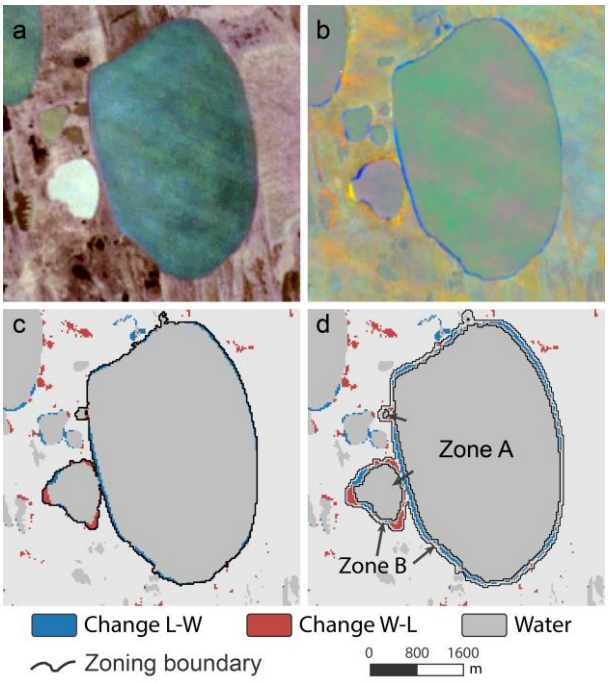

Figure 3.6: Example of workflow steps from satellite image to lake zoning on a lake in the Alaska North Slope study site: (a) raw Landsat satellite image (R-G-B); (b) RGB-Visualization of Tasseled Cap Index Trends with R: Brightness, G: Greenness and B: Wetness; (c) classified trend data and lake object delineation; and (d) subdivision into stable (A) and dynamic (B) lake zones.

During the next step, each LO was sub-divided into a static (Zone A) and a dynamic (Zone B) zone (Figure 3.6). For the static Zone A, we used the hard-classified water mask (class *S-W*) within each object and applied a morphological erosion to reduce the lake's radius by 1 pixel to avoid the lake margin, where mixed pixels may occur. This zone represents the non-changing water surface. Zone B represents the dynamic boundary of the lake objects, which is comprised of two different parts. B-1 includes the outside boundary of the stable water zone A with a width of 2 pixels, where thermokarst lake expansion likely occurs on a sub-pixel scale (<30 m). Zone B-2 represents the change region (classes *C-WL* and *C-LW*), which is dilated by 1 pixel to capture the transition zone to stable land. Both zones, B-1 and B-2, are merged into a single zone B. Finally, lake objects of less than 1 ha in area were removed.

Lake Change Calculation

During the final step, we calculated the areal extent of spatial dynamics for each lake object. Each of the two defined zones was treated differently. The stable Zone A was regarded as permanent water and its area was therefore calculated as static surface water over the entire period. For Zone B we chose a more dynamic sub-pixel analysis approach to account for its

location on the lake margins and the transition zone. Each class' area is represented by the classification probability (*p*-values), which is assumed to be the fraction of each endmember/class and they were tested for plausibility on high-resolution imagery as well as field measurements and observations, which were available for selected locations. These *p*-values were used as a weighing factor of each class within each pixel of Zone B. A calculation example for the 3-pixel transect through the margin of a large thermokarst lake in the NSL study site is presented in Table 3.3 and Figure 3.7. The western pixel has a *p*-value of 0.705 for stable water representing 70.5% of the 900 m² pixel, hence 634.5 m² are calculated as steady water surface within this pixel. The same applies to each class and pixel. Within this short transect 720 m² of the 2700 m² were subject to a transition from land to water caused by lake shore erosion through thermokarst (cf. Figure 3.12).

Table 3.3: Calculation example for three pixels through the margin of a thermokarst lake.

Example Pixel	S-W		S-L		C-LW		C-WL	
	p-Value	m²	*p*-Value	m²	*p*-Value	m²	*p*-Value	m²
px-West	0.705	634.5	0.005	4.5	0.29	261	0	0
px-Central	0.065	58.5	0.39	351	0.51	459	0.035	31.5
px-East	0	0	1	900	0	0	0	0
Σ	0.77	693	1.395	1255.5	0.8	720	0.035	31.5

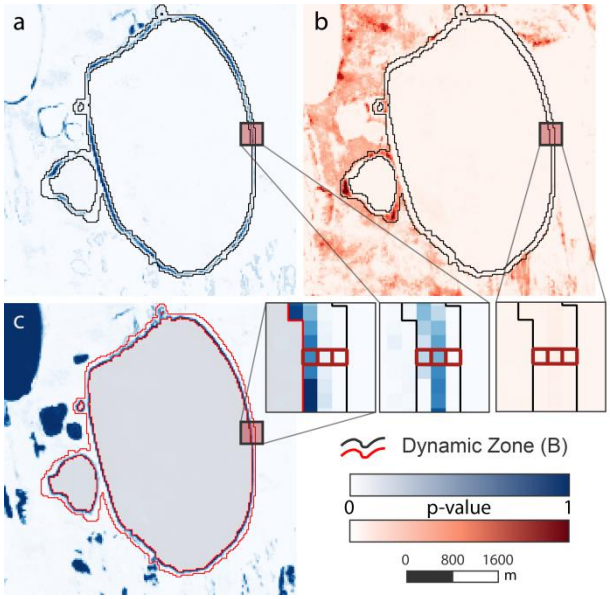

Figure 3.7: *p*-value datasets for the calculation of sub-pixel fractions of lake objects: (a) Change land to water (*C-LW*); (b) Change water to land (*C-WL*); and (c) Stable water (*S-W*). Example pixel locations highlighted.

3.4.4 Data Quality and Post-Processing

In order to optimize the data quality for the lake change analysis we applied a two-step filtering mechanism to exclude non-lake water bodies, such as rivers or sea areas and their related changes, since these are subject to strong dynamics and would have influence on the lake statistics. In addition, waterbodies intersecting the edge of the study area were removed. Although the defined classes are perfectly separable, other unrelated disturbances, such as burn scars or cast shadows in mountain areas were classified as stable water or one of the change classes in several instances and needed to be addressed in the post-processing.

For the automated removal of these invalid or false positive objects, we classified the water objects based on spatial statistics and shape attributes as well as using topographic information from a pan-Arctic DEM (Santoro & Strozzi, 2012) and vegetation information from the Global Forest Change dataset (Hansen, et al., 2013) as auxiliary data. Spatial statistics and shape parameters were calculated with the *scikit-image python* software package for each identified lake. They include shape parameters, such as area, perimeter, orientation, eccentricity, and solidity, as well as spatial statistics of the classified data, DEM data (elevation, slope), and binary forest change dataset information.

We created a spatially stratified training dataset with a binary distinction of manually selected valid and invalid (rivers, cast shadows, and burn scars) lake objects to train a Random Forest machine-learning classifier. The classification model was then applied to each lake object. All lake objects classified as invalid were removed from the analysis. In general, rivers were detected by their particular shape, whereas shadows and fire are predominantly located in sloped terrain during this post-processing procedure. In a second and final filtering step, all objects with a maximum *p*-value (any class) of less than 0.95 were automatically discarded, which further allowed the removal of remaining false positive lake objects.

3.4.5 Calculation of Lake Change Statistics

We calculated area specific metrics (water area, water gain, water loss) to map and characterize individual lake specific changes. Regional statistics were then calculated based on the individual lake change metrics (c.f. Table 3.4). Furthermore, gridded results were calculated for the spatial representation of lake specific water area changes. Each region was subdivided into 3 × 3 km large squares and net lake area changes per pixel within each grid

cell were accumulated. Only pixels belonging to detected lakes were included to the calculation.

Table 3.4: Regional results of lake analysis.

Attribute	Unit	NSL	AKS	CYA	KOL
Total land area	km²	31,715	31,135	56,700	73,339
Number of lake objects	#	19,922	9771	13,254	38,838
Net lake area change	%	−0.69	−2.82	48.48	−0.51
Net lake area change	ha	−3849.25	−2806.63	45,288.11	−6083.14
Lake area 1999	ha	555,478.54	99,398.59	93,417.39	1,197,262.70
Lake area 2014	ha	551,629.28	96,591.97	138,705.50	1,191,179.56
Lake area gain	ha	3936.53	2024.47	50,115.75	21,826.55
Lake area loss	ha	7785.78	4831.10	4827.64	27,909.69
Mean lake size 1999	ha	27.88	10.17	7.05	30.83
Mean lake size 2014	ha	27.69	9.89	10.47	30.67
Median lake size 1999	ha	3.91	3.23	2.28	5.58
Median lake size 2014	ha	3.84	3.01	3.56	5.59
Max lake size 1999	ha	84,847.11	2384.02	1828.07	22,445.77
Max lake size 2014	ha	84,732.23	2427.16	5008.44	22,448.93
Lakes with strong growth	#	4	16	1720	64
Lakes with strong loss	#	43	394	183	205
Stable water >95%	#	12,736	5547	2076	23,515
Change <1 ha, % lakes	%	96.61	88.77	56.35	90.24

3.5 Results

3.5.1 NSL (Alaska North Slope)

Within the NSL study site, 19,922 lakes were detected (cf. Table 3.4). During the observation period, the overall lake area changed from 555,478 ha to 551,629 ha, which translates to a net loss of 2806 ha or −0.69%. Lake growth accounted for 3937 ha, while shrinkage resulted in 7786 ha lake area loss. Most lakes remained predominantly stable over the observation period from 1999 to 2014 with 96% of the lakes having a net area change of less than 1 ha. In contrast to the majority of lakes with little or no change, few water bodies accounted for the majority of fluctuations in both directions. Strong relative changes as lake formation or full lake drainage (greater than 300% increase or 75% decrease) occurred infrequently with 4 and 43, respectively.

The largest lakes are typically located in the Younger Outer Coastal Plain (YOCP). A second cluster of large lakes can be found in the Outer and Inner Coastal Plain (OCP, ICP) region. Between the larger lakes, many small lakes and ponds are distributed within the entire study area. The lake area distribution is dominated by a large number of small lakes with a median area of 3.84 ha and a maximum size of 84,732 ha for Teshekpuk Lake. The overall lake density is very high in nearly the entire study site, with only small regions of low limnicity, predominantly in the rolling hills of the Arctic Foothills (AF). Overall, the lake area accounted for 17.5% of the land surface in the NSL study site.

Spatially, the strongest lake dynamics were on the YOCP, where both strong lake growth and shrinkage were detected (Figure 3.8). Particularly, northeast of Teshekpuk Lake (TL) there was a distinct cluster of lake drainage activity, while lake expansion is dominant north of TL, where the strongest individual lake expansion (+70.2 ha) was measured. The western YOCP is also characterized by widespread lake growth. Based on in-situ observations and overflights (Figure 3.13), lake change rates were clearly dominated by thermokarst processes, but localized flooding or drying of these very shallow lakes and basins also played an important role for lake water budgets on the YOCP. At Teshekpuk Lake, water area loss, e.g., due to sediment input or drying, outweighed lake growth by 111 ha which translates to 0.14% of the total lake surface.

The OCP and ICP were dominated by lake stability with fluctuations around zero net change. Apart from the dominating stable pattern, several instances of partial lake drainage were registered on the OCP, e.g., west of Teshekpuk Lake (Figures 3.8b-2 and 3.14). In the so-called Pik Dunes basin (Figures 3.8b-3 and 3.15), a flat drained lake basin in the ICP region with exposed sand, a more dynamic pattern was observed with fluctuating lake levels inside the basin. In addition, a new lake of around 7 ha area had been naturally dammed up by the formation of large sand dunes at this site.

The AF region, which has a lower lake density, showed a slightly more dynamic pattern, with predominantly growing lakes, but also occasional lake drainage. Within the oil extraction region in the eastern margin of the study site, few occurrences of lake drainages and the construction of artificial water basins were detected.

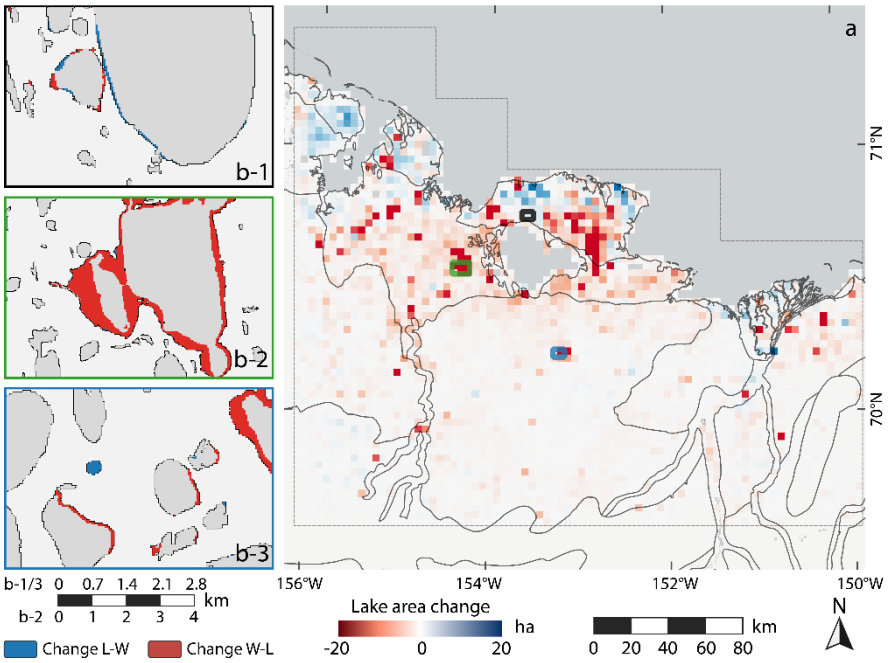

Figure 3.8: Regional lake change of NSL study site: (a) gridded spatial net lake change distribution in ha. Gridsize: 3 × 3 km; (b-1) detailed view of thermokarst lake expansion and drainage on the Younger Outer Coastal Plain north of Teshekpuk Lake; (b-2) detailed view of partial lake drainage on the Outer Coastal Plain west of Teshekpuk Lake; and (b-3) detailed view of lake dynamics within Pik Dunes Basin with the formation of a new lake.

3.5.2 AKS (Alaska Kobuk-Selawik Lowlands)

Within the AKS study site, 9771 lakes were detected (cf. Table 3.4). During the observation period the overall lake area changed from 99,399 ha to 96,592 ha, which translates to a net loss of 2807 ha or 2.82%. Lake growth accounted for 2024 ha, while shrinkage resulted in 4831 ha lake area loss. The majority of lakes remained predominantly stable over the observation period from 1999 to 2014 with 88.8% of the lakes having a net area change of less than 1 ha. However, 16 and 394 lakes were subject to strong expansion (>+300%) or drainage (<−75%), respectively.

The median area of lakes is 3.01 ha and a maximum size of 2430 ha. The large *Inland Lake* and *Selawik Lake*, as well as few other lakes within the Kobuk Delta are connected to the open sea and therefore automatically excluded. Generally, the largest lakes are predominantly located within or close to the Kobuk and Selawik deltas. In the inland regions and the Baldwin Peninsula, lake sizes are generally smaller. Overall, the lake area accounts for 3.2% of the land surface in the AKS study site, but can be much higher locally.

This region has a highly heterogeneous pattern of lake area change (Figure 3.9). Within the Kobuk and Selawik river deltas, we observed mostly lake growth. The largest increase in lake area predominantly took place in the Kobuk Delta close to the deltaic front and in proximity to the river's main channels with a similar pattern in the Selawik Delta. However, despite the general lake expansion pattern within these sub-regions, several individual lakes were affected by lake area loss.

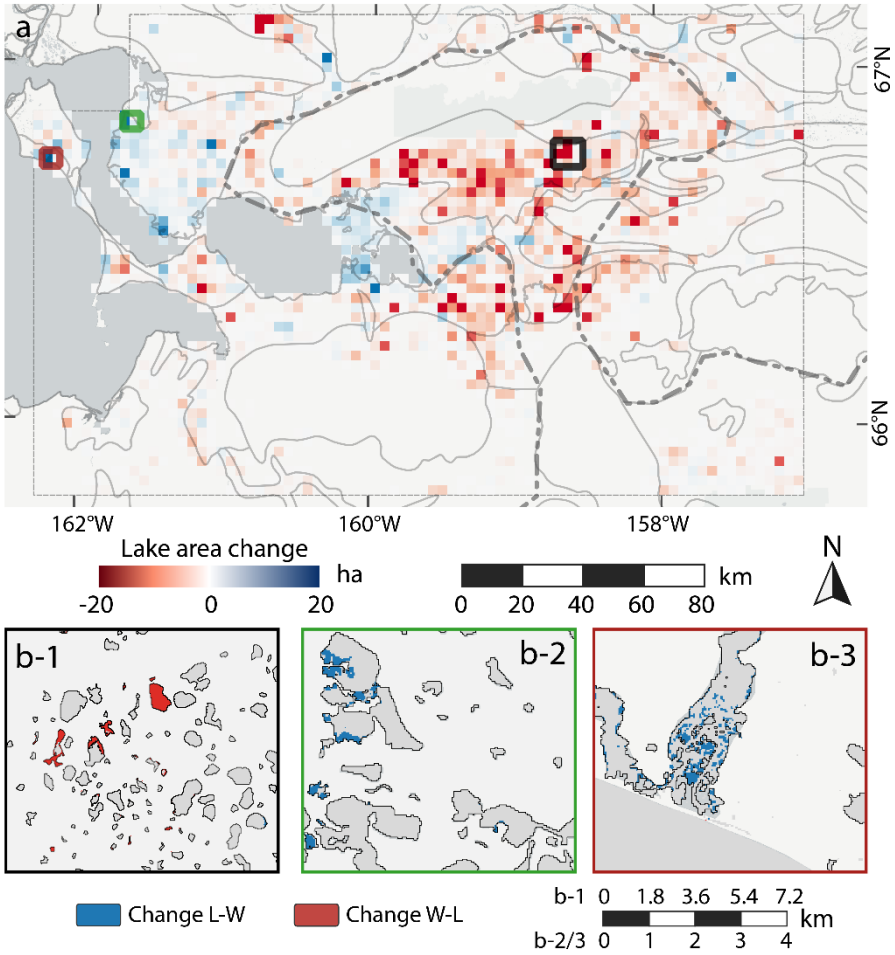

Figure 3.9: Regional lake change of AKS study site: (a) gridded spatial net lake change distribution in ha. Gridsize: 3 × 3 km; (b-1) detailed view of catastrophic lake drainage in the northern Selawik valley; (b-2) detailed view of lake area growth in the northern Kobuk river delta; and (b-3) detailed view of flooding on a lagoon on the western Baldwin Peninsula.

In contrast to the deltas, the river valleys exhibit a much more diverse pattern. These regions were characterized by highly dynamic lake change patterns where widespread lake drainage was the dominating change process, though lake expansion occurred frequently in close proximity. Aerial survey flights in summer 2016 confirmed the spatial pattern of high

dynamics and hydrological connectivity of this wetland region (see Figures 3.8b-1 and 3.16). These dynamics can be observed along the Kobuk and Selawik rivers and its tributaries. Along the northern Selawik valley, many potential small lakes of up to 5 ha were not detected by the lake detection algorithm.

On the Baldwin Peninsula, lake changes of both directions were common, with several drainage events of different intensities and frequent thermokarst lake expansion. The lagoons on the western shore were detected as lakes and were subject to strong wetting, where the northern lagoon was subject to a water area gain of 80.6 ha alone (see Figures 3.8b-3 and 3.17).

3.5.3 CYA (Central Yakutia)

Within the CYA study site, 13,254 lakes were detected (cf. Table 3.4). During the observation period the overall lake area changed from 93,417 ha to 138,705 ha, which translates to a net gain of 45,288 ha or highly exceptional 48.5%. Lake growth accounted for 50,116 ha, while shrinkage resulted in 4828 ha lake area loss. Barely half of lakes remained predominantly stable over the observation period from 1999 to 2014 with 56.3% of the lakes having a net area change of less than 1 ha. The large lake area increase comes with 1720 lakes, which were subject to a large lake expansion, while 188 were subject to strong water area loss. Among all study regions, the ratio of newly formed or very strongly expanded lakes versus near complete drainage was the opposite in CYA.

The median area of lakes grew from 2.28 ha to 3.56 ha. The largest lake, which is located close to the confluence of the Lena and Aldan rivers nearly tripled in area from 1828 ha to 5008 ha (Figure 3.10b-2). At the end of the observation period, the limnicity was at 2.4% for the entire study area, up from 1.6% at the beginning of the study period.

The proximal eastern terraces of the Lena river (Bestyakhskaya and Tyungyulyunskaya), as well as the southeastern corner of the study area (Abalakhskaya T.) exhibited an extraordinary increase in lake area (Figure 3.10). In this region, formerly dry (Desyatkin, 2008) or only partially filled thermokarst basins (alas) apparently were re-filled with water during the 16-year observation period. Additionally, thermokarst activity formed new ponds and widened lake basins (Figure 3.10b-3). Furthermore, numerous large basins were severely affected by the same flooding trend leading to this massive increase in lake area. The northeastern part

and southern margin of the CYA study site (Maganskaya T., Abalakhskaya T., Emilskaya T.) were apparently not affected by the exceptional lake growth, which occurred in other parts of the region.

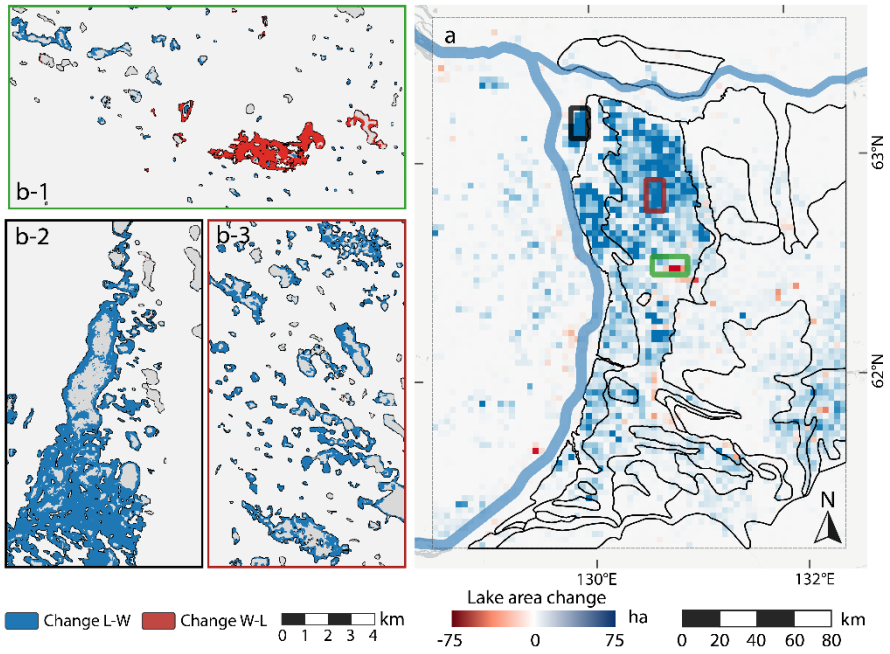

Figure 3.10: Regional lake change of CYA study site: (a) gridded spatial net lake change distribution in ha. Gridsize: 3 × 3 km; (b-1) detailed view of lake area loss due agricultural practices; (b-2) detailed view of very strong lake area growth close to the confluence of the Lena and Aldan rivers; and (b-3) detailed view of widespread lake growth on the Tyungyulyuy Terrace.

Lake drainage was less widespread than expansion in this part of the study region, but some clusters of lake drainages exist. Most occurrences can be found on the eastern margin of the Tyungyulyunskaya T., in particular within larger alases, for example around the villages Syrdakh and Tyungyulyu, where anthropogenic activity, e.g., through intense water management practices for agriculture in alas basins, likely had a strong influence on the detected lake area (Figure 3.10b-1). On the lake-poor western bank of the Lena river, lake change was not as drastic as east of the river and rather evenly distributed between growth and shrinkage.

3.5.4 KOL (Kolyma Lowland)

Within the KOL study site, 38,838 lakes were detected (cf. Table 3.4). During the observation period, the overall lake area changed from 1,197,263 ha to 1,191,180 ha, which translates to a net loss of 6083 ha or 0.51%. Lake growth accounted for 21,827 ha, while shrinkage resulted in 27,910 ha lake area loss. The majority of lakes remained predominantly stable over the observation period from 1999 to 2014 with 90.2% of the lakes having a net area change of less than 1 ha. In total, 64 lakes were affected by strong lake expansion or formation, whereas 205 lakes were subject to near complete lake drainage. The median area of lakes is 5.59 ha and the largest lake has size of 22,449 ha.

Within this study region, several spatial clusters of noticeable change can be distinguished (Figure 3.11). The Yedoma-Alas Complex (YAC) is clearly structured into a northern part, where lake expansion and a southern part, where drainage were the dominant lake change processes. The boundary of these zones nearly forms a straight line from northeast to southwest, which coincides with the boundary between the elevated ice-rich yedoma deposits in the south and the low-lying thermokarst basins in the north. Particularly, in the northeastern coastal region, very strong lake expansion rates of up to 1097 ha for one lake were measured (Figure 3.11b-1). This particular lake exemplifies probably the two main drivers of lake expansion in this region. First, thermokarst caused lake expansion occurs along the shorelines of most lakes in this region. The second driver is the flooding of shallow and low-lying basins along the coast, which might be caused by seawater inundation.

The southern part of the YAC is dominated by lake area loss. Most of the lake area reduction was fueled by the partial drainage of several large lakes, e.g., Bolshoy Oler lake on the western margin of the study region (Figure 3.11b-3). This particular lake alone lost 752 ha of its water surface. Several other lakes were also affected by lake are loss of more than 100 ha, each. Lake expansion was measured for a large fraction of lakes, but does not outweigh the widespread water area loss.

In the YAC, south of the Kolyma river, lake area loss was more pronounced than lake growth, predominantly caused by the partial drainage of several large lakes. The majority of lakes did not follow a specific spatial pattern and changes in both directions were recorded.

The Alluvial-Marine Complex region west of the Kolyma river mouth showed widespread lake area loss in nearly the entire region. Particularly the northern part, where several large lakes are located, was affected by a strong reduction of lake area (Figure 3.11b-2). Lake growth was infrequent and only measured for the minority of lakes.

The floodplain of the Kolyma river is dominated by strong dynamics, predominantly as lake expansion. Several individual lakes were affected by drainage of varying degrees. In the river delta, lake drainage and expansion was more evenly distributed with a slight excess of lake area loss.

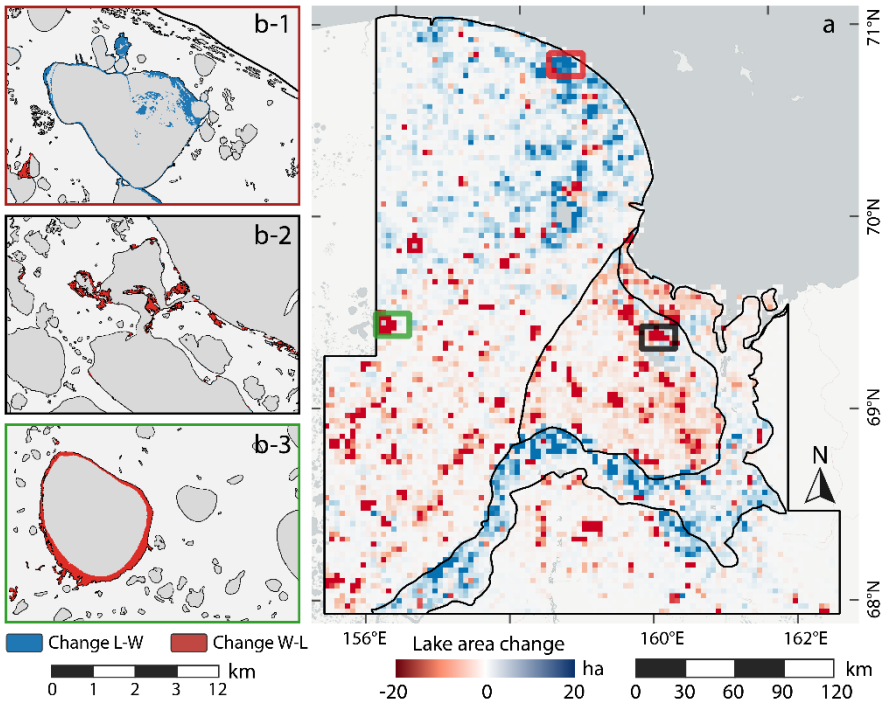

Figure 3.11: Regional lake change of KOL study site: (a) gridded spatial net lake change distribution in ha. Gridsize: 3 × 3 km; (b-1) detailed view of lake growth in the coastal region of the Yedoma-Alas Complex; (b-2) detailed view of lake area loss in the Alluvial-Marine Complex; and (b-3) detailed view of lake drainage at Bolshoy Oler lake.

3.6 Discussion

3.6.1 Data Analysis

Within the KOL study site, 38,838 lakes were detected (cf. Table 3.4). During the observation period, the overall lake area changed from 1,197,263 ha to 1,191,180 ha, which translates to a

net loss of 6083 ha or 0.51%. Lake growth accounted for 21,827 ha, while shrinkage resulted in 27,910 ha lake area loss. The majority of lakes remained predominantly stable over the observation period from 1999 to 2014 with 90.2% of the lakes having a net area change of less than 1 ha. In total, 64 lakes were affected by strong lake expansion or formation, whereas 205 lakes were subject to near complete lake drainage. The median area of lakes is 5.59 ha and the largest lake has size of 22,449 ha.

Within this study region, several spatial clusters of noticeable change can be distinguished (Figure 3.11). The Yedoma-Alas Complex (YAC) is clearly structured into a northern part, where lake expansion and a southern part, where drainage were the dominant lake change processes. The boundary of these zones nearly forms a straight line from northeast to southwest, which coincides with the boundary between the elevated ice-rich yedoma deposits in the south and the low-lying thermokarst basins in the north. Particularly, in the northeastern coastal region, very strong lake expansion rates of up to 1097 ha for one lake were measured (Figure 3.11b-1). This particular lake exemplifies probably the two main drivers of lake expansion in this region. First, thermokarst caused lake expansion occurs along the shorelines of most lakes in this region. The second driver is the flooding of shallow and low-lying basins along the coast, which might be caused by seawater inundation.

The southern part of the YAC is dominated by lake area loss. Most of the lake area reduction was fueled by the partial drainage of several large lakes, e.g., Bolshoy Oler lake on the western margin of the study region (Figure 3.11b-3). This particular lake alone lost 752 ha of its water surface. Several other lakes were also affected by lake are loss of more than 100 ha, each. Lake expansion was measured for a large fraction of lakes, but does not outweigh the widespread water area loss.

In the YAC, south of the Kolyma river, lake area loss was more pronounced than lake growth, predominantly caused by the partial drainage of several large lakes. The majority of lakes did not follow a specific spatial pattern and changes in both directions were recorded.

The Alluvial-Marine Complex region west of the Kolyma river mouth showed widespread lake area loss in nearly the entire region. Particularly the northern part, where several large lakes are located, was affected by a strong reduction of lake area (Figure 3.11b-2). Lake growth was infrequent and only measured for the minority of lakes.

The floodplain of the Kolyma river is dominated by strong dynamics, predominantly as lake expansion. Several individual lakes were affected by drainage of varying degrees. In the river delta, lake drainage and expansion was more evenly distributed with a slight excess of lake area loss.

The combined MLC and OBIA classification into four classes (land, water, and temporal transitions between both) based on the 16-year (1999–2014) Landsat trend data yielded an excellent separation of the input data based on different metrics, such as RF's internal accuracy estimator (OOB) or five-fold cross-validated classification accuracy and Cohen's kappa. Area estimates of pure pixels of the defined classes can therefore be considered as highly accurate within the spatial resolution of the data.

However, as thermokarst lakes are characterized by a dynamic, asymmetric behavior with a large number of slowly growing lakes and a low number of quickly draining lakes, and Landsat's spatial resolution of 30 m, sub-pixel analysis becomes crucial to properly account for the magnitude and direction of changes. Therefore, we included a sub-pixel analysis of changes along the lake margins based on the probability values of the MLC.

The processing step from pixel based classification to lake or lake-change objects worked generally well in most cases. Lakes embedded in tundra, boreal or transitional environments were clearly detected and separated without notable differences between the different eco-zones. However, more dynamic zones without a clear distinction of water and land, e.g., wetlands, are a potential error source for lake change calculations, due to their constantly changing surface conditions, local-scale permafrost landscape features conditions, and its transitional nature between water and non-water, which is a common issue identified in previous studies e.g., (Karlsson, Lyon, & Destouni, 2014; Boike, et al., 2016; Chen, Rowland, Wilson, Altmann, & Brumby, 2013). These particular settings usually occurred in coastal or delta regions and river valleys or flat drained lake basins. Such regions might be more susceptible to larger errors than for most other regions. Particularly, the highly dynamic AKS study site was affected by this effect, where many small basins constantly changed their surface water conditions.

Few misclassifications were identified in regions of frequent wildfires, such as boreal taiga or forest tundra regions as wildfires were occasionally classified as change in either direction, due to its strong spectral change over time. The use of global forest cover change information

(Hansen, et al., 2013) and DEM data (Santoro & Strozzi, 2012) helped to detect and mask these regions by automatically discarding false positive classified lake objects. However, as large regions in the tundra-taiga transitional zone are not accounted for in the global forest cover change map, the removal of false positive lake objects due to fire may lack the reliability of boreal regions.

3.6.2 Comparison of Sites and Prior Studies

Each of the four analyzed regions shows a slightly different behavior in the dynamics of its lakes. The more northerly coastal regions NSL and KOL, have a small decline in lake area with 0.69% and 0.51%, respectively. Lake dynamics are locally varying, and spatial differences, based on several factors, such as geology (types of sediments, ice-content) and geographical setting (e.g., proximity to the coast or rivers) have an influence on the lake dynamics. The western Alaskan site (AKS) is subject to a decrease in lake area by 2.8% and is characterized by frequent dynamics, predominantly as lake drainage. As in the first two regions, clear small-scale local spatial patterns can be distinguished. The Central Yakutian study site (CYA) is characterized by extreme lake expansion of 48.48% between 1999 and 2014, which strongly deviates from the other sites.

The predominantly stable conditions on the Alaska North Slope (NSL) compare well with Jones et al. (2009), who found no significant long-term trends of lake area change between 1985 and 2007. Our characterization of mostly stable conditions over most of the North Slope study site confirms Hinkel et al. (2007) who found two lake drainage events per year from the mid 1970s to 2001/2002 on a similar sized and largely overlapping part of the North Slope. Considering the same criteria, we observed 2.44 drainage events per year. Arp et al. (2011) detected net lake expansion of 3.4% using high-resolution data and 4.1% using Landsat data, between 1979 and 2002 on a small sample of 13 lakes in a more dynamic subset on the YOCP, north of Teshekpuk Lake. For twelve of the same lakes together, we found a zero net change, but strong changes in both directions for individual lakes. The missing lake *L195* drained catastrophically in summer 2015 (Jones & Arp, 2015) and lost a significant portion of its 80 ha area. Due to the close proximity to the sea, the lake was automatically discarded in our processing, as it was detected as connected to the sea.

In the Kolyma Lowland region, our calculated net lake area decrease of 0.5% reveals a strong discrepancy to Walter et al. (2006), who detected a lake area increase of 14.7% along the

Kolyma river for a longer time period from 1974 to 2000. The strong difference can be explained by the extent and setting of study areas, as we also found a strong lake area increase within the Kolyma floodplain. Their use of sensors with a different spatial resolution (Landsat MSS to ETM+), may have also had an influence on the results. Considering the discrepancy to the regional statistics, this particular subset is not representative for the entire region, which stresses the spatial variety of lake change processes, particularly within this region. Veremeeva and Gubin (2009) found a trend of lake area decrease in the range of 0.9 to 10.7% for a small region in the western Yedoma-Alas Complex from 1973 to 2001. Within this specific region, our results also indicate a strong loss of lake area, largely due to the partial drainage of the around 50 km² large Bolshoy Oler lake. The sharp boundary of lake growth trends and lake shrinkage trends coincided very well with boundary of geomorphology with old low-lying thermokarst basins in the Yedoma-Alas Complex region.

In a comparable Arctic coastal lowland setting, to NSL and KOL, with thick continuous permafrost on the NW Canadian Tuktoyaktuk Peninsula, Olthof et al. (2015) found a slight lake area increase of 0.64% over eight years with strong inter-annual fluctuations of up to 4%. Within the same region Plug et al. (2008) found substantial lake area fluctuations for large lakes of +14% from 1978 to 1992 and −11% from 1991 to 2001, however with an anomalously low lake area in 2001.

In the western Alaskan study site (AKS), located in the transition zone from continuous to discontinuous permafrost, we observed a net lake area loss of 2.8%. It compares well to Roach et al. (2013) who measured a lake area loss of 0.81% per year. Their study site largely covers the area affected by widespread lake drainage and trends of lake change nicely resemble the spatial pattern we found in our study, e.g., lake growth in the Selawik river delta and widespread loss in the northern Selawik river valley. In a more continental site east of the *Kobuk Dunes*, Necsoiu et al. (2013) found an overall decreasing lake area trend from 1978 to 2005 within 22 lakes or ponds. We could detect 14 of these lakes and found a lake area loss of 13.4%, largely fueled by the partial drainage of one lake. Similar trends were detected on the nearby northern Seward Peninsula where Jones et al. (2011) found 11% lake area loss where the drainage events of few large lakes were the main drivers for a net lake area loss. Each of the coastal sites showed trends of lake area increase in near-shore areas. To our knowledge this effect has not been described or discussed in other lake change studies. It may be caused

by several factors, such as local climatic effects; surface geology, e.g. sediments more prone to erosion; or very flat terrain, which is affected to sea water inundation.

The abundance of disappearing lakes in discontinuous permafrost regions in Central Alaska (Riordan, Verbyla, & McGuire, 2006; Rover, Ji, Wylie, & Tieszen, 2012) has been linked to increased connectivity to groundwater (Jepsen, Voss, Walvoord, Minsley, & Rover, 2013; Yoshikawa & Hinzman, Shrinking thermokarst ponds and groundwater dynamics in discontinuous permafrost near Council, Alaska, 2003). Permafrost degradation or disappearance along the continuous-discontinuous permafrost interface in the AKS site would be a good explanation for the strong lake drainage trend within this region. Other causes in areas with relative high continentality, such as the central Alaskan Yukon Flats or northwest Canadian Old Crow Flats, include increased evapotranspiration (Lantz & Turner, 2015; Riordan, Verbyla, & McGuire, 2006; Labrecque, Lacelle, Duguay, Lauriol, & Hawkings, 2009).

However, for the highly continental Central Yakutia site, we calculated a 48.48% increase in lake area for the 1999–2014 period, which is a significant outlier in terms of thermokarst lake dynamics. The same wetting pattern has been described by Boike et al. (2016), who used Landsat snapshots and found an increase of around 85% from 2002 to 2009 within the strongest wetting part of the CYA study site. The strongest increase in lake area occurred in 2007 after above-average precipitation in the prior year (Tarasenko, 2013). Furthermore, this particular region has been subject to very strong rates of lake expansion over the last decades due to several factors, including anthropogenic activity and the change of climatic conditions (Ulrich, et al., 2017; Fedorov, Ivanova, Park, Hiyama, & Iijima, 2014). The recharge of lakes here may be connected to a wetter and warmer climate over the recent decades (Boike, et al., 2016; Ulrich, et al., 2017; Iijima, et al., 2010) and shifting agriculture practices, where meadows and grasslands in alas basins are increasingly managed to produce richer pastures (Crate, et al., 2017). In addition to the climatic conditions and anthropogenic influence, the local geological conditions seemingly had a strong influence on the lake area changes, where the terraces with ice-rich sediments showed a much more pronounced lake area expansion in comparison to the remaining area.

The comparison of different studies as well as the analysis of local trends highlights the variability of lake dynamics within the northern permafrost region. The wide variety of spatial scales poses a large challenge for the comparison of different studies and regions, as results

may vary strongly even for nearby locations. Furthermore, seasonal or short-term lake area fluctuations, which can exceed long-term trends (Olthof, Fraser, & Schmitt, 2015), may mask long-term trends in studies based on the widely applied practice of using snapshots (Jones B. M., et al., 2011; Karlsson, Lyon, & Destouni, 2014; Smith L. C., Sheng, MacDonald, & Hinzman, 2005; Riordan, Verbyla, & McGuire, 2006; Hinkel, et al., 2007; Walter, Zimov, Chanton, Verbyla, & Chapin, 2006). The trend analysis of single date lake masks (Olthof, Fraser, & Schmitt, 2015; Roach, Griffith, & Verbyla, 2013) can help to suppress short-term fluctuations and produce more reliable and comparable results. In our study we applied the trend analysis at an earlier stage and translated spectral trends to semantic information with MLC, which allowed us to accurately distinguish between zones of stable water or land and changing transition zones around lake margins. With the inclusion of classification probability values, we exploited sub-pixel information to detect permafrost region specific thermokarst lake growth.

Using the trend calculation helps generalize the input data regardless of its location and enables the comparison and upscaling across multiple spatial scales, starting from individual lakes up to very large regional scales. The successful application of the method to different study sites across the permafrost zone proved the transferability and scalability of the highly automated processing method and highlights its strong potential for applying it to the entire permafrost domain to fully characterize lake changes and associated permafrost dynamics.

3.7 Conclusions

We used a highly automated and hybrid approach based on Landsat TM, ETM+ and OLI data, robust trend analysis, machine-learning classification and object oriented analysis to quantify lake change dynamics for four large study regions in Alaska (North Slope and Kobuk-Selawik Lowlands) and Siberia (Central Yakutia and Kolyma Lowland) encompassing a total area of about 200,000 km². Landsat trend data analysis allowed for the comparison of different study sites over a specific period (1999–2014) and the observation of trends where short-term fluctuations do not affect the long-term change trajectories. In total, around 80,000 individual lakes larger than 1 ha were mapped and analyzed regarding their spatial dynamics over a 16-year period from 1999 to 2014. Regional lake area statistics revealed weak lake area loss for the more northerly Alaska North Slope (−0.69%) and Kolyma Lowland regions (−0.51%), while the lake area in the west Alaskan Kobuk-Selawik Lowlands was subject to a more

pronounced area loss (−2.82%). Lake area in Central Yakutia grew considerably by 48.48%. In this latter area, massive recharging of large lakes in alas basins was likely connected to climatic wetting and warming and changes in agricultural practices.

Despite similar regional net change, considerable differences in local dynamics were distinguishable. The lakes in northern Alaska within continuous permafrost exhibited a rather stable and uniform behavior with widespread lake stability and a limited region of pronounced lake dynamics. Lakes in the Kolyma Lowland region showed a low net area change, but were subject to a clear regional zonation of lake growth and drainage. In the warmer west Alaska site, widespread drainage of lakes in inland regions dominated the lake change dynamics. Within this region, where permafrost is transitioning from continuous to discontinuous, the spatial dynamics were locally very diverse and likely affected more strongly by the landscape surface geology and local permafrost conditions.

As lakes and lake dynamics are an important driver of change in the northern permafrost lowlands, these findings will help to better understand the landscape response to a rapidly warming Arctic and degrading permafrost with all its hydrological and biogeochemical consequences. For example, the improved knowledge of large scale lake change dynamics will allow for a better quantification of thermokarst lake-related fluxes of the greenhouse gases methane and carbon dioxide. With the global availability and continuity of Landsat data, the increasing availability of comparable Sentinel-2 data, and the scalability of our method, we envision the expansion of the analysis to a pan-arctic scale.

3.8 Supplementary Materials

Supplementary data are available at the PANGAEA data repository (Nitze I. , et al., 2017) (https://doi.org/10.1594/PANGAEA.876553). They include the georeferenced outlines and centroids of detected lakes with major lake area statistics. Furthermore, gridded net lake changes are also made available.

3.9 Acknowledgements

I.N. and G.G. were supported by the European Research Council ERC#338335, the Initiative and Networking Fund of the Helmholtz Association (ERC-0013), and the European Space

Agency (ESA GlobPermafrost). M.U. was supported by the German Research Foundation (DFG Grant No. UL426/1-1). B.M.J. was supported by the USGS Land Remote Sensing and Land Change Science Programs. C.D.A was supported by a grant from the National Science Foundation (ARC-1417300). Use of trade, product, or firm names is for descriptive purposes only and does not imply endorsement by the U.S. Government. We would like thank Kimberly Casey and two anonymous reviewers as well as the academic editors whose comments helped to improve this manuscript.

3.10 Appendix A

Figure 3.12 Photo of example location (Figure 3.7) with thermokarst lake shore erosion. Looking north. Photo taken on 14 July 2015 by I. Nitze.

Figure 3.13: Oblique aerial photo of partially drained lake on the Alaska North Slope presented in Figure 3.8b-1. Looking southeast. Photo taken on 15 July 2015 by I. Nitze.

Figure 3.14: Oblique aerial photo of partially drained lake on the Alaska North Slope presented in Figure 3.8b-2. Looking northwest. Photo taken on 19 July 2015 by I. Nitze.

Figure 3.15: Oblique aerial photo of refilled, naturally dammed lake on the Alaska North Slope presented in Figure 3.8b-3. Looking southwest. Photo taken on 19 July 2015 by I. Nitze.

Figure 3.16: Oblique aerial photo of drained and filled lakes in Kobuk-Selawik Lowlands in Figure 3.9b-1. Looking north. Photo taken on 8 August 2016 by J. Lenz.

Figure 3.17: Oblique aerial photo of wetting lagoon on the western Baldwin Peninsula in Figure 3.9b-3. Looking northeast. Photo taken on 8 August 2016 by M. Fuchs.

4. Remotely sensing recent permafrost region disturbances across Arctic to Subarctic transects

Nitze, I.[1,2]; Grosse, G.[1,2]; Jones, B.M.[3]; Boike, J.[1] & Romanovsky, V.[4,5]

[1] Alfred Wegener Institute Helmholtz Centre for Polar and Marine Research, Periglacial Research Unit, Potsdam, Germany

[2] Institute of Earth and Environmental Science, University of Potsdam, Potsdam, Germany

[3] U.S. Geological Survey, Alaska Science Center, Anchorage, AK, USA

[4] Geophysical Institute, University of Alaska Fairbanks, Fairbanks, AK, USA

[5] Tyumen State Oil and Gas University, Tyumen Oblast, Tyumen, Russia

In Preparation for: Nature Scientific Communications

4.1 Abstract

Earth's permafrost region is becoming increasingly vulnerable in response to rapid climate change and shifting disturbance regimes. Permafrost degradation results in rapid alteration to biogeochemical cycles, hydrology, and ecosystems in Arctic and Boreal environments. Here, we quantify the abundance and distribution of three primary permafrost region disturbances (lakes and lake dynamics, wildfires, and retrogressive thaw slumps) using dense time series of 30-m resolution Landsat satellite imagery and Pan-Arctic data products across four continental-scale transects in North America and Eurasia. We identify these disturbances across 2.3×10^6 km², or 10% of the permafrost region, during a period of recent, rapid climate change (1999 to 2014). More than 640,000 analyzed lakes indicate that their influence on permafrost disturbances are likely decreasing through widespread lake drainage (Net decrease of -1737 km² or -0.98%). Fires on the other hand are widespread across all boreal permafrost regions (6.62%) as well as the Alaska tundra region (1.07%). Retrogressive thaw slumps, while dramatic, only impact less than 10^{-5}% of the permafrost region analyzed and are highly spatially restricted. Our comprehensive remote sensing analysis allows for correlation of disturbances with ground thermal regime, permafrost extent, and permafrost characteristic and indicates the vulnerability of permafrost terrain to disturbance and potentially future thaw.

4.2 Introduction

Climate change and disturbance regime shifts are amplified in the northern high-latitudes and global and regional projections indicate that environmental thresholds will be crossed during this century (IPCC, RPC 8.5) (Lenton, 2012). Permafrost, which underlies roughly 24% of Earth's land surface, is an important component of cryosphere. It is warming in response to these changes (Romanovsky, et al., 2017; Streletskiy, et al., 2017) and from 50 to 90 % of near surface permafrost in Arctic and Boreal regions are projected to be lost by 2100 (Lawrence, Slater, & Swenson, 2012). Widespread loss of near surface permafrost will mobilize a large reservoir of perennially frozen soil carbon (Hugelius, et al., 2014) which will have ramifications for Earth's climate system (Schuur, et al., 2015). Increased carbon emissions from thawing permafrost may further enhance warming temperatures, a process known as permafrost carbon feedback (Schaefer, Lantuit, Romanovsky, Schuur, & Witt, 2014). A recent synthesis study combining spatial datasets of permafrost, soil carbon, and terrain with an empiric classification scheme of landscape-scale thaw-vulnerability indicates that landscapes vulnerable to rapid thaw processes contain a major portion of the permafrost-stored soil carbon (Olefeldt, et al., 2016). Due to rapidly changing climate and increased local anthropogenic influences from economic development in high northern latitude regions, permafrost increasingly shows signs of rapid degradation in many Arctic and Boreal regions (Jorgenson, Racine, Walters, & Osterkamp, 2001; Jorgenson, Shur, & Pullman, 2006; Liljedahl, et al., 2016; Raynolds, et al., 2014; Kokelj S. V., Lantz, Tunnicliffe, Segal, & Lacelle, 2017; Ulrich, et al., 2017; Jones, et al., 2016). However, spatially and temporally consistent inventories of permafrost region disturbances in sufficiently high spatial resolution are currently lacking.

The northern permafrost region (Figure 4.1) varies with respect to spatial extent and characteristics of ground thermal regime, ground-ice content, climate, topography, hydrology, and land cover (Olefeldt, et al., 2016; Jorgenson, et al., 2008; Walker, et al., 2005; Brown, Ferrians Jr, Heginbottom, & Melnikov, 1997). Each of these factors interacts in complex ways such that predicting the response of permafrost terrains to climate change and disturbances is extremely difficult (Nicolsky, Romanovsky, Panda, Marchenko, & Muskett, 2017). For example, changes in climate and disturbance regimes may trigger an increase or a decrease in thermokarst lake numbers (Ulrich, et al., 2017; Jones B. M., et al., 2011) they also may cause

widespread ice-wedge degradation or promote stabilization through paludification (Liljedahl, et al., 2016; Jorgenson & Shur, 2007), and they may initiate retrogressive thaw slumps or detachment slides or promote regional stabilization of currently active features (Grosse, et al., 2011; Jorgenson & Osterkamp, 2005). In addition, with climate warming high northern latitude fire regimes are expected to shift towards shorter fire return intervals, increased burn severity, and more widespread occurrence (Stocks, et al., 1998; Hu, et al., 2015). Fire events, which are already frequent in boreal regions (Hansen, et al., 2013; Kasischke & Turetsky, 2006; Conard & Ivanova, 1997), but scarcely studied in tundra (Jones, et al., 2013; Liljedahl A. , Hinzman, Busey, & Yoshikawa, 2007), have the ability to initiate or strengthen permafrost disturbances depending on fire severity and timing (Jones B. M., et al., 2015). Feedbacks and local-scale consequences may trigger widespread changes of permafrost related processes, causing the mobilization and potential release of carbon to the atmosphere as well as a wide range of ecological and hydrological impacts that remain poorly documented (Jorgenson, et al., 2010).

Currently, contemporary permafrost region disturbances (PRDs) are poorly represented in the global system due to the previously unresolved conflict of scales between a large quantity of rapid local scale processes and coarse-resolution continental scale remote sensing data and processing capabilities. The vast majority of permafrost areas are underrepresented in studies and PRDs may remain undocumented, resulting in significant uncertainty of the current magnitude of rapid permafrost degradation processes and their role in global scale biogeochemical dynamics. With growing archives of freely accessible earth observation data of adequate spatial resolution and coverage for permafrost remote sensing as well as rapidly growing computational processing capacities, we now have the potential to detect and observe widely distributed PRDs in high spatial and temporal resolution across very large regions.

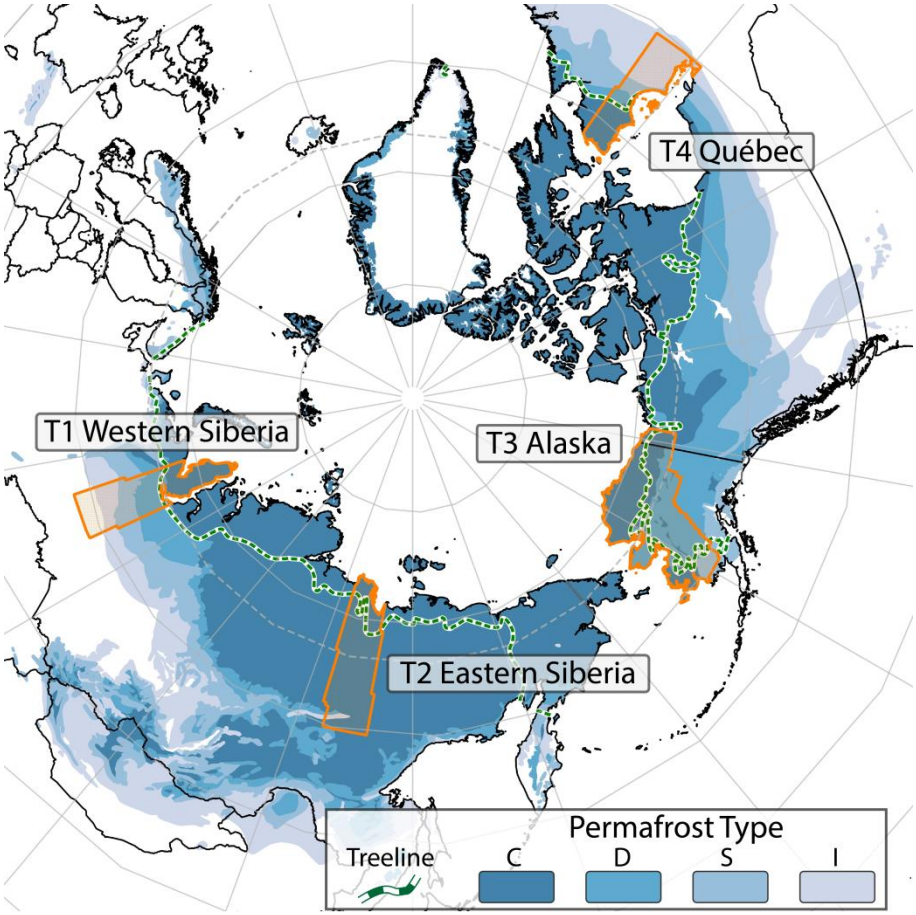

Figure 4.1: Study sites with distribution of permafrost types and treeline (Walker et al., 2005) in the northern Hemisphere.

In this study, we analyzed 16 years of 30-m resolution earth observation data from the Landsat archive in conjunction with Pan-Arctic scale data products, from 1999 through 2015, to track three key PRDs (lake extents and their dynamics, retrogressive thaw slump activation, and wildfire regimes; Figure 4.2) across four extensive North-South transects in Alaska, Eastern Canada, Western Siberia, and Eastern Siberia that cover more than 2.3 x 10^6 km² (10 % of the permafrost region) and feature a broad range of permafrost, climate, topographic, and geo-ecological zones (Figure 4.1). We combined temporal trend-analysis with machine-learning to map the spatial distribution of PRDs and their relation to permafrost properties, ecological zones and climate, allowing comprehensive and unique insights into PRD distribution, abundance, and dynamics. Our results provide a baseline for improving future landscape models and carbon emission estimations from permafrost region disturbances.

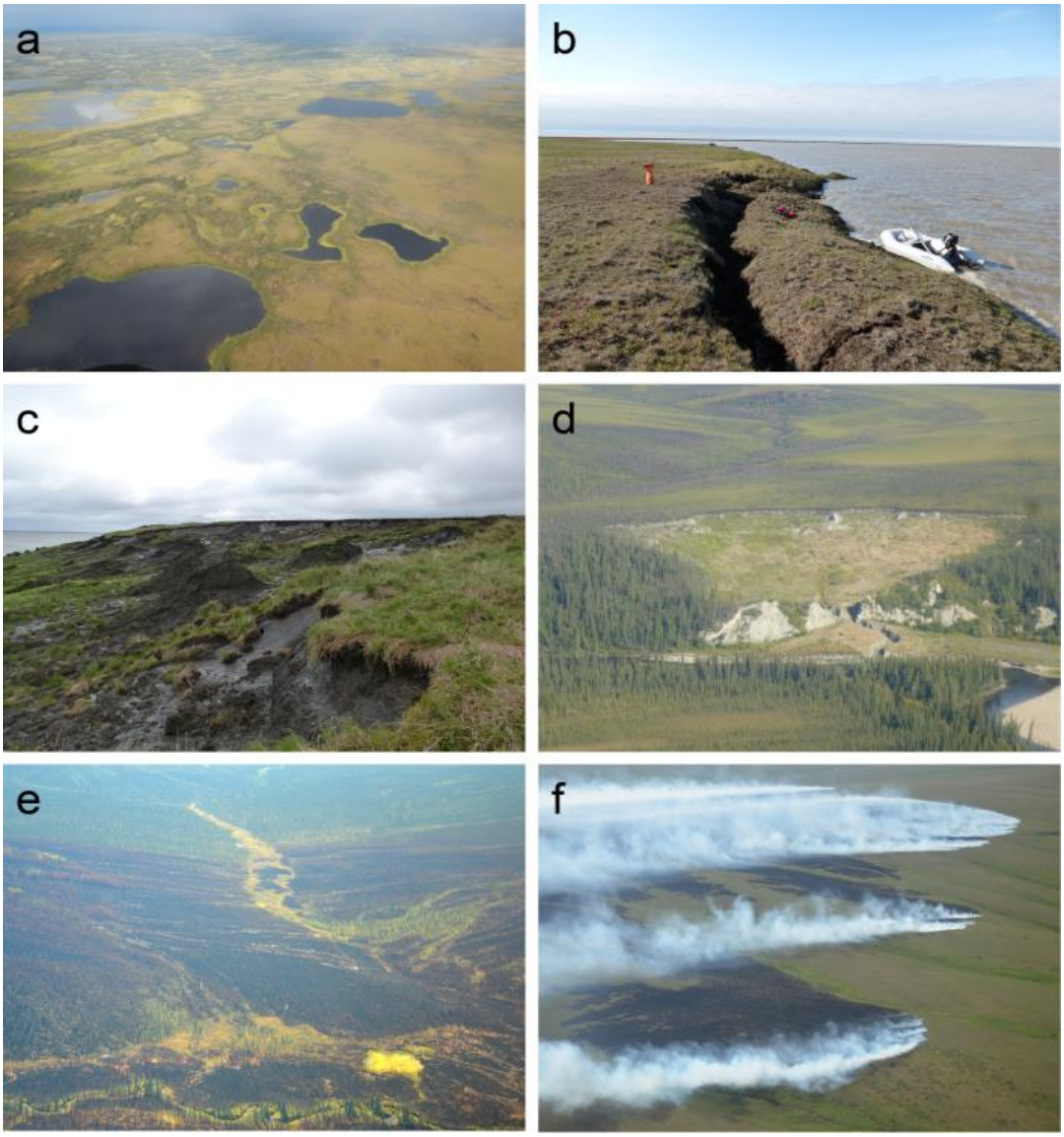

Figure 4.2: Examples of disturbances in permafrost landscapes. a) Dynamic lake rich region in western Alaska with frequent drainage, b) Expanding thermokarst lake in northern Alaska, c) coastal retrogressive thaw slump on Bykovsky peninsula in northeastern Siberia, d) Selawik slump in western Alaska, e) burn scar of wildfire in boreal Alaska, and f) burning tundra fire (Anaktuvuk Fire) in northern Alaska.

4.3 Results

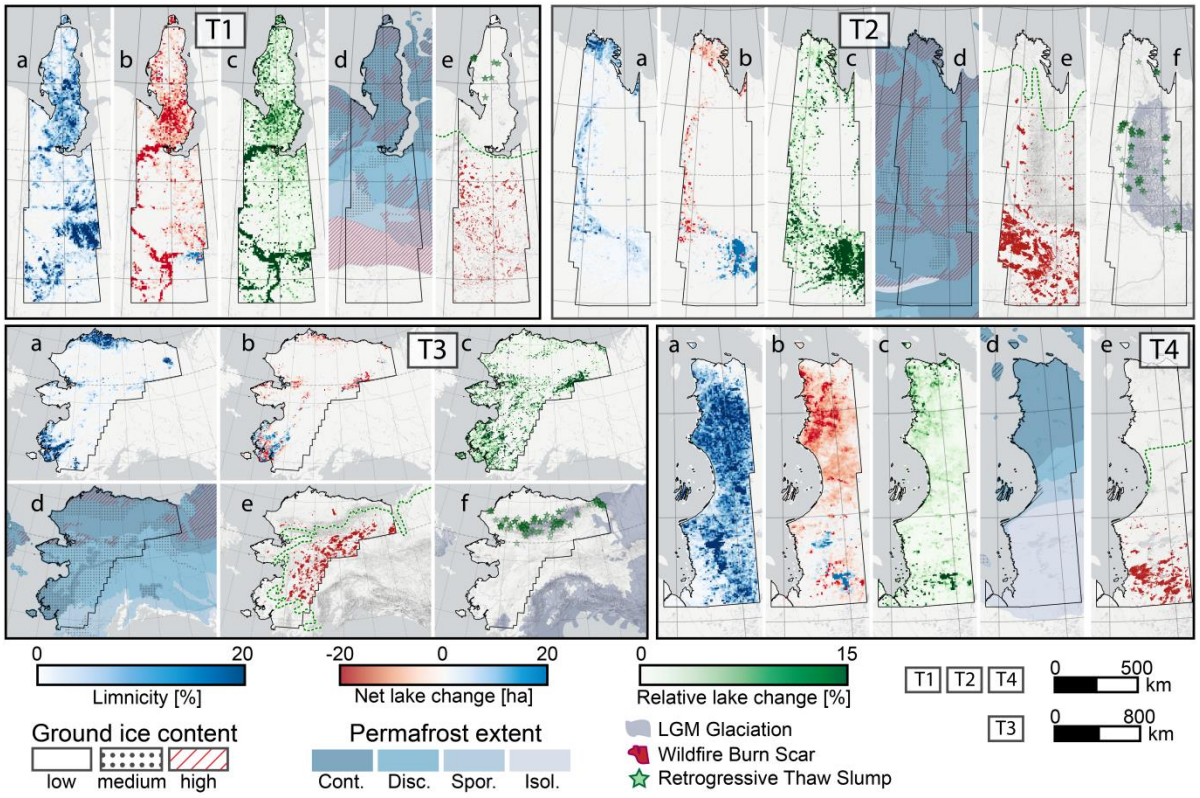

Figure 4.3: Lake statistics and permafrost conditions in the four selected transects: T1 Western Siberia, T2 Eastern Siberia, T3 Alaska, T4 Quebec. a) Limnicity: Lake fraction of land surface, b) Net lake change: lake area change per grid cell (7.5x7.5 km), c) Relative lake change: fraction of changing lake area, and d) permafrost conditions with permafrost extent in shades of blue and ice content based on IPA Permafrost map (Brown, Ferrians Jr, Heginbottom, & Melnikov, 1997), e) wildfire burn scars with treeline, f) retrogressive thaw slumps and LGM glaciation extent (Ehlers & Gibbard, 2003). Retrogressive thaw slumps for T1 in e). LGM glacial coverage omitted in T4 for visual purposes.

4.3.1 Lakes

Regional lake changes

Observed lake changes (lake size > 1 ha; n=643,304) were highly diverse in the Alaskan and the two Siberian transects with a wide range from stability to rapid high magnitude changes, which aligned with the heterogeneous spatial patterns of surface geology, geomorphology, permafrost extent and ground-ice conditions (Figure 4.3;

Table 4.1). In contrast, the spatial dynamics of lakes in the Eastern Canadian Region were coherent with the geomorphological homogeneity and followed a latitudinal gradient of increasing lake area loss from south to north. Overall lake area loss outweighed lake area gain, particularly in western Siberia with a net change of -5.41% (gross increase and gross decrease in brackets hereafter; +1.58; -7.45%) as well as in Alaska and eastern Canada with net changes of -0.62% (+3.31%; 3.96%) and -0.24% (+1.87%, -2.12%) respectively. The East Siberian transect is characterized by a positive lake area trend with a net change of +3.67% (+7.77%; -3.95%). Overall lake area loss totaled 4767 km², whereas lake growth accounted for 3030 km² leading to a net loss of 1737 km².

Lake change and permafrost extent

Lake area loss is the dominant lake related process in discontinuous and around the continuous-to-discontinuous permafrost boundary. Western Siberia and Alaska had a net lake loss of 7.89% and 5.96%, respectively in discontinuous permafrost. Intensive gross lake area loss, e.g. through drainage or drying, was the key driver of negative lake area balance particularly in Alaska with 12.11% gross loss and simultaneous 5.43% gross gain, which signifies the rapid lake dynamics in this region with drainage on the one hand and lake expansion on the other. Lakes in this region, e.g. Yukon Flats, Kobuk-Selawik Lowlands or northern Seward Peninsula were among the most dynamic regions of lake change with dominating lake area loss. In western Siberia, zones of strong lake area loss extended from the discontinuous into the continuous permafrost zone, where a large cluster of lakes on the southern and southeastern Yamal peninsula were particularly affected by partial drainage of large lakes (> 10 km²). This pattern may indicate that thermokarst lake changes are likely related to the transition between different hydrological regimes when permafrost becomes discontinuous. For the other two transects no such relationship was observed since the eastern Siberian transect lies nearly completely within continuous permafrost whereas the eastern Canadian transect is dominated by bedrock geology, where lakes of non-thermokarst origin dominate but still impact the underlying permafrost.

Lake changes were highly diverse in the continuous permafrost zone. Enormous and widespread lake expansion took place on the eastern banks of the Lena River in central Yakutia within ice-rich thick continuous permafrost, where lake area increased by a staggering 50% within a short time period, fueled by strong precipitation events in 2006 and

2007 (Boike, et al., 2016; Ulrich, et al., 2017). Lake area loss dominated the continuous permafrost section of western Siberia (-4.29%; +1.7%; -6.26%), with increasing lake stability towards the north. The continuous permafrost zone in Alaska had a diverse pattern of local lake change dynamics, with regions of intensive lake dynamics but little net change (North Slope-Outer Coastal Plain, YK-Delta), regions with nearly stable conditions (North Slope-Inner Coastal Plain), or strong lake area loss (Northern Seward Peninsula). Overall lake change is nearly evenly distributed between lake area gain and loss (-0.24%; 3.21%, 3.46%).

Apart from the continuous to discontinuous permafrost transition zone, the permafrost extent did not show a general influence on the net direction and magnitude of (thermokarst) lakes. Lake growth consistently increased towards continuous PF in both regions with significant discontinuous and continuous permafrost, but much more variable lake area loss rates determined the net lake change budget (Figure 4.4, Table 4.1). We could not find a general and consistent correlation of ground ice content with the magnitude and direction of lake dynamics (Figure 4.4, Table 4.1). However, ground ice content and geomorphological differences may have a strong influence on local and regional-scale lake dynamics (Nitze I. , et al., 2017), but the coarse resolution and quality of globally available datasets of permafrost properties only covers coarser spatial scales, which do not resolve local scale variation present in many locations such as northern Alaska, highlighting the need for improved data on permafrost distribution and especially on permafrost ice content.

Non-thermokarst lakes

Due to the bedrock geology and the complete glaciation during the last glacial maximum, lakes in the Eastern Canadian transect are of non-thermokarst origin, which was reflected in the homogeneous behavior of gradually increasing intensity of lake dynamics of both growth and loss from south to north. The difference was also reflected in suppressed gross growth rates, compared to thermokarst in Siberia and Alaska. Strong lake area loss in the northern and northwestern coastal and near-coastal zone outweighed weak lake growth with a net lake area loss of -2.01% (+0.77%; -2.84%) in the northern continuous permafrost zone, whereas the central and southern portions of the transect show little change with a few clusters of lake growth, which has been found in earlier studies (Carroll, Townshend, DiMiceli, Loboda, & Sohlberg, 2011). The spike in lake area gain at 53-54°N, was caused by the filling of the Eastmain-1A reservoir (+470 km²), which is part of a larger series of hydro-electrical dams.

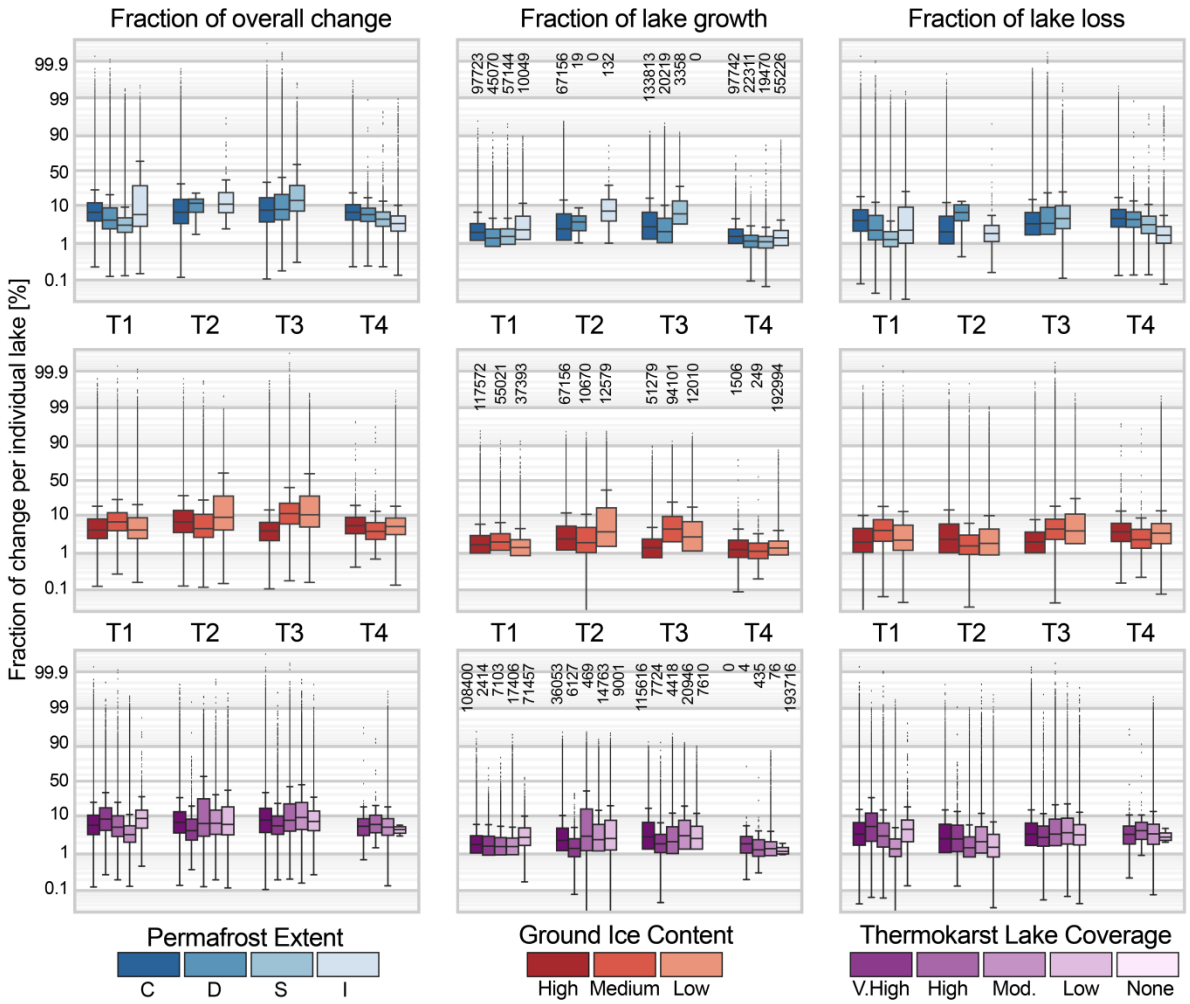

Figure 4.4: Boxplot of individual relative lake change statistics of any change (left), lake growth (center), and lake loss (right) by Permafrost extent (top), Ground Ice content (middle), and Thermokarst Lake Coverage (bottom). Sample sizes per group (n lakes) indicated in middle column.

Due to the non-thermokarst origin, permafrost extent and ground ice can be disregarded as significant influence factors of lake change. The gradual lake change on a latitudinal gradient indicates an influence of large scale climatic patterns. The entire transect was affected by an increase of temperatures (+1.2 to +1.7 K), in conjunction with a marginal increase in precipitation north of 56°N (+1 to +18 mm), but stronger precipitation increase in the southern part (+25 to +63 mm) of the observation period in comparison to 1979 to 1998.

Table 4.1: Regional lake change results per transect as net change, gross lake area growth and gross lake area loss, subdivided by permafrost extent, and ice content.

			Overall	Permafrost Extent				Ice Content		
		unit		C	D	S	I	High	Medium	Low
T1	Net	km²	-1759.50	-556.19	-390.11	-155.99	-300.98	-636.69	-347.67	-418.89
		%	-5.46	-4.29	-7.89	-1.94	-13.58	-3.67	-5.35	-9.70
	Growth	km²	509.93	220.93	58.24	87.86	114.55	324.59	108.00	48.99
		%	1.58	1.70	1.18	1.09	5.17	1.87	1.66	1.13
	Loss	km²	2269.42	777.12	448.35	243.84	415.52	961.28	455.67	467.88
		%	7.45	6.26	9.85	3.10	3.10	5.75	7.40	12.00
	n Lakes		218882	97723	45070	57144	10049	117572	55021	37393
T2	Net	km²	313.81	320.08	-0.02	0.00	0.00	32.00	97.82	190.65
		%	3.67	3.81	-3.12	0.00	0.00	0.55	8.30	13.99
	Growth	km²	663.76	657.23	0.02	0.00	0.00	248.28	147.56	262.11
		%	1.87	7.83	3.16	0.00	0.00	4.24	12.52	19.24
	Loss	km²	349.96	337.14	0.04	0.00	0.00	216.28	49.74	71.46
		%	3.95	3.87	6.48	0.00	0.00	3.67	3.90	4.60
	n Lakes		69151	67156	19	0	0	44058	10670	12579
T3	Net	km²	-161.45	-55.61	-109.08	3.20	0.00	-123.32	43.21	-81.38
		%	-0.62	-0.24	-5.96	0.28	0.00	-1.12	0.34	-3.53
	Growth	km²	862.19	736.96	99.40	20.92	0.00	105.48	672.12	79.68
		%	3.31	3.21	5.43	1.83	0.00	0.96	5.34	3.45
	Loss	km²	1023.64	792.57	208.48	17.72	0.00	228.81	628.91	161.06
		%	3.96	3.46	12.11	1.54	0.00	2.10	4.98	7.23
	n Lakes		158453	133813	20219	3358	0	51279	94101	12010
T4	Net	km²	-129.77	-438.72	-82.18	-52.62	447.60	-2.91	-0.27	-122.74
		%	-0.24	-2.02	-1.50	-1.07	2.15	-1.32	-1.55	-0.23
	Growth	km²	994.59	167.69	26.43	22.51	774.63	2.02	0.18	989.06
		%	1.87	0.77	0.48	0.46	3.71	0.91	1.03	1.87
	Loss	km²	1124.36	606.41	108.61	75.13	327.03	4.93	0.46	1111.80
		%	2.12	2.84	2.02	1.55	1.55	2.26	2.63	2.11
	n Lakes		196818	97742	22311	19470	55226	1506	249	192994

4.3.2 Retrogressive Thaw Slumps

Actively expanding retrogressive thaw slumps (RTS) and landslides were identified in sloped terrain in and along the foot slopes of mountain ranges, as well as coastal bluffs, lake shores

or valleys in ice-rich permafrost terrain. They typically formed regional clusters of up to 25 individual RTS and were limited to the continuous permafrost zone (Figure 4.3).

On the western and central Yamal Peninsula we identified 23 RTS which are distributed in spatial clusters along the western coast and in the vicinity of the Bovanenkovo gas field (cf. Table 4.2). In the Lena Delta region of the east Siberian Transect different clusters of 8 RTS were detected on steep coastal shores in the south-eastern Lena Delta region, where very ice-rich Yedoma Ice-Complex sediments are eroded (see Figure 4.2c). Several isolated clusters of 115 thaw slumps were detected in the western and southern, but only 18 in the eastern foreland of the Verkhoyansk mountain range in most cases along lake shores in hummocky terrain, which most likely are caused by decaying buried glacial ice (Figure 4.5). In the Alaskan transect several clusters of RTS and landslides were detected within the Brooks Range and along its northern and western foothills (n=184), most notably in the upper Noatak valley (n=52). Furthermore, 31 coastal thaw slumps were observed on the formerly glaciated Herschel Island and Yukon coast (Canada), whereas 9 RTS were detected on steep coastal bluffs on the northwestern coast of Alaska. The large Selawik Slump (see Figure 4.2d) in western Alaska was detected, but it remains a singular feature in its vicinity and marks the southernmost detected RTS in the Alaskan Transect. RTS were absent in the east Canadian Transect.

Table 4.2: Number, area and location (transect) of detected retrogressive thaw slumps.

Transect	# of RTS	Area km^2
T1 – Western Siberia	23	0.2079
T2 – Eastern Siberia	140	1.0809
T3 – Alaska	245	4.0014
T4 – Eastern Canada (Quebec)	0	0
SUM	408	5.2902

4.3.3 Wildfire

Burn scars of wildfires for the 2000-2015 period (see Methods section for description of temporal shift) were widespread in all transects, particularly within the densely forested boreal region. Southern inland locations with continental climatic conditions characterized by high annual temperature amplitudes and dry conditions throughout the entire year had a higher abundance of fires (cf. Table 4.3).

Eastern Siberia was among the most strongly affected region with large fire affected area, where around 7.78% of the total area and 8.15% of non-tundra area were burned with different intensities between 2000 and 2015. In its southernmost region west of the Lena river, around 17% of the land surface was affected by wildfires, predominantly during few severe fire seasons (Boike, et al., 2016). Wildfires also affected large swaths of boreal Alaska with 8.89% burned non-tundra area, correlating with drying conditions over the observation period (Figure 4.4). In the Canadian Transect fires were a common occurrence in the southern boreal region where they affected 5.06% of non-tundra area, and sharply decreasing wildfire frequency north of 53° latitude. In more humid and wetland dominated western Siberia fires were less widespread with a total extent of 1.7% or 2.43% in non-tundra area (Figure 4.4).

Generally, fire frequency and extent decreased sharply towards the taiga tundra ecotone, where the density of available fuel decreases and less favorable climatic conditions prevail. Tundra fires occurred infrequently and were mostly limited to a small extent. Alaska stands out as the only region with tundra fires, most prominently the major Anaktuvuk Fire in 2007 in northern Alaska (Figure 4.2f) which affected an area of ~1000km². Overall tundra fires in northern and western Alaska burned nearly 4600 km² or 1.07% of the tundra region.

Table 4.3: Overall and Transect-specific wildfire coverage divided by Fire location (overall, boreal/forest, tundra).

Transect	Unit	Overall	Boreal	Tundra
T1 – Western Siberia	km²	8470.28	8470.28	0.00
	%	1.70	2.43	0.00
T2 – Eastern Siberia	km²	43047.93	43047.93	0.00
	%	7.78	8.15	0.00
T3 – Alaska	km²	46162.35	41580.53	4581.82
	%	5.14	8.89	1.07
T4 – Eastern canada (Quebec)	km²	13642.20	13642.20	0.00
	%	3.46	5.06	0.00
SUM	km²	111322.76	106740.94	4581.82
	%	4.75	6.62	0.63

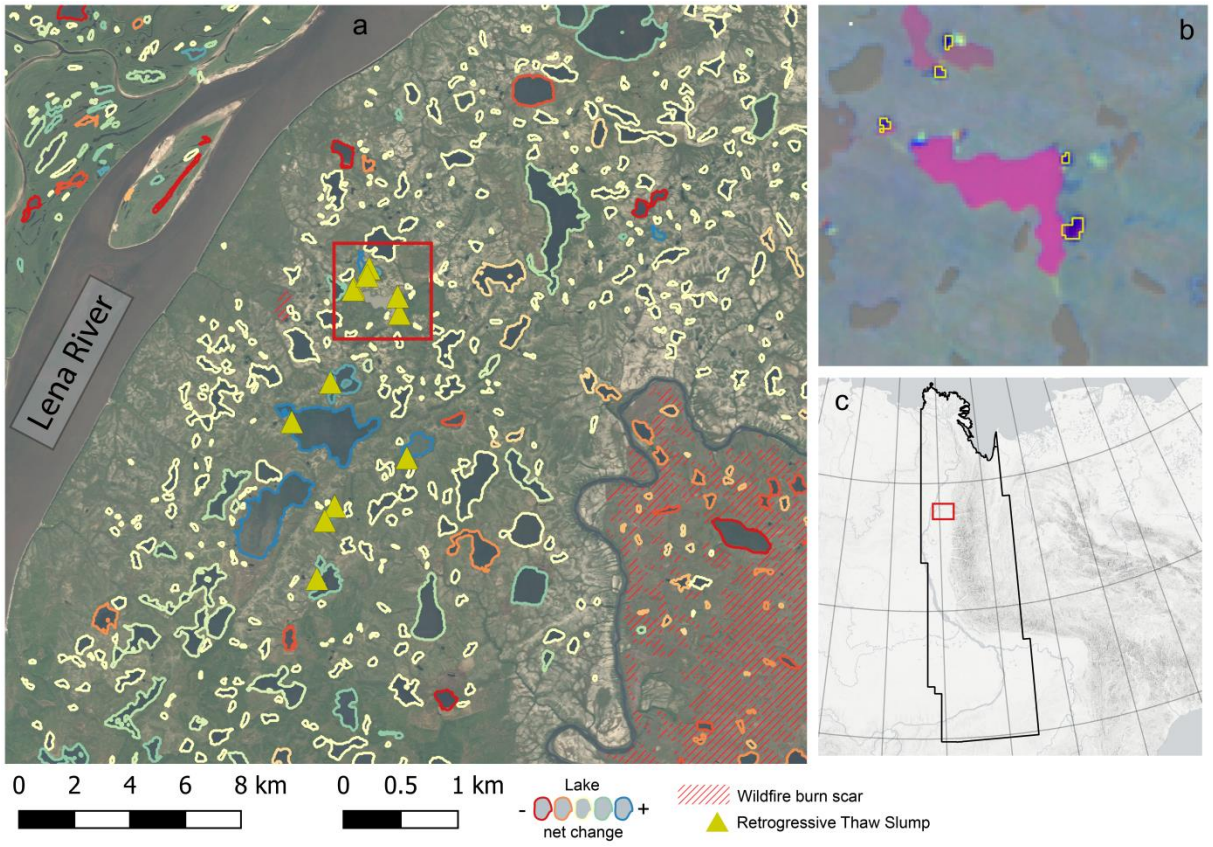

Figure 4.5: Local example of lake changes, retrogressive thaw slumps (RTS) and wildfire burn scars along the Lena river in north-eastern Siberia. a) Lake perimeters with net change direction and location of RTS and wildfire burn scars, b) detailed view of Landsat trend images with RTS perimeters indicated along lake shores. Magenta color indicates strong increase in suspended sediments within the lake, c) Overview of site location in East Siberian Transect (T2)

4.4 Discussion

Permafrost region disturbances (PRDs) cover specific spatial scales, which are diametrical to their local change intensity. Fires are the disturbance with the largest spatial extent of 111,323 km² in the studied transects of 2.3 x 10^6 km^2. They have a wide range of impacts on the ground thermal regime, depending on the burn severity and soil moisture conditions (Yoshikawa, Bolton, Romanovsky, Fukuda, & Hinzman, 2002; Jafarov, Romanovsky, Genet, McGuire, & Marchenko, 2013), and have the potential to rapidly cause permafrost degradation (Burn, 1998; Jones B. M., et al., 2015). In consequence, wildfires may cause other disturbances, including triggering of thermokarst lake formation (Edwards, Grosse, Jones, & McDowell, 2016) or drainage (Jorgenson & Grunblatt, 2013) as well as retrogressive

thaw slump development (Huscroft, Lipovsky, & Bond, 2004; Jones B. M., et al., 2015), particularly in forested regions. The relatively infrequent occurrence and sparse distribution of tundra fires shows its limited impact on continental scales. However, locally tundra fires can lead to strong permafrost degradation several years post-fire (Jones B. M., et al., 2015) and with continued warming, tundra fires are predicted to increase in frequency (Hu, et al., 2015) and may spread to tundra regions where fires are currently exceptional.

In contrast to fire, lake changes affect a much smaller fraction of the land surface, but have a more direct and partially severe impact on the ground thermal regime. Thermokarst and lake expansion can lead to a release of the greenhouse gases carbon dioxide or methane (Schuur, et al., 2015) due to rapid lake shore erosion or thaw bulb (talik) development underneath lakes (Langer, et al., 2016; Arp, et al., 2016). As lake growth is a more gradual process with less variance, compared to highly dynamic and variable lake loss, GHG emissions are potentially more predictable. In contrast, shrinking lakes may have the potential of carbon sequestration due to permafrost aggradation (Briggs, et al., 2014; Grosse, Jones, & Arp, 2013) and peat accumulation (Walter Anthony, et al., 2014; Jones M. C., Grosse, Jones, & Walter Anthony, 2012). The analysis of large regions spread out over the northern permafrost region revealed that the key drivers of lake change are highly diverse and could not be linked to single mechanisms alone such as permafrost extent, ground ice or climate making lake area dynamics a difficult to interpret indicator of climate change impacts on permafrost regions.

Active RTS are the most localized and smallest PRD as they affected only 5.3 km² of the total study area, much smaller than the disturbance footprint of lake changes (4767km²) or fire (111,323 km²), but have the most severe and direct impact on permafrost by their ability to remove large quantities of ground material within a short period. RTS impact the thermal ground regime, downstream bio-geochemical cycles, and may decrease terrain stability triggering further mass wasting activity (Kokelj S. V., Lantz, Tunnicliffe, Segal, & Lacelle, 2017). Active RTS. However, due to the small footprint of RTS following an exponential distribution with features from few m² to a maximum of approximately 70 ha for the largest RTS (Batagaika crater), large quantities of particularly smaller features may not be sufficiently detected with 30m resolution data. Their clustered occurrence within narrow environmental parameters can help to make efficient use of very high-resolution imagery to find much smaller RTS and related landscape disturbances and to predict future occurrence.

Once permafrost is affected by degradation caused by PRD, different feedback mechanisms may get activated leading to changes in the hydrological and carbon cycles. Our comprehensive overview of the spatial extent and distribution of three key PRD over more than 2.3 x 10^6 km² provides an unprecedented dataset for a range of use cases. It provides insight into the key drivers and their complexity of PRD. The information may serve as valuable guidance into which ones and how these disturbances need to be parameterized in large scale models to better understand and predict the complexity of landscape processes and bio-geochemical cycles in permafrost environments in the present, the past, and the future.

4.5 Methods

4.5.1 Remote Sensing Data Processing

Trend calculation

We applied trend analyses on all available Landsat (TM, ETM+ and OLI) surface reflectance data of the study regions in a defined range of parameters. Data were pre-processed to surface reflectance and provided by the ESPA processing interface of the United States Geological Survey (USGS) (https://espa.cr.usgs.gov). In order to capture peak-summer season only information and to ensure an acceptable data quality, we only used data with land cloud cover of less than 70% and imagery from July and August. We narrowed down the observation period to years 1999 through 2014, to keep the data amount and quality as consistent as possible, because large parts of Siberia and some coastal regions of Alaska have large gaps in the Landsat archive before 1999. We masked all low-quality pixels, including clouds, cloud shadow and snow, with the FMask layer (Zhu, Wang, & Woodcock, 2015), which is distributed with the data products. Between 13 and 169 valid observations were recorded for each pixel.

We calculated six widely used multi-spectral-indices (MSI), NDVI, NDMI, NDWI as well as Tasseled Cap Brightness (TCB), -Greenness (TCG) and -Wetness (TCW), which were chosen to represent a range of different physical surface properties, such as moisture, albedo or vegetation. For each pixel and MSI we calculated robust trends based on the Theil-Sen algorithm (Theil, 1992; Sen, 1968), which is more robust against outliers than traditional

least-squares regression (Fernandes & Leblanc, 2005) has been applied in several remote sensing studies (Fraser R. H., et al., 2014; Nitze & Grosse, 2016; Nitze I. , et al., 2017). The trend analysis returned the slope and intercept parameters, as well as the confidence intervals of the trend slopes.

Landscape process classification

For the detection and delineation of permafrost related disturbances, we translated the spectral trend information to semantic classes of land cover and change processes using supervised machine-learning classification. Depending on the classification target, lake changes (scenario 1: 4 classes) or retrogressive thaw slumps and fire (scenario 2: 6 classes), we applied machine-learning models based on the Random Forest method (Breiman, 2001). For the training process, we selected 973 for scenario 1 and 1254 point locations of known land cover and land cover change for scenario 2, which are distributed over several locations in the permafrost region (Table 4.4). Due to the spatial heterogeneity and spatial distribution occurrence frequency, a randomized or gridded location selection was not feasible. Therefore, we applied a mixture of random and manual selection of locations of known land cover or changes, based on high-to-moderate resolution imagery (<= 30m). For each of the classes we calculated the probability values for each of the defined landscape change/no-change classes. The classification model was trained with four calculated trend parameters of the six MSI (see above) as well as elevation and slope information, in total 30 different attributes, which were calculated for each 30x30m pixel. Both classification scenarios were 5-fold cross-validated. Classification results and single class probabilities were used for later object based analysis of lakes, wildfires and retrogressive thaw slumps.

Table 4.4: Overview of number of sample locations and classification scenario for landcover- and change classification.

Class	# of reference locations	Classification scenario
Stable Water	299	1
Stable Land	403	1
Change Land to Water	85	1
Change Water to Land	186	1
Wildfire (tundra and boreal)	201	1, 2
Retrogressive thaw slumps	80	1, 2

Extraction of lake changes

Lake locations and lake change information were extracted using object-based image analysis and sub-pixel analysis of machine learning classified landcover and land cover change probabilities, based on the workflow described in Nitze et al. (2017).

Extraction of Retrogressive Thaw Slumps

We extracted individual Retrogressive thaw slumps segments (RTS) from the classification dataset (scenario 2), where probability values exceeded 30% and extracted the bounding box (bbox) of these segments. Due to potentially small object size and expected mixed-pixels, we chose a low threshold to 30 %. Final segment boundaries were defined based on a 2-class k-means clustering algorithm, locally applied on the bbox of each segment, where the class of higher p-values was selected as an RTS candidate.

The initial segmentation includes a high false positive rate, which required data filtering. We calculated statistics of RTS-classification p-values, slope and spatial shape attributes. Slope values in angular degrees were calculated using the gdaldem software based on 90m ESA DUE ARCTIC DEM (Santoro & Strozzi, 2012) (data resampled to 30 m to match Landsat resolution). We automatically discarded objects with a mean spectral probability of <0.4 %. The final RTS selection was carried out manually on the remaining object candidates with the support of Landsat trend data and high-resolution optical imagery, where applicable.

Extraction of wildfire burn scars

We used the publicly available Global Forest Change data in version 1.3 (Hansen, et al., 2013) available at https://earthenginepartners.appspot.com/science-2013-global-forest/download_v1.3.html. This dataset covers the period from 2000 until 2015, which is shifted by one year, compared to the trend analysis, but also covers a 16 year period.

We used the “forest cover loss” data, as a predictor for fire, because wildfires are the dominant source for forest loss within the study site. Other non-fire forest loss, such as infrastructure development (e.g. oil field development in western Siberia, railway construction eastern Siberia) or wood harvest affected very small regions (<1%). Furthermore,

the fire dataset contained several small speckle objects, which due to their limited size were discarded as non-wildfire.

As the GFC dataset is only sensitive to densely forested area changes, we used the multi-spectral trend dataset to delineate fires in tundra and improved burned area perimeters sparsely forested regions (forest tundra), which occurred in Alaska (T3) and Eastern Siberia (T2). We applied the same machine-learning based 6-class classification methodology as for RTS. Pixels with a fire probability of > 50% were added to the trend based fire mask (TBFM).

For removing noise in the GFC and TBFM, we applied several morphological filters where we removed objects smaller than 64 pixels (px) (20ha), filled holes smaller than 36 px and morphologically opened/closed with a round element with a diameter of 5 pixels (150 m) and again removed objects smaller than 20ha to remove further noise or non-fire forest loss, such as infrastructure development. Image cleaning operations were carried out using the *scikit-image* package for the python programming language.

The TBFM was filtered to fire perimeters, which intersected fire perimeters of the processed GFC datasets. The Alaska fire perimeter dataset was further used for selecting (spatial intersection) correct fire perimeters in tundra and forest tundra regions. Finally, we merged the preprocessed and filtered TBFM and the preprocessed GFC data to a contiguous fire extent map.

For the distinction of tundra and non-tundra wildfires we used the circumpolar Arctic vegetation map (CAVM) (Walker, et al., 2005). Tundra extent was calculated from the intersection of transect land areas and CAVM. Fire perimeters intersecting the CAVM footprint were calculated as tundra fire, the remaining fire perimeters were defined as non-tundra/boreal fires.

4.5.2 Auxiliary Data Sources

We used the permafrost map (Brown, Ferrians Jr, Heginbottom, & Melnikov, 1997) of the International Permafrost Association (IPA) for the extraction of ice content and permafrost extent. We intersected the centroids of lake objects with permafrost extent polygons for the extraction of permafrost extent and ground-ice class statistics.

We used ERA-Interim Reanalysis data from 1979 to 2014, which were provided by the European Centre for Medium-Range Forecast (ECMWF). We downloaded monthly means of temperatures (id: 130) and total precipitation (id:228). Midday and midnight temperatures were averaged to receive monthly temperatures. Precipitation values of 12 hour-periods were summed to monthly totals. For the comparison of time periods data were split into the period from January 1979 through December 1998 and January 1999 through December 2014.

5. Tundra landform and vegetation productivity trend maps for the Arctic Coastal Plain of northern Alaska

Lara, M.J.[1,2]; Nitze, I.[3,4]; Grosse, G. [3,4] & McGuire, A.D.[5]

[1] Department of Plant Biology, University of Illinois Urbana-Champaign, Urbana, IL, USA.

[2].Institute of Arctic Biology, University of Alaska Fairbanks, Fairbanks, AK, USA

[3] Alfred Wegener Institute Helmholtz Centre for Polar and Marine Research, Periglacial Research Unit, Potsdam, Germany

[4] Institute of Earth and Environmental Science, University of Potsdam, Potsdam, Germany

[5] U.S. Geological Survey, Alaska Cooperative Fish and Wildlife Research Unit, University of Alaska Fairbanks, Fairbanks, AK, USA

In Revision for: Nature Scientific Data

5.1 Abstract

Arctic tundra landscapes are composed of a complex mosaic of patterned ground features, varying in soil moisture, vegetation composition, and surface hydrology over small spatial scales (10-100 m). The importance of microtopography and associated geomorphic landforms in influencing ecosystem structure and function is well founded, however, spatial data products describing local to regional scale distribution of patterned ground or polygonal tundra geomorphology are largely unavailable. Thus, our understanding of local impacts on regional scale processes (e.g. carbon dynamics) may be limited. We produced two key spatiotemporal datasets spanning the Arctic Coastal Plain of northern Alaska (~60,000 km^2), to evaluate climate-geomorphological controls on arctic tundra productivity change (i.e. greening and browning), using (1) a novel 30 m classification of polygonal tundra geomorphology and (2) decadal trends in surface greenness using the Landsat archive (1999-2014). These datasets can be easily integrated and adapted for use in an array of local to regional applications such as (1) upscaling plot-level measurements (e.g. carbon/energy fluxes), (2) mapping of soils, vegetation, or permafrost, and/or (3) initializing ecosystem biogeochemistry, hydrology, and/or habitat modeling.

5.2 Background & Summary

Arctic polygonal tundra landscapes are highly heterogeneous, disproportionately distributed across mesotopographic gradients, varying in surficial geology, ground ice content, and soil thermal regimes (Farquharson, Mann, Grosse, Jones, & Romanovsky, 2016; Walker D. A., 2000). The high density of ice wedges present in this low relief landscape facilitates subtle variations (~0.5 m) in surface microtopography, markedly influencing hydrology (Liljedahl, Hinzman, & Schulla, 2012; Engstrom, Hope, Kwon, Stow, & Zamolodchikov, 2005), biogeochemistry (Lara, et al., 2015; Zona, Lipson, Zulueta, Oberbauer, & Oechel, 2011; Olivas, et al., 2011; Rhew, Teh, & Abel, 2007; Lipson, et al., 2012; Newman, et al., 2015), and vegetation structure (Villarreal, et al., 2012; Brown, Miller, Tieszen, & Bunnell, 1980). Fine-scale differences in microtopography have been shown to control a variety of key ecosystem attributes and processes that influence ecosystem function, such as snow distribution and depth (Liljedahl, et al., 2016), surface and subsurface hydrology (Liljedahl, et al., 2016; Throckmorton, et al., 2016), vegetation composition (Walker D. A., 2000; Villarreal, et al., 2012; Brown, Miller, Tieszen, & Bunnell, 1980), carbon dioxide and methane fluxes (Lara, et al., 2015; Zona, Lipson, Zulueta, Oberbauer, & Oechel, 2011; Lara, et al., 2012; Wainwright, et al., 2015), soil carbon and nitrogen content (Bockheim, Everett, Hinkel, Nelson, & Brown, 1999; Bockheim, Hinkel, Eisner, & Dai, 2004; Biasi, et al., 2005), and an array of soil characteristics (Bockheim, Everett, Hinkel, Nelson, & Brown, 1999; Johnson, et al., 2011). Despite the prominent control of microtopography and associated geomorphology on ecosystem function, land cover data products available to represent landforms across the Pan-Arctic are strikingly limited (Bartsch, Höfler, Kroisleitner, & Trofaier, 2016). The relative absence of these key geospatial datasets characterizing permafrost lowlands, may severely limit our ability to understand local scale controls on regional to global scale patterns and processes (Bartsch, Höfler, Kroisleitner, & Trofaier, 2016).

Datasets presented here were developed to investigate the potential local to regional controls on past and future trajectories of arctic tundra vegetation productivity (Lara, Nitze, Grosse, & McGuire, in revision), inferred from spatiotemporal patterns of change in the Normalized Difference Vegetation Index (NDVI). We present two geospatial data products, (1) a 30 m resolution tundra geomorphology map, and (2) a decadal scale NDVI trend map (1999-2014), developed to represent the landform heterogeneity and associated productivity change across

the Arctic Coastal Plain (ACP) of northern Alaska (~60,000 km^2). We validated the tundra geomorphology map using 1000 reference sites, and evaluated the sensor bias used to develop the NDVI trend map. Produced geospatial datasets will be useful for an array of applications, some of which may include the (1) upscaling of plot-level measurements (e.g. carbon and energy fluxes), (2) mapping of soils, vegetation, or permafrost, and/or (3) initializing ecosystem biogeochemistry, hydrology, and/or habitat modeling.

5.3 Methods

5.3.1 Polygonal tundra geomorphology mapping

We focused this mapping initiative on the Arctic Coastal tundra region of northern Alaska, which stretches from the western coast along the Chukchi sea to the Beaufort coastal plains at the Alaskan-Canadian border (latitude: 68-71° N; longitude: 140-167° W). Two ecological landscape units (~60,000 km^2), the Arctic peaty lowlands and the Arctic sandy lowlands were used to define the spatial extent of the ACP (Jorgenson & Grunblatt, 2013). The region is dominated by continuous permafrost several hundred meters thick (Sellmann & Brown, 1973). Permafrost ground ice content ranges from low in sandy lowlands to very high in peaty lowlands (Jorgenson & Grunblatt, 2013; Jorgenson, et al., 2008), while the maximum active layer depth ranges from 20-120cm (Nelson, Anisimov, & Shiklomanov, 2001). These two arctic tundra regions (i.e. sandy and peaty lowlands) were specifically targeted in this analysis, due to their geomorphologic similarity to ~1.9 million km^2 of tundra across the Pan-Arctic (Walker, et al., 2005). The tundra mapping approach described here will be useful for the development of comparable products across northern latitudes. Refer to the primary research article (Lara, Nitze, Grosse, & McGuire, in revision), for detailed site descriptions.

5.3.2 Image processing

Twelve cloud free Landsat 8 satellite images were acquired during the summers of 2013 and 2014, used in the tundra geomorphology classification (Table 5.1). All Landsat data products were downloaded from the United States Geological Survey (USGS) earth explorer web-based platform (https://earthexplorer.usgs.gov). We used only the 9 spectral bands provided by the Operational Land Imager (OLI) instrument for mapping, while ignoring the 2

additional Thermal Infrared Sensor (TIRS) bands due to defective optics in the infrared sensor (Montanaro, Gerace, Lunsford, & Reuter, 2014). Landsat 8 OLI spectral bands include (1) coastal/aerosol (Ultra blue), (2) blue, (3) green, (4) red, (5) near infrared (NIR), (6) shortwave infrared 1 (SWIR1), (7) shortwave infrared 2 (SWIR2), (8) panchromatic, and (9) cirrus. Prior to image mosaicking, reflectance values were normalized across satellite scenes, by calculating top-of-atmosphere reflectance (Chavez, 1996), which minimized the radiometric difference between images associated with varying atmospheric conditions, acquisition dates, and solar zenith angles (Chavez, 1996), while the Landsat Surface Reflectance Code (LaSRC) was used for atmospheric correction. Images were mosaicked within ArcGIS™ 10.4 (ESRI).

5.3.3 Image Classification

We expand upon geomorphic mapping procedures developed for a subregion of the ACP of northern Alaska on the Barrow Peninsula (1800 km^2) (Lara, et al., 2015), using a novel automated object based image analysis (OBIA) approach for tundra geomorphic mapping across the ACP (58,691 km^2). The OBIA land cover classifier (eCognition™ version 9.1, Trimble) was parameterized using various rules, thresholds, spectral indices, and proximity functions using individual and combined spectral bands, spectral indices, and geometric object shapes/sizes (i.e. perimeter, area, roundness) and corresponding reference data (i.e. field/ground truth points and high resolution aerial/satellite imagery) to differentiate between geomorphic landforms (Figure 5.1). Fifteen tundra geomorphic landforms were mapped at 30 x 30 m spatial resolution (Figure 5.2a), including (qualitatively ranked from wet to dry), coastal saline water (CS), lakes (large:>90ha, medium:≤90 and >20ha, small:≤20ha), rivers, ponds, coalescent low-center polygons (CLC), nonpatterned drained thaw lake basins (nDTLB), low-center polygons (LC), sandy barrens (SB), flat-center polygons (FC), riparian corridors (RC), high-center polygons (HC), drained slopes (DS), sand dunes (SD), ice/snow (Ice), and urban. Spectral indices used in image classification included Albedo (Liang, 2001), Normalized Difference Vegetation Index (NDVI) (Rouse Jr, Haas, Schell, & Deering, 1974) ($\frac{\rho_{NIR}-\rho_{Red}}{\rho_{NIR}+\rho_{Red}}$), Normalized Difference Water Index (NDWI) (Gao, 1996) ($\frac{\rho_{Green}-\rho_{NIR}}{\rho_{Green}+\rho_{NIR}}$), and BlueMax ($\frac{\rho_{Blue}}{\rho_{MaxDiff}}$), where MaxDiff refers to the maximum difference between all bands (1-9).

All pixels within the processed Landsat 8 image mosaic were aggregated into clusters or image "objects" based on similar spectral properties of neighbouring pixels using multiresolution segmentation and spectral difference algorithms. These segmentation algorithms were parameterized to represent object characteristics such as shape, compactness, and spectral similarity. We split all image objects into two broad classes, wet tundra and dry tundra using NDWI thresholds, identified using landform specific field observations (Lara, et al., 2012; Lara, et al., 2015). The following classification procedure (Figure 5.1), extracts all image objects from wet and dry tundra and reclassifies them into specific geomorphic landforms.

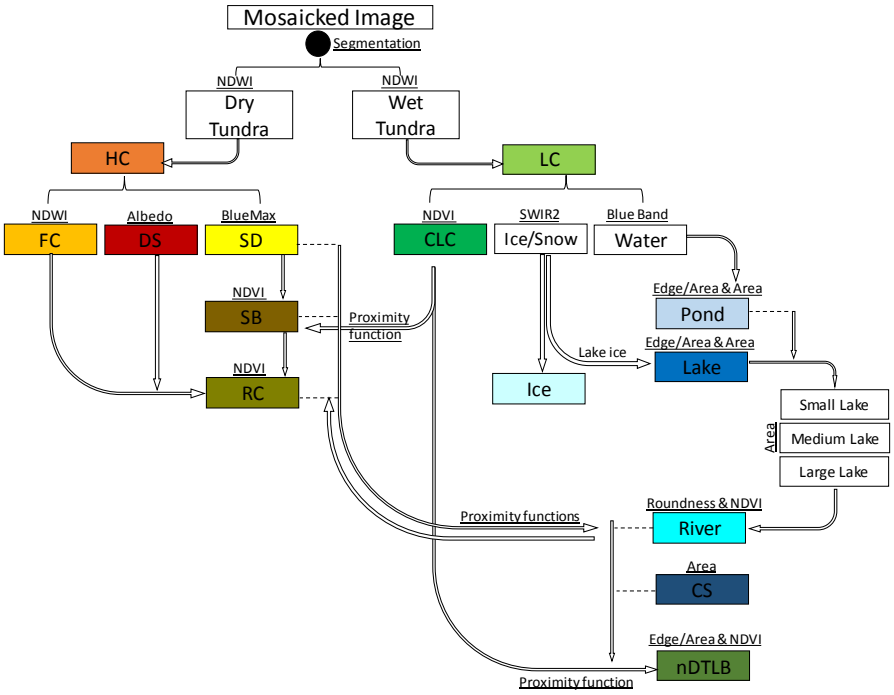

Figure 5.1: Simplistic schematic representation of the classification procedure used to map polygonal tundra geomorphology on the ACP. Underlined text represents Band, Area, Function, or Index thresholds used for assigning classes. Proximity functions are used to reclassify image objects based on distance from another geomorphic landform. See "Tundra Classification" section for acronym definitions.

Table 5.1: Mosaicked Landsat scenes used to create the tundra geomorphology map

Product ID	Sensor	Satellite	Year*	Month*	Day*
LC80690112013249LGN00	OLI/TIRS	Landsat 8	2013	Sept.	5
LC80720112013254LGN00	OLI/TIRS	Landsat 8	2013	Sept.	10
LC80740112014191LGN00	OLI/TIRS	Landsat 8	2014	July	9
LC80770102013193LGN00	OLI/TIRS	Landsat 8	2013	July	11
LC80770112013193LGN00	OLI/TIRS	Landsat 8	2013	July	11
LC80790102013191LGN00	OLI/TIRS	Landsat 8	2013	July	9
LC80800102014217LGN00	OLI/TIRS	Landsat 8	2014	Aug.	4
LC80800112014249LGN00	OLI/TIRS	Landsat 8	2014	Sept.	5
LC80820122013244LGN00	OLI/TIRS	Landsat 8	2013	Aug.	31
LC80830102014222LGN00	OLI/TIRS	Landsat 8	2014	Aug.	9
LC80830112014190LGN00	OLI/TIRS	Landsat 8	2014	July	8
LC80840122013194LGN00	OLI/TIRS	Landsat 8	2013	July	12

*Acquisition date

Wet Tundra Classification

We decomposed our classification of wet tundra into three steps, (1) extraction of CLC and nDTLB, (2) open water body differentiation, and (3) rectification of misclassifications. Initially, we differentiated CLC from all wet tundra objects using a low productivity (NDVI) threshold, which was associated with sparse vegetation cover and the presence of open water. Although, both CLC and nDTLB are found in aquatic to wet environments, we differentiated CLC from nDTLB landforms using the characteristically high NDVI values of nDTLB (Lara, et al., 2012; Lara, et al., 2015) and morphological features. Due to the rapid formation of nDTLB following lake drainage (Jorgenson & Shur, 2007), this young geomorphic landform often contains a relatively large non-polygonal surface area (Bockheim & Hinkel, 2012) (i.e. limited effects of ice aggregation and heaving processes associated with microtopographic variability), thus we use a moderate edge to area ratio and high NDVI threshold for nDTLB feature extraction.

All unvegetated open water pixels were extracted using a low-moderate blue band threshold (Figure 5.1). A spectral difference segmentation algorithm, was looped 5x to iteratively combine all neighbouring open water objects with similar spectral properties. This object merging process enabled the identification of each spatially isolated water body (i.e. lake, pond, or river), where structural properties such as area, perimeter, or edge (i.e. perimeter) to

area ratio can be used to differentiate waterbodies. Therefore, we defined CS, lakes, and ponds using structural properties, area and edge to area ratio. Water bodies were decomposed into CS (>100,000 ha) large lakes (≤ 100,000 > 90 ha), medium lakes (≤ 90 > 20 ha), small lakes (≤ 20 >1 ha), and ponds (≤ 1 ha). The 100,000 ha area threshold was used to define CS to avoid large lake misclassification errors, as Teshekpuk Lake (70.61˚ N, -153.56˚ W), has an area of ~83,000 ha. Due to misclassifications of ponds as lakes, associated with the high interconnectivity between irregularly structured open water objects, we used a low edge to area ratio on lakes, to ensure accurate classification of ponds. Rivers were differentiated from all open water objects using a NDVI threshold and a "roundness" function. Integrating both approaches successfully extracted rivers, as high NDVI thresholds were used to differentiate open water from vegetated aquatic standing water objects, and low roundness values identified the characteristic elongated and meandering structure of rivers. Despite the late summer image acquisition dates used in this classification (Table 5.1), ice/snow image objects identified using high SWIR2 thresholds, were found in large lakes or adjacent to steep topographic gradients such as river valleys or near a snow fence. All ice/snow objects that occurred on lakes were reclassified as lake area, while the remaining ice/snow was reclassified as Ice.

Although, classification functions developed for wet tundra performed well, the majority of misclassifications were associated with the relatively course spatial resolution object patch size (30 m). To rectify these misclassifications, we used neighborhood or proximity functions to develop relationships between nearby geomorphic landforms using spectral and structural parameters for nDTLB, CLC, pond, and lakes. For example, nDTLB was often misclassified as CLC or pond, occurring near lake perimeters. Because aquatic-wet landforms occurring near lake perimeters are typically represented by nDTLB, having recently formed after partial or complete lake drainage, we reclassified older landforms such as CLC and ponds adjacent to lakes as nDTLBs. All remaining unclassified wet tundra objects that did not meet the criteria for nDTLB, CLC, pond, river, CS, or lakes in wet tundra were classified as LC (i.e. dominant wet geomorphic landform).

Dry Tundra Classification

We differentiated landforms in dry tundra following two steps, (1) threshold identification and extraction of FC and RC, and (2) rectification of misclassifications. A series of reference sites

identified from ground based observations and/or oblique aerial photography were used to define NDWI and NDVI thresholds needed to extract FC and RC, respectively. These two geomorphic landforms were difficult to classify due to the similarity in vegetation composition and surface hydrology. However, we were able to differentiate between these two landforms, as FC was slightly higher in surface wetness, associated with the 2 fold difference in trough area relative to HC (Lara, et al., 2015). The high variability in NDVI of shrub canopies in RC relative to other landforms, made RC difficult to extract. Nevertheless, because RC typically occurred near riverine environments, we used both a low-moderate NDVI threshold and a proximity function adjacent to rivers to extract RC. Sand and gravel objects were easily extracted using a high BlueMax threshold. All lightly vegetated wet-moist sand and gravel objects were classified as SB using a moderate-high NDVI threshold, whereas drier sand and gravel objects were classified as SD. Due to the use of sand and gravel in the development of urban infrastructure such as roads and buildings, automated procedures initially classified these feature as SD, as they had a similar spectral signature. However, we manually reclassified SD as Urban near native Alaskan villages and oil drilling platforms (i.e. near Prudhoe Bay). Although, we made significant progress with the development of classification procedures for Urban landforms using spectral patterns and geometric structures, we abandoned this development due to the relatively limited area impacted by urban infrastructure across the ACP. Additionally, DS was extracted using a high albedo threshold, as this landform was very dry and often dominated by lichen plant communities, which are highly reflective (Lara, et al., 2012). Similar to misclassifications associated with object patch size identified in wet tundra, we found analogous misclassifications of SB near rivers as CLC and ponds. Therefore, we reclassified CLC and pond classes that were adjacent to rivers as SB. All remaining unclassified dry tundra objects not classified as DS, FC, RC, SB, SD, or Urban were classified as HC (i.e. dominant dry geomorphic landform).

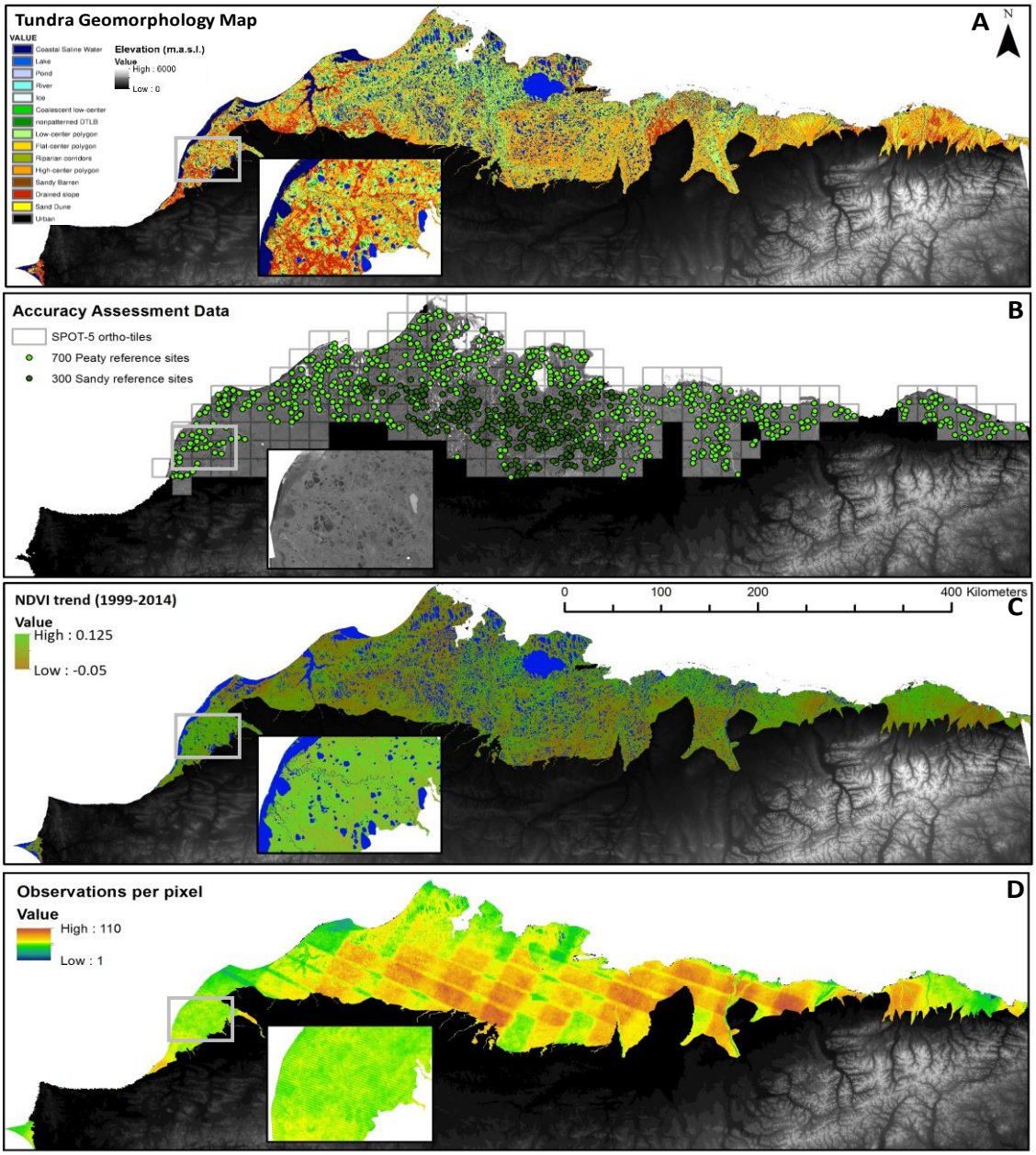

Figure 5.2: Geospatial datasets representing the heterogeneity in both landform and NDVI across the ACP of northern Alaska. The tundra geomorphology map (panel A) was validated with 1000 reference sites (700 and 300 in the Arctic Peaty Lowlands and Arctic Sandy Lowlands, respectively) using 249 SPOT-5 ortho-tiles (panel B), while the NDVI trend map (panel C) was developed using between 40 to 110 image observations per 30 m pixel (panel D).

5.3.4 Decadal scale NDVI trend analysis

Following the approach of Nitze & Grosse (2016), the NDVI trend map (Figure 5.2d) was computed using all available imagery collected from the Landsat sensors Thematic Mapper (TM), Enhanced Thematic Mapper+ (ETM+), and Observing Land Imager (OLI), acquired between July 1st and August 30th (i.e. peak growing season) of 1999-2014, across the ACP. We excluded imagery preceding 1999 due to the paucity of image acquisition and limited coverage across the ACP. All surface reflectance data used to derive this product were downloaded as radiometrically and geometrically terrain-corrected product from the USGS EROS Science Processing Architecture interface (https://espa.cr.usgs.gov). The "FMask" algorithm (Zhu, Wang, & Woodcock, 2015) was used to detect and mask out all non-valid data, such as clouds, shadows, snow/ice, and nodata pixels. For each pixel, linear trends of NDVI were calculated using the non-parametric Theil-Sen linear regression method, which calculates the median of all possible slopes across every point in time (Sen, 1968; Theil, 1992). The Theil-Sen regression is robust against outliers and outperforms least-squares regression in remote sensing data (Fernandes & Leblanc, 2005). Each pixel within the NDVI trend map was based on a total of 40-110 Landsat images (Figure 5.2c) for the Theil-Sen slope calculation. The final NDVI trend product was spatiotemporally similar to coarser resolution products (Bhatt, et al., 2010; Ju & Masek, 2016) identifying heterogeneous patterns of greening and browning across the ACP of northern Alaska.

5.4 Data Records

The presented ACP tundra geomorphology map (Data Citation 1: Alaskan Arctic Coastal Plain Polygonal Tundra Geomorphology Map https://doi.org/10.21429/C9JS8S) and NDVI trend map (Data Citation 2: Alaskan Arctic Coastal Plain NDVI trend (1999-2014) Map https://doi.org/10.21429/C9F04D) are both archived at the USGS Sciencebase Climate Science Center. These maps were clipped to the ACP domain and formatted as geotiff rasters. Additionally, all spatial and climate data used in Lara et al. (Lara, Nitze, Grosse, & McGuire, in revision) are archived in the Scenarios Network of Alaska and Arctic Planning (SNAP) data portal (http://ckan.snap.uaf.edu/).

Although the tundra geomorphic map was developed using OBIA which clusters spectrally similar nearby pixels into objects, the final map was resampled at the original 30 x 30 m pixel resolution and presented as a single-band raster (Figure 5.2a). The map attribute table includes the following data columns: geomorphic landform (i.e. sand dune, low-center polygon), area (km^2), and soil moisture regime (SMR). In addition, a color palette file (.clc) is provided to reproduce map (Figure 5.2a). The annotated functions and code used for the classification of tundra landforms within eCognition™ v. 9.1, are made available in the supplementary information. All threshold values were replaced with qualitative ranges (i.e. low, low-moderate, moderate, moderate-high, or high) as reflectance values and image statistics will vary between scenes, thus user specific refinement will be required. Further, it is important to note that the classification procedure developed here has only been evaluated in lowland arctic tundra ecosystems and misclassifications may arise if applied in dissimilar tundra environments. For example, we applied the developed classification procedure to higher elevation drier hillslope tundra, south of the ACP, finding the rate of misclassification to increase, as algorithms/functions were initially developed explicitly for polygonal tundra similar to the ACP of northern Alaska. To include different tundra landforms with different vegetation, hydrology, and soil characteristics, further development will be required.

The NDVI trend map is presented as a four-band raster (Figure 5.2d). Band 1 represents the decadal scale rate of change or slope calculated by the Theil-Sen regression. Band 2 represents the intercept or the NDVI data scaled to the year 2014. While, Band 3 and 4 are the upper and lower 95% confidence intervals of the slope of each individual pixel.

5.5 Technical Validation

5.5.1 Tundra Geomorphology Map

To validate the tundra geomorphology map, we used an array of oblique aerial/ground based photography and 249 high resolution Satellite Pour l'Observation de la Terre 5 (SPOT-5) orthorectified image tiles covering >80% of the ACP, provided by the Geographic Information Network of Alaska (GINA, gina.alaska.edu). A stratified random sampling of 700 and 300 reference sites in the Arctic peaty lowlands and Arctic sandy lowlands (Jorgenson & Grunblatt, 2013), respectively (Figure 5.2b), were used for the accuracy assessment. At each

of the 1000 sites, we manually generated a reference dataset for geomorphic landforms using high resolution products. This process has been used previously (Lara, et al., 2015), identifying 95.5% agreement between reference sites (e.g. geomorphology) generated from satellite platforms relative to that observed on the ground.

Table 5.2: Accuracy assessment represented as a confusion matrix. Bolded diagonal values within the matrix represent correctly identified pixels, where User and Producer accuracies are presented on the right vertical axis and bottom horizontal axis.

		Reference Sites												User
Geomorphic type		SB	SD	RC	DS	HC	FC	LC	nDTLB	CLC	Pond	River	Lake	CS	accuracy
Sandy Barren	Classification	**12**				2	2			2		1			**63.2%**
Sand Dune		3	**12**			2									**70.6%**
Riparian Corridors				**4**				1							**80.0%**
Drained Slope					**50**	19	4								**68.5%**
High Center					35	**215**	30	22	2						**70.7%**
Flat Center						11	**32**	3							**69.6%**
Low Center				1	6	34	11	**152**	5	7			2		**69.7%**
NonpatternedDTLB						3		16	**53**	1		1	2		**69.7%**
Coalescent Low C								2	2	**15**			2		**71.4%**
Pond											**18**				**100.0%**
River		2							2	2		**10**			**62.5%**
Lake								1	1				**156**		**98.7%**
Coastal Saline Water													1	**28**	**96.6%**
Producer accuracy		70.6%	100.0%	80.0%	54.9%	75.2%	40.5%	77.2%	81.5%	55.6%	100.0%	83.3%	95.7%	100.0%	**1000**
Overall accuracy			**75.7%**												
Cohens Kappa			**0.725**												

Overall map accuracy was 75.7% and Cohens Kappa was 0.725 (Table 5.2), suggesting the strength of agreement between the independent validation (i.e. reference) dataset and classification to be good to very good (Fleiss, Cohen, & Everitt, 1969; Congalton, 1988). Our map had relatively high user and producer accuracies (Table 5.2), with the exception of FC, which had a producer accuracy of 40.5%. This relatively low producer accuracy was expected as we had difficulties identifying unique spectral and structural characteristics of FC that that differed from HC. This identification challenge was highlighted in the accuracy assessment, as 64% of misclassified FC were classified as HC, similar to other tundra geomorphic classifications (Lara, et al., 2015). The relatively low producer accuracies for FC, CLC, and DS are likely associated with the challenge of decomposing a complex continuously evolving geomorphic landscape (Liljedahl, et al., 2016; Jorgenson & Shur, 2007; Billings & Peterson, 1980; Jorgenson, Shur, & Pullman, 2006) such as the Arctic tundra into discrete landform units. Despite these difficulties, our accuracy assessment suggests the tundra geomorphology map well represented the spatial distribution and heterogeneity of tundra landforms. We

present for the first time, a detailed framework for characterizing arctic tundra landforms across the Pan-Arctic.

5.5.2 NDVI Trend Map

We evaluated the potential sensor bias between TM, ETM+, and OLI, used to derive the NDVI Trend Map by comparing the mean value for each pixel, year, and sensor computed from three different locations in northern Alaska (Figure 5.3). Each location was composed of 40,000 pixels (~36 km^2). The three centroids of each location are found in the (1) Arctic sandy lowlands of the ACP (longitude: -154.50, latitude: 70.09), (2) foothills of the Brooks Range on the North Slope (longitude: -159.61, latitude: 66.60), and (3) Selawik lowlands in northwestern Alaska (longitude : -152.92, latitude: 69.29). Minor discrepancies were to be expected between sensor platforms as the images were not acquired at the same time or day.

We identified minor NDVI sensor biases between sensors (Figure 5.3), while sensor specific NDVI distributions were consistent. Most of the data used to generate the NDVI trend map was acquired from the ETM+ sensor, as it was available throughout our data acquisition window (i.e. 1999-2014), whereas data from TM and OLI were only available between 2005-2011 and 2013-2014, respectively. Mean sensor bias estimates for TM and OLI across all subregions of Alaska, indicate NDVI to be slightly under- and overestimated relative to ETM+, though the variability was high within each year and subregion (Figure 5.3). The minor sensor bias identified here, was similar to that identified across North American high latitude terrestrial ecosystems (Ju & Masek, 2016). Although, it is likely that sensors are slightly positively (OLI) and negatively (TM) biased with respect to ETM+ across northern Alaska, sensor calibrations appeared to well represent the tundra subregion on the ACP (Figure 5.3). NDVI values from both TM and OLI sensors clustered above and below the 1 to 1 line for the subregion on the ACP (Figure 5.3), suggesting NDVI data was not positively or negatively skewed between sensors. A slight positive linear NDVI bias (+0.00063) was detected across all sensor data, suggesting a satisfactory agreement between sensors used to compute NDVI on the ACP.

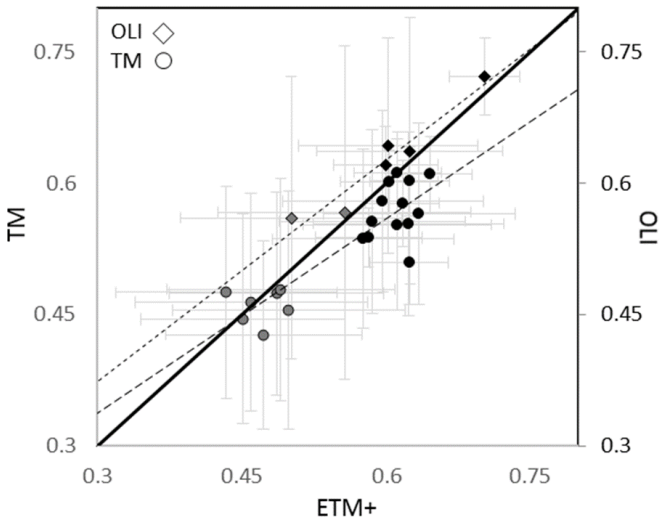

Figure 5.3: Estimate of NDVI bias between Landsat sensors, represented at three subregions of northern Alaska. Each point represents the mean (± standard deviation) of NDVI for a single year and subregion. Circles and diamonds represent TM and OLI plotted against ETM+. Grey points represent means from polygonal tundra within the ACP, while black points represent more southerly sites (i.e. foothills of the Brooks Range and Selawik lowlands). Dashed and dotted lines represent trend lines for TM and ETM+ and OLI and ETM+, respectively. The solid black line indicates a 1:1 line.

5.6 Data Citation

Lara, M. J. *SNAP Data Portal* https://doi.org/10.21429/C9JS8S (2017).

Lara, M. J. *SNAP Data Portal* https://doi.org/10.21429/C9F04D (2017).

6. Discussion/Synthesis

This PhD thesis was aimed to detect and characterize landscape dynamics and particularly rapid disturbances in permafrost landscapes with remote sensing and to determine underlying spatial patterns and causes. In the past these changes were difficult to analyze in their full breadth due their small size, large abundance, and quick dynamics in a very large, sparsely populated, and logistically difficult region. This knowledge gap was primarily caused by scarce data availability, challenging environmental conditions, and limited processing technology. The impact of landscape changes and disturbances on local-to-global scale bio-geo-chemical cycles remained therefore highly uncertain. The synthesis discusses the results of my thesis in the scope of the research questions.

6.1 Landsat-based trend analysis

I developed a highly automated approach for the detection of land surface changes based on Landsat time-series (Chapter 2). One single image can only cover the spatial dimension at one point in time, which may help to characterize the spatial distribution and the status of specific features or land surface properties. Using several images over a longer period adds the temporal dimension to track changes or dynamics, which adds a third dimension in addition to the spatial analysis alone.

6.1.1 Spatial Scale

The trend analysis proved to be a helpful source to identify a large variety of different landscape change processes in the north-east Siberian Lena Delta (Chapter 2). Typical processes of thermokarst lakes, such as expansion or drainage, coastal inundation, or fluvial dynamics were among the detected processes, which can be found in permafrost regions.

As lake drainage is usually a quick (hours to few years) and spatially expansive process (Jones & Arp, 2015; Jones B. M., et al., 2011), images with coarser spatial resolution (e.g. MODIS) may detect that event temporally, but with limited spatial accuracy and higher uncertainty due to the common problem of mixed pixels. Lake expansion in contrast, is a much slower, more continuous, and more localized process. Its detection is dependent on very-high resolution images, which are not always available and in most cases very expensive

to acquire. However, with the inclusion of time-series and the observation of longer time periods, local sub-pixel dynamics (<30m) can be detected as they change over time (see chapters 2 and 3).

Disturbances or landscape features in permafrost regions typically follow exponential distributions with a large quantity of small features and only few large features. However, the bias towards quick and large-footprint processes may persist even in the used high Landsat resolution, which is particularly significant in permafrost environments with many very small features, such as ponds or initial thermokarst (Muster, Heim, Abnizova, & Boike, 2013).

The heterogeneity of Arctic tundra landscapes with a pronounced variation of local scale microtopography, hydrology, biogeochemistry, and vegetation composition plays an important role for lowland tundra ecosystems (Walker D. A., 2000; Villarreal, et al., 2012; Brown, Miller, Tieszen, & Bunnell, 1980). Datasets representing detailed land cover and the influence of geomorphic landforms across the pan-Arctic are limited (Bartsch, Höfler, Kroisleitner, & Trofaier, 2016). The combination of decadal-scale trends of vegetation (Chapter 2) and detailed mapping of local-scale geo-morphological landforms in a representative site in northern Alaska (Lara, et al., 2015) was used to create a comprehensive high-resolution dataset (Chapter 5) to detect recent and to predict future tundra vegetation productivity (appendix). Although a resolution of 30 m is rather detailed in comparison to large scale tundra vegetation analysis e.g. (Walker, et al., 2005; Beck & Goetz, 2011), lowland tundra landscapes are locally highly heterogeneous and local landscape features can be better accounted for with such spatial resolution.

6.1.2 Time series analysis

Using time-series over several years and with a large amount of observations helps to reduce the influence of the intra-seasonal variation of vegetation and hydrology, which could otherwise be masking the long-term trend while using only few images. Finally, using trend analysis with the robust linear Theil-Sen regression method (Theil, 1992; Sen, 1968) on multi-spectral indices, provides the magnitude and direction of surface properties. As most typical landscape change processes have characteristic trajectories of surface properties, it becomes possible to relate them to individual trend signals in conjunction with spatial context. Lake drainage e.g. evolves in different development stages, starting from the lake initiation stage with a dark wet surface, to the drained lake stage with a bare moist intermediately bright

surface of the former lake bottom to the vegetation succession stage with a brighter surface with a spectral signal of greening. This creates typical linear trends in the multi-spectral index response, such as in increase in brightness and greenness as well as a decrease in wetness.

6.1.3 Model complexity

The linear temporal trend model is a very simple time-series model, which captures slow and gradual (e.g. greening), but also rapid high-magnitude processes (e.g. lake drainage, wildfire) in one direction. Simple models, with only few degrees of freedom, are robust against overfitting and therefore better suited for broad and general applications (Hawkins, 2004). This allowed for the spatial transferability of the method, where the ground conditions, image acquisition dates, and data quality may vary, but where the same type of input data is used. The trend analysis, which was tested and developed in the Lena Delta region (Chapter 2) and later transferred to several large regions across the northern high latitude (Chapters 3 to 5) with a total extent of more than 2.3 million km², proved to be a helpful and transferrable methodology for the detection of local to regional scale landscape disturbances and changes.

However, landscape process are often non-linear, therefore more complex models may be more accurate to capture short-term dynamics of landscape processes. Landscape processes are often characterized by more complex dynamics, e.g. cyclic behavior (Kokelj S. V., Lantz, Kanigan, Smith, & Coutts, 2009) or dynamics with several breaks and recovery periods (Kennedy, Yang, & Cohen, 2010). Complex models can be successful for large-scale and specialized analysis, such as global forest change (Hansen, et al., 2013) or water dynamics (Pekel, Cottam, Gorelick, & Belward, 2016), but still tend to be more inaccurate at the edges or extreme data as well as for regions with sparse data of limited quality, such as in the high Arctic. Furthermore, a higher model complexity is much more computationally intensive, which increases processing time, and is associated with a lower level of generalization, which may reduce the spatial transferability and decrease interpretability of results.

6.2 Mapping of permafrost landscape dynamics

Land surface disturbances are an omnipresent feature of permafrost landscapes and they can be an indicator of permafrost degradation. Increasing average and maximum air temperatures in the Arctic are projected to put further pressure on the stability of permafrost. Lake changes,

retrogressive, thaw slumps and fire are some of the most important pulse disturbances in permafrost regions (Grosse, et al., 2011), which can be readily analyzed with remote sensing techniques.

6.2.1 Lake dynamics

I analyzed the distribution and dynamics of lakes over several large regions in Siberia and Alaska with a more local to-regional scale focus in the second research paper (Chapter 3) and a broader spatial scale in our third research paper (Chapter 4). The approach, based on a combination of the previously developed trend analysis (Chapter 2), machine learning and object-based analysis is novel and able to detect individual lakes larger than 1 ha and their changes with subpixel accuracy from 1999 through 2014 (Chapter 3). The focus on statistics of individual lake changes on Landsat-like spatial scale (30m) and large extent (>2.3 million km²) is novel and applied in only few studies (Chapter 4). Global products of dynamic lake extent based on Landsat data have been published recently (Pekel, Cottam, Gorelick, & Belward, 2016; Donchyts, et al., 2016), but they locally have large inaccuracies, e.g. strong bias of wetting, in Arctic environments due to ice and snow cover and other data challenges. There are many local scale analyses in usually lake rich-regions (Jones B. M., et al., 2011; Riordan, Verbyla, & McGuire, 2006; Tarasenko, 2013; Lantz & Turner, 2015; Jones, et al., 2017), which capture local dynamics, but cannot take regional- or continental-scale landscape heterogeneity into account.

Lakes are a highly frequent feature in the northern high latitudes, where they have the highest abundance globally (Lehner & Döll, 2004; Pekel, Cottam, Gorelick, & Belward, 2016). Most of the lakes in permafrost regions are thermokarst lakes that actively degrade surrounding and underlying frozen ground (Grosse, Jones, & Arp, 2013). Within the analyzed regions their spatial distribution follows different patterns, which are dependent on several parameters, such as geology and geomorphology, permafrost extent and ground-ice content or glacial history (Kokelj & Jorgenson, 2013; Olefeldt, et al., 2016). Thermokarst lakes are most abundant in lowlands of sedimentary surface geology, such as coastal plains, river deltas or interior basins, where the land surface is sufficiently flat to develop lakes due to suppressed or absent water runoff. These general patterns became apparent within the lake analysis in this project, where very high lake densities (>20%) were predominantly located in ice-rich lowland permafrost. However, ice-poor sediments, which are less affected by thermokarst (Farquharson, Mann, Grosse, Jones, & Romanovsky, 2016) can still have very high lake

densities (>20%), e.g. in northern Alaska. They may have different underlying processes compared to the typical thermokarst cycle with multiple generations in ice-rich sediments (Jorgenson & Shur, 2007).

Lakes in permafrost have a wide range of dynamics from stagnation to quick growth or rapid drainage. Overall lake area loss outweighed lake area gain with strong spatial heterogeneity (Chapter 4). The magnitude and direction of lake changes and dynamics is dependent on a complex set of cryo-geological, geomorphological, climatic and spatial influencing factors. In discontinuous permafrost and in the transition zone from discontinuous to continuous permafrost frequent and widespread lake drainage has been observed in thermokarst lakes (Chapters 3 and 4). Degradation and destabilization of permafrost has been identified or proposed as a potentially important factor along the margins of continuous permafrost (Riordan, Verbyla, & McGuire, 2006; Jones B. M., et al., 2011; Smith L. C., Sheng, MacDonald, & Hinzman, 2005). Vertical connectivity to groundwater due to talik penetration (Yoshikawa & Hinzman, 2003) as well as lateral exchange following lake shore erosion, breaching, and overflow due to near-surface permafrost degradation (Jones B. M., et al., 2011) or tapping by rivers (Hinkel, et al., 2007), are among the most likely scenarios, which would explain the accelerated lake area loss (Grosse, Jones, & Arp, 2013). Within this transition zone, lake expansion occurs simultaneously with drainage in Alaska, whereas the transition zone in western Siberia (southern Yamal Peninsula) is only affected by drainage without significant lake expansion (Chapter 4). The difference in expansion rates indicates diverse underlying mechanisms of lake area loss in different regions, which could be a great scientific topic to target in further, local scale studies.

I found that other regions have a large diversity from net growth (e.g. Central Yakutia, Kobuk Delta or northern Kolyma Lowland) to loss (Northern Seward Peninsula, Yukon Flats, Yamal peninsula, northern Quebec). The spatial pattern is very diverse and does not follow simple relationships that could be linked to one single environmental factor. The studies in this thesis showed very localized regional dynamics, which related to geological and geomorphological heterogeneity. The strongest changes were recorded in Central Yakutia, within very ice-rich yedoma ice-complex sediments, where lake area expanded by nearly 50% (Chapter 3) within a very short period, from 2006 to 2008 caused by strong precipitation events and local agricultural practices (Boike, et al., 2016; Ulrich, et al., 2017). In contrast, large net lake area

loss occurred in several clusters on the Yamal Peninsula in western Siberia, also in ice-rich sediments.

Ground ice is generally claimed as an important driver of thermokarst initiation and lake dynamics (Grosse, Jones, & Arp, 2013; Olefeldt, et al., 2016). Lake change analysis results and the correlation to ground-ice distribution maps (Chapter 4) could not generally back up this proposed effect on a pan-arctic scale. However, local-scale analysis (Chapter 3), where the spatial diversity of large scale patterns (e.g. climate) are minimized and more accurate auxiliary site-specific datasets are available, revealed intensified lake dynamics in ice-rich sediments. With the spatial expansion of the analysis, more large-scale environmental factors (e.g. climate) potentially come into effect in addition to local-scale influencing factors.

6.2.2 Wildfire

Wildfires are caused by the availability of dry climatic conditions, sufficient fuel/biomass, and ignition mechanisms (Johnson E. A., 1996; Veraverbeke, et al., 2017). These conditions prevail in highly continental climates in eastern-central Siberia (8.15%) and a wide swath from interior Alaska (8.89%) to north-western Canada. More humid conditions, as in boreal western Siberia and eastern Canada, suppressed wildfires, where they affected a smaller area (2.43%; 5.06%) (Chapter 4). Most of the fires are limited to forested regions of the boreal zone, where many studies on wildfire have focused their efforts (Kasischke & Turetsky, 2006; Stocks, et al., 1998; Yoshikawa, Bolton, Romanovsky, Fukuda, & Hinzman, 2002).

Due to the decreased amounts of dry biomass and less favorable climatic conditions tundra wildfires occurred very rarely and were restricted to Alaska. With the trend analysis and machine learning classification several tundra fires were detected affecting a total area of 4600 km² (out of 732,000 km^2 of tundra in the analyzed study area) (Chapter 4) including the Kougarok fire in western Alaska (Liljedahl A. , Hinzman, Busey, & Yoshikawa, 2007) and the severe Anaktuvuk fire in northern Alaska (Jones B. M., et al., 2015). With current technology tundra fires can be detected and monitored, e.g. with coarse resolution MODIS fire products (Giglio, Csiszar, & Justice, 2006), but past fire events may not have been recognized properly even in official fire databases (Jones, et al., 2013), which leaves a high uncertainty in estimates of tundra fire abundances. The multi-spectral trend analysis developed in this thesis (Chapter 2) allows detecting old burn scars from before the actual observation period, due to the trajectory of vegetation succession and the potential occurrence of thermokarst. However,

due to the changing climate the frequency and intensity of tundra fires is predicted to increase (Hu, et al., 2015) and the method developed here could be used to monitor and quantify these developments.

The influence of fire on permafrost is dependent on fire extent, burn intensity and local permafrost and ground conditions (Liljedahl A. , Hinzman, Busey, & Yoshikawa, 2007). With current monitoring techniques, fire extent in can be quantified with sufficient accuracy. Burn intensity in contrast is not sufficiently monitored over large spatial scales, which leaves large uncertainties about the consequences of wildfire on the ground thermal regime and subsurface carbon stocks and fluxes in permafrost.

6.2.3 Retrogressive Thaw Slumps

The occurrence of retrogressive thaw slumps (RTS) is bound to a narrow margin of environmental conditions. They are primarily limited to regions with very ice-rich permafrost conditions, topographic gradients and sufficiently cold conditions in the past to preserve the ground-ice (Chapter 4) (Kokelj S. V., Lantz, Tunnicliffe, Segal, & Lacelle, 2017). Ground ice in these regions may have different origins, including buried glacial ice or syngenetic ice wedge ice. In large regions along the margins of the former Laurentide ice sheet in northern and north-western Canada large amounts of massive buried glacial ice remains in the ground and is prone to melting upon disturbance (Kokelj S. V., Lantz, Tunnicliffe, Segal, & Lacelle, 2017).

The spatial analyses over several large regions from this thesis support prior findings (Kokelj S. V., Lantz, Tunnicliffe, Segal, & Lacelle, 2017) that RTS are generally located in ice-rich conditions and sloped terrain, where disturbances of the ground thermal regime may cause the ground ice to degrade or collapse. RTS typically occur in clusters, where favorable conditions for their initiation occur. These clusters, some more, some less extensively studied, were found in the vicinity of formerly glaciated mountain ranges, e.g. the northern Alaska Brooks Range (Balser, Jones, & Gens, 2014), or the Verkhoyansk mountain range in eastern Siberia, along former ice-sheet margins in northwestern Canada, e.g. Herschel Island and the Yukon Coast (Lantuit, et al., 2012; Obu, et al., 2017) or in very ice-rich yedoma ice-complex deposits in the Lena delta region (Lantuit, et al., 2011) and northern Alaska. The occurrence of a single RTS in a region, such as the large Selawik slump in western Alaska, is rare and an outlier from the typical clustered pattern.

The relation of RTS clusters to former glacial ice margins has great potential for applying this method for the reconstruction of past ice sheet and glacier extents in northern Siberia and northern Canada. Several clusters of RTS I identified in the vicinity of the Verkhoyansk mountain range (Chapter 4) are an indicator of former glaciations extent for a region where such information is very sparse so far and datasets of LGM extent (Ehlers & Gibbard, 2003) are potentially inaccurate.

Retrogressive thaw slumps and other thermo-erosion features such as active layer detachment slides or thermo-erosion gullies usually cover small spatial footprints ranging from few m² up to nearly one km² (Balser, Jones, & Gens, 2014; Kokelj S. V., Lantz, Tunnicliffe, Segal, & Lacelle, 2017; Murton, et al., 2017). The majority of small features have an aerial extent below the detection limit of Landsat data, but larger features are observable. RTS-abundant regions can be outlined based on the developed analysis methods within the framework of this PhD thesis (Chapter 4). Analysis with high-resolution imagery and field work could provide detailed information and monitoring capabilities on appropriate spatial scales. As RTS are three-dimensional landscape features, high-resolution digital elevation models (DEM) derived from space-borne, air-borne or field-based instruments (LiDAR, RADAR, Stereo photogrammetry), will provide improved understanding and quantification of RTS on bio-geochemical cycles.

6.3 Pan-arctic scale distribution and consequences of changes in permafrost

The key disturbances in permafrost landscapes affect different regions and spatial extent as they are bound to specific climatic, geomorphological, and permafrost conditions. The local impact of disturbances is often inversely related to its spatial extent.

Retrogressive thaw slumps (RTS) and related mass wasting processes can have a massive influence on the local environment and bio-geochemical cycles. However, the spatial extent of single RTS and accompanied clusters cover very small total areas (5.4 km²) compared to lake changes or fire, and particularly compared to the full extent of the permafrost region. However, their narrow range of conditions, where they could occur (Chapter 4), makes them a significant disturbance in regions of high abundance (Kokelj, et al., 2015; Balser, Jones, & Gens, 2014).

The impact of individual lake changes is locally not as severe as RTS and often less expansive. Due to the sheer quantity of several million lakes and ponds (Muster, et al., 2017; Paltan, Dash, & Edwards, 2015) and their widespread distribution, their individual impact adds up to a potentially large impact on for example the carbon cycle. Lake change is an important process in the scope of carbon emissions where expanding lakes are a likely source of GHG emissions (Walter, Zimov, Chanton, Verbyla, & Chapin, 2006), whereas draining lakes are considered potential GHG sinks (Walter Anthony, et al., 2014). In contrast, wildfires in boreal regions are frequent and affect large areas, but their local impact on permafrost varies strongly. The impact of wildfires on permafrost stability is largely dependent on burn severity, and below ground permafrost conditions.

The gained knowledge about areas of morphological and ecological changes in permafrost regions, based on novel trend analysis of Landsat time-series, has the potential to bridge the gap between local high-resolution information and coarse scale regional models of permafrost change and consequently carbon fluxes. On the one hand, local high-resolution and field studies can be better targeted based on spatially and temporally detailed knowledge of landscape processes. On the other hand, regional to global scale permafrost and climate models may in the future benefit from the spatially and temporally detailed knowledge about permafrost landscape dynamics and improved process quantification for enhanced model parametrization and validation.

6.4 Outlook

The recent and ongoing technological advance with the continuing paradigm shift from local computer-based to cloud-based processing is a great opportunity to automatically process and analyze a huge amount of data. These technologies can help to examine an unprecedented amount of rapidly growing remote sensing data archives to retrieve information, in highly improved spatial and particularly temporal detail over very large regions. These new techniques and data sources provide approaches to better understand the response of permafrost to a changing climate:

1) Detection of change events

The knowledge about short term fluctuations and the particular timing of disturbances is not well monitored yet. Several processes, such as lake initiation, lake drainage or retrogressive thaw slumps have shown a cyclic behavior, but the available data records are still very sparse. Enhancing information about trend details and event identification would be an important step to understand the triggers and key factors of non-linear thermokarst processes.

2) Spatial upscaling

The analyses in this thesis covered a very large spatial extent of over 2 million km². However, the permafrost region covers an area about 10 times larger and an upscaling from the currently processed transects to the pan-arctic scale would allow the full understanding of permafrost-related landscape processes and better estimations of carbon budgets. The synergistic use of the presented methodologies and state-of-the art computing facilities would allow to process a pan-arctic scale analysis.

3) Near-real-time monitoring

Past permafrost landscape changes from 1999 to 2014 were analyzed within this thesis. This period covers only a portion of the available satellite record, but the permafrost landscape is currently and will be changing constantly. Recently launched constellations of similar sensors, e.g. Landsat-8 and Sentinel-2 or Planet, further decrease satellite revisit times and shift focus to near-real time monitoring and up-to-date information of the Earth's surface processes. Adaptation of the presented methods to additional sensors as well as integration of different sensors would significantly enhance the information content for longer observation periods and increase monitoring detail. In addition, near-real time processing would allow enhanced field work planning for expeditions.

Bibliography

Abbott, B. W., Jones, J. B., Schuur, E. A., Chapin III, F. S., Bowden, W. B., Bret-Harte, M. S., . . . others. (2016). Biomass offsets little or none of permafrost carbon release from soils, streams, and wildfire: an expert assessment. *Environmental Research Letters, 11*, 034014.

ACIA. (2005). *Arctic climate impact assessment report.* Cambridge, UK: Cambridge University Press.

Andresen, C. G., & Lougheed, V. L. (2015). Disappearing Arctic tundra ponds: Fine-scale analysis of surface hydrology in drained thaw lake basins over a 65 year period (1948--2013). *Journal of Geophysical Research: Biogeosciences, 120*, 466-479.

Are, F., & Reimnitz, E. (2000). An overview of the Lena River Delta setting: geology, tectonics, geomorphology, and hydrology. *Journal of Coastal Research*, 1083-1093.

Arp, C. D., Jones, B. M., Grosse, G., Bondurant, A. C., Romanovsky, V. E., Hinkel, K. M., & Parsekian, A. D. (2016). Threshold sensitivity of shallow Arctic lakes and sublake permafrost to changing winter climate. *Geophysical Research Letters, 43*, 6358-6365.

Arp, C. D., Jones, B. M., Schmutz, J. A., Urban, F. E., & Jorgenson, M. T. (2010). Two mechanisms of aquatic and terrestrial habitat change along an Alaskan Arctic coastline. *Polar biology, 33*, 1629-1640.

Arp, C. D., Jones, B. M., Urban, F. E., & Grosse, G. (2011). Hydrogeomorphic processes of thermokarst lakes with grounded-ice and floating-ice regimes on the Arctic coastal plain, Alaska. *Hydrological Processes, 25*, 2422-2438.

Baig, M. H., Zhang, L., Shuai, T., & Tong, Q. (2014). Derivation of a tasselled cap transformation based on Landsat 8 at-satellite reflectance. *Remote Sensing Letters, 5*, 423-431.

Balser, A. W., Jones, J. B., & Gens, R. (2014). Timing of retrogressive thaw slump initiation in the Noatak Basin, northwest Alaska, USA. *Journal of Geophysical Research: Earth Surface, 119*, 1106-1120.

Barrett, B., Nitze, I., Green, S., & Cawkwell, F. (2014). Assessment of multi-temporal, multi-sensor radar and ancillary spatial data for grasslands monitoring in Ireland using machine learning approaches. *Remote Sensing of Environment, 152*, 109-124.

Bartsch, A., Höfler, A., Kroisleitner, C., & Trofaier, A. M. (2016). Land Cover Mapping in Northern High Latitude Permafrost Regions with Satellite Data: Achievements and Remaining Challenges. *Remote Sensing, 8*, 979.

Batzli, G. O., Pitelka, F. A., & Cameron, G. N. (1983). Habitat use by lemmings near Barrow, Alaska. *Ecography, 6*, 255-262.

Beck, I., Ludwig, R., Bernier, M., Lévesque, E., & Boike, J. (2015). Assessing Permafrost Degradation and Land Cover Changes (1986–2009) using Remote Sensing Data over Umiujaq, Sub-Arctic Québec. *Permafrost and Periglacial Processes*, n/a--n/a. doi:10.1002/ppp.1839

Beck, P. S., & Goetz, S. J. (2011). Satellite observations of high northern latitude vegetation productivity changes between 1982 and 2008: ecological variability and regional differences. *Environmental Research Letters, 6*, 045501.

Belgiu, M., & Dragut, L. (2016). Random forest in remote sensing: A review of applications and future directions. *ISPRS Journal of Photogrammetry and Remote Sensing, 114*, 24-31.

Bhatt, U. S., Walker, D. A., Raynolds, M. K., Bieniek, P. A., Epstein, H. E., Comiso, J. C., . . . Polyakov, I. V. (2013). Recent declines in warming and vegetation greening trends over pan-Arctic tundra. *Remote Sensing, 5*, 4229-4254.

Bhatt, U. S., Walker, D. A., Raynolds, M. K., Comiso, J. C., Epstein, H. E., Jia, G., . . . others. (2010). Circumpolar Arctic tundra vegetation change is linked to sea ice decline. *Earth Interactions, 14*, 1-20.

Bhatt, U. S., Walker, D. A., Walsh, J. E., Carmack, E. C., Frey, K. E., Meier, W. N., . . . others. (2014). Implications of Arctic sea ice decline for the Earth system. *Annual Review of Environment and Resources, 39*, 57-89.

Biasi, C., Wanek, W., Rusalimova, O., Kaiser, C., Meyer, H., Barsukov, P., & Richter, A. (2005). Microtopography and plant-cover controls on nitrogen dynamics in hummock tundra ecosystems in Siberia. *Arctic, Antarctic, and Alpine Research, 37*, 435-443.

Bieniek, P. A., Bhatt, U. S., Walker, D. A., Raynolds, M. K., Comiso, J. C., Epstein, H. E., . . . others. (2015). Climate drivers linked to changing seasonality of Alaska coastal tundra vegetation productivity. *Earth Interactions, 19*, 1-29.

Billings, W. D., & Peterson, K. M. (1980). Vegetational change and ice-wedge polygons through the thaw-lake cycle in Arctic Alaska. *Arctic and Alpine Research*, 413-432.

Bockheim, J. G., & Hinkel, K. M. (2012). Accumulation of excess ground ice in an age sequence of drained thermokarst lake basins, arctic Alaska. *Permafrost and Periglacial Processes, 23*, 231-236.

Bockheim, J. G., Everett, L. R., Hinkel, K. M., Nelson, F. E., & Brown, J. (1999). Soil organic carbon storage and distribution in arctic tundra, Barrow, Alaska. *Soil Science Society of America Journal, 63*, 934-940.

Bockheim, J. G., Hinkel, K. M., Eisner, W. R., & Dai, X. Y. (2004). Carbon pools and accumulation rates in an age-series of soils in drained thaw-lake basins, Arctic Alaska. *Soil Science Society of America Journal, 68*, 697-704.

Boike, J., Grau, T., Heim, B., Günther, F., Langer, M., Muster, S., . . . Lange, S. (2016). Satellite-derived changes in the permafrost landscape of central Yakutia, 2000–2011: Wetting, drying, and fires . *Global and Planetary Change , 139*, 116-127. doi:http://dx.doi.org/10.1016/j.gloplacha.2016.01.001

Boike, J., Kattenstroth, B., Abramova, K., Bornemann, N., Chetverova, A., Fedorova, I., . . . others. (2013). Baseline characteristics of climate, permafrost and land cover from a new permafrost observatory in the Lena River Delta, Siberia (1998-2011). *Biogeosciences, 10*, 2105-2128.

Boike, J., Wille, C., & Abnizova, A. (2008). Climatology and summer energy and water balance of polygonal tundra in the Lena River Delta, Siberia. *Journal of Geophysical Research: Biogeosciences, 113*, n/a--n/a. doi:10.1029/2007JG000540

Bokhorst, S. F., Bjerke, J. W., Tommervik, H., Callaghan, T. V., & Phoenix, G. K. (2009). Winter warming events damage sub-Arctic vegetation: Consistent evidence from an experimental manipulation and a natural event. *Journal of Ecology, 97*, 1408-1415.

Bokhorst, S., Bjerke, J. W., Street, L. E., Callaghan, T. V., & Phoenix, G. K. (2011). Impacts of multiple extreme winter warming events on sub-Arctic heathland: phenology, reproduction, growth, and CO2 flux responses. *Global Change Biology, 17*, 2817-2830.

Bokhorst, S., Tommervik, H., Callaghan, T. V., Phoenix, G. K., & Bjerke, J. W. (2012). Vegetation recovery following extreme winter warming events in the sub-Arctic estimated using NDVI

from remote sensing and handheld passive proximal sensors. *Environmental and Experimental Botany, 81*, 18-25.

Breiman. (2001). Random Forests. *Machine Learning*, 5-32.

Briggs, M. A., Walvoord, M. A., McKenzie, J. M., Voss, C. I., Day-Lewis, F. D., & Lane, J. W. (2014). New permafrost is forming around shrinking Arctic lakes, but will it last? *Geophysical Research Letters, 41*, 1585-1592. doi:10.1002/2014GL059251

Brooker, A., Fraser, R. H., Olthof, I., Kokelj, S. V., & Lacelle, D. (2014). Mapping the activity and evolution of retrogressive thaw slumps by tasselled cap trend analysis of a Landsat satellite image stack. *Permafrost and Periglacial Processes*.

Brown, J., Ferrians Jr, O. J., Heginbottom, J. A., & Melnikov, E. S. (1997). *Circum-Arctic map of permafrost and ground-ice conditions.*

Brown, J., Miller, P. C., Tieszen, L. L., & Bunnell, F. (1980). *An arctic ecosystem: the coastal tundra at Barrow, Alaska.* Dowden, Hutchinson & Ross, Inc.

Burn, C. R. (1998). The response (1958-1997) of permafrost and near-surface ground temperatures to forest fire, Takhini River valley, southern Yukon Territory. *Canadian Journal of Earth Sciences, 35*, 184-199.

Burn, C. R., & Kokelj, S. V. (2009). The environment and permafrost of the Mackenzie Delta area. *Permafrost and Periglacial Processes, 20*, 83-105.

Cable, W. L., Romanovsky, V. E., & Jorgenson, M. T. (2016). Scaling-up permafrost thermal measurements in western Alaska using an ecotype approach. *The Cryosphere, 10*, 2517.

Carroll, M. L., & Loboda, T. V. (2017). Multi-Decadal Surface Water Dynamics in North American Tundra. *Remote Sensing, 9*, 497.

Carroll, M. L., Townshend, J. R., DiMiceli, C. M., Loboda, T., & Sohlberg, R. A. (2011). Shrinking lakes of the Arctic: Spatial relationships and trajectory of change. *Geophysical Research Letters, 38*, n/a--n/a. doi:10.1029/2011GL049427

Chambers, M., White, D., Busey, R., Hinzman, L., Alessa, L., & Kliskey, A. (2007). Potential impacts of a changing Arctic on community water sources on the Seward Peninsula, Alaska. *Journal of Geophysical Research: Biogeosciences, 112*.

Chavez, P. S. (1996). Image-based atmospheric corrections-revisited and improved. *Photogrammetric engineering and remote sensing, 62*, 1025-1035.

Chen, M., Rowland, J. C., Wilson, C. J., Altmann, G. L., & Brumby, S. P. (2013). The importance of natural variability in lake areas on the detection of permafrost degradation: A case study in the Yukon Flats, Alaska. *Permafrost and Periglacial Processes, 24*, 224-240.

Conard, S. G., & Ivanova, G. A. (1997). Wildfire in Russian boreal forests—Potential impacts of fire regime characteristics on emissions and global carbon balance estimates. *Environmental Pollution, 98*, 305-313.

Congalton, R. G. (1988). A comparison of sampling schemes used in generating error matrices for assessing the accuracy of maps generated from remotely sensed data. *Photogrammetric engineering and remote sensing (USA)*.

Crate, S., Ulrich, M., Habeck, J. O., Desyatkin, A. R., Desyatkin, R. V., Fedorov, A. N., . . . Takakura, H. (2017). Permafrost livelihoods: A transdisciplinary review and analysis of thermokarst-based systems of indigenous land use. *Anthropocene, 18*, 89-104. doi:https://doi.org/10.1016/j.ancene.2017.06.001

Crist, E. P. (1985). A TM tasseled cap equivalent transformation for reflectance factor data. *Remote Sensing of Environment, 17*, 301-306.

de Jong, R., Bruin, S., Wit, A., Schaepman, M. E., & Dent, D. L. (2011). Analysis of monotonic greening and browning trends from global NDVI time-series. *Remote Sensing of Environment, 115*, 692-702.

Desyatkin, R. (2008). *Soil Formation in Thermokarst Depression—Alases of Cryolithozone.* Novosibirsk, Russia: Nauka.

Donchyts, G., Baart, F., Winsemius, H., Gorelick, N., Kwadijk, J., & Giesen, N. (2016). Earth's surface water change over the past 30 years. *Nature Climate Change, 6*, 810-813.

Edwards, M., Grosse, G., Jones, B. M., & McDowell, P. (2016). The evolution of a thermokarst-lake landscape: Late Quaternary permafrost degradation and stabilization in interior Alaska. *Sedimentary Geology*, -. doi:http://dx.doi.org/10.1016/j.sedgeo.2016.01.018

Ehlers, J., & Gibbard, P. L. (2003). Extent and chronology of glaciations. *Quaternary Science Reviews, 22*, 1561-1568.

Elith, J., Leathwick, J. R., & Hastie, T. (2008). A working guide to boosted regression trees. *Journal of Animal Ecology, 77*, 802-813.

Elmendorf, S. C., Henry, G. H., Hollister, R. D., Bj{\"o}rk, R. G., Bjorkman, A. D., Callaghan, T. V., . . . others. (2012). Global assessment of experimental climate warming on tundra vegetation: heterogeneity over space and time. *Ecology Letters, 15*, 164-175.

Elsakov, V., & Marushchak, I. (2011). The inter-Year changes of thermokarst lakes on North -East part of European Russia (in Russian). *Issledovanie Zemli iz Kosmosa (the study of the Earth from space)*.

Emmerton, C. A., St Louis, V. L., Humphreys, E. R., Gamon, J. A., Barker, J. D., & Pastorello, G. Z. (2016). Net ecosystem exchange of CO2 with rapidly changing high Arctic landscapes. *Global change biology, 22*, 1185-1200.

Engstrom, R., Hope, A., Kwon, H., Stow, D., & Zamolodchikov, D. (2005). Spatial distribution of near surface soil moisture and its relationship to microtopography in the Alaskan Arctic coastal plain. *Hydrology Research, 36*, 219-234.

Epstein, H. E., Raynolds, M. K., Walker, D. A., Bhatt, U. S., Tucker, C. J., & Pinzon, J. E. (2012). Dynamics of aboveground phytomass of the circumpolar Arctic tundra during the past three decades. *Environmental Research Letters, 7*, 015506.

Ericson, J. P., Vörösmarty, C. J., Dingman, S. L., Ward, L. G., & Meybeck, M. (2006). Effective sea-level rise and deltas: Causes of change and human dimension implications. *Global and Planetary Change , 50*, 63-82. doi:http://dx.doi.org/10.1016/j.gloplacha.2005.07.004

Ershov, E. (1989). *Geocryology of the USSR; East Siberia and Far East.* Moscow, Russia.

Farquharson, L. M., Mann, D. H., Grosse, G., Jones, B. M., & Romanovsky, V. E. (2016). Spatial distribution of thermokarst terrain in Arctic Alaska. *Geomorphology, 273*, 116-133. doi:http://dx.doi.org/10.1016/j.geomorph.2016.08.007

Fedorov, A. N., Ivanova, R. N., Park, H., Hiyama, T., & Iijima, Y. (2014). Recent air temperature changes in the permafrost landscapes of northeastern Eurasia. *Polar Science, 8*, 114-128.

Fedorova, I., Chetverova, A., Bolshiyanov, D., Makarov, A., Boike, J., Heim, B., . . . others. (2015). Lena Delta hydrology and geochemistry: long-term hydrological data and recent field observations. *Biogeosciences, 12*, 345-363.

Fensholt, R., & Proud, S. R. (2012). Evaluation of earth observation based global long term vegetation trends—Comparing GIMMS and MODIS global NDVI time series. *Remote sensing of Environment, 119*, 131-147.

Fernandes, R., & Leblanc, S. (2005). Parametric (modified least squares) and non-parametric (Theil--Sen) linear regressions for predicting biophysical parameters in the presence of measurement errors. *Remote Sensing of Environment, 95*, 303-316.

Fleiss, J. L., Cohen, J., & Everitt, B. S. (1969). Large sample standard errors of kappa and weighted kappa. *Psychological Bulletin, 72*, 323.

Forbes, B. C., Fauria, M., & Zetterberg, P. (2010). Russian Arctic warming and 'greening'are closely tracked by tundra shrub willows. *Global Change Biology, 16*, 1542-1554.

Fraser, R. H., Olthof, I., Kokelj, S. V., Lantz, T. C., Lacelle, D., Brooker, A., . . . Schwarz, S. (2014). Detecting Landscape Changes in High Latitude Environments Using Landsat Trend Analysis: 1. Visualization. *Remote Sensing, 6*, 11533-11557.

Fraser, R., Olthof, I., Carrière, M., Deschamps, A., & Pouliot, D. (2012). A method for trend-based change analysis in Arctic tundra using the 25-year Landsat archive. *Polar Record, 48*, 83-93.

Friedl, M. A., McIver, D. K., Hodges, J. C., Zhang, X. Y., Muchoney, D., Strahler, A. H., . . . others. (2002). Global land cover mapping from MODIS: algorithms and early results. *Remote Sensing of Environment, 83*, 287-302.

Frost, G. V., Epstein, H. E., & Walker, D. A. (2014). Regional and landscape-scale variability of Landsat-observed vegetation dynamics in northwest Siberian tundra. *Environmental Research Letters, 9*, 025004.

Gao, B.-C. (1996). NDWI—A normalized difference water index for remote sensing of vegetation liquid water from space. *Remote sensing of environment, 58*, 257-266.

GCOS. (2010). *Implementation plan for the global observing system for climate in support of the UNFCCC (2010 update). GCOS Rep. 138, 186 pp.*

Giglio, L., Csiszar, I., & Justice, C. O. (2006). Global distribution and seasonality of active fires as observed with the Terra and Aqua Moderate Resolution Imaging Spectroradiometer (MODIS) sensors. *Journal of geophysical research: Biogeosciences, 111*.

Goetz, S. J., Bunn, A. G., Fiske, G. J., & Houghton, R. A. (2005). Satellite-observed photosynthetic trends across boreal North America associated with climate and fire disturbance. *Proceedings of the National Academy of Sciences of the United States of America, 102*, 13521-13525.

Goetz, S. J., Epstein, H. E., Bhatt, U. S., Jia, G. J., Kaplan, J. O., Lischke, H., . . . others. (2011). Recent changes in arctic vegetation: satellite observations and simulation model predictions. In *Eurasian Arctic land cover and land use in a changing climate* (pp. 9-36). Springer.

Goward, S., Arvidson, T., Williams, D., Faundeen, J., Irons, J., & Franks, S. (2006). Historical Record of Landsat Global Coverage. *Photogrammetric Engineering \& Remote Sensing, 72*, 1155-1169.

Grigoryev, M. N. (1993). Cryomorphogenesis of the Lena Delta mouth area. *Permafrost Institute, Academy of Science USSR, Siberian Department, Yakutsk*, 1-176.

Grosse, G., Harden, J., Turetsky, M., McGuire, A. D., Camill, P., Tarnocai, C., . . . others. (2011). Vulnerability of high-latitude soil organic carbon in North America to disturbance. *Journal of Geophysical Research: Biogeosciences, 116*.

Grosse, G., Jones, B., & Arp, C. (2013). Thermokarst lakes, drainage, and drained basins.

Günther, F., Overduin, P. P., Sandakov, A. V., Grosse, G., & Grigoriev, M. N. (2013). Short-and long-term thermo-erosion of ice-rich permafrost coasts in the Laptev Sea region. *Biogeosciences, 10*, 4297-4318.

Hansen, M. C., DeFries, R. S., Townshend, J. R., & Sohlberg, R. (2000). Global land cover classification at 1 km spatial resolution using a classification tree approach. *International journal of remote sensing, 21*, 1331-1364.

Hansen, M. C., Potapov, P. V., Moore, R., Hancher, M., Turubanova, S. A., Tyukavina, A., . . . others. (2013). High-resolution global maps of 21st-century forest cover change. *science, 342*, 850-853.

Hawkins, D. (2004). The problem of overfitting. *Journal of chemical information and computer sciences*, 1-12.

Hinkel, K. M., Jones, B. M., Eisner, W. R., Cuomo, C. J., Beck, R. A., & Frohn, R. (2007). Methods to assess natural and anthropogenic thaw lake drainage on the western Arctic coastal plain of northern Alaska. *Journal of Geophysical Research: Earth Surface, 112*.

Hinkel, K. M., Sheng, Y., Lenters, J. D., Lyons, E. A., Beck, R. A., Eisner, W. R., & Wang, J. (2012). Thermokarst Lakes on the Arctic Coastal Plain of Alaska: Geomorphic Controls on Bathymetry. *Permafrost and Periglacial Processes, 23*, 218-230. doi:10.1002/ppp.1744

Hu, F. S., Higuera, P. E., Duffy, P., Chipman, M. L., Rocha, A. V., Young, A. M., . . . Dietze, M. C. (2015). Arctic tundra fires: natural variability and responses to climate change. *Frontiers in Ecology and the Environment, 13*, 369-377.

Huang, C., Wylie, B., Yang, L., Homer, C., & Zylstra, G. (2002). Derivation of a tasselled cap transformation based on Landsat 7 at-satellite reflectance. *International Journal of Remote Sensing, 23*, 1741-1748. doi:10.1080/01431160110106113

Hubberten, H.-W., Wagner, D., Pfeiffer, E.-M., Boike, J., & Gukov, A. Y. (2006). The Russian-German research station Samoylov, Lena Delta-A key site for polar research in the Siberian Arctic. *Polarforschung, 73*, 111-116.

Hugelius, G., Strauss, J., Zubrzycki, S., Harden, J. W., Schuur, E. A., Ping, C.-L., . . . Kuhry, P. (2014). Estimated stocks of circumpolar permafrost carbon with quantified uncertainty ranges and identified data gaps. *Biogeosciences, 11*, 6573-6593. doi:10.5194/bg-11-6573-2014

Huscroft, C. A., Lipovsky, P. S., & Bond, J. D. (2004). *A regional characterization of landslides in the Alaska Highway corridor, Yukon.* Yukon Geological Survey.

Iijima, Y., Fedorov, A. N., Park, H., Suzuki, K., Yabuki, H., Maximov, T. C., & Ohata, T. (2010). Abrupt increases in soil temperatures following increased precipitation in a permafrost region, central Lena River basin, Russia. *Permafrost and Periglacial Processes, 21*, 30-41.

IPCC. (2013). *Climate Change 2013: The Physical Science Basis. Contribution of Working Group I to the Fifth Assessment Report of the Intergovernmental Panel on Climate Change.* Cambridge, United Kingdom and New York, USA: Cambridge University Press.

Ivanov, M. S. (1984). Cryogenic structure of Quaternary deposits of the Lena-Aldan-Depression. Nauka, Novosibirsk.

Jafarov, E. E., Romanovsky, V. E., Genet, H., McGuire, A. D., & Marchenko, S. S. (2013). The effects of fire on the thermal stability of permafrost in lowland and upland black spruce forests of interior Alaska in a changing climate. *Environmental Research Letters, 8*, 035030.

Jamali, S., Jönsson, P., Eklundh, L., Ardö, J., & Seaquist, J. (2015). Detecting changes in vegetation trends using time series segmentation. *Remote Sensing of Environment, 156*, 182-195. doi:http://dx.doi.org/10.1016/j.rse.2014.09.010

Jepsen, S. M., Voss, C. I., Walvoord, M. A., Minsley, B. J., & Rover, J. (2013). Linkages between lake shrinkage/expansion and sublacustrine permafrost distribution determined from remote sensing of interior Alaska, USA. *Geophysical Research Letters, 40*, 882-887.

Jia, G. J., Epstein, H. E., & Walker, D. A. (2003). Greening of arctic Alaska, 1981--2001. *Geophysical Research Letters, 30*.

Johnson, E. A. (1996). *Fire and vegetation dynamics: studies from the North American boreal forest.* Cambridge University Press.

Johnson, K. D., Harden, J., McGuire, A. D., Bliss, N. B., Bockheim, J. G., Clark, M., . . . others. (2011). Soil carbon distribution in Alaska in relation to soil-forming factors. *Geoderma, 167*, 71-84.

Jones, B. M., & Arp, C. D. (2015). Observing a catastrophic thermokarst lake drainage in northern Alaska. *Permafrost and Periglacial Processes, 26*, 119-128.

Jones, B. M., Arp, C. D., Hinkel, K. M., Beck, R. A., Schmutz, J. A., & Winston, B. (2009). Arctic lake physical processes and regimes with implications for winter water availability and management in the National Petroleum Reserve Alaska. *Environmental Management, 43*, 1071-1084.

Jones, B. M., Arp, C. D., Whitman, M. S., Nigro, D., Nitze, I., Beaver, J., . . . others. (2017). A lake-centric geospatial database to guide research and inform management decisions in an Arctic watershed in northern Alaska experiencing climate and land-use changes. *Ambio*, 1-18.

Jones, B. M., Baughman, C. A., Romanovsky, V. E., Parsekian, A. D., Babcock, E. L., Stephani, E., . . . Berg, E. E. (2016). Presence of rapidly degrading permafrost plateaus in south-central Alaska. *The Cryosphere, 10*, 2673-2692. doi:10.5194/tc-10-2673-2016

Jones, B. M., Breen, A. L., Gaglioti, B. V., Mann, D. H., Rocha, A. V., Grosse, G., . . . Walker, D. A. (2013). Identification of unrecognized tundra fire events on the north slope of Alaska. *Journal of Geophysical Research: Biogeosciences, 118*, 1334-1344. doi:10.1002/jgrg.20113

Jones, B. M., Grosse, G., Arp, C. D., Jones, M. C., Walter Anthony, K. M., & Romanovsky, V. E. (2011). Modern thermokarst lake dynamics in the continuous permafrost zone, northern Seward Peninsula, Alaska. *Journal of Geophysical Research: Biogeosciences, 116*, n/a--n/a. doi:10.1029/2011JG001666

Jones, B. M., Grosse, G., Arp, C. D., Miller, E., Liu, L., Hayes, D. J., & Larsen, C. F. (2015). Recent Arctic tundra fire initiates widespread thermokarst development. *Scientific reports, 5*.

Jones, M. C., Grosse, G., Jones, B. M., & Walter Anthony, K. (2012). Peat accumulation in drained thermokarst lake basins in continuous, ice-rich permafrost, northern Seward Peninsula, Alaska. *Journal of Geophysical Research: Biogeosciences, 117*.

Jorgenson, M. T., & Grosse, G. (2016). Remote sensing of landscape change in permafrost regions. *Permafrost and Periglacial Processes, 27*, 324-338.

Jorgenson, M. T., & Grunblatt, J. (2013). Landscape-level ecological map-ping of northern Alaska and field site photography, Report prepared for the Arctic Landscape Conservation Cooperative.

Jorgenson, M. T., & Heiner, M. (2003). Ecosystems of Northern Alaska. 1: 2.5 million-scale map. *ABR Inc., Fairbanks, AK and The Nature Conservancy, Anchorage, AK*.

Jorgenson, M. T., & Osterkamp, T. E. (2005). Response of boreal ecosystems to varying modes of permafrost degradation. *Canadian Journal of Forest Research, 35*, 2100-2111.

Jorgenson, M. T., & Shur, Y. (2007). Evolution of lakes and basins in northern Alaska and discussion of the thaw lake cycle. *Journal of Geophysical Research: Earth Surface, 112*, n/a--n/a. doi:10.1029/2006JF000531

Jorgenson, M. T., Racine, C. H., Walters, J. C., & Osterkamp, T. E. (2001). Permafrost degradation and ecological changes associated with a warmingclimate in central Alaska. *Climatic change, 48*, 551-579.

Jorgenson, M. T., Romanovsky, V., Harden, J., Shur, Y., O'Donnell, J., Schuur, E. A., . . . Marchenko, S. (2010). Resilience and vulnerability of permafrost to climate change. *Canadian Journal of Forest Research, 40*, 1219-1236.

Jorgenson, M. T., Roth, J. E., Miller, P. F., Macander, M. J., Duffy, M. S., Pullman, E. R., . . . Talbot, S. (2009). An ecological land survey and landcover map of the Selawik National Wildlife Refuge. *Kotzebue, AK*.

Jorgenson, M. T., Shur, Y. L., & Pullman, E. R. (2006). Abrupt increase in permafrost degradation in Arctic Alaska. *Geophysical Research Letters, 33*.

Jorgenson, M. T., Yoshikawa, K., Kanevskiy, M., Shur, Y., Romanovsky, V., Marchenko, S., . . . Jones, B. (2008). Permafrost characteristics of Alaska. *Proceedings of the Ninth International Conference on Permafrost*, *29*, pp. 121-122.

Ju, J., & Masek, J. G. (2016). The vegetation greenness trend in Canada and {US} Alaska from 1984–2012 Landsat data. *Remote Sensing of Environment, 176*, 1-16. doi:http://dx.doi.org/10.1016/j.rse.2016.01.001

Kanevskiy, M., Shur, Y., Jorgenson, M. T., Ping, C.-L., Michaelson, G. J., Fortier, D., . . . Tumskoy, V. (2013). Ground ice in the upper permafrost of the Beaufort Sea coast of Alaska. *Cold Regions Science and Technology, 85*, 56-70.

Kaplina, T. (1981). History of permafrost in Northern Yakutia (in Russian). In *History of the Development of Perennial Frozen* (pp. 153-181). Noskow, Russia: Nauka.

Karlsson, J. M., Lyon, S. W., & Destouni, G. (2014). Temporal Behavior of Lake Size-Distribution in a Thawing Permafrost Landscape in Northwestern Siberia. *Remote Sensing, 6*, 621-636. doi:10.3390/rs6010621

Kasischke, E. S., & Turetsky, M. R. (2006). Recent changes in the fire regime across the North American boreal region—spatial and temporal patterns of burning across Canada and Alaska. *Geophysical research letters, 33*.

Kennedy, R. E., Cohen, W. B., & Schroeder, T. A. (2007). Trajectory-based change detection for automated characterization of forest disturbance dynamics. *Remote Sensing of Environment, 110*, 370-386. doi:http://dx.doi.org/10.1016/j.rse.2007.03.010

Kennedy, R. E., Yang, Z., & Cohen, W. B. (2010). Detecting trends in forest disturbance and recovery using yearly Landsat time series: 1. LandTrendr—Temporal segmentation algorithms. *Remote Sensing of Environment, 114*, 2897-2910.

Kokelj, S. V., & Jorgenson, M. T. (2013). Advances in thermokarst research. *Permafrost and Periglacial Processes, 24*, 108-119.

Kokelj, S. V., Lantz, T. C., Kanigan, J., Smith, S. L., & Coutts, R. (2009). Origin and polycyclic behaviour of tundra thaw slumps, Mackenzie Delta region, Northwest Territories, Canada. *Permafrost and Periglacial Processes, 20*, 173-184. doi:10.1002/ppp.642

Kokelj, S. V., Lantz, T. C., Tunnicliffe, J., Segal, R., & Lacelle, D. (2017). Climate-driven thaw of permafrost preserved glacial landscapes, northwestern Canada. *Geology*, G38626--1.

Kokelj, S. V., Tunnicliffe, J., Lacelle, D., Lantz, T. C., Chin, K. S., & Fraser, R. (2015). Increased precipitation drives mega slump development and destabilization of ice-rich permafrost terrain, northwestern Canada. *Global and Planetary Change, 129*, 56-68. doi:http://dx.doi.org/10.1016/j.gloplacha.2015.02.008

Koven, C. D., Ringeval, B., Friedlingstein, P., Ciais, P., Cadule, P., Khvorostyanov, D., . . . Tarnocai, C. (2011). Permafrost carbon-climate feedbacks accelerate global warming. *Proceedings of the National Academy of Sciences, 108*, 14769-14774.

Koven, C. D., Schuur, E. A., Schädel, C., Bohn, T. J., Burke, E. J., Chen, G., . . . others. (2015). A simplified, data-constrained approach to estimate the permafrost carbon--climate feedback. *Phil. Trans. R. Soc. A, 373*, 20140423.

Kravtsova, V. I., & Bystrova, A. G. (2009). Changes in thermokarst lake sizes in different regions of Russia for the last 30 years. *Kriosfera Zemli (Earth Cryosphere), 13*, 16-26.

Kravtsova, V. I., & Tarasenko, T. V. (2011). The Dynamics of thermokarst lakes under climate change since 1950. *Central Yakutia Kriosfera Zemli, 15*, 31-42.

Kutzbach, L., Wagner, D., & Pfeiffer, E.-M. (2004). Effect of microrelief and vegetation on methane emission from wet polygonal tundra, Lena Delta, Northern Siberia. *Biogeochemistry, 69*, 341-362.

Labrecque, S., Lacelle, D., Duguay, C. R., Lauriol, B., & Hawkings, J. (2009). Contemporary (1951-2001) evolution of lakes in the Old Crow Basin, Northern Yukon, Canada: Remote sensing, numerical modeling, and stable isotope analysis. *Arctic*, 225-238.

Langer, M., Westermann, S., Boike, J., Kirillin, G., Grosse, G., Peng, S., . . . others. (2016). Rapid degradation of permafrost underneath waterbodies in tundra landscapes-towards a representation of thermokarst in land surface models. *Journal of Geophysical Research: Earth Surface*.

Lantuit, H., Atkinson, D., Overduin, P. P., Grigoriev, M., Rachold, V., Grosse, G., & Hubberten, H.-W. (2011). Coastal erosion dynamics on the permafrost-dominated Bykovsky Peninsula, north Siberia, 1951-2006. *Polar Research, 30*.

Lantuit, H., Pollard, W. H., Couture, N., Fritz, M., Schirrmeister, L., Meyer, H., & Hubberten, H.-W. (2012). Modern and late Holocene retrogressive thaw slump activity on the Yukon coastal plain and Herschel Island, Yukon Territory, Canada. *Permafrost and Periglacial Processes, 23*, 39-51.

Lantz, T. C., & Turner, K. W. (2015). Changes in lake area in response to thermokarst processes and climate in Old Crow Flats, Yukon. *Journal of Geophysical Research: Biogeosciences, 120*, 513-524.

Lara, M. J., Johnson, D. R., Andresen, C., Hollister, R. D., & Tweedie, C. E. (2017). Peak season carbon exchange shifts from a sink to a source following 50+ years of herbivore exclusion in an Arctic tundra ecosystem. *Journal of Ecology, 105*, 122-131.

Lara, M. J., McGuire, A. D., Euskirchen, E. S., Tweedie, C. E., Hinkel, K. M., Skurikhin, A. N., . . . Genet, H. (2015). Polygonal tundra geomorphological change in response to warming alters future CO2 and CH4 flux on the Barrow Peninsula. *Global change biology, 21*, 1634-1651.

Lara, M. J., Nitze, I., Grosse, G., & McGuire, A. (in revision). Reduced arctic tundra productivity linked with landform and climate change interactions. *Nature Scientific Reports*.

Lara, M. J., Nitze, I., Grosse, G., & McGuire, A. (in revision). Tundra landform and vegetation productivity trend maps for the Arctic Coastal Plain of northern Alaska. *Nature Scientific Data*.

Lara, M. J., Villarreal, S., Johnson, D. R., Hollister, R. D., Webber, P. J., & Tweedie, C. E. (2012). Estimated change in tundra ecosystem function near Barrow, Alaska between 1972 and 2010. *Environmental Research Letters, 7*, 015507.

Larsen, A. S., O'Donnell, J. A., Schmidt, J. H., Kristenson, H. J., & Swanson, D. K. (2017). Physical and chemical characteristics of lakes across heterogeneous landscapes in arctic and subarctic Alaska. *Journal of Geophysical Research: Biogeosciences*.

Lawrence, D. M., Slater, A. G., & Swenson, S. C. (2012). Simulation of present-day and future permafrost and seasonally frozen ground conditions in CCSM4. *Journal of Climate, 25*, 2207-2225.

Lawrence, D. M., Slater, A. G., Tomas, R. A., Holland, M. M., & Deser, C. (2008). Accelerated Arctic land warming and permafrost degradation during rapid sea ice loss. *Geophysical Research Letters, 35*.

Lehner, B., & Döll, P. (2004). Development and validation of a global database of lakes, reservoirs and wetlands. *Journal of Hydrology, 296*, 1-22.

Lenton, T. M. (2012). Arctic climate tipping points. *Ambio, 41*, 10-22.

Lenz, J., Jones, B. M., Wetterich, S., Tjallingii, R., Fritz, M., Arp, C. D., . . . Grosse, G. (2016). Impacts of shore expansion and catchment characteristics on lacustrine thermokarst records in permafrost lowlands, Alaska Arctic Coastal Plain. *arktos, 2*, 25. doi:10.1007/s41063-016-0025-0

Liang, S. (2001). Narrowband to broadband conversions of land surface albedo I: Algorithms. *Remote sensing of environment, 76*, 213-238.

Liljedahl, A. K., Boike, J., Daanen, R. P., Fedorov, A. N., Frost, G. V., Grosse, G., . . . others. (2016). Pan-Arctic ice-wedge degradation in warming permafrost and its influence on tundra hydrology. *Nature Geoscience*.

Liljedahl, A. K., Hinzman, L. D., & Schulla, J. (2012). Ice-wedge polygon type controls low-gradient watershed-scale hydrology. *Proceedings of the Tenth International Conference on Permafrost*, *1*, pp. 231-236.

Liljedahl, A., Hinzman, L., Busey, R., & Yoshikawa, K. (2007). Physical short-term changes after a tussock tundra fire, Seward Peninsula, Alaska. *Journal of Geophysical Research: Earth Surface, 112*, n/a--n/a. doi:10.1029/2006JF000554

Lindgren, P., Grosse, G., Romanovsky, V., & Farquharson, L. (2016). Landsat-based lake distribution and changes in western Alaska permafrost regions between 1972 and 2014. *International Conference on Permafrost.* Potsdam, Germany.

Lipson, D. A., Zona, D., Raab, T. K., Bozzolo, F., Mauritz, M., & Oechel, W. C. (2012). Water-table height and microtopography control biogeochemical cycling in an Arctic coastal tundra ecosystem. *Biogeosciences, 9*, 577.

Los, S. O. (2013). Analysis of trends in fused AVHRR and MODIS NDVI data for 1982--2006: Indication for a CO2 fertilization effect in global vegetation. *Global Biogeochemical Cycles, 27*, 318-330.

Lougheed, V. L., Butler, M. G., McEwen, D. C., & Hobbie, J. E. (2011). Changes in tundra pond limnology: Re-sampling Alaskan ponds after 40 years. *AMBIO: A Journal of the Human Environment, 40*, 589-599.

Macander, M. J., Swingley, C. S., Joly, K., & Raynolds, M. K. (2015). Landsat-based snow persistence map for northwest Alaska. *Remote Sensing of Environment , 163*, 23-31. doi:http://dx.doi.org/10.1016/j.rse.2015.02.028

Marino, E. (2012). The long history of environmental migration: Assessing vulnerability construction and obstacles to successful relocation in Shishmaref, Alaska. *Global environmental change, 22*, 374-381.

Markham, B. L., & Helder, D. L. (2012). Forty-year calibrated record of earth-reflected radiance from Landsat: A review . *Remote Sensing of Environment , 122*, 30-40. doi:http://dx.doi.org/10.1016/j.rse.2011.06.026

Markus, T., Stroeve, J. C., & Miller, J. (2009). Recent changes in Arctic sea ice melt onset, freezeup, and melt season length. *Journal of Geophysical Research: Oceans, 114*, n/a--n/a. doi:10.1029/2009JC005436

Montanaro, M., Gerace, A., Lunsford, A., & Reuter, D. (2014). Stray light artifacts in imagery from the Landsat 8 Thermal Infrared Sensor. *Remote Sensing, 6*, 10435-10456.

Morgenstern, A., Grosse, G., & Schirrmeister, L. (2008). Genetic, morphological, and statistical characterization of lakes in the permafrost-dominated Lena Delta. *Proceedings of the Ninth International Conference on Permafrost.*, (pp. 1239-1244).

Morgenstern, A., Grosse, G., Günther, F., Fedorova, I., & Schirrmeister, L. (2011). Spatial analyses of thermokarst lakes and basins in Yedoma landscapes of the Lena Delta. *The Cryosphere, 5*, 849-867. doi:10.5194/tc-5-849-2011

Morton, D. C., Masek, J. G., Wang, D., Sexton, J. O., Nagol, J. R., Ropars, P., . . . others. (2012). Satellite-based evidence for shrub and graminoid tundra expansion in northern Quebec from 1986 to 2010. *Global Change Biology, 18*, 2313-2323.

Murton, J. B., Edwards, M. E., Lozhkin, A. V., Anderson, P. M., Savvinov, G. N., Bakulina, N., . . . others. (2017). Preliminary paleoenvironmental analysis of permafrost deposits at Batagaika megaslump, Yana Uplands, northeast Siberia. *Quaternary Research, 87*, 314-330.

Muster, S., Heim, B., Abnizova, A., & Boike, J. (2013). Water Body Distributions Across Scales: A Remote Sensing Based Comparison of Three Arctic Tundra Wetlands. *Remote Sensing, 5*, 1498-1523. doi:10.3390/rs5041498

Muster, S., Langer, M., Heim, B., Westermann, S., & Boike, J. (2012). Subpixel heterogeneity of ice-wedge polygonal tundra: a multi-scale analysis of land cover and evapotranspiration in the Lena River Delta, Siberia. *Tellus B, 64*.

Muster, S., Roth, K., Langer, M., Lange, S., Aleina, F. C., Bartsch, A., . . . others. (2017). PeRL: a circum-Arctic Permafrost Region Pond and Lake database. *Earth System Science Data, 9*, 317.

Myers-Smith, I. H., Forbes, B. C., Wilmking, M., Hallinger, M., Lantz, T., Blok, D., . . . others. (2011). Shrub expansion in tundra ecosystems: dynamics, impacts and research priorities. *Environmental Research Letters, 6*, 045509.

Necsoiu, M., Dinwiddie, C. L., Walter, G. R., Larsen, A., & Stothoff, S. A. (2013). Multi-temporal image analysis of historical aerial photographs and recent satellite imagery reveals evolution of water body surface area and polygonal terrain morphology in Kobuk Valley National Park, Alaska. *Environmental Research Letters, 8*, 025007.

Nelson, F. E., Anisimov, O. A., & Shiklomanov, N. I. (2001). Subsidence risk from thawing permafrost. *Nature, 410*, 889.

Newman, B. D., Throckmorton, H. M., Graham, D. E., Gu, B., Hubbard, S. S., Liang, L., . . . others. (2015). Microtopographic and depth controls on active layer chemistry in Arctic polygonal ground. *Geophysical Research Letters, 42*, 1808-1817.

Nicolsky, D. J., Romanovsky, V. E., Panda, S. K., Marchenko, S. S., & Muskett, R. R. (2017). Applicability of the ecosystem type approach to model permafrost dynamics across the Alaska North Slope. *Journal of Geophysical Research: Earth Surface, 122*, 50-75. doi:10.1002/2016JF003852

Nitze, I., & Grosse, G. (2016). Detection of landscape dynamics in the Arctic Lena Delta with temporally dense Landsat time-series stacks. *Remote Sensing of Environment, 181*, 27-41.

Nitze, I., Barrett, B., & Cawkwell, F. (2015). Temporal optimisation of image acquisition for land cover classification with Random Forest and MODIS time-series. *International Journal of Applied Earth Observation and Geoinformation, 34*, 136-146.

Nitze, I., Grosse, G., Jones, B. M., Arp, C. D., Ulrich, M., Fedorov, A., & Veremeeva, A. (2017). Landsat-Based Trend Analysis of Lake Dynamics across Northern Permafrost Regions. *Remote Sensing, 9*, 640.

Nitze, I., Grosse, G., Jones, B., Arp, C., Ulrich, M., Fedorov, A., & Veremeeva, A. (2017). Landsat-based trend analysis of lake dynamics across northern permafrost regions, supplementary material. PANGAEA.

Nitze, I., Schulthess, U., & Asche, H. (2012). Comparison of machine learning algorithms random forest, artificial neural network and support vector machine to maximum likelihood for supervised crop type classification. *Proc. of the 4th GEOBIA*, 7-9.

NOAA. (2017, May 2). *Climate Data Online: 1981–2010 Normals.* Retrieved from https://www.ncdc.noaa.gov/cdo-web/datatools/normals

Obu, J., Lantuit, H., Grosse, G., Günther, F., Sachs, T., Helm, V., & Fritz, M. (2017). Coastal erosion and mass wasting along the Canadian Beaufort Sea based on annual airborne LiDAR elevation data. *Geomorphology, 293*, 331-346.

Olefeldt, D., Goswami, S., Grosse, G., Hayes, D., Hugelius, G., Kuhry, P., . . . others. (2016). Circumpolar distribution and carbon storage of thermokarst landscapes. *Nature communications, 7*.

Olivas, P. C., Oberbauer, S. F., Tweedie, C., Oechel, W. C., Lin, D., & Kuchy, A. (2011). Effects of fine-scale topography on CO2 flux components of Alaskan Coastal Plain tundra: response to contrasting growing seasons. *Arctic, Antarctic, and Alpine Research, 43*, 256-266.

Olofsson, J., Tommervik, H., & Callaghan, T. V. (2012). Vole and lemming activity observed from space. *Nature Climate Change, 2*, 880-883.

Olthof, I., & Fraser, R. H. (2014). Detecting Landscape Changes in High Latitude Environments Using Landsat Trend Analysis: 2. Classification. *Remote Sensing, 6*, 11558-11578.

Olthof, I., Fraser, R. H., & Schmitt, C. (2015). Landsat-based mapping of thermokarst lake dynamics on the Tuktoyaktuk Coastal Plain, Northwest Territories, Canada since 1985. *Remote Sensing of Environment, 168*, 194-204. doi:http://dx.doi.org/10.1016/j.rse.2015.07.001

Paltan, H., Dash, J., & Edwards, M. (2015). A refined mapping of Arctic lakes using Landsat imagery. *International Journal of Remote Sensing, 36*, 5970-5982.

Pattison, R. R., Jorgenson, J. C., Raynolds, M. K., & Welker, J. M. (2015). Trends in NDVI and Tundra Community Composition in the Arctic of NE Alaska Between 1984 and 2009. *Ecosystems, 18*, 707-719. doi:10.1007/s10021-015-9858-9

Pekel, J.-F., Cottam, A., Gorelick, N., & Belward, A. S. (2016). High-resolution mapping of global surface water and its long-term changes. *Nature*.

Pflugmacher, D., Cohen, W. B., & Kennedy, R. E. (2012). Using Landsat-derived disturbance history (1972--2010) to predict current forest structure. *Remote Sensing of Environment, 122*, 146-165.

Phoenix, G. K., & Bjerke, J. W. (2016). Arctic browning: extreme events and trends reversing arctic greening. *Global change biology, 22*, 2960-2962.

Plug, L. J., Walls, C., & Scott, B. M. (2008). Tundra lake changes from 1978 to 2001 on the Tuktoyaktuk Peninsula, western Canadian Arctic. *Geophysical Research Letters, 35*, n/a--n/a. doi:10.1029/2007GL032303

Post, E., Bhatt, U. S., Bitz, C. M., Brodie, J. F., Fulton, T. L., Hebblewhite, M., . . . Walker, D. A. (2013). Ecological consequences of sea-ice decline. *Science, 341*, 519-524.

Raynolds, M. K., & Walker, D. A. (2016). Increased wetness confounds Landsat-derived NDVI trends in the central Alaska North Slope region, 1985--2011. *Environmental Research Letters, 11*, 085004.

Raynolds, M. K., Comiso, J. C., Walker, D. A., & Verbyla, D. (2008). Relationship between satellite-derived land surface temperatures, arctic vegetation types, and {NDVI}. *Remote Sensing of Environment , 112*, 1884-1894. doi:http://dx.doi.org/10.1016/j.rse.2007.09.008

Raynolds, M. K., Walker, D. A., Ambrosius, K. J., Brown, J., Everett, K. R., Kanevskiy, M., . . . Webber, P. J. (2014). Cumulative geoecological effects of 62 years of infrastructure and

climate change in ice-rich permafrost landscapes, Prudhoe Bay Oilfield, Alaska. *Global Change Biology, 20*, 1211-1224. doi:10.1111/gcb.12500

Raynolds, M. K., Walker, D. A., Verbyla, D., & Munger, C. A. (2013). Patterns of change within a tundra landscape: 22-year Landsat NDVI trends in an area of the northern foothills of the Brooks Range, Alaska. *Arctic, antarctic, and alpine research, 45*, 249-260.

Reyes, F. R., & Lougheed, V. L. (2015). Rapid nutrient release from permafrost thaw in arctic aquatic ecosystems. *Arctic, Antarctic, and Alpine Research, 47*, 35-48.

Rhew, R. C., Teh, Y. A., & Abel, T. (2007). Methyl halide and methane fluxes in the northern Alaskan coastal tundra. *Journal of Geophysical Research: Biogeosciences, 112*.

Riordan, B., Verbyla, D., & McGuire, A. D. (2006). Shrinking ponds in subarctic Alaska based on 1950--2002 remotely sensed images. *Journal of Geophysical Research: Biogeosciences (2005--2012), 111*.

Roach, J. K., Griffith, B., & Verbyla, D. (2013). Landscape influences on climate-related lake shrinkage at high latitudes. *Global Change Biology, 19*, 2276-2284. doi:10.1111/gcb.12196

Romanovsky, V. E., Smith, S., Shiklomanov, N. I., Streletskiy, D., Isaksen, K., Kholodov, A., . . . Marchenko, S. (2017). Terrestrial Permafrost. In J. Blunden, & D. Arndt, *State of the Climate* (pp. 147-149). Bull. Amer. Meteor. Soc.

Rosenau, R., Scheinert, M., & Dietrich, R. (2015). A processing system to monitor Greenland outlet glacier velocity variations at decadal and seasonal time scales utilizing the Landsat imagery. *Remote Sensing of Environment, 169*, 1-19.

Rouse Jr, J., Haas, R. H., Schell, J. A., & Deering, D. W. (1974). Monitoring vegetation systems in the Great Plains with ERTS.

Rover, J., Ji, L., Wylie, B. K., & Tieszen, L. L. (2012). Establishing water body areal extent trends in interior Alaska from multi-temporal Landsat data. *Remote Sensing Letters, 3*, 595-604. doi:10.1080/01431161.2011.643507

Sachs, T., Giebels, M., Boike, J., & Kutzbach, L. (2010). Environmental controls on CH4 emission from polygonal tundra on the microsite scale in the Lena river delta, Siberia. *Global Change Biology, 16*, 3096-3110.

Sannel, A. B., & Brown, I. A. (2010). High-resolution remote sensing identification of thermokarst lake dynamics in a subarctic peat plateau complex. *Canadian Journal of Remote Sensing, 36*, S26--S40.

Santoro, M., & Strozzi, T. (2012). Circumpolar digital elevation models> 55 N with links to geotiff images.

Schaefer, K., Lantuit, H., Romanovsky, V. E., Schuur, E. A., & Witt, R. (2014). The impact of the permafrost carbon feedback on global climate. *Environmental Research Letters, 9*, 085003.

Schirrmeister, L., Froese, D., Tumskoy, V., Grosse, G., & Wetterich, S. (2013). Yedoma: Late Pleistocene ice-rich syngenetic permafrost of Beringia. In *Encyclopedia of Quaternary Science. 2nd edition* (pp. 542-552). Elsevier.

Schirrmeister, L., Grosse, G., Schwamborn, G., Andreev, A. A., Meyer, H., Kunitsky, V. V., . . . others. (2003). Late Quaternary history of the accumulation plain north of the Chekanovsky Ridge (Lena Delta, Russia): a multidisciplinary approach. *Polar Geography, 27*, 277-319.

Schirrmeister, L., Grosse, G., Wetterich, S., Overduin, P. P., Strauss, J., Schuur, E. A., & Hubberten, H.-W. (2011). Fossil organic matter characteristics in permafrost deposits of the northeast Siberian Arctic. *Journal of Geophysical Research: Biogeosciences, 116*.

Schneider von Deimling, T., Grosse, G., Strauss, J., Schirrmeister, L., Morgenstern, A., Schaphoff, S., . . . Boike, J. (2015). Observation-based modelling of permafrost carbon fluxes with accounting for deep carbon deposits and thermokarst activity. *Biogeosciences, 12*, 3469-3488.

Schneider, J., Grosse, G., & Wagner, D. (2009). Land cover classification of tundra environments in the Arctic Lena Delta based on Landsat 7 ETM+ data and its application for upscaling of methane emissions. *Remote Sensing of Environment, 113*, 380-391.

Schuur, E. A., Bockheim, J., Canadell, J. G., Euskirchen, E., Field, C. B., Goryachkin, S. V., . . . others. (2008). Vulnerability of permafrost carbon to climate change: Implications for the global carbon cycle. *AIBS Bulletin, 58*, 701-714.

Schuur, E. A., McGuire, A. D., Schädel, C., Grosse, G., Harden, J. W., Hayes, D. J., . . . others. (2015). Climate change and the permafrost carbon feedback. *Nature, 520*, 171-179.

Schwamborn, G., Rachold, V., & Grigoriev, M. N. (2002). Late Quaternary sedimentation history of the Lena Delta. *Quaternary International, 89*, 119-134. doi:http://dx.doi.org/10.1016/S1040-6182(01)00084-2

Sellman, P. V., Brown, J., Lewellen, R. I., McKim, H., & Merry, C. (1975). The classification and geomor-phic implications of thaw lakes of the arctic coastal plain, Alaska. *Hanover (NI-l): US Army Cold Regions Research and Engineering Laboratory*.

Sellmann, P. V., & Brown, J. (1973). Stratigraphy and diagenesis of perennially frozen sediments in the Barrow, Alaska, region. *Permafrost: North American Contribution to the Second International Conference. Washington, DC: National Academy of Sciences*, (pp. 171-181).

Sen, P. K. (1968). Estimates of the regression coefficient based on Kendall's tau. *Journal of the American Statistical Association, 63*, 1379-1389.

Serreze, M. C., & Barry, R. G. (2011). Processes and impacts of Arctic amplification: A research synthesis. *Global and Planetary Change, 77*, 85-96.

Shmelev, D., Veremeeva, A., Kraev, G., Kholodov, A., Spencer, R. G., Walker, W. S., & Rivkina, E. (2017). Estimation and Sensitivity of Carbon Storage in Permafrost of North-Eastern Yakutia. *Permafrost and Periglacial Processes*.

Shur, Y. L., & Jorgenson, M. T. (2007). Patterns of permafrost formation and degradation in relation to climate and ecosystems. *Permafrost and Periglacial Processes, 18*, 7-19.

Smith, L. C., Sheng, Y., & MacDonald, G. M. (2007). A first pan-Arctic assessment of the influence of glaciation, permafrost, topography and peatlands on northern hemisphere lake distribution. *Permafrost and Periglacial Processes, 18*, 201-208.

Smith, L. C., Sheng, Y., MacDonald, G. M., & Hinzman, L. D. (2005). Disappearing arctic lakes. *Science, 308*, 1429-1429.

SNAP. (2017). Scenarios Network for Alaska and Arctic Planning. University of Alaska.

Solomon, S. M. (2005). Spatial and temporal variability of shoreline change in the Beaufort-Mackenzie region, Northwest Territories, Canada. *Geo-Marine Letters, 25*, 127-137.

Soloviev, P. (1959). *Cryolithozone of the Northern Part of the Leno-Amga Interfluve.* Moscow: Publishing House of the USSR Academy of Sciences.

Spector, V. (1980). Quaternary Deposits of the Coastal Lowland (Khallerchin Tundra). In *The Cenozoic of East Yakutia* (pp. 87-97). Yakutsk, USSR: Yakut Branch of the Siberian Department of the USSR Academy of Sciences:.

Stocks, B. J., Fosberg, M. A., Lynham, T. J., Mearns, L., Wotton, B. M., Yang, Q., . . . McKENNEY, D. W. (1998, 1 01). Climate Change and Forest Fire Potential in Russian and Canadian Boreal Forests. *Climatic Change, 38*, 1-13. doi:10.1023/A:1005306001055

Stow, D. A., Hope, A., McGuire, D., Verbyla, D., Gamon, J., Huemmrich, F., . . . Myneni, R. (2004). Remote sensing of vegetation and land-cover change in Arctic Tundra Ecosystems. *Remote Sensing of Environment, 89*, 281-308. doi:http://dx.doi.org/10.1016/j.rse.2003.10.018

Strauss, J., Schirrmeister, L., Grosse, G., Wetterich, S., Ulrich, M., Herzschuh, U., & Hubberten, H.-W. (2013). The deep permafrost carbon pool of the Yedoma region in Siberia and Alaska. *Geophysical Research Letters, 40*, 6165-6170.

Streletskiy, D., Biskaborn, B., Noetzli, J., Lanckman, J.-P., Romanovsky, V. E., Schoeneich, P., . . . Zhao, L. (2017). Permafrost Thermal State. In J. Blunden, & D. Arndt, *State of the Climate* (pp. 19-21). Bull. Amer. Meteor. Soc.

Tarasenko, T. V. (2013). Interannual variations in the areas of thermokarst lakes in Central Yakutia. *Water Resources, 40*, 111-119.

Terenzi, J., Jorgenson, M. T., Ely, C. R., & Giguère, N. (2014). Storm-surge flooding on the Yukon-Kuskokwim Delta, Alaska. *Arctic*, 360-374.

Theil, H. (1992). A rank-invariant method of linear and polynomial regression analysis. In *Henri Theil's Contributions to Economics and Econometrics* (pp. 345-381). Springer.

Throckmorton, H. M., Newman, B. D., Heikoop, J. M., Perkins, G. B., Feng, X., Graham, D. E., . . . others. (2016). Active layer hydrology in an arctic tundra ecosystem: quantifying water sources and cycling using water stable isotopes. *Hydrological Processes, 30*, 4972-4986.

Ulrich, M., Grosse, G., Chabrillat, S., & Schirrmeister, L. (2009). Spectral characterization of periglacial surfaces and geomorphological units in the Arctic Lena Delta using field spectrometry and remote sensing. *Remote Sensing of Environment, 113*, 1220-1235.

Ulrich, M., Matthes, H., Schirrmeister, L., Schütze, J., Park, H., Iijima, Y., & Fedorov, A. N. (2017). Differences in behavior and distribution of permafrost-related lakes in Central Yakutia and

their response to climatic drivers. *Water Resources Research*, n/a--n/a. doi:10.1002/2016WR019267

Urban, M., Forkel, M., Eberle, J., Hüttich, C., Schmullius, C., & Herold, M. (2014). Pan-Arctic Climate and Land Cover Trends Derived from Multi-Variate and Multi-Scale Analyses (1981–2012). *Remote Sensing, 6*, 2296-2316. doi:10.3390/rs6032296

USGS. (2006). Alaska Watershed and Stream Hydrography Enhanced Dataset Project, Alaska Watersheds - 5th Level, compiled by the Conservation Biology Institute.

Van Everdingen, R. (2005). Multi-language glossary of permafrost and related ground-ice terms. Retrieved from http://nsidc. org/fgdc/glossary

Veraverbeke, S., Rogers, B. M., Goulden, M. L., Jandt, R. R., Miller, C. E., Wiggins, E. B., & Randerson, J. T. (2017). Lightning as a major driver of recent large fire years in North American boreal forests. *Nature Climate Change, 7*, 529-534.

Verbesselt, J., Hyndman, R., Newnham, G., & Culvenor, D. (2010). Detecting trend and seasonal changes in satellite image time series. *Remote sensing of Environment, 114*, 106-115.

Verbyla, D. (2008). The greening and browning of Alaska based on 1982--2003 satellite data. *Global Ecology and Biogeography, 17*, 547-555.

Veremeeva, A. A., & Glushkova, N. V. (2016). Formation of relief in the regions of Ice complex deposits distribution: remote sensing and GIS studies in the Kolyma lowland tundra. *Earth's Cryosphere XX*, 14-24.

Veremeeva, A., & Gubin, S. (2009). Modern tundra landscapes of the Kolyma Lowland and their evolution in the Holocene. *Permafrost and Periglacial Processes, 20*, 399-406.

Villarreal, S., Hollister, R. D., Johnson, D. R., Lara, M. J., Webber, P. J., & Tweedie, C. E. (2012). Tundra vegetation change near Barrow, Alaska (1972--2010). *Environmental Research Letters, 7*, 015508.

Wainwright, H. M., Dafflon, B., Smith, L. J., Hahn, M. S., Curtis, J. B., Wu, Y., . . . Hubbard, S. S. (2015). Identifying multiscale zonation and assessing the relative importance of polygon geomorphology on carbon fluxes in an Arctic tundra ecosystem. *Journal of Geophysical Research: Biogeosciences, 120*, 788-808.

Walker, D. A. (2000). Hierarchical subdivision of Arctic tundra based on vegetation response to climate, parent material and topography. *Global change biology, 6*, 19-34.

Walker, D. A., Raynolds, M. K., Daniels, F. J., Einarsson, E., Elvebakk, A., Gould, W. A., . . . others. (2005). The circumpolar Arctic vegetation map. *Journal of Vegetation Science, 16*, 267-282.

Walker, H. J. (1998). Arctic deltas. *Journal of Coastal Research*, 719-738.

Walsh, J. E., Chapman, W. L., Romanovsky, V., Christensen, J. H., & Stendel, M. (2008). Global climate model performance over Alaska and Greenland. *Journal of Climate, 21*, 6156-6174.

Walter Anthony, K. M., Anthony, P., Grosse, G., & Chanton, J. (2012). Geologic methane seeps along boundaries of Arctic permafrost thaw and melting glaciers. *Nature Geoscience, 5*, 419-426.

Walter Anthony, K. M., Zimov, S. A., Grosse, G., Jones, M. C., Anthony, P. M., Chapin III, F. S., . . . others. (2014). A shift of thermokarst lakes from carbon sources to sinks during the Holocene epoch. *Nature, 511*, 452-456.

Walter Anthony, K., Daanen, R., Anthony, P., Deimling, T. S., Ping, C.-L., Chanton, J. P., & Grosse, G. (2016). Methane emissions proportional to permafrost carbon thawed in Arctic lakes since the 1950s. *Nature Geoscience*.

Walter, K. M., Zimov, S. A., Chanton, J. P., Verbyla, D., & Chapin, F. S. (2006). Methane bubbling from Siberian thaw lakes as a positive feedback to climate warming. *Nature, 443*, 71-75.

Westermann, S., Duguay, C. R., Grosse, G., & Kääb, A. (2015). Remote sensing of permafrost and frozen ground. In *Remote Sensing of the Cryosphere* (pp. 307-344). John Wiley & Sons, Ltd. doi:10.1002/9781118368909.ch13

White, D. M., Gerlach, S. C., Loring, P., Tidwell, A. C., & Chambers, M. C. (2007). Food and water security in a changing arctic climate. *Environmental Research Letters, 2*, 045018.

Wilson, E. H., & Sader, S. A. (2002). Detection of forest harvest type using multiple dates of Landsat TM imagery. *Remote Sensing of Environment, 80*, 385-396.

Woodcock, C., Allen, R., Anderson, M., Belward, A., Bindschadler, R., Cohen, W., . . . Wynne, R. (2008). Free access to Landsat imagery. *Science*, 1011.

Wulder, M. A., Masek, J. G., Cohen, W. B., Loveland, T. R., & Woodcock, C. E. (2012). Opening the archive: How free data has enabled the science and monitoring promise of Landsat. *Remote Sensing of Environment, 122*, 2-10.

Wulder, M. A., White, J. C., Loveland, T. R., Woodcock, C. E., Belward, A. S., Cohen, W. B., . . . Roy, D. P. (2016). The global Landsat archive: Status, consolidation, and direction. *Remote Sensing of Environment, 185*, 271-283.

Yang, D., Kane, D. L., Hinzman, L. D., Zhang, X., Zhang, T., & Ye, H. (2002). Siberian Lena River hydrologic regime and recent change. *Journal of Geophysical Research: Atmospheres (1984--2012), 107*, ACL--14.

Yoshikawa, K., & Hinzman, L. D. (2003). Shrinking thermokarst ponds and groundwater dynamics in discontinuous permafrost near Council, Alaska. *Permafrost and Periglacial Processes, 14*, 151-160.

Yoshikawa, K., Bolton, W. R., Romanovsky, V. E., Fukuda, M., & Hinzman, L. D. (2002). Impacts of wildfire on the permafrost in the boreal forests of Interior Alaska. *Journal of Geophysical Research: Atmospheres, 107*.

Zhang, T., Barry, R. G., Knowles, K., Heginbottom, J. A., & Brown, J. (2008). Statistics and characteristics of permafrost and ground-ice distribution in the Northern Hemisphere. *Polar Geography, 31*, 47-68.

Zhu, Z. (2017). Change detection using landsat time series: A review of frequencies, preprocessing, algorithms, and applications. *ISPRS Journal of Photogrammetry and Remote Sensing, 130*, 370-384.

Zhu, Z., & Woodcock, C. E. (2012). Object-based cloud and cloud shadow detection in Landsat imagery. *Remote Sensing of Environment, 118*, 83-94. doi:http://dx.doi.org/10.1016/j.rse.2011.10.028

Zhu, Z., Piao, S., Myneni, R. B., Huang, M., Zeng, Z., Canadell, J. G., . . . others. (2016). Greening of the Earth and its drivers. *Nature climate change, 6*, 791-795.

Zhu, Z., Wang, S., & Woodcock, C. E. (2015). Improvement and expansion of the Fmask algorithm: cloud, cloud shadow, and snow detection for Landsats 4–7, 8, and Sentinel 2 images. *Remote Sensing of Environment, 159*, 269-277. doi:http://dx.doi.org/10.1016/j.rse.2014.12.014

Zona, D., Lipson, D. A., Zulueta, R. C., Oberbauer, S. F., & Oechel, W. C. (2011). Microtopographic controls on ecosystem functioning in the Arctic Coastal Plain. *Journal of Geophysical Research: Biogeosciences, 116*.

Zubrzycki, S., Kutzbach, L., Grosse, G., Desyatkin, A., & Pfeiffer, E.-M. (2013). Organic carbon and total nitrogen stocks in soils of the Lena River Delta. *Biogeosciences, 10*, 3507.

A-1. Appendix: Reduced arctic tundra productivity linked with landform and climate change interactions

Lara, M.J.[1,2]; Nitze, I.[3,4]; Grosse, G.[3,4]; Martin, P.[5] & McGuire, A.D.[6]

[1] Department of Plant Biology, University of Illinois Urbana-Champaign, Urbana, IL, USA.

[2].Institute of Arctic Biology, University of Alaska Fairbanks, Fairbanks, AK, USA

[3] Alfred Wegener Institute Helmholtz Centre for Polar and Marine Research, Periglacial Research Unit, Potsdam, Germany

[4] Institute of Earth and Environmental Science, University of Potsdam, Potsdam, Germany

[5] U.S. Fish and Wildlife Service, Fairbanks, AK, USA

[6] U.S. Geological Survey, Alaska Cooperative Fish and Wildlife Research Unit, University of Alaska Fairbanks, Fairbanks, AK, USA.

In Revision for: Nature Scientific Reports

A-1.1 Abstract

Arctic tundra ecosystems have experienced unprecedented change associated with climate warming over recent decades. Across the Pan-Arctic, vegetation productivity and surface greenness have trended positively over the period of satellite observation. However, since 2011 these trends have slowed considerably, showing signs of browning in many regions. It is unclear what factors are driving this change and which regions/landforms will be most sensitive to future browning. Here we provide evidence linking decadal patterns in arctic greening and browning with regional climate change and local permafrost-driven landscape heterogeneity. We analyzed the spatial variability of decadal-scale trends in surface greenness across the Arctic Coastal Plain of northern Alaska (~60,000 km²) using the Landsat archive (1999-2014), in combination with novel 30 m classifications of polygonal tundra and regional watersheds, finding landscape heterogeneity and regional climate change to be the most important factors controlling historical greenness trends. Browning was linked to increased temperature and precipitation, with the exception of young landforms (developed following lake drainage), which will likely continue to green. Spatiotemporal model forecasting suggests carbon uptake potential to be reduced in response to warmer and/or wetter climatic

conditions, potentially increasing the net loss of carbon to the atmosphere, at a greater degree than previously expected.

A-1.2 Introduction

Over the past few decades, greening or increased vegetation productivity in Arctic tundra lowlands has been inferred from trends in satellite-derived Normalized Difference Vegetation Index (NDVI) (Bhatt, et al., 2010; Goetz, Bunn, Fiske, & Houghton, 2005; Jia, Epstein, & Walker, 2003). Researchers have speculated that these positive NDVI trends may be in response to reduced snow cover or warming, which may manifest on the landscape in the form of shrubification (Myers-Smith, et al., 2011), increased vegetation biomass (height, length, density) (Jia, Epstein, & Walker, 2003; Elmendorf, et al., 2012), changing phenoperiods (Bokhorst S. , Bjerke, Street, Callaghan, & Phoenix, 2011), or increased surface water associated with thermokarst (Liljedahl, et al., 2016). However, others have hypothesized that greening trends may have been in response to summer sea ice retreat (Bhatt, et al., 2014) or increased rates of infrastructure development associated with oil drilling and exploration (Raynolds & Walker, 2016). It is important to recognize that arctic tundra landscapes are highly heterogeneous and have historically been in a slow but continuous state of change associated with permafrost thaw and aggradation processes related to periglacial landscape dynamics (Jorgenson & Grosse, 2016). Consequently, patches of browning or negative NDVI trends have also been commonly observed across arctic tundra regions, but until recently the greening signal prevailed (Bhatt, et al., 2013). Since 2011, regional shifts toward surface browning have reversed the direction of the trend after nearly 33 years of arctic greening (Bhatt, et al., 2013). If such change in greening indeed corresponds with a reduction in vegetation productivity or carbon uptake capacity via photosynthesis, then nearly all ecosystem and earth system models have not foreseen this shift. Therefore, it is urgent to understand what may be controlling this spatiotemporal shift in browning across the Arctic and if this change is anomalous or represents a new long-term trajectory towards reduced vegetation productivity and carbon uptake in the Arctic tundra (Phoenix & Bjerke, 2016).

To date, our knowledge of circumpolar patterns of greening are derived from coarse-resolution sensors on board satellites, such as the global 8 km and 1 km resolution Advanced Very High Resolution Radiometer (AVHRR) and to a lesser extent the 1 to 0.25 km resolution

Moderate Resolution Imaging Spectroradiometer (MODIS) (Bhatt, et al., 2010; Jia, Epstein, & Walker, 2003), all of which robustly produce spectral observations spanning gradients of time and space. However, data products generated by these observation platforms are limited in their ability to evaluate meso- to fine-scale patterns that may control greening and browning at coarser resolutions (Bhatt, et al., 2013). Although, notable progress in the evaluation of landscape-level patterns of Arctic NDVI at fine-scales has been made (Raynolds & Walker, 2016; Nitze & Grosse, 2016; Pattison, Jorgenson, Raynolds, & Welker, 2015; Emmerton, et al., 2016; Frost, Epstein, & Walker, 2014; Morton, et al., 2012), these studies typically feature a similar physiography and/or climate, limiting the evaluation of how similar vegetation types and/or landforms may respond to different climate regimes. It is difficult to assess such patterns across Arctic regions for a variety of reasons, but perhaps most importantly because of the limited availability of high quality land cover datasets, which do not exist, are only regionally specific, or do not adequately represent heterogeneity across the tundra landscape to decipher meaningful patterns (Bartsch, Höfler, Kroisleitner, & Trofaier, 2016). Thus, without adequate spatial coverage and resolution of land cover data products used to link plot to landscape-level datasets, our ability to monitor and interpret patterns of change in the Arctic remains severely limited (Bartsch, Höfler, Kroisleitner, & Trofaier, 2016).

The Arctic Coastal Plain (ACP) of northern Alaska represents an expansive geographic region of tundra where decadal trends in greening have recently strengthened (Bhatt, et al., 2010; Bhatt, et al., 2013; Goetz, Bunn, Fiske, & Houghton, 2005), yet the magnitude of change varied nearly two-fold between the western and eastern ACP (i.e. eastern Chukchi and Beaufort, respectively) (Bhatt, et al., 2013). Concurrently, the climate of the ACP has changed and appears to be regionally specific, with some regions warming more extensively than others and increasing/decreasing in precipitation. Additionally, across the ACP, the spatial distribution of fine-scale tundra landforms (here after referred to as “geomorphic types”), varies significantly (Lara, et al., 2015; Jorgenson & Grunblatt, 2013; Jorgenson & Heiner, 2003), likely with different sensitivities to climate variability and change (Phoenix & Bjerke, 2016; Lara, et al., 2012). Here we focus on evaluating key factors controlling decadal scale surface NDVI (i.e. greening versus browning), and evaluate what regions and geomorphic types are most sensitive to future climate change. We calculated decadal NDVI trends using Landsat imagery from sensors, Thematic Mapper (TM), Enhanced Thematic Mapper Plus

(ETM+), and the Observing Land Imager (OLI), and assessed the variability in greenness from local to regional scales by using novel mapping techniques (Lara, et al., 2015) to create a polygonal tundra map (30 x 30 m resolution), which represents fifteen of the most dominant tundra geomorphic types (e.g., high/low-center polygon; Figure A-1.1), nested within regional watersheds (USGS, 2006), and ecological landscapes (Jorgenson & Grunblatt, 2013) spanning the ACP.

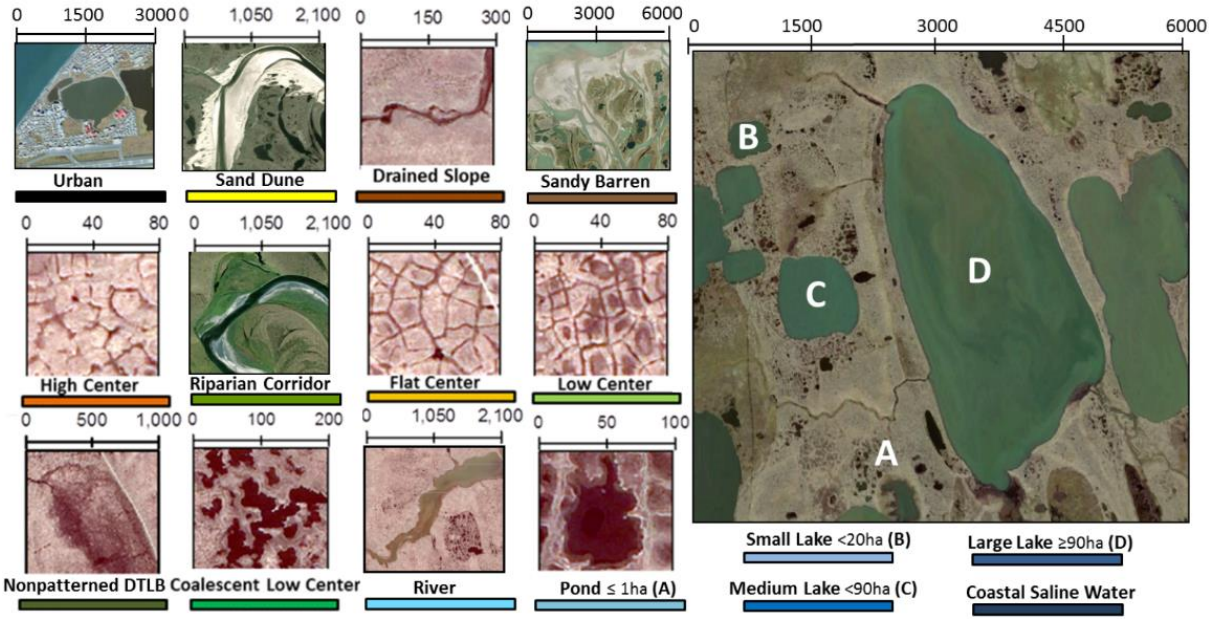

Figure A-1.1: Dominant geomorphic types on the Arctic Coastal Plain of northern Alaska, as observed from high resolution satellite imagery (de Jong, Bruin, Wit, Schaepman, & Dent, 2011) (copyright DigitalGlobe, Inc.). Figure created in Esri® ArcMap™ 10.4.

A-1.3 Methods

We studied the effects of climate and tundra geomorphic types on decadal scale trends in greening across the ACP, which stretches from the western coast along the Chukchi sea to the Beaufort coastal plains at the Alaskan/Canadian border (latitude: 68-71° N; longitude: 140-167° W). This region is representative of ~1.9 million km^2 of Arctic coastal tundra (Walker, et al., 2005), characterized by low topographic relief, with abundant ice wedge polygons (Kanevskiy, et al., 2013), thick permafrost (Jorgenson & Grunblatt, 2013), and predominantly wet sedge or herbaceous vegetation (Jorgenson & Heiner, 2003). Summer and winter temperatures range from 5 to 15 °C and -18 to -40 °C, respectively (www.ncdc.noaa.gov).

Annual precipitation is variable but typically ranges from 120-200 mm. We defined the ACP spatial domain by the geographic land area within the Northern/Southern Chukchi Sea Coast, Beaufort Sea Coast, Beaufort Coastal Plain, and a section of the Brooks Range Foothills on the Krusenstern Coastal Plain, all of which are composed of a high density of polygonal tundra or patterned ground (Figure A-1.1).

We expand upon a novel automated object based image analysis (OBIA) geomorphic mapping approach (Lara, et al., 2015), for characterizing tundra geomorphology across the ACP (58,691 km^2). The initial application of tundra mapping was developed for a polygonal coastal tundra ecosystem on the Barrow Peninsula (1800 km^2) (Lara, et al., 2015). Twelve LandSat-8 OLI (summer) satellite images (Supplementary Table 1) were processed and mosaicked within ArcGIS™ 10.4 (ESRI) for tundra geomorphology mapping. An OBIA land cover classifier (eCognition™ v.9.1, Trimble) was parameterized using various rules, thresholds, spectral indices, and proximity functions to differentiate between geomorphic types (Lara, Nitze, Grosse, & McGuire, in revision). Multiresolution segmentation and spectral difference algorithms were used to separate pixels into "image objects", which were divided into open water, aquatic, wet, moist, dry classes using reference data (i.e. field/ground truth points and high resolution aerial/satellite imagery) and class thresholds based on Normalized Difference Water Index (NDWI).

A series of proceeding functions were developed using individual and combined spectral bands, geometric object shapes/sizes (i.e. perimeter, area, roundness), and proximity functions to further differentiate respective geomorphology classes (Lara, Nitze, Grosse, & McGuire, in revision). Using this approach we mapped fifteen geomorphological and hydrologically distinct geomorphic types (Figure A-1.1, Figure A-1.2) at 30 x 30 m spatial resolution, including (qualitatively ranked from wet to dry), 1) coastal saline water, which commonly encroach into terrestrial lakes due to processes related to coastal erosion or lagoon formation, 2) lakes (large:>90ha, medium:≤90 and >20ha, small:≤20ha), 3) rivers, 4) ponds, 5) coalescent low-center polygons, 6) nonpatterned drained thaw lake basins, 7) low-center polygons, 8) flat-center polygons,9) riparian corridors 10) high-center polygons, 11) sandy barrens, 12) drained slopes, 13) sand dunes, 14) ice/snow, and 15) urban. Refer to Supplementary Table 2 for surface characteristics related to moisture, relief, and vegetation

communities specific to geomorphic type. For this analysis, all lake sizes were grouped into one “Lake” category.

The tundra geomorphic map (Figure A-1.2) was validated using an array of oblique aerial/ground based photography (Jorgenson & Heiner, 2003) and 249 high resolution (2.5 m resolution) SPOT-5 orthorectified image tiles covering >80% of the ACP (Supplementary Table 3; gina.alaska.edu) (Lara, Nitze, Grosse, & McGuire, in revision). We used a stratified random sampling design, where 1000 reference sites were used to evaluate map accuracy within both the Arctic Peaty Lowlands and the Arctic Sandy Lowlands (Jorgenson & Grunblatt, 2013).

We computed and analyzed NDVI trends using Landsat imagery following workflows developed for the Siberian, Lena River Delta (Nitze & Grosse, 2016), where each pixel has a temporal coverage of 40 to 110 observations collected between 1999-2014 (Lara, Nitze, Grosse, & McGuire, in revision). Throughout this paper, we refer to greening and browning as increased and decreased NDVI, respectively. Prior to data extraction from NDVI maps (Figure A-1.2), all coastal saline water, lakes, rivers, and urban pixels were removed. Primarily due to limited data acquisition across the ACP prior to 1999, we restrict decadal greenness trends (i.e. absolute change and percent change relative to 1999) to 1999-2014 throughout this paper.

Due to our use of multiple Landsat sensors (i.e. TM, ETM+, and OLI) within the NDVI trend map product, we calculated the sensor bias of NDVI at three different locations across Alaska, each containing a sample of 40,000 pixels (Lara, Nitze, Grosse, & McGuire, in revision). We found minor calibration differences between sensors (i.e. one percent of the signal), while sensor specific NDVI distributions were consistent (Lara, Nitze, Grosse, & McGuire, in revision).

Two data subsets were extracted from decadal NDVI products (i.e. absolute and percent change), where local to regional absolute and percent change in greenness was extracted for each geomorphic type in each Hydrological unit code 8 (HUC 8) watershed (Supplementary Figure 1, Supplementary Table 4), for use in boosted regression tree (BRT) (Elith, Leathwick, & Hastie, 2008) and multivariate regression model analysis (Supplementary Table 5), respectively. Hydrological unit code 8 watersheds were computed by the Alaska Watershed

and Stream Hydrography Enhanced Dataset Project (USGS, 2006), where each watershed was divided into two subunits (i.e. lowland/upland) associated with the second elevation quantile. Prior to spatial analysis, we identified outlier pixels by determining if NDVI change was > 75.0% or < -75.0% per decade, and used a nearest neighbor filtering algorithm for the recalculation of pixels within a 5 x 5 pixel window, which represented < 0.1% of all pixels on the ACP (residual unfiltered open water pixels).

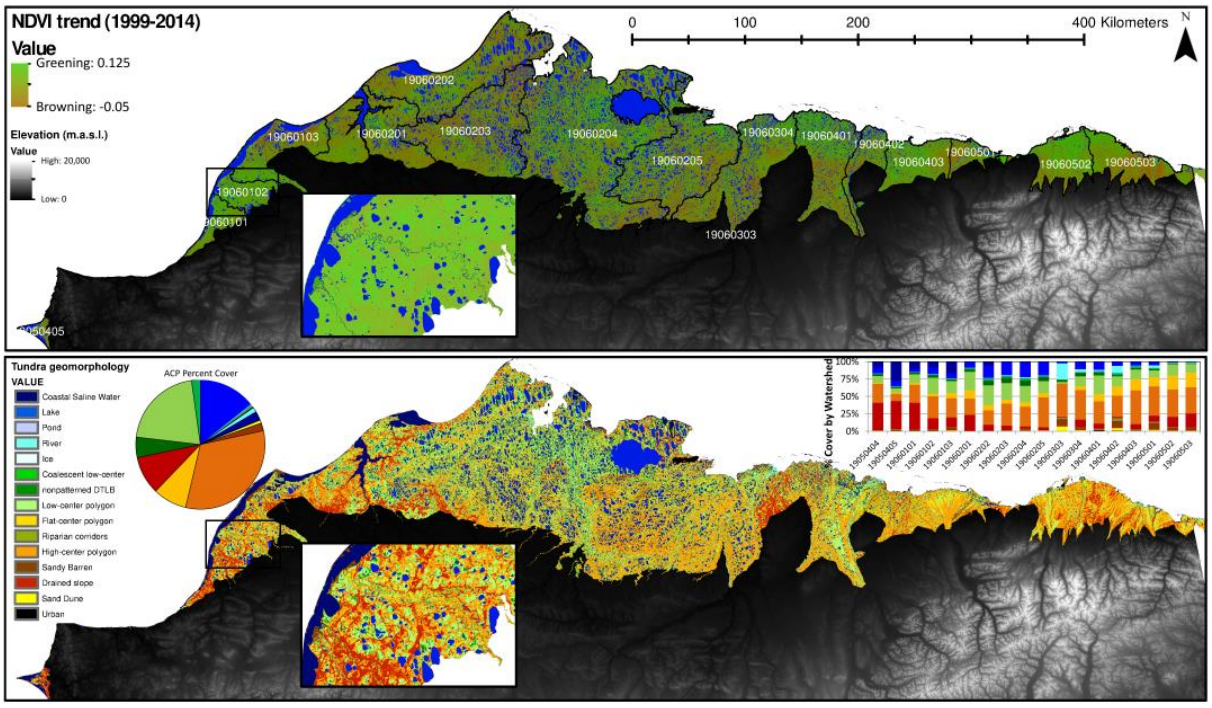

Figure A-1.2: Decadal time scale Landsat derived greenness (NDVI) trend and regional watersheds (top panel), and tundra geomorphology map (bottom panel). Tundra geomorphology map was developed at a 30 x 30 m spatial resolution (see methods for more details). Note the variability in geomorphology distribution associated with regional watersheds (stacked bar chart). Greenness Trend map was created following established workflows (Nitze & Grosse, 2016), while tundra geomorphology map was created in Trimble® eCognition™ v.9.1, both maps projected in Esri® ArcMap™ 10.4.

Datasets used in all analyses included the following predictor variables: elevation (60 m resolution), climate *normals* (1960-1999), *change* (difference between 2000-2010 and "normals"), and *anomalies* ("change"/"normal") for annual temperature, precipitation, and potential evapotranspiration downscaled to 771 m resolution by the Scenarios Network for Alaska and Arctic Planning (SNAP, 2017). In addition, we calculated the percent cover of soil moisture regime for each 771 x 771 m pixel (resolution standardized with input climate data), estimated by associations between geomorphic type and field observations[20,23,30]. We

combined geomorphic classes into their respective moisture categories as follows: *open water* (coastal saline water, lakes, rivers), *aquatic* (ponds, coalescent low-center polygons), *wet* (nonpatterned drained thaw lake basins, low-center polygons), *moist* (flat-center polygons, riparian corridors), *dry* (high-center polygons, drained slopes) and *other* (sandy barrens, sand dunes, ice/snow, urban).

The TreeNet Gradient Boosting machine, developed within the Salford Predictive Modeler™ v.8.0 (Salford Systems), was used to run all BRT analyses. A "shaving" procedure was used to iteratively remove and rerun the BRT analysis to minimize the mean squared error, where 80% (n=276) of the dataset was used for model development (i.e. learning) and 20% (n=53) was used for independent model evaluation (i.e. testing). BRT learning rate, tree complexity, and loss criterion, was set to 0.1, 6, and Huber-M, respectively. To ensure reproducibility, we used a seed state of 987654321 for model initialization. Partial dependency plots were used to show the response of individual predictor variables to the BRT analysis, using fitted functions[28]. Fitted functions detail the effect of a variable on the response after accounting for average effects of all other variables in the model (Elith, Leathwick, & Hastie, 2008).

Stepwise multivariate regression and Pearson's correlation analyses were ran in Jmp Pro™ v.10 (SAS). Input datasets used in the stepwise procedure (Supplementary Table 5) were all transformed to fit the assumptions of normality, and only important factors identified by the preceding BRT analysis were input into the stepwise procedure, used to predict regional greenness trends by fitting potentially important climate and/or environmental variables. A five-fold cross validation was concurrently performed, which divided the dataset into 5 subsets or 80:20 and iteratively used each 80% subset to predict the other 20% (e.g. k-1). The average R2 of all models was then calculated. Multivariate regression models were used to forecast change in the NDVI over the next decade (i.e. 2020-29), forced by the top five climate models to accurately represent Arctic and Alaskan regions (SNAP, 2017; Walsh, Chapman, Romanovsky, Christensen, & Stendel, 2008) used in the IPCC Fifth Assessment Report (). These included the Community Earth System Model 4 (NCAR-CCSM4), Coupled Model 3.0 (GFDL-CM3), ModelE/Russell (GISS-E2-R), Institut Pierre-Simon Laplace Coupled Model v5A (IPSL-CM5A), and the Coupled General Circulation Model v3.0 (MRI-CGCM3). Selected model runs included the AR5 representative concentration pathways RCPs

8.5 (high) and 4.5 (low). We assumed no change in tundra geomorphic type distribution for model simulations.

Table A-1.1: Projected change in precipitation and temperature (2020-2029) relative to climate normals for the Arctic Coastal Plain of northern Alaska by climate model and RCP emission scenario. Models are generally listed from lowest to highest projected change.

	Climate Model	RCP 4.5		RCP 8.5	
		Mean	Stdev	Mean	Stdev
Temperature change (°C)	MRI-CGCM3	1.37	0.22	1.21	0.18
	GISS-E2-R	1.4	0.767	1.94	0.114
	IPSL-CM5A	1.62	0.129	3.45	0.2
	NCAR-CCSM4	2.93	0.19	2.56	0.2
	GFDL-CM3	5.46	0.58	4.63	0.44
Precipitation change (mm)	MRI-CGCM3	9.27	15.96	17.18	10.28
	GISS-E2-R	31.27	10.31	16.52	11.98
	IPSL-CM5A	35.15	11.15	9.48	7.93
	NCAR-CCSM4	14.85	8.22	28.4	10.19
	GFDL-CM3	46.6	19.99	45.47	9.45

Temp. Normal (1960-1999): -11.51 °C, ±0.93
Precip. Normal (1960-1999): 236.63 mm, ±21.29

A-1.4 Results

We found the regional distribution of tundra geomorphic types and greenness to vary markedly across the Arctic Coastal Plain of northern Alaska (Figure A-1.2, Supplementary Figure 1). The newly developed tundra geomorphology map represented the spatial distribution of polygonal tundra well with an overall map accuracy and Cohen's Kappa coefficient of 76% and 0.73, respectively (Supplementary Table 3) (Lara, Nitze, Grosse, & McGuire, in revision). Map statistics indicated that high-center polygons, low-center polygons, and lakes were the predominant features across the ~60,000 km² ACP representing 69.3% of the total land cover area (Figure A-1.2). Watersheds ranged from 15 to 13,406 km² with a median of 2,128 km², which also varied in geomorphic type distribution (Figure A-1.2, Supplementary Figure 1). Historical NDVI trends varied between regional watersheds (Supplementary Figure 1), and across geomorphic types (Supplementary Tables S4-S5), suggesting that indeed trends in greening and browning are locally and regionally specific. Generally, across the ACP historical trends in NDVI (±standard deviation) differed by

geomorphic type as observed in ponds (0.005 ± 0.22), coalescent low-center (0.035 ± 0.11), nonpatterned drained thaw lake basins (0.032 ± 0.14), low-center (0.044 ± 0.06), flat-center (0.046 ± 0.05), riparian corridor (0.039 ± 0.13), high-center (0.041 ± 0.05), and drained slope (0.042 ± 0.04).

The gradient boosting analysis used 183 regression trees to construct a robust model that well represented the variability in historical greenness trends (learning/testing, R^2= 0.72, 0.62). After "shaving" or recursive predictor elimination procedures were complete, the final BRT analysis determined geomorphic type (100.0), temperature change (64.5), precipitation change (61.5), elevation (49.1), and precipitation normal (50.3) to be the most important factors (i.e. "variable importance", expressed as a percentage, scaled to the most important factor) controlling greenness trends (Figure A-1.3, Supplementary Figure 2). Partial dependency plots illustrate the strong control of geomorphic type on NDVI (Figure A-1.3), as generally, the higher the soil moisture the lower the rate of decadal greening. This is in line with partial dependency plots for precipitation and temperature change, which indicate that NDVI increased (i.e. greening) with reduced precipitation and cooler temperatures, whereas the NDVI decreased (i.e. browning) with increased precipitation and warmer temperatures (Figure A-1.4). Specifically, precipitation change greater than +31 mm was associated with substantial decreases in NDVI, while precipitation change associated with drier conditions, less than -10 mm increased NDVI. Interestingly, partial dependency plots for temperature change reveal that a potential NDVI threshold exists, inferring that if warming is limited to below +1.06 ^{o}C, the tundra continues to experience increased NDVI, but if warming exceeds that threshold NDVI is substantially reduced (Figure A-1.3, Supplementary Figure 2). However, greening may slowly resume after +1.70 ^{o}C of warming. Although elevation and precipitation normal did not account for most of the BRT model variability, they nevertheless notably impacted tundra geomorphology greenness (Figure A-1.3). Because temperature and precipitation change predictors did not meet the assumption of normality, we used log transformed temperature and precipitation anomalies in the ensuing multivariate analysis.

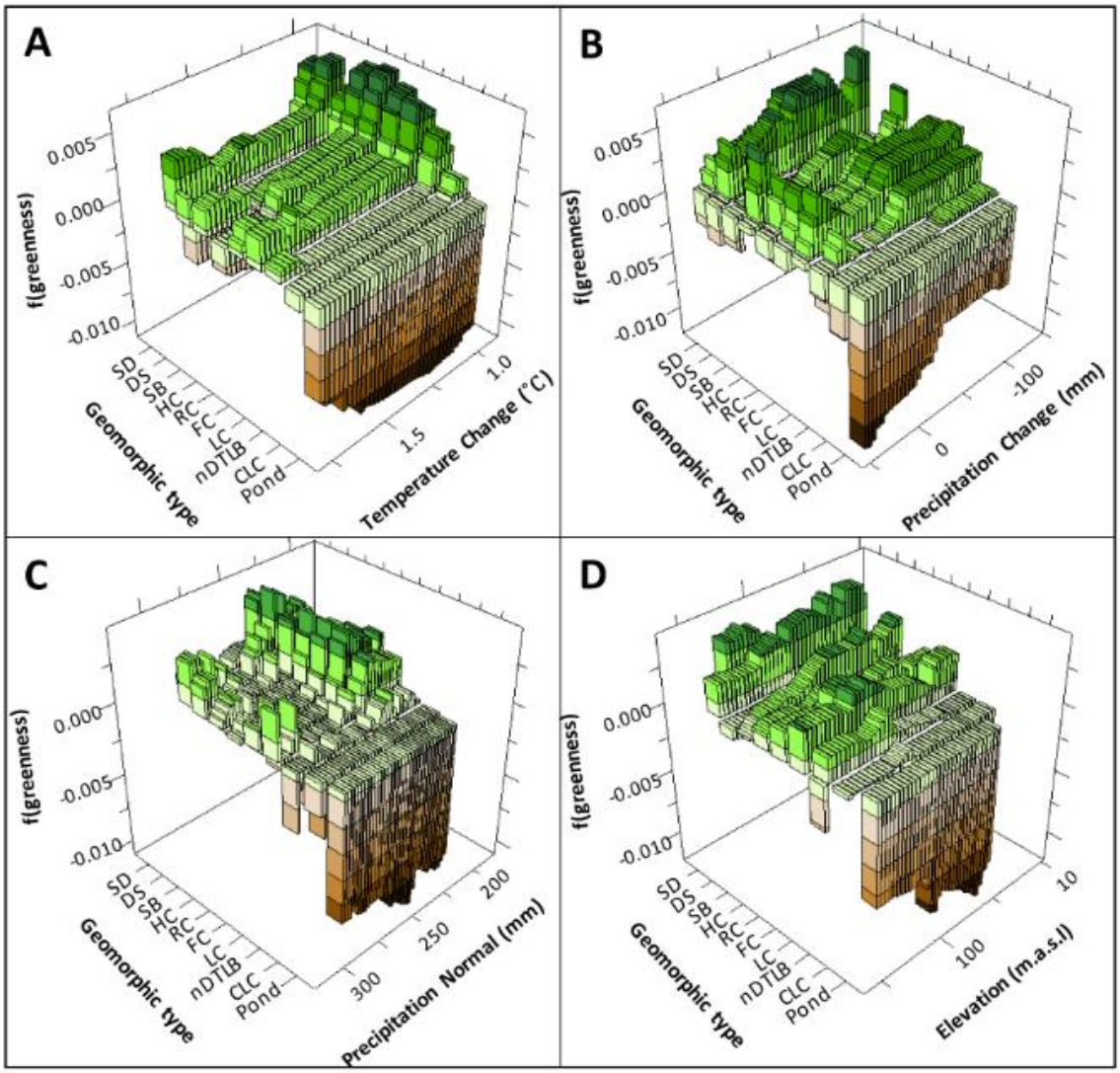

Figure A-1.3: Three dimensional partial dependency plots from gradient boosting analysis, illustrating the strong interaction between geomorphic type and temperature change (A), precipitation change (B), precipitation normal (C), and elevation (D). Generally, green and brown colors indicate positive and negative NDVI trends, respectively. Geomorphic type acronyms correspond to sandy barren (SB), sand dune (SD), drainage slope (DS), high-center polygon (HC), flat-center polygon (FC), low-center polygon (LC), riparian corridors (RC), nonpatterned drained thaw lake basins (nDTLB), and coalescent low-center polygon (CLC). Figure created in Salford Systems® TreeNet Salford Predictive Modeler™ v.8.0.

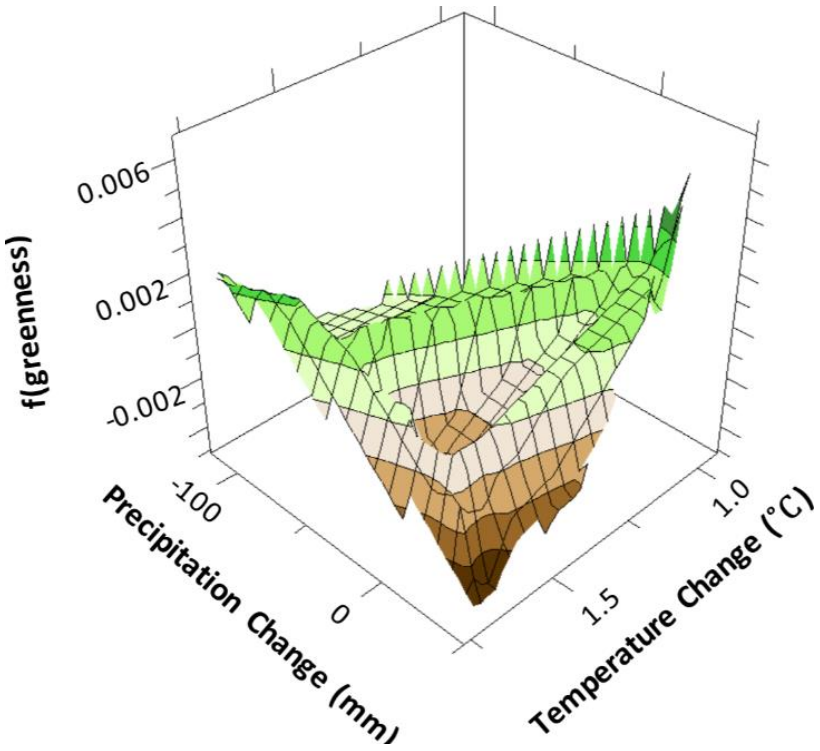

Figure A-1.4: Three dimensional partial dependency plot from gradient boosting analysis, illustrating the impact both temperature change and precipitation change may have on NDVI trends. Figure created in Salford Systems® TreeNet Salford Predictive Modeler™ v.8.0.

Table A-1.2: Pearson correlation coefficients for geomorphic type and potential drivers of NDVI change. Positive and negative correlations indicate greening and browning, respectively, with increasing climate or elevation parameters. See Figure A-1.3 for geomorphic type definitions. Bolded = p≤0.05; Italics = p ≤ 0.1.

Geomorphic Type	Temperature Anomaly	Precipitation Anomaly	Elevation
SD	0.13	**-0.43**	0.14
DS	-0.15	**-0.36**	-0.07
SB	**-0.58**	0.13	0.12
HC	**-0.42**	-0.07	-0.27
RC	**-0.48**	0.23	0.1
FC	-0.27	-0.13	-0.02
LC	**-0.49**	0.18	-0.18
nDTLB	*-0.31*	-0.19	0.03
CLC	-0.21	-0.21	0.17
Pond	**0.53**	**-0.60**	0.27

Regionally, the cross-validated multivariate regression model identified climate anomalies of precipitation and temperature, wet%, and elevation to be the most important predictors of historical NDVI trends ($R^2 = 0.49$, $p < 0.001$; five-fold cross validation $R^2=0.30$), which

suggests that increasing the decadal precipitation and temperature anomalies will decrease NDVI trends (i.e. browning), whereas an increase in wet% (i.e. nonpatterned drained thaw lake basins and low-center polygons) area will increase NDVI trends, both consistent with the BRT analysis. Furthermore, NDVI correlations with temperature and precipitation anomalies specific to geomorphic type, provide insight into regional scale controls on decadal NDVI change, as nearly all geomorphic types were sensitive to either temperature or precipitation anomalies (Table A-1.2). Significant decreases in NDVI with warmer temperatures were found for high-center polygons, low-center polygons, sandy barrens, nonpatterned drained thaw lake basins, and riparian corridors, whereas pond NDVI increased with warming. Decreases in NDVI were also identified for sand dunes, drained slopes, and ponds associated with increased precipitation (Table A-1.2). The geomorphic type most sensitive to temperature-mediated NDVI change, inferred from the highest decadal rate of change, were ponds (R^2 =0.28, p = 0.002, n=30) and riparian corridors (R^2 =0.30, p = 0.001, n=31), which increased and decreased NDVI with warming, respectively. In contrast, the geomorphic types most sensitive to precipitation-mediated reduction in the NDVI trend, were ponds (R^2 =0.36, p < 0.001, n=30), followed closely by drained slopes (R^2 =0.22, p = 0.008, n=31). We did not identify any significant relationships linking increased greening with increased precipitation among geomorphic types (Table A-1.2), consistent with BRT analysis and regression model. We associated climate sensitivities to patterns of greenness in sandy barrens and sand dunes to spectral differences associated with saturated versus unsaturated soils in response to warmer/wetter conditions and not explicitly a vegetation response in these sparsely vegetated types (Table A-1.2). Cumulatively, the relative importance of regional climate change for predicting the trajectory of greening versus browning was made strikingly apparent as ~61% or 35,800 km^2 of the ACP were sensitive to change in temperature, whereas only ~10% or 5,900 km^2 were sensitive to change in precipitation.

To evaluate how NDVI trends may change over the next decade (i.e. 2020-2029) derived multivariate models were applied across the ACP using five IPCC climate models and two emission scenarios (i.e. RCP 8.5 and 4.5). Generally, we find the projected change in NDVI will likely vary in magnitude and spatial distribution (Figure A-1.5) associated with future climate change (

Table A-1.1). Simulations suggest the greatest magnitude of change in greening and browning relative to long term trends (1984-2014) were for the MRI-CGCM3 RCP 8.5 and GFDL-CM3 RCP 8.5 climates, respectively (Figure A-1.6). However, although, predicted change in NDVI notably varied between climate models, emission scenarios add another degree of uncertainty, as highlighted by the trajectory shift from greening to browning found with NCAR-CCSM4 and IPSL-CM5A (Figure A-1.6). Moreover, predicted change in NDVI may be expected to vary spatially (Figure A-1.5), as all models indicate the western Chukchi coast will experience the greatest browning (Figure A-1.5) and the northeastern Beaufort coastal plain will experience the most greening. However, regions anticipated to have the highest greening trends by 2020-2029, also have the highest uncertainty or disagreement among model outputs (Figure A-1.5, Figure A-1.6).

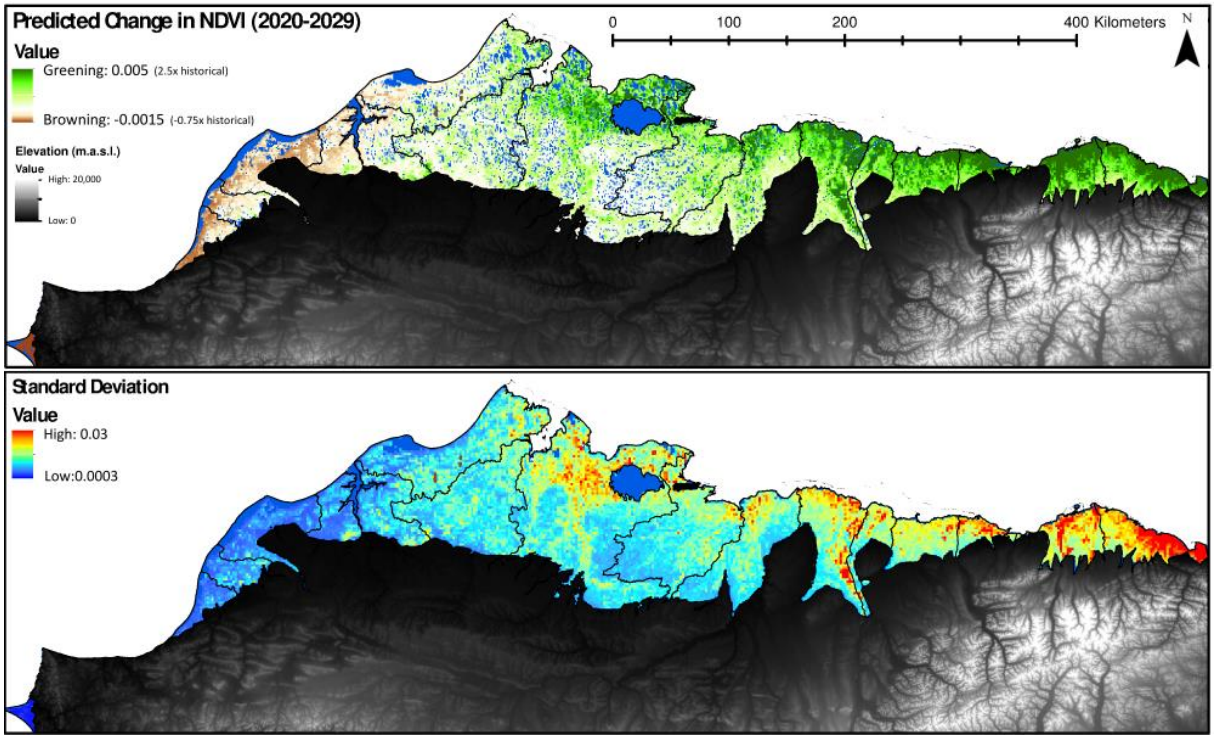

Figure A-1.5: Forecasted change in greenness (2020-2029) relative to the long-term (1984-2014: +0.002) trend, using the five model mean and AR5 8.5 emission scenario (top panel). As a metric of future greenness uncertainty, the standard deviation is computed for all model outputs and emission scenarios (bottom panel). Maps created in Esri® ArcMap™ 10.4.

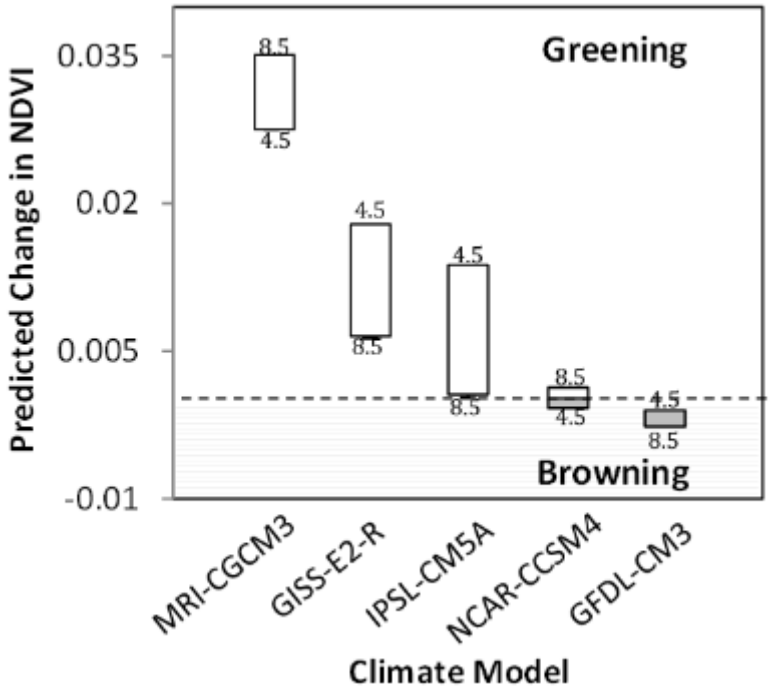

Figure A-1.6: Projected variability in greenness (2020-2029) using five climate models and two emission scenarios. Above and below dotted line represent greening and browning relative to long-term trends, respectively, while RCP emission scenario highs and lows are indicated by 8.5 and 4.5, respectively.

A-1.5 Discussion

As the climate continues to warm, we can expect an increased occurrence of browning across the Arctic Coastal Plain of northern Alaska (Figure A-1.2, A-1.5), but the rate at which the landscape browns, depends on the magnitude of temperature and precipitation change (Figure A-1.4), with the exception of young geomorphic types from recently drained lakes (e.g. nonpatterned drained thaw lake basins and low-center polygons) that will likely continue to green. These patterns were highlighted in our analysis as historical NDVI trends varied by tundra geomorphic type (Figure A-1.3). Browning was particularly sensitive to elevated temperature and/or precipitation (Table A-1.2), both of which are expected to increase across arctic tundra regions (ACIA, 2005).

To evaluate how NDVI might change over the next decade (2020-2029) we developed a predictive multivariate model using a range of decadal scale climate and geospatial data inputs (Supplementary Table 5), selected as important predictors in the BRT analysis.

However, because of the decadal scale input datasets (Bieniek, et al., 2015), we are unable to explicitly and directly evaluate year-specific observations of browning (i.e. 2011) (Bhatt, et al., 2013) within this modeling framework. We still were able to provide insights into potential controls on greenness. Generally, it has been postulated that recent observations of browning, may have arisen from an array of annual/seasonal regional/site level changes that are largely correlated with decadal climate and land cover datasets, such as the delayed onset of the growing season and longer snow cover (Bieniek, et al., 2015), summer cloudiness (Bieniek, et al., 2015), winter warming (Bokhorst S. F., Bjerke, Tommervik, Callaghan, & Phoenix, 2009; Bokhorst, Tommervik, Callaghan, Phoenix, & Bjerke, 2012), or thermokarst development (Raynolds & Walker, 2016). Model NDVI forecasting (Figure A-1.5, Figure A-1.6) identified greening to likely continue on the ACP, but will be highly dependent on the amplitude of future climate change (Figure A-1.6,

Table A-1.1). Predicted NDVI by 2020-2029 was found to be variable dependent on climate model and RCP (Figure A-1.6), but the magnitude in greening versus browning was generally explained by the inverse relationship between temperature and NDVI change, as the greater the temperature change the lower the NDVI. Generally, all simulations find regional specific browning to occur on the southwestern Chukchi coast and greening to occur on the northeastern Beaufort coastal plains but the magnitudes vary by climate model (Figure A-1.6).

Trends in MaxNDVI estimated from Global Inventory Modeling and Mapping Studies (GIMMS) datasets[11], were similar to that evaluated using Landsat imagery (Figure A-1.2), though, higher resolution imagery and newly developed maps enabled the evaluation of spatiotemporal heterogeneity in greenness, highlighting the strong interaction between landforms and climate influencing greenness trends (Table A-1.2, Figure A-1.3). We found trends in greenness were specific to geomorphic type and sensitive to either temperature or precipitation change (Table A-1.2), with the exception of tundra ponds, which was found to be sensitive to both climatic drivers. The climatic sensitivity of tundra ponds is in line with hypothesized drivers of vegetation change (Lara, et al., 2012; Andresen & Lougheed, 2015; Villarreal, et al., 2012), as warmer temperatures may thaw permafrost and increase available nutrients in the water column (Lougheed, Butler, McEwen, & Hobbie, 2011; Reyes & Lougheed, 2015), potentially enabling the expansion of aquatic macrophytes (Andresen & Lougheed, 2015; Villarreal, et al., 2012). Increased precipitation is likely to increase the ratio

of standing water to macrophyte distribution in ponds, manifesting as an increased browning signal. Although, relationships between decreasing NDVI and increasing temperature were identified for high-center polygons, low-center polygons, and riparian corridors (Table A-1.2), it is important to note that significant greening occurred across all geomorphic types until temperatures warmed beyond +1.06 ^{o}C, where NDVI decreases sharply (Figure A-1.3, Supplementary Figure 2). However, the greening trend may begin to increase if warming is greater than ~+1.70 ^{o}C. Generally, at the landscape scale, we find greening to increase if precipitation decreases more than -10 mm relative to normal precipitation patterns, whereas browning increased with precipitation. This pattern was likely identified in response to either wetting/drying of water saturated tundra soils and/or increased cloudiness (associated with increased precipitation) that may decrease productivity in response to a reduction in photosynthetically active radiation (Bieniek, et al., 2015). However, although NDVI generally decreased with increased precipitation, this pattern was not able to explain the regionally specific variability in NDVI that occurred among landforms (Figure A-1.3).

Although this work increases our understanding of past and future greenness patterns in arctic coastal tundra ecosystems, it is unclear if differences in greening versus browning trends for each geomorphic type (Table A-1.2) were associated with local disturbances. For example, the prevalence of thermokarst pits (upland tundra: drained slopes and high-center polygons) and associated increases in surface wetness (Liljedahl, et al., 2016; Jorgenson, Shur, & Pullman, 2006), seasonally dependent patterns of herbivore activity (low-center polygons, nonpatterned drained thaw lake basins, and drained slopes) (Batzli, Pitelka, & Cameron, 1983), and/or plant community change (ponds, nonpatterned drained thaw lake basins, low-center polygons) (Villarreal, et al., 2012). The interpretation of greening and browning signals spanning small to large spatiotemporal scales (i.e plot to pan-Arctic) is difficult, as multiple climatic and environmental factors influence NDVI trends, which are likely related but spatially dependent. For example, at the Pan-Arctic scale, greening has been linked to extra-Arctic processes such as CO_2 fertilization (Zhu, et al., 2016; Los, 2013), atmospheric nitrogen deposition (Zhu, et al., 2016), as well as marine-terrestrial interactions related to ocean circulation patterns and sea ice decline (Bhatt, et al., 2010; Bhatt, et al., 2013). At the landscape scale, other local processes such as the frequency and magnitude of wildfires (Goetz, Bunn, Fiske, & Houghton, 2005), regional climate change (Bhatt, et al., 2010; Goetz, Bunn, Fiske, & Houghton, 2005; Bhatt, et al., 2013; Zhu, et al., 2016; Los, 2013),

infrastructure development (Raynolds & Walker, 2016), and shrubification (Forbes, Fauria, & Zetterberg, 2010) are important. We find the distribution of tundra geomorphology (Figure A-1.3, Table A-1.2, Supplementary Figure 2) is another major factor modulating greening and browning signals in ways previously not recognized. At the fine scale, processes related to changing patterns of phenology (de Jong, Bruin, Wit, Schaepman, & Dent, 2011), plant community change (Lara, et al., 2012), herbivory (Lara, Johnson, Andresen, Hollister, & Tweedie, 2017; Olofsson, Tommervik, & Callaghan, 2012) and surface hydrology driven by thermokarst (Liljedahl, et al., 2016; Raynolds, et al., 2014) can also notably impact vegetation productivity and NDVI. A holistic ecosystem perspective is required to unravel the spatiotemporal complexity involved with changing tundra greenness, which we are beginning to understand, but are limited by few observational data and comprehensive analyses across scales and platforms of observation.

Our findings indicate tundra geomorphic heterogeneity and regional climate change are dominant factors controlling decadal scale trends in greenness. Thus, a detailed understanding of how climate interacts with landforms is necessary for evaluating the spatiotemporal ecosystem interactions that impact regional-global patterns of plant productivity. Although, correlations between NDVI and vegetation productivity are robust across latitudinal gradients (Epstein, et al., 2012), our findings have several implications for local controls on vegetation productivity in the expansive (~1.9 million km^2) (Walker, et al., 2005) arctic coastal tundra ecosystem. Ecosystem and earth system models generally predict plant productivity to increase associated with projected climate change across northern latitudes. However, assuming our observed greenness trends correspond with productivity trends, we predict a reduction in carbon uptake potential across much of the ACP of northern Alaska in response to projected warmer and/or wetter climatic conditions. In combination, with deeper active layer depths (Koven, et al., 2015) exposing increased soil carbon to decomposition (Koven, et al., 2015), this further increases the potential for a net loss of carbon to the atmosphere, at a greater degree than previously expected. It is important to better understand how regional-global trends in greening and browning correspond to both local and regional phenomena to enhance our predictive capacity and ability to detect change in plant productivity across the Pan-Arctic to constrain our predictive uncertainty related to the future state and fate of global climate change (Abbott, et al., 2016).

Supplementary Table 1: Mosaicked Landsat scenes used to create the tundra geomorphology map

Product ID	Sensor	Satellite	Year*	Month*	Day*
LC80690112013249LGN00	OLI/TIRS	Landsat 8	2013	Sept.	5
LC80720112013254LGN00	OLI/TIRS	Landsat 8	2013	Sept.	10
LC80740112014191LGN00	OLI/TIRS	Landsat 8	2014	July	9
LC80770102013193LGN00	OLI/TIRS	Landsat 8	2013	July	11
LC80770112013193LGN00	OLI/TIRS	Landsat 8	2013	July	11
LC80790102013191LGN00	OLI/TIRS	Landsat 8	2013	July	9
LC80800102014217LGN00	OLI/TIRS	Landsat 8	2014	Aug.	4
LC80800112014249LGN00	OLI/TIRS	Landsat 8	2014	Sept.	5
LC80820122013244LGN00	OLI/TIRS	Landsat 8	2013	Aug.	31
LC80830102014222LGN00	OLI/TIRS	Landsat 8	2014	Aug.	9
LC80830112014190LGN00	OLI/TIRS	Landsat 8	2014	July	8
LC80840122013194LGN00	OLI/TIRS	Landsat 8	2013	July	12

*Acquisition date

Supplementary Table 2: Characteristics of dominant Alaskan Arctic Coastal Plain tundra geomorphic types

Geomorphic Type	Moisture Regime	Relief	Vegetation Community
Coastal saline water	Open water	Low	vegetation absent
Lakes & River	Open water	Low	vegetation absent
Pond	Aquatic	Low	(i) Aquatic Arctophila, Carex, (ii) Dupontia graminoid , (iii) Seasonal short grass
Coalescent low-center	Aquatic	Intermediate	(i) Seasonally flooded Carex, Dupontia, Eriophorum graminoid tundra, (ii) Aquatic Arctophila, Carex, Dupontia graminoid tundra
Nonpatterned DTLB	Moist-Wet	Low	(i) Moist Carex, Poa, Luzula graminoid tundra, (ii) Wet Carex, Sphagnum graminoid tundra, (iii) Seasonally flooded Carex, Dupontia, Eriophorum graminoid
Low-center	Moist-Wet	Intermediate	(i) Moist Carex, Poa, Luzula graminoid tundra, (ii) Wet Carex, Sphagnum graminoid tundra, (iii) Seasonally flooded Carex, Dupontia, Eriophorum graminoid tundra
Sandy barren	Moist-Wet	Low	(i) Deciduous scrub
Flat-center	Dry-Moist	Intermediate	(i) Dry Arctagrostis, Luzula, Poa, Carex graminoid tundra, (ii) Moist Carex, Poa, Luzula graminoid tundra
Riparian corridors	Dry-Moist	Intermediate	(i) Deciduous dwarf scrub, (ii) Evergreen dwarf scru b
High-center	Dry	High	(i) Dry Arctagrostis, Luzula, Poa, Carex graminoid tundra
Drainage slope	Very Dry	Very high	(i) Dry Lichen Heath,(ii) Dry Arctagrostis, Luzula, Poa, Carex graminoid tundra
Sand dune	Very Dry	Very high	(i) Seasonal desert herb vegetation, (ii) Deciduous desert scrub

DTLB = Drained Thaw Lake Basin

Supplementary Table 3: Accuracy assessment represented as a confusion matrix. Bolded diagonal values within the matrix represent correctly identified pixels, where User and Producer accuracies are presented on the right vertical axis and bottom horizontal axis.

		Reference Sites												User accuracy
Classification	Geomorphic type	SB	SD	RC	DS	HC	FC	LC	nDTLB	CLC	Pond	River	Lake	CS	
	Sandy Barren	**12**				2	2			2		1			**63.2%**
	Sand Dune	3	**12**			2									**70.6%**
	Riparian Corridors			**4**				1							**80.0%**
	Drained Slope				**50**	19	4								**68.5%**
	High Center				35	**215**	30	22	2						**70.7%**
	Flat Center					11	**32**	3							**69.6%**
	Low Center			1	6	34	11	**152**	5	7			2		**69.7%**
	NonpatternedDTLB					3		16	**53**	1		1	2		**69.7%**
	Coalescent Low C							2	2	**15**			2		**71.4%**
	Pond										**18**				**100.0%**
	River	2							2	2		**10**			**62.5%**
	Lake							1	1				**156**		**98.7%**
	Coastal Saline Water												1	**28**	**96.6%**
	Producer accuracy	70.6%	100.0%	80.0%	54.9%	75.2%	40.5%	77.2%	81.5%	55.6%	100.0%	83.3%	95.7%	100.0%	**1000**
	Overall accuracy		**75.7%**												
	Cohens Kappa		**0.725**												

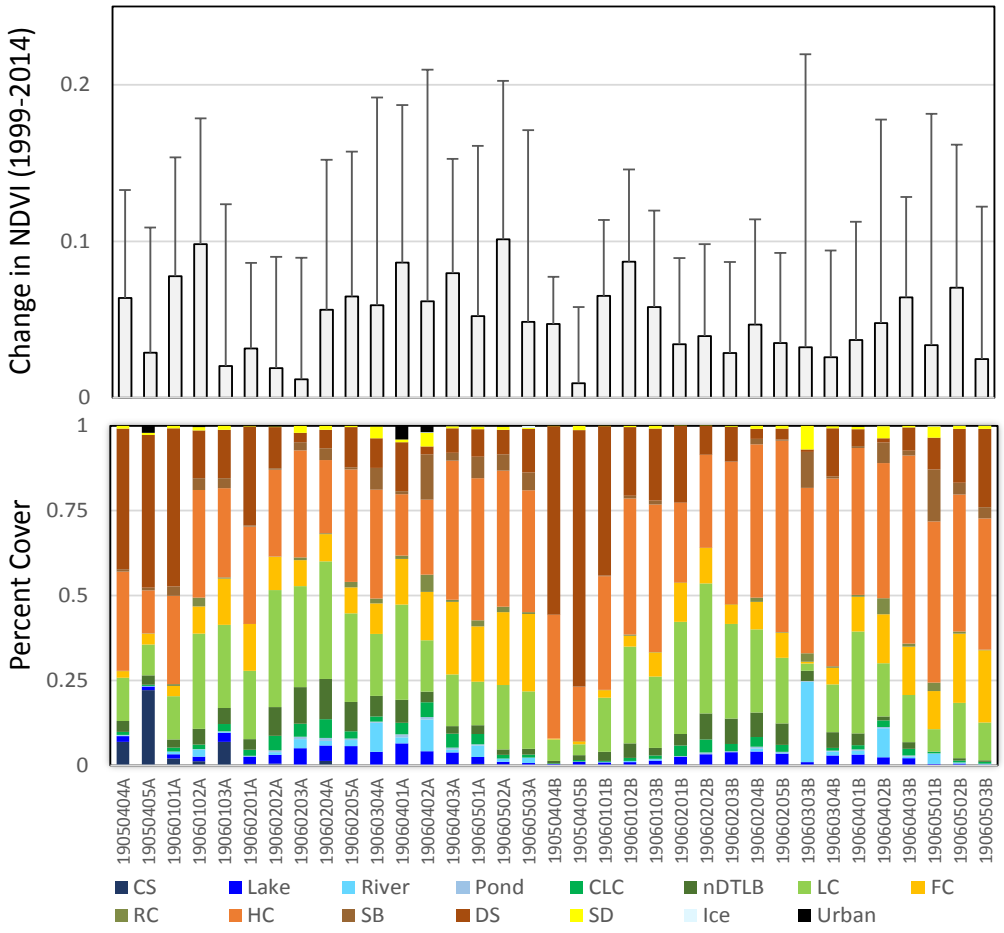

Supplementary Figure 1: Watershed specific patterns in NDVI with standard deviation bars (top panel) and percent cover of tundra geomorphic type (bottom panel).

Supplementary Table 4: Absolute change (1999-2014) in NDVI by geomorphic type within each watershed on the Alaskan Arctic Coastal Plains. Blank cells indicate the geomorphic type was not present in the associated watershed

HUC_8	Low/ Upland	CLC	DS	FC	HC	LC	nDTLB	POND	RC	SB	SD
19050405a	Low	0.015	0.010	0.022	0.020	0.031	0.005	-0.027	0.036	0.021	0.047
19050405b	Up	0.010	-0.001	0.019	0.020	0.043	0.037	0.000	0.036	0.014	0.031
19060101a	Low	0.021	0.044	0.042	0.050	0.056	0.041	-0.019	0.037	0.032	0.011
19060101b	Up	0.021	0.044	0.042	0.050	0.056	0.041	-0.019	0.037	0.032	0.011
19060102a	Low	0.034	0.046	0.050	0.056	0.057	0.060		0.060	0.041	0.036
19060102b	Up	0.039	0.043	0.048	0.050	0.060	0.050		0.048	0.033	0.045
19060103a	Low	-0.007	0.010	0.005	0.016	0.014	-0.005	-0.050	0.035	0.013	0.015
19060103b	Up	0.036	0.025	0.032	0.031	0.043	0.032	-0.006	0.047	0.026	0.055
19060201a	Low	0.010	0.017	0.017	0.017	0.019	0.011	-0.003	0.013	0.009	0.003
19060201b	Up	0.013	0.018	0.018	0.022	0.020	0.008	-0.011	0.005	0.014	-0.006
19060202a	Low	0.005	0.008	0.010	0.010	0.012	0.008	-0.013	0.000	0.007	0.018
19060202b	Up	0.013	0.013	0.021	0.023	0.021	0.013	0.005	0.020	0.026	0.006
19060203a	Low	-0.002	0.004	0.007	0.011	0.005	0.000	-0.015	0.001	0.012	0.009
19060203b	Up	0.007	0.014	0.017	0.021	0.014	0.006	-0.010	0.010	0.006	0.008
19060204a	Low	0.024	0.030	0.028	0.029	0.027	0.022	0.011	0.026	0.011	0.026
19060204b	Up	0.019	0.028	0.028	0.025	0.024	0.017	0.002	0.022	0.021	0.027
19060205a	Low	0.023	0.036	0.035	0.034	0.032	0.025	0.014	0.004	0.009	0.021
19060205b	Up	0.014	0.023	0.022	0.019	0.019	0.012	0.000	0.016	0.009	0.023
19060303b	Up		0.109	0.056	-0.001	0.000	-0.009	-0.026	0.076	0.028	0.022
19060304a	Low	0.006	0.040	0.029	0.023	0.029	0.019	-0.004	0.011	0.018	0.040
19060304b	Up	0.007	0.019	0.021	0.011	0.016	0.009	-0.002	0.014	0.026	0.035
19060401a	Low	0.022	0.049	0.040	0.039	0.036	0.026	-0.002	0.018	0.009	0.021
19060401b	Up	0.014	0.024	0.021	0.014	0.019	0.012	0.001	0.018	0.005	0.024
19060402a	Low	0.015	0.031	0.022	0.024	0.024	0.015	-0.021	0.019	0.003	0.015
19060402b	Up	0.021	0.019	0.017	0.016	0.015	0.018	0.002	0.006	0.019	0.030
19060403a	Low	0.029	0.043	0.034	0.041	0.034	0.037	0.008	0.040	0.022	0.043
19060403b	Up	0.033	0.034	0.034	0.031	0.036	0.037	0.012	0.041	0.024	0.047
19060501a	Low	0.019	0.051	0.012	0.027	0.019	0.029	0.023	0.007	0.011	0.016
19060501b	Up	0.011	0.026	-0.002	0.011	0.002	0.026	0.015	0.003	0.009	0.025
19060502a	Low	0.030	0.064	0.062	0.056	0.049	0.036	0.001	0.019	0.018	0.041
19060502b	Up	0.029	0.035	0.043	0.037	0.034	0.034	0.028	0.020	0.018	0.042
19060503a	Low	0.004	0.041	0.022	0.025	0.005	0.008	0.009	-0.013	0.021	0.031
19060503b	Up	0.020	0.015	0.011	0.012	-0.001	0.028	0.029	0.011	0.015	0.034

Supplementary Table 5: Percent change in NDVI by geomorphic type within each watershed on the Alaskan Arctic Coastal Plains. Blank cells indicate the geomorphic type was not present in the associated watershed.

HUC_8	Lowland/ Upland	CLC	DS	FC	HC	LC	MDW	POND	RSHB	SB	SD
19050405a	L	3.4%	2.5%	4.5%	4.1%	6.1%	1.7%	-3.7%	6.9%	4.4%	8.8%
19050405b	U	2.6%	0.7%	4.0%	4.3%	8.1%	7.1%	0.8%	7.0%	3.3%	6.1%
19060101a	L	4.5%	8.3%	7.9%	9.3%	10.3%	7.8%	-2.4%	7.1%	6.3%	2.6%
19060101b	U	4.5%	8.3%	7.9%	9.3%	10.3%	7.8%	-2.4%	7.1%	6.3%	2.6%
19060102a	L	6.6%	8.6%	9.3%	10.4%	10.6%	11.0%		11.0%	7.8%	7.0%
19060102b	U	7.5%	8.2%	9.0%	9.3%	11.0%	9.3%		8.9%	6.5%	8.4%
19060103a	L	-0.4%	2.6%	1.7%	3.5%	3.3%	0.0%	-7.7%	6.8%	3.0%	3.3%
19060103b	U	6.9%	5.1%	6.2%	6.2%	8.2%	6.3%	-0.2%	8.8%	5.2%	10.2%
19060201a	L	2.6%	3.6%	3.7%	3.7%	4.0%	2.7%	0.4%	3.0%	2.4%	1.4%
19060201b	U	3.0%	3.8%	3.9%	4.6%	4.2%	2.3%	-1.0%	1.6%	3.3%	-0.1%
19060202a	L	1.7%	2.2%	2.6%	2.6%	2.8%	2.3%	-1.3%	0.9%	2.0%	3.8%
19060202b	U	3.1%	3.1%	4.4%	4.8%	4.4%	3.0%	1.7%	4.2%	5.3%	1.9%
19060203a	L	0.5%	1.6%	2.0%	2.7%	1.8%	0.8%	-1.7%	1.0%	2.9%	2.4%
19060203b	U	2.0%	3.3%	3.6%	4.3%	3.2%	1.9%	-0.8%	2.6%	1.9%	2.3%
19060204a	L	4.9%	5.9%	5.6%	5.7%	5.5%	4.6%	2.7%	5.2%	2.7%	5.3%
19060204b	U	4.0%	5.6%	5.6%	5.1%	5.0%	3.7%	1.2%	4.6%	4.4%	5.4%
19060205a	L	4.8%	7.0%	6.7%	6.6%	6.2%	5.1%	3.3%	1.6%	2.3%	4.4%
19060205b	U	3.2%	4.8%	4.6%	4.1%	4.0%	2.9%	0.9%	3.5%	2.4%	4.7%
19060303b	U	0.8%	19.2%	10.3%	0.6%	0.9%	-0.7%	-3.6%	13.8%	5.6%	4.6%
19060304a	L	1.8%	7.7%	5.8%	4.8%	5.8%	4.0%	0.2%	2.8%	3.9%	7.6%
19060304b	U	2.1%	4.1%	4.3%	2.6%	3.5%	2.4%	0.4%	3.3%	5.2%	6.7%
19060401a	L	4.5%	9.2%	7.6%	7.5%	7.0%	5.3%	0.4%	3.8%	2.3%	4.4%
19060401b	U	3.2%	4.9%	4.4%	3.2%	4.0%	2.8%	1.1%	3.9%	1.7%	4.8%
19060402a	L	3.5%	6.1%	4.5%	5.0%	4.9%	3.5%	-2.7%	4.0%	1.4%	3.4%
19060402b	U	4.5%	4.1%	3.7%	3.5%	3.4%	3.9%	1.2%	1.8%	4.0%	5.8%
19060403a	L	5.8%	8.1%	6.7%	7.8%	6.6%	7.1%	2.2%	7.6%	4.5%	8.2%
19060403b	U	6.5%	6.6%	6.7%	6.1%	6.9%	7.2%	2.8%	7.8%	5.0%	8.8%
19060501a	L	4.0%	9.4%	2.8%	5.3%	4.0%	5.7%	4.7%	2.1%	2.7%	3.5%
19060501b	U	2.7%	5.3%	0.5%	2.6%	1.2%	5.2%	3.4%	1.3%	2.3%	5.2%
19060502a	L	6.0%	11.7%	11.3%	10.3%	9.1%	7.0%	0.9%	4.1%	3.8%	7.7%
19060502b	U	5.7%	6.8%	8.2%	7.1%	6.5%	6.6%	5.6%	4.2%	4.0%	8.0%
19060503a	L	1.5%	7.8%	4.6%	5.2%	1.6%	2.2%	2.4%	-1.4%	4.3%	6.1%
19060503b	U	4.3%	3.3%	2.8%	2.8%	0.7%	5.5%	5.8%	2.7%	3.3%	6.5%

Supplementary Table 6: Summary of parameters used in multiple regression analysis. Variables Tnorm, Tdiff, Pnorm, Pdiff, Elev, represent the long term temperature normal (°C), temperature change (°C), precipitation normal (mm), precipitation change (mm), and elevation (m). See methods for soil moisture details.

HUC_8	Low/ Upland	NDVI trend	NDVI% change	Tnorm	Tdiff	Pnorm	Pdiff	Elev	Dry%	Moist%	Wet%	Aqua%	Water%	Other%
19050405a	L	0.0147	2.9	-6.669	1.032	286.99	17.58	20.78	65.1	2.8	20.0	0.7	9.4	2.0
19060101a	L	0.0459	7.8	-9.973	0.964	265.51	27.44	40.16	70.4	2.6	21.9	1.6	1.9	1.7
19060102a	L	0.0535	9.8	-10.04	0.954	238.65	26.23	43.66	41.6	7.2	44.6	1.6	2.8	2.2
19060103a	L	0.0105	2.0	-10.48	1.058	243.74	28.48	34.9	38.3	9.9	41.3	2.8	5.7	1.9
19060201a	L	0.0168	3.1	-11.1	1.355	240.6	39.27	48.9	53.6	9.6	32.3	2.2	2.0	0.3
19060202a	L	0.0098	1.9	-11.7	1.634	214.57	36.58	34.99	30.7	6.0	52.3	4.9	5.8	0.3
19060203a	L	0.0062	1.2	-11.89	1.685	224.45	38.97	44.4	29.0	5.4	51.5	4.8	7.5	1.9
19060204a	L	0.0261	5.6	-12.05	1.657	225.27	20.04	21.31	22.1	5.1	57.0	6.5	7.3	1.9
19060205a	L	0.0317	6.5	-11.92	1.658	224.08	-3.44	29.18	38.9	6.0	45.0	2.8	7.0	0.4
19060304a	L	0.026	5.9	-11.73	1.618	214.84	-13.3	29.43	41.6	7.9	37.2	2.4	5.7	5.1
19060401a	L	0.0368	8.6	-11.8	1.627	214.93	-19.5	37.13	29.8	9.9	47.7	4.9	5.2	2.6
19060402a	L	0.0181	6.2	-11.66	1.629	221.92	-26.4	35.31	28.1	16.6	31.4	7.3	5.5	11.1
19060403a	L	0.0372	8.0	-11.66	1.645	234.16	-41.3	29.24	48.0	16.4	26.2	5.8	2.0	1.5
19060501a	L	0.0232	5.2	-11.66	1.679	254.92	-65.3	22.97	51.3	14.0	23.7	4.4	2.9	3.7
19060502a	L	0.0531	10.1	-11.67	1.748	284.63	-108	34.68	46.9	17.2	30.5	1.4	1.0	2.9
19060503a	L	0.0225	4.9	-11.56	1.598	267.57	-95.3	32.86	49.1	17.6	28.0	1.3	0.9	3.1
19060303b	U	0.0081	3.2	-11.45	1.5	240.19	-9.94	158.9	65.9	3.0	10.3	0.3	8.7	11.7
19060304b	U	0.0132	2.6	-11.69	1.556	226.36	-11.7	159.7	65.1	3.7	26.3	1.3	2.9	0.7
19060401b	U	0.0166	3.7	-11.32	1.561	218.74	-17.4	208.9	43.1	7.2	44.8	2.0	2.3	0.7
19060402b	U	0.0159	4.8	-11.3	1.553	223.7	-21	216.5	44.9	15.7	27.6	3.2	3.3	5.3
19060403b	U	0.0324	6.4	-11.56	1.602	240.41	-38.9	188.8	60.7	11.1	23.2	2.8	1.2	0.9
19060501b	U	0.01	3.4	-11.57	1.64	255.37	-60.2	163.6	64.5	11.7	11.5	0.7	1.0	10.7
19060502b	U	0.0367	7.0	-11.15	1.732	297.35	-114	345.4	55.8	15.7	25.3	0.8	0.3	2.1
19060503b	U	0.0114	2.5	-11.2	1.647	280.61	-104	262.3	63.0	16.4	17.7	0.7	0.2	2.1
19050405b	U	0.0053	0.9	-6.81	1.022	288.75	18.01	99.39	89.3	0.7	6.8	0.7	1.8	0.7
19060101b	U	0.0405	6.5	-10.65	0.979	270.54	28.97	98.68	71.0	1.6	25.6	0.3	1.3	0.1
19060102b	U	0.0509	8.7	-11.14	1.035	253.25	29.55	104.4	51.5	2.3	42.0	1.0	2.7	0.5
19060103b	U	0.0325	5.8	-10.95	1.115	246.75	31.17	114	59.7	5.0	32.1	1.2	1.0	0.9
19060201b	U	0.019	3.4	-11.36	1.396	242.85	41.79	98.99	39.8	7.5	47.1	3.6	2.0	0.0
19060202b	U	0.0199	4.0	-11.6	1.568	223.78	41.05	75.89	29.5	6.5	56.8	4.5	2.7	0.0
19060203b	U	0.0162	2.9	-11.87	1.629	234.99	42.76	98.78	44.8	3.7	45.5	2.6	3.3	0.1
19060204b	U	0.0242	4.7	-11.95	1.564	241.61	20.29	156.7	42.4	6.1	41.9	3.7	4.7	1.1
19060205b	U	0.0187	3.5	-11.86	1.582	232.67	-0.72	162.2	52.8	5.0	34.1	2.6	5.0	0.5

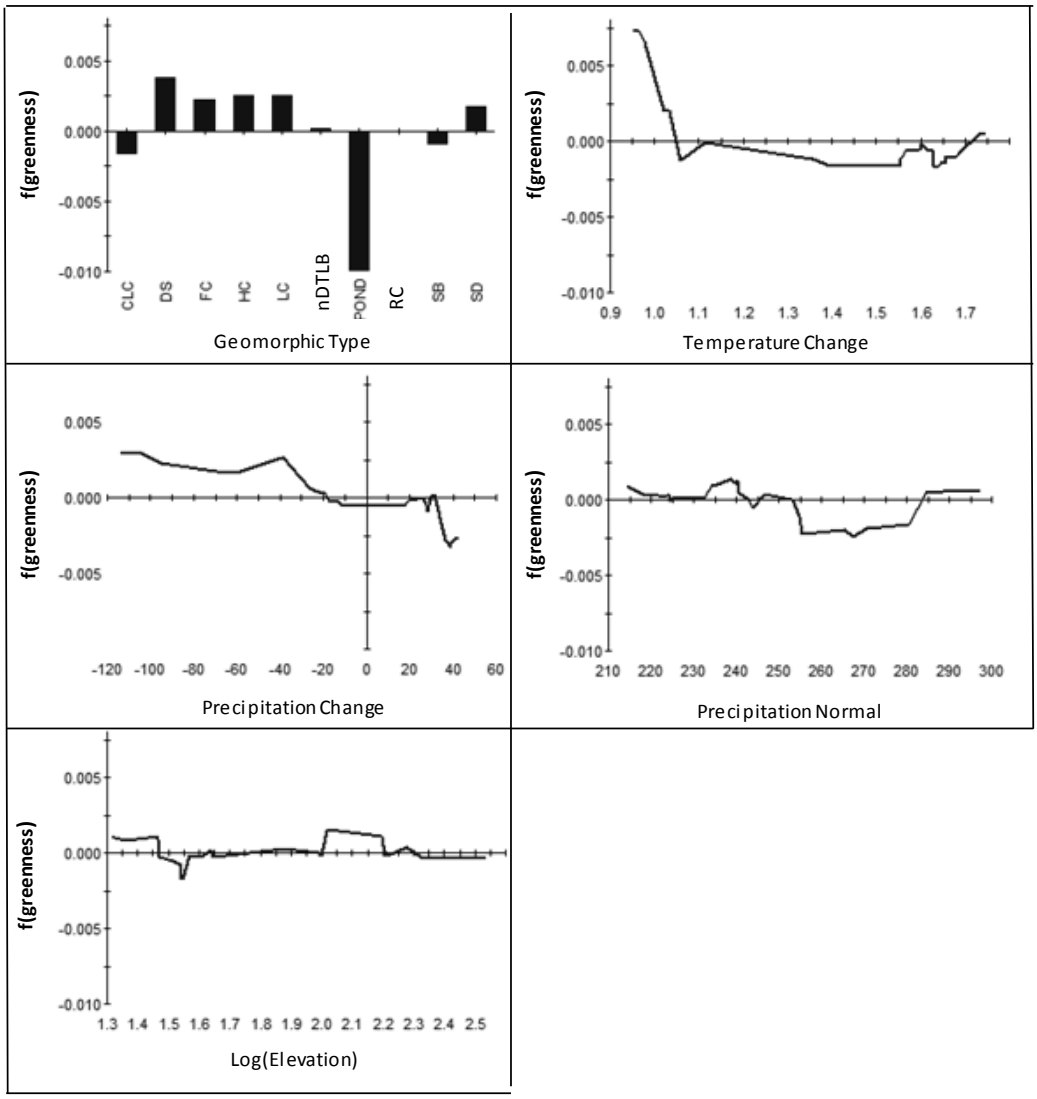

Supplementary Figure 2: Two dimensional partial dependency plots, illustrating the effect of Land cover, Temperature change, Precipitation change, Precipitation normal, and elevation on surface greenness.

Danksagung/Acknowledgements

First and foremost, I want to thank Guido Grosse my main supervisor. He provided me with the amazing opportunity to work at AWI, introduced me to permafrost science and its awesome community. He made all adventurous journeys to amazing places in Alaska and Siberia possible and he supported me in all work related and personal matters.

Furthermore, I would also thank my two other Committee members Hartmut Asche and Christian Hüttich, who helped me to keep on track and focus on the important tasks to finish my PhD project.

I participated in four different amazing expeditions. Each of them was unique in a kind and an unforgettable experience. Without all the participants and organizers, this would not have been possible. Specific thanks go to the pilots Jim Webster and Jim Kincaid and the POLAR 5 crew, who brought me and my dear colleagues home safely after long working days in the field or many hours in the air on many exciting aerial survey flights. In this regard I specifically want to thank Ben Jones, who is a great, helpful and inspiring colleague. It has been and will be a pleasure working with you.

Furthermore, I want to thank the colleagues of the PETA-CARB group, specifically my office mates Matthias Fuchs, Sebastian Laboor, and Lydia Stolpmann. Merci vielmals. I had some real fun time with you and received a lot of support over the last years. I also want to acknowledge my fellow Post-Doc PETA-CARBians Jens Strauss, Josefine Lenz and Frank Günther for their company during expeditions, and their help in every regard. Michael Angelopoulos, Anna Irrgang and George Tanski motivated and supported me during the final weeks of my thesis. I want to acknowledge all my other colleagues at AWI Potsdam and anywhere else, who have not been named so far, but helped me in many different regards, e.g. science, logistics and also personal matters.

The POLMAR Team, Claudia Hanfland and Claudia Sprengel, organized many helpful courses to improve my skills in many aspects and provided funding for different conferences. Here, I also want to acknowledge Potsdam Graduate School (PoGS) for their travel support.

I want to thank all my co-authors, who helped me working on my papers, supporting me with a lot of insight to the different topics we worked on. I really appreciate your effort and

exceptionally quick response times. I also want to thank all the authors, who invited me to join their paper projects, particularly Mark Lara.

Although not directly related to this PhD, I want to acknowledge all my former colleagues, particularly Fiona Cawkwell and Brian Barrett, who introduced me into science and paved the way to my PhD project.

Furthermore, I want to thank the European Research Council and the European Space Agency for funding my work.

Schlussendlich möchte ich mich bei meiner Familie bedanken, meinen Eltern Sieglinde und Jürgen, aber insbesondere bei meiner Frau Anja, die mich immer auf meinem Weg begleitet hat.

Eidesstattliche Erklärung

Hiermit versichere ich, dass ich die vorliegende Arbeit selbstständig verfasst und keine anderen als die angegebenen Quellen und Hilfsmittel verwendet habe.

Ich habe diese kumulative Dissertation am Alfred-Wegener-Institut, Helmholtz Zentrum für Polar und Meeresforschung in Potsdam erarbeitet und in englischer Sprache angefertigt. Diese Dissertation wird erstmalig und ausschließlich an der Universität Potsdam eingereicht.

Die dem Promotionsverfahren zugrundeliegende Promotionsordnung vom 18.09.2013 ist mir bekannt.

Potsdam, den 15.11.2017

_____

Ingmar Nitze